A MODEL-BASED CLINICALLY-RELEVANT CHEMOTHERAPY SCHEDULING ALGORITHM FOR ANTICANCER AGENTS

by

Thang Ho

B.S., Chemical Engineering, University of Arkansas, 2007

M.S., Chemical Engineering, University of Arkansas, 2009

Submitted to the Graduate Faculty of

the Swanson School of Engineering in partial fulfillment

of the requirements for the degree of

Doctor of Philosophy

University of Pittsburgh

2014

UNIVERSITY OF PITTSBURGH

SWANSON SCHOOL OF ENGINEERING

This dissertation was presented

by

Thang Ho

It was defended on

November 24, 2014

and approved by

Robert S. Parker, Ph.D., Professor, Department of Chemical and Petroleum Engineering

Ipsita Banerjee, Ph.D., Assistant Professor, Department of Chemical and Petroleum Engineering

Gilles Clermont, Ph.D., Professor, Department of Critical Care Medicine

Sanjeev Shroff, Ph.D., Distinguished Professor, Department of Biological Engineering

Dissertation Director: Robert S. Parker, Ph.D., Professor, Department of Chemical and Petroleum Engineering

A MODEL-BASED CLINICALLY-RELEVANT CHEMOTHERAPY SCHEDULING ALGORITHM FOR ANTICANCER AGENTS

Thang Ho, PhD

University of Pittsburgh, 2014

Chemotherapy is the most commonly employed method for systemic cancer treatment of solid tumors and their metastases. The balance between cancer cell elimination and host toxicity minimization remains a challenge for clinicians when deploying chemotherapy treatments. Our approach explicitly incorporates treatment-induced toxicities into the schedule design. As a case study, we synthesize administration schedules for docetaxel, a widely used chemotherapeutic employed as a monoagent or in combination for the treatment of a variety of cancers. The primary adverse effect of docetaxel treatment is myelosuppression, characterized by neutropenia, a low plasma absolute neutrophil count (ANC). Through the use of model-based systems engineering tools, this thesis provides treatment schedules for docetaxel used alone and in combination therapies with platinum-based agents that reduce toxic side effects and improve patient outcomes.

The algorithm employs models of tumor growth, drug pharmacokinetics, and pharmacodynamics for both anticancer effects and toxicity, as characterized by ANC. Also included is a toxicity-rescue therapy, granulocyte colony stimulating factor (G-CSF), that serves to elevate ANC. The single-agent docetaxel chemotherapy schedule minimizes tumor volume over a multi-cycle horizon, subject to toxicity and logistical constraints imposed by clinical practice.

This single-agent chemotherapy scheduling formulation is extended to combination chemotherapy using docetaxel-cisplatin or docetaxel-carboplatin drug pairs. The two platinum agents display different toxicities, with cisplatin exhibiting loss of kidney function as measured by

creatinine clearance and carboplatin demonstrating the same myelosuppressive effects as docetaxel. These case studies provide two different challenges to the algorithm: (i) cisplatin scheduling significantly increases the number of variables and constraints, as well as an additional toxicity, thereby challenging the computational engine and formulation; (ii) carboplatins overlapping toxicity tests the ability of the algorithm to schedule drugs with different mechanisms of action (they act in different phases of the cellular growth cycle) with the same toxic side effects. The simulated results demonstrate the algorithms flexibility in scheduling both docetaxel and cisplatin or carboplatin treatments for effective tumor elimination and clinically acceptable toxicities.

Overall, a clinically-relevant chemotherapy scheduling and optimization algorithm is provided for designing single-agent and combination chemotherapies, when toxicity and pharmacokinetic/pharmacodynamic information is available. Furthermore, the algorithm can be extended to patient-specific treatment by updating the pharmacokinetic/pharmacodynamic models as data are collected during treatment.

TABLE OF CONTENTS

LIST OF TABLES

LIST OF FIGURES

PREFACE

Ralp Waldo Emerson said: "Life is a journey, not a destination". My PhD journey has been a humbling experience where obstacles and challenges have made me who I am today. I would not be able to complete this journey without the support of my dearest family, friends, co-workers, students, and professors. I would like to thank my dearest family for their enduring efforts in supporting me for the past 11 years in the U.S. You are the world to me. My mother has been my inspiration to continue my education and become a life long learner. My father has been a champion in teaching me about the business side of education and how to build my network. I am blessed to have them as my parents and as guidance throughout my PhD.

I am thankful for the friends I made throughout my study in the U.S. Some of them, I no longer keep in touch with due to various circumstances. I am still thankful to encounter and have them as parts of my journey. I would like to thank Chris, Dameon, Heather, Alice, Tom, Brady, and Christina for their support during the time when I was changing my PhD study to Pittsburgh. I would like to thank Ari, Natania, and Tim for making the PhD process less painful and stressful and their time and effort to edit this document.

I would like to thank professor Bob and Karen Beitle, who helped me during my time in the U.S. Finally, I would like to thank professor Bob Parker for his expertise and encouragement during my PhD. He has made the PhD process enjoyable and inspirational.

"Whatsoever thy hand findeth to do, do it with thy might; for there is no work, nor device, nor knowledge, nor wisdom, in the grave, whither thou goest." Ecclesiastes 9:10

1.0 INTRODUCTION

The cost of healthcare has become a burden for many families in the United States. In 2012, the countrys total health expenditure was $2.8 trillion, with a cost per capita of $9,000 [10, 11], and U.S. healthcare spending was 17.9% of the national gross domestic product [11]. From 2008-2011, the average annual growth in healthcare cost was 3.9% [11]. With the Affordable Care Act (ACA) taking effect in the beginning of 2014, national healthcare spending is projected to grow at an average of 6% annually from 2014-2020 [12]. Moreover, by 2020, the U.S. population is projected to be at 334 million with 18% of the population greater than 65 years old [13]. The implementation of ACA and the aging population will not only impact the national healthcare cost but also burden the current healthcare system. More specifically, the U.S. is projected to experience a shortage of 91,500 doctors by 2020 [14]. In order to aid the current healthcare system and ease the burden for clinicians and nurses, systems medicine is an emerging field that bridges mathematics, computer science, and engineering and applies these tools to problems in the clinical setting. The tools developed by systems researchers can help clinicians to understand patient dynamics, disease progression, and drug interactions so that they can design the best treatment for patients.

A main focus in the field of systems medicine is to develop a decision support system (DSS) – a model-based tool employing patient-specific or patient-tailorable mathematical models and systems engineering tools that can help clinicians improve treatment decision-making by providing treatment recommendations, and the underlying rationale, through a clinician-friendly interface. A schematic of how a typical DSS would be implemented in current clinical settings is shown in Figure 1. Patient data and clinician input are entered into the DSS through the interface, where the mathematical representation of the patient and treatment design algorithm are executed to provide suggested treatments or interventions.

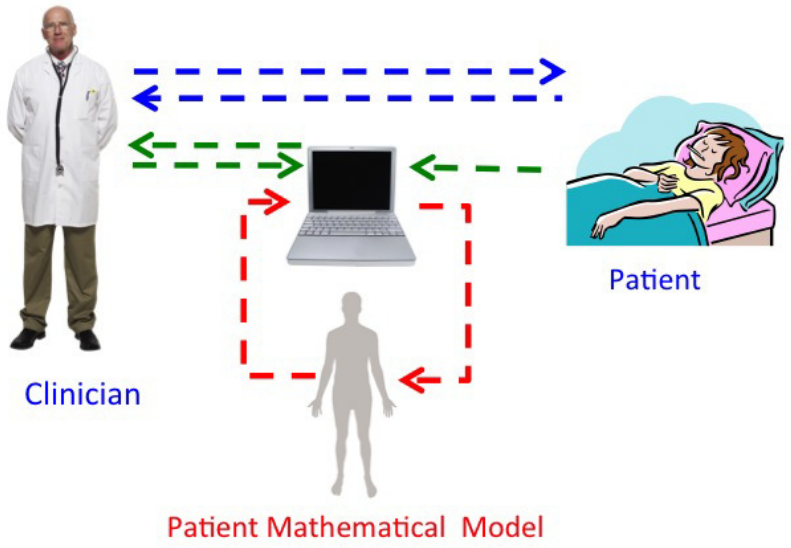

Figure 1: Schematic of systems medicine role in current healthcare settings

The DSS, through its patient-tailored mathematical models, is able to predict the patient's disease trajectory and response to modeled interventions over a clinician-selected future time window in order design treatments and minimize complications over that span.

A model plays an important role in designing model based DSS because it is a communication gate between the clinicians and the DSS developers. It helps to capture patient and disease dynamics and predict future dynamics for the optimization algorithm to design treatment. A successful model would be a key in DSS development. Patient dynamics are often modeled by different types of mathematical models from empirical to biologically based models. Empirical models are often correlation between effects and outcomes represented by one or two equations and often lack predictive ability [15, 16]. Compartmental models are also used to capture the patient dynamics. In this case, each compartment is represented by a differential equation (*i.e.* change in drug concentration versus time), and more compartments are added to capture different dynamics [17, 18]. Compartmental models have better predictive capacities than empirical models but can only be used to capture simple

systems (*i.e.* pharmacokinetic model) [17, 18]. Physiologically-based models are also used to capture patient dynamics [5, 19]. Tissues in a patient body are modeled as different compartments (set of differential equations) with blood flow connecting each compartment. The physiologically-based model captures different local dynamics at tissue level [5, 19]. Biologically-based models are also used to capture patient dynamics. In this case, the each equation (often ordinary differential equation) represents an element (*i.e.* cells, biomarkers) in a signaling cascades [8, 20]. Physiologically-based models and biologically-based models not only accurately capture patient dynamics but also have better patient dynamic prediction than empirical models and simple compartmental models [8, 5].

While physiologically based models and biologically models accurately capture patients dynamics, they often have a large number of equations and parameters with nonlinearities inherent in the nature of the biological system. These large models create difficulties in capturing patient specific dynamics and treatment optimization. The difficulty is the challenge in real-time tailoring patient dynamics because existences of local minima in parameter optimization landscape. Another challenge is the number of variables and constraints increases dramatically during optimization when these models are used [21]. Therefore, the number of equations and parameters in a physiologically based model and a biologically based model should be reduced in order to facilitate implementation into a DSS more effectively. Physiologically based models and biologically-based models are often used as the starting point for model reduction and parameter reduction due to their large equation dimension and complex parameter interaction space. Through mathematical methods [22, 23], a model is reduced to the smallest number of equations that are still able to capture the data, or in the case of dynamic models, the process response. The output sensitive parameters are then identified for model adjustment to capture patient-specific dynamics. Model reduction and parameter identification helps a model to be easily implement an optimization algorithm to design patient treatment action.

Another important aspect of the DSS is the treatment design. The treatment design algorithm should be clinically driven rather than just theory driven. This is because in a clinical setting, the treatment decisions made by clinicians are discrete in time (act/do not) and follow certain protocols or experience. Therefore, the goal of the DSS is to aid clinicians

in patient treatment design and to help the current healthcare system. A DSS should then be able to design a clinically-relevant treatment that can be deployed in clinical settings without major modifications to current practice.

The synthesis of a mathematical model from biological information will be provided through an example of neutrophil response to both an inflammatory challenge and myelosuppression-inducing chemotherapy. From this biologically-based model structure, formal model reduction reduction will provide a lower-order model that can be more readily used within an optimization algorithm for chemotherapy scheduling. A clinically-relevant chemotherapy scheduling problem with docetaxel alone and in combination with platinum agents provides a generalizable DSS design for chemotherapy scheduling. This combination of dynamic modeling, analysis, and systems engineering tools are a demonstration of how mathematical tools can be translated to address clinical problems with the goal of improving patient outcome, reducing healthcare costs, and lowering the tedious work burden for caregivers.

1.1 NEUTROPHIL DYNAMICS AND MODELS

1.1.1 Neutrophil Biology

Neutrophils comprise 55-70% of all leukocytes [24]. As core components of the innate immune response, their main biological functions include chemotaxis to sites of inflammation, phagocytosis of microbial products or particles, and microbial killing [24, 25]. Under the influence of the Granulocyte-Colony Stimulating Factor (G-CSF), pluripotent hematopoietic stem cell types commit to becoming granulocytes or precursor cells [25]. These precursor cells mature continuously through different cell phases and become circulating neutrophils [26]. Stem cells committed to becoming granulocytes are converted into mature neutrophils andreside in the bone marrow [27]. The mature neutrophil count in plasma is tightly regulated by G-CSF [28]. G-CSF also maintains neutrophils, known as the marginal pool, that are ready for rapid recruitment in case of an infection. However, neutrophils only circulate for 6-8 hours in the blood stream before undergoing apoptosis [26].

Apoptotic neutrophils are digested by macrophages. A decrease in neutrophil degradation rate (resulting from depletion of the circulating neutrophil count, from any cause) causes macrophages to release interleukin-23 (IL-23) [29]. The increase in IL-23 production activates T-cells to secrete interleukin-17 (IL-17) [29]. The increase in IL-17 production activates stromal cells, which produce G-CSF to increase neutrophil production and ultimately circulating neutrophil count [29].

1.1.1.1 Inflammatory Response of Neutrophils:

1.1.1.2 Inflammatory Response of Neutrophils When the host has been invaded by bacteria or pathogens, macrophages first come into contact with them [30]. Macrophages release inflammatory cytokines, including TNF-α, IL-1α, and IL-6. These inflammatory cytokines activate the endothelial layer and recruit neutrophils toward the site of infection [31, 32]. Neutrophils are activated by these cytokines and kill bacteria or pathogens at the site of infection by its apoptotic mechanism. When bacteria or pathogens are eliminated from the host, anti-inflammatory cytokines, including IL-12, IL-1ra, and IL-10, are secreted to deactivate or neutralize the inflammatory response [32]. Neutrophils undergo apoptosis when the body begins to return to its homeostasis state.

When an injury or infection is severe, the inflammatory response could be overactivated. In this case, the resulting cytokine release leads to elevated circulating (systemic) levels, which results in the activation of remote endothelial layers in non-infected tissues [26]. As a side-effect, neutrophils migrate into these tissues and cause damage to them as a result of activated neutrophils creating a cell-killing local environment with no pathogen to attack. In a severe case, it could lead to multi-organ failure, as seen in sepsis [24].

A balance in the inflammatory response needs to be maintained for patients with infection or trauma to improve outcomes and survival rates. Understanding neutrophils and inflammatory response dynamics through experiments and mathematical models provides information to develop new treatments and interventions. For example, the mouse model has been used to study how sepsis can occur [32]. The cecal ligation and puncture (CLP) procedure has been used to mimic the effects of sepsis injury in the patient [32]. The CLP

model includes a punctuation of the cecum allowing the release of fecal material into the peritoneal cavity to trigger to immune response due to a polymicrobial infection [32]. Time series blood samples are drawn and analyzed for inflammatory and anti-inflammatory markers. The hypothesis of CLP challenge could trigger the same inflammatory response in sepsis. The data observed in this study suggested that CLP is a good model to capture the inflammatory response observed in sepsis.. However, the mouse inflammatory system does not represent the human system. Although certain differences in inflammatory responses between mice and humans have been established [33, 34, 35], the CLP mouse model can be used to explain certain inflammatory response in human sepsis and test the effectiveness of sepsis treatments.

The human inflammatory response is also studied through the infusion of bacterial endotoxin (lipopolysaccharide (LPS)) into healthy volunteers to trigger the inflammatory response [32, 7, 36]. The infusion of endotoxin triggers the inflammatory response, and blood samples are drawn to analyze different inflammatory markers during the experiment [7]. LPS challenge is believed to trigger the same inflammatory cascade as sepsis. However, since endotoxin challenge is the injection of a very small quantity of gram-negative bacterial membrane components into the patient, recovery will always occur, meaning that the inflammatory system will always return to homeostasis. The advantage of the LPS challenge in humans is that it can elucidate certain key mechanisms specific to the human inflammatory response. Neutrophil and G-CSF time series data can be used to develop a mathematical model to capture the neutrophil and G-CSF responses to the inflammatory challenge.

1.1.1.3 Chemotherapy-Induced Neutropenia: Cancer chemotherapy is a systemic treatment targeting the elimination of cancerous cells, but often having negative side-effects (*i.e.*, toxicity) on other cells in the body. Toxicity is the main limitation imposed on cancer chemotherapy, and the side-effects vary among chemotherapeutic agents [1, 37, 38]. Docetaxel and paclitaxel cause myelosuppression, often manifesting as neutropenia (low absolute neutrophil count (ANC)) [1, 38]. Cisplatin causes kidney damage referred to as nephrotoxicity [39]. Clinicians often monitor the toxicity profile, as it impacts the timing and magnitude of the following chemotherapeutic dose.

Myelosuppression, as measured by ANC, is one of the common toxic effects of docetaxel, paclictaxel, topotecan, and carboplatin chemotherapies[1]. Neutropenic toxicity is divided into different grades in the clinic. The toxicity grades range from 0 to 5, with 0 being no toxicity and grade 5 being death [40]. High neutropenia grades could cause an immune system breakdown in patients, and in extreme cases, it could lead to death [41]. Neutropenic toxicity is often observed during chemotherapy between days 5 and 7 after drug infusion. Chemotherapeutic agents do not eliminate circulating neutrophils in the body but instead target the neutrophil progenitor cells. As the progenitor population decreases during chemotherapy, the number of cells that can mature into neutrophils becomes low, and this effect eventually causes the drop in ANC. The ANC recovers after chemotherapy because the depletion of neutrophils triggers the release of G-CSF, which triggers stem cells to produce more neutrophil progenitors as described in Section 1.1.1. In the cases where patients suffer severe neutropenic toxicity, clinicians use G-CSF prophylactically to increase neutrophil production and recruitment to circulation [42]. Models of ANC data can be used to understand neutrophil dynamics during chemotherapy.

1.1.2 Neutrophil-GCSF Models

G-CSF has been successfully used by clinicians in the prevention of neutropenia related to myelosuppressive chemotherapy [43, 44, 45, 46, 47]. Numerous trials have evaluated the efficacy of G-CSF in patients receiving high-dose chemotherapies for a variety of solid tumors (*i.e* docetaxel- metastatic cancer , methotrexate head and neck cancer)[43, 44, 45, 46, 47]. These studies concluded that G-CSF therapy is associated with significantly shorter hospital stays and reduced rates of severe neutropenia. For example, in a study of 44 women with metastatic cancer, patients receiving G-CSF had shorter hospital stays and achieved an ANC of at least $500/\mu$L earlier than patients who did not receive G-CSF [44]. A study performed by Bergh *et al.*, showed that G-CSF allows higher doses of a fluorouracil, epirubicin, and cyclophosphamide (FEC) combination chemotherapy [47]. Patients were given drugs every three weeks for nine courses either with G-CSF or without G-CSF. The drug dose was increased at every cycle. The chemotherapy was able to be administered to

patients receiving G-CSF therapy at significantly higher doses, but with comparable levels of haematological toxicity compared to patients not receiving G-CSF therapy [47]. G-CSF promotes neutrophil production and recruitment, which allows clinicians to treat with higher doses of chemotherapy. Understanding the impact of G-CSF on neutrophil dynamics would help develop better G-CSF administration guidelines resulting in improved chemotherapy scheduling that helps to avoid severe neutropenia.

Malka *et al.* built a six parameter model to analyze the bistability of neutrophils and bacteria for an *in vitro* system [48]. The bacterial elimination rate depends on both the neutrophil and bacteria concentrations. When the author scaled the model up for *in vivo* systems, the neutrophils were integrated with G-CSF dynamics via a two state model. However, there is no interaction between the bacteria and neutrophil states. Although the authors recognized G-CSF as an important part of the neutrophils dynamics, G-CSF alone does not contribute to all of the dynamics of neutrophils during an inflammatory challenge.

G-CSF effects on neutrophil dynamics have been studied in different models during chemotherapy to capture neutrophil production and recruitment when G-CSF is injected into the body. Most of the models incorporate G-CSF in neutrophil dynamics implicitly, and few include the effects of neutrophils on endogenous G-CSF production dynamics. Sochat *et al.* developed a two state model to capture neutrophil-G-CSF dynamics after a G-CSF injection [49]. In this model, the G-CSF endogenous production is a function of neutrophil count in the plasma. As the number of neutrophils in the plasma decreases, the rate of G-CSF production increases. In turn, more neutrophils are produced to return the system to steady state. This model was able to capture both neutrophil and G-CSF dynamics after intravenous and subcutaneous infusion, as seen in the data published by Wang *et al.* [6]. The model developed by Sochat *et al.* was one of the few models that incorporated G-CSF production explicitly. However, the model described the direct effect of G-CSF on circulating neutrophils and was unable capture the effects of chemotherapy on G-CSF dynamics. During chemotherapy, the drug affects the neutrophil precursor population, and the model does not include any neutrophil precursor state(s). Nevertheless, the model explicity captures the interaction of neutrophils and G-CSF. While G-CSF has showed an impact on neutrophil dynamics during chemotherapy, there is few models are able to capture this dynamics. Therefore, to

capture neutrophil and G-CSF dynamics after myelosuppessive chemotherapy and how G-CSF infusion impact ANC, certain biological information about the signaling cascade must be retained in a neutrophils GCSF dynamic model.

1.1.3 Dynamic Neutrophil Models Responding to Inflammatory Challenges

Modeling the inflammatory response, especially the innate immune response, is of great interest theoretically and clinically [50, 51, 52]. Capturing the inflammatory response in mathematics would help aid clinicians in designing interventions that improve patient outcomes and survival rates. The inherent problem is that early intervention aimed at down-regulating the inflammatory response increases the risk of infection that could overwhelm the immune system, while later intervention may be too late – attempting to prevent damage that has already been done. Thus, the timing for intervention in the case of the inflammatory response is critical for successful treatments. One of the first inflammatory models was developed by Hamers *et al.* [53]. This model studied how human neutrophils clear *Escherichia coli in vitro*. The three state of the model represent free bacteria, ingested bacteria, and perforated bacteria with linear dynamics. The neutrophil concentration was held constant throughout the simulation and the model was able to capture the population of bacteria over time. However, *in vivo*, the neutrophil population varies in the presence of infection. Thus, the constant neutrophil population and linear models describing the bacteria dynamics by Hamers *et al.* are not applicable. Despite these shortcomings, the model was one of the first to describe the rate of bacterial clearance by neutrophils.

Chow *et al.* studied the inflammatory response in different shock states with mathematical models using mouse data to calibrate the dynamics [52]. For calibration, mice were subjected to the following challenges: LPS intraperitoneal injection at 3 mg/kg, 6 mg/kg, 12 mg/kg, surgical trauma, and surgical trauma plus hemorrhaging. The available experimental data includes concentrations of TNF-α, IL-10, IL-6, and NO_2^-/NO_3^-. The model has 15 differential equations representing the different components in the inflammatory response such as cytokine concentrations, LPS dynamics, levels of both resting and activated macrophages and neutrophils, blood pressure, and tissue damage. Note that both the resting

and activated neutrophil populations are modeled as function of LPS, TNF-α, IL-6, and IL-10, and the activated neutrophils contribute to cytokines and nitric oxide production. This model was able to capture the dynamics of cytokines in the different LPS challenge levels and trauma challenges. In the model, the resting neutrophil population is represented by the number of neutrophils in circulation and those recruited during the inflammatory challenge. The activated population is comprised of the neutrophils that are able to clear out endotoxin. The two neutrophil states represent the dynamics of neutrophils in circulation, but do not account for neutrophil maturation and production. In this model, neutrophil states are supplementary states to capture dynamics of cytokines.

Reynolds *et al.* developed a reduced-order mathematical model of the inflammatory response [54]. The model has 4 ordinary differential equations representing pathogen dynamics, neutrophil dynamics, tissue damage, and anti-inflammatory cytokine concentration. Their study examined different stabilities within the model and patient outcome based on model parameters. The neutrophil dynamics are represented by only one equation, which describes the activated neutrophil population. Again, the neutrophil equation only captures the dynamics of neutrophils after recruitment and migration to the site of infection. Like the previous models of an inflammatory challenge that have been developed, this model is limited to only neutrophil dynamics at the site of infection.

In 2006, Day *et al.* used the same model structure of Reynolds *et al.* [54] to analyze the inflammatory response under repeated endotoxin administration [55]. The model was able to recapitulate different endotoxin infusion scenarios including lethal and non-lethal endotoxin doses. The model was able to capture the less severe inflammatory response found in preconditioned mice, as well as the more severe inflammation dynamics displayed by non-preconditioned groups. Here the preconditioned group received more than one dose of endotoxin while non-preconditioned group received only one dose of endotoxin. Like in the work of Reynolds *et al.*, the neutrophil dynamics captured in the model only account for the activated neutrophil population. The other neutrophil dynamics are neglected although they play important roles in the inflammatory response.

Similar model structures have also been developed by others to capture different endotoxin and other inflammatory challenges [27, 51, 56, 57, 58]. Common to all of these models

is a neutrophil functionality that captures the circulating neutrophil dynamics. Most of the models use either bacteria or cytokines as a recruiter to increase the neutrophil count in the plasma. The assumption is that neutrophils are not depleted in bone marrow. These models do not include any feedback mechanism in neutrophil production when the circulating neutrophil count drops. Due to the fast dynamics of the inflammatory response, these assumptions are plausible; however, to extend these models to accurately capture the dynamics of neutrophils, the biological response of neutrophils and the associated signaling cascade should be considered.

During a severe injury or pathogenic invasion, a number of different neutrophil groups are recruited to the circulation and eventually the site of infection: mature circulating neutrophils, neutrophils from the marginal pool, and immature neutrophils – neutrophils that are maturing in the bone marrow but are not yet fully mature. As the severity of injury increases, the number of premature neutrophils migrating to circulation increases. Orr *et al.* developed a model to capture this phenomenon [15, 16]. The model has one equation to capture the number of neutrophils in circulation where the recruitment rate of neutrophils to circulation is a function of neutrophils along the maturation trajectory. The experimental data were collected every two hours each day for a period of 7 days. The authors were then used piecewise linear function to fit data for each day. Thus, seven linear functions were used to capture experimental data. Although the model was able to capture the piecewise data, the piecewise approximation cannot be extended to different systems for the lack of generalized structure. Nevertheless, this model began to take into consideration the recruitment of different neutrophil populations to circulation and account for the fact that there are a limited number of neutrophils residing in bone marrow.

Song *et al.* developed a 19 state model to capture cecal ligation and puncture (CLP)-induced sepsis in rats. CLP-induced sepsis in rats was initiated via ligation of 25% of the length of the cecum and two punctures with a 20-gauge needle [50]. The hypothesis was that dysregulated neutrophil trafficking in severe sepsis may contribute to mortality. The models main focus is neutrophil trafficking and phenotype variation. The three main spatial compartments in the model are blood, peritoneum, and lung. The neutrophil phenotypes were resting, primed, and systemically activated. The model captured the inflammatory

response between the survivor and non-survivor rat populations. Blood purification was incorporated into the model to evaluate its benefits and it was found that 18% of rats from the non-survivor group can be saved when treated using blood purification. The Song *et al.* model was one of the few models to include different neutrophil phenotypes and explicitly account for neutrophil trafficking in different tissues. The authors did not consider the effects of neutrophil production and maturation on these dynamics.

A mathematical description of neutrophil dynamics during an inflammatory challenge in most models takes into consideration the process of neutrophil recruitment to the site of infection and also functionality to produce inflammatory and anti-inflammatory cytokines. When neutrophils become the main focus of the models, they are often modeled as an infinite source (no depletion), with an accurate description of recruitment and migration toward to site of infection as the primary concern. Neutrophil production through the G-CSF signaling cascade has not been modeled explicitly in inflammatory challenges. Modeling this cascade will improve understanding of neutrophil dynamics during inflammatory challenge and elucidate how the neutrophil production cascade contributes to the neutrophil recruitment process.

1.1.4 Neutropenic Toxicity Models

Mathematical models have been developed by several authors to capture neutrophil dynamics during chemotherapy treatment [1, 37, 59, 60]. Zamboni *et al.* developed a three-compartment model to represent neutrophil dynamics in pediatric patients [59]. The three compartments represent the stem cell population, a delay compartment, and neutrophils in peripheral blood. Twenty one children were administered topotecan (1.2-2.4 mg/m^2/day). Ten of the children were not treated with G-CSF after topotecan infusion, and 11 were treated with G-CSF following topotecan infusion. Although the children treated with G-CSF had a higher topotecan dose (30%) than children without G-CSF treatment, the neutrophil nadir of the two populations was within the same grade. The model results showed that the maturation rate of neutrophils is the same for the two populations; however, the toxicity parameters of topotecan on neutrophil production for patients receiving G-CSF is twice as high

as the patients not receiving G-CSF for more topotecan was administered. During topotecan chemotherapy, G-CSF does not help to increase the maturation rate; however, it helps to increase neutrophil production from stem cells. The increase in neutrophil production allows more drug to be administered to the patient. The Zamboni *et al.* model provides insight into how G-CSF impacts neutrophil dynamics. Friberg *et al.* posed a semi-mechanistic model to capture the myelosuppressive effects of different chemotherapeutic drugs [1]. The model addresses the slow effect of chemotherapeutic drugs on ANC and was able to capture the neutrophil response to five different chemotherapeutics. Although the maturation of neutrophils from progenitors in this model is biological grounded, the effects of circulating neutrophils on the progenitor production of neutrophils is represented by a nonlinear feedback term with the mathematical function, $(Circ(t)/Circ_0)^\gamma$. $Circ(t)$ is circulating neutrophil concentration as a function of time, $Circ_0$ is the basal/steady state neutrophil concentration, and γ is a factor to capture the effect of this ratio on progenitor cell proliferation rate. In subsequent papers, the authors acknowledged the ratio is a heuristic interpretation of the effects of G-CSF on neutrophil production. The Friberg *et al.* model has been used widely in modeling myelosuppression for various drugs and patient populations. However, when the model is used to capture the effects of G-CSF injection, it requires recalibration (change of parameters). Nevertheless, this model recognizes that neutrophil prercursors needs to be modeled to accurately capture the neutropenic toxicity effects of chemotherapy. A Friberg *et al.* model with the easy to implement structure has been utilized by various authors to capture the neutrophil response for different chemotherapy agents in a variety of different studies [37, 38, 61, 62, 60]. Kathman *et al.* studied the effects of ispinesib and docetaxel for 24 patients using the model developed by Friberg *et al.* [62]. The models toxicity and neutrophil proliferation rates were adjusted accordingly to capture docetaxel and ispinesib toxicity effects as well as patient-specific toxicity dynamics. The Kathman *et al.* parameters set is able to capture the neutrophil dynamics under ispinesib and docetaxel combination chemotherapy.

Panetta *et al.* studied neutrophil dynamics in pediatric patients after topotecan infusion [60]. The neutrophil model employed by the authors has five compartments, with a similar structure to that of Friberg *et al.*, where circulating neutrophils drive stem cell proliferation.

When G-CSF is infused into the patients, it increases the neutrophil maturation rate and the stem cell proliferation rate. Topotecan was infused daily over 30 minutes for five consecutive days over two consecutive weeks. G-CSF was given subcutaneously at 5 μg/kg/day beginning 24 h after the last topotecan dose of each cycle for a minimum of 10 days or until the ANC exceed 500/μL in two consecutive measurements after the expected nadir. The model was able to capture the neutrophil dynamics of twenty five pediatric patients over two cycles of topotecan chemotherapy. Engel *et al.* studied the response of neutrophils during the administration of 10 different multidrug multicylce chemotherapy treatments [63]. A similar structure to that of the Friberg*et al.* model was used. The five compartments in the model represent different neutrophil precursor populations. In this model, toxicity effects eliminate cells from all of the neutrophil precursor compartments except for circulating neutrophils. There are two main differences between this model and previously published models with similar structures. The first being the incorporation of a basal production of G-CSF in the model and the second being that the neutrophil states regulate the G-CSF dynamics. When the neutrophil cell counts are low, G-CSF is cleared out of the plasma more slowly than when neutrophil cell counts are high. The Engel *et al.* model was one of the first to incorporate the effects of neutrophils on G-CSF dynamics, and although the model did not capture the exact dynamics between neutrophils and G-CSF, it began to acknowledge the explicit importance of G-CSF in neutrophil models. Vainas *et al.* developed a model to capture the neutrophil dynamics of 38 breast cancer patients treated with docetaxel [64] . The model has 5 compartments that represent different neutrophil cell types. The model has a similar structure to the Friberg *et al.* model. The differences are that in the Vainas model the neutrophil precursors can proliferate, a portion of neutrophils are eliminated in the bone marrow, G-CSF affects the transition rates between compartments and slows the neutrophil degradation rate, and docetaxel eliminates cells from the three precursor states. The model was able to capture the dynamic response of 38 patients under 100 mg/m^2 every three weeks docetaxel chemotherapy. Pastor *et al.* capture the toxicity effects of carboplatin for patients with and without G-CSF treatment [4]. Out of 375 patients in this study, 47 received G-CSF. Using the Friberg*et al.* model, Pastor *et al.* recalibrated the parameters to successfully capture patients both with and without G-CSF dynamics (no G-CSF dynamics

were modeled. The Friberg *et al.* model recognized the slow neutrophil maturation process, and successfully described that phenomena via a mathematical model. The maturation structure has been used in various models, some of which were described above. However, the lack of G-CSF dynamics incorporated in these models limits their use to cases where the decision to use G-CSF or not is *a priori* (if [4] is used). Engal *et al.* made an effort to incorporate the endogenous G-CSF dynamics into the model [63]. However, improvements can be made in the current neutrophil-G-CSF models to better represent the true dynamics observed in this signalling cascade. Moreover, with a more biologically-relevant model, it would be unnecessary to recalibrate the parameters governing neutrophil dynamics when G-CSF is infused.

1.2 CHEMOTHERAPY SCHEDULE DESIGN

The design of chemotherapy schedules for the safe and efficient treatment of cancer has long been a challenge for clinicians. The balance between efficacy and toxicity makes chemotherapy scheduling difficult. Since patient dynamics change throughout the treatment, the chemotherapy schedules may require re-adjustment throughout the treatment to maximize tumor elimination while maintaining a tolerable toxicity profile in the patient. Schedule design for chemotherapy has been an interest in engineering, and engineers have been trying to solve the chemotherapy scheduling problem in order to aid clinicians in treatment design [65, 66, 67, 68, 69, 70, 71, 72, 73, 74, 75, 76, 77, 78]. However, engineering solutions to the clinical problem have often been optimal in simulation, but lacking in their clinical implementability as a result of requiring extended-duration low-dose infusion, withholding treatment at the start of therapy, and/or incorporating toxicity effects implicitly as dosing limits rather than providing an explicit model representing the side effects. Within a last decade, engineer solutions begun to address the explicit modeling of toxicity and its impact in chemotherapy treatment scheduling [76, 79, 80].To minimize the gap, thereby yielding a clinically-deployable DSS, the constraints imposed by clinical reality have to be explicitly incorporated into the design algorithm.

1.2.1 Clinical Chemotherapy Treatment Design

The development of chemotherapy schedule is a process from the testing anticancer agent *in vitro* to clinical trials to establish its specific standard schedules. Promising cancer agent in *in vitro* study (eliminating cancer cells on the dish) is then tested with animal models in preclinical trials to established treatment administration, drug efficacy with different cancer types, and toxicity measurements . The drug with high efficacy and manageable toxicity is then entered clinical trials. In phase I, the drug toxicity is examined to determine the toxicity constraints in human. Phase II determines the drug efficacy for specific cancer types based on schedules developed from experience with drug, toxicity profile, and logistical constraints. The successful drug with manageable toxicity in Phase I and high efficacy in Phase II enters Phase III to compare its performance against current standard chemotherapy for a specific cancer type. The drug can be used as single agent or in combination with other approved anticancer agents. A successful drug schedule would be more efficacious than current standard chemotherapy. Thus, the optimal clinical schedule of anticancer chemotherapy is determined through a series of experimentation and clinical trials yielding a better performance than current schedule.

In the clinic, chemotherapy schedules are designed for a specific drug or drug combination and then oncologists use that specific protocol to administer the chemotherapy drugs [60, 4]. Based on the response of the patient, clinicians adjust the dose magnitude and schedule. The patient response is evaluated for both tumor elimination and toxicity profile. If, after several cycles, the drug or drug combination does not reduce tumor size, the treatment is stopped, and the patient is switched to a different drug or perhaps an agent in clinical trials. Regardless of antitumor effect, the toxicity profile of the patient is carefully monitored throughout treatment. The method by which drug toxicity is evaluated is drug-dependent. For instance, when docetaxel is used, neutropenia is the primary toxicity concern in the clinic. However, when docetaxel is used in combination with cisplatin, clinicians also evaluate nephrotoxicity during the treatment [39], a direct result of adding cisplatin to the regimen. Thus, specific toxicities for each drug and drug combination are considered throughout patient treatment. If the patient suffers significant toxicity, the clinician either decreases the amount of drug

administered per dose or withholds a dose to make sure the toxicity becomes manageable prior to administering the next dose. Chemotherapy treatment continues until the patient suffers an untreatable toxicity, becomes cancer free, or fails to respond to treatment.

1.2.2 Model-Based Design of Chemotherapy Treatment Schedules

The mathematical models representing patient dynamics (Figure 1) are often integrated into an optimizer or an algorithm to design a treatment using patient current dynamics and model predictions. The use of patient dynamic models to design a treatment regimen (drug delivered, intervention) to achieve an objective goal (patient recovery, fastest tumor elimination) is called model-based control. Model-based design of chemotherapy schedule is the used of patient pharmacokinetic, pharmacodynamic, and toxicity models to manipulate the amount of drug administered and the timing of drug administration to minimize tumor volume within a set of toxicity and logistical constraints [75].

Model-based design of chemotherapy schedules has been a topic of study for more than 30 years [65, 66, 67, 68, 69, 70, 71, 72, 73, 74, 75, 76, 77, 78, 81, 82]. From an early work of Swan *et al.* [81] to recent works of Harrold *et al.* [76] and Pefani *et al.* [80], model based design of chemotherapy has advanced in patient models, problem formulation, and clinically relevant toxicity and logistical constraints inclusion to bring algorithm optimal solutions closer to clinical settings. Since the early work of Swan *et al.* [81], all of the chemotherapy optimization problems include equation/equations to describe tumor growth. Logistical growth model was used by Swan [81]. Gompertizian growth model was used by Martin and Teo [77, 78], Ziet and Nicolini [82], Iliadis and Barbolosi [74], and Nanda *et al.* [83], and different cell cycles is used by Pereira *et al.* [84], Panetta *et al.* [85], Ledzewicz and Schättler[86, 87], and Pefani *et al.* [80]. These tumor growth models described the dynamics of cancer cells in the chemotherapy scheduling optimization.

The drug dynamic model in patients and how it affects tumor dynamics are also included in chemotherapy scheduling problems. The drug pharmacokinetics were modeled by using a system of (non)linear equations [65, 66, 72, 75, 81]. The drug efficacy on tumor dynamics is modeled as a saturating function [81, 80] or a bilinear kill function depending on drug

concentration and tumor size with the rate constant calculated from *in vitro* experiment [65, 66, 67, 76]. In the works by Swan [81], Martin and Teo [77, 78], Costa *et al.* [71], Pereira *et al.* [84], Tse *et al.* [88], the drug pharmacokinetics and dynamics were non specific to any particular drug-tumor pairs. Realizing drug-tumor pairs are specific in clinical settings, specific drug and its mechanism are considered in recent works by Iliadis and Barbolosi [74], Harrold *et al.* [76], Nanda *et al.* [83], and Pefani *et al,* [80]. Iliadis and Barbolosi considered in the dynamics of etoposide [74]. 9-nitrocamptothecin (9-NC) was used in Harrold *et al.* work. Nanda analyzed the combination of dasatinib and nilotinib effects on chronic leukemia. Combination chemotherapy of daunorubicin (DNR) and cytarabine (Ara-C), a standard drug combination used to treat acute myeloid leukemia (AML), was studied by Pefani *et al.*. Departing form using the general anticancer dynamics in chemotherapy, the patient models associating with drug pharmacokinetics and its efficacy in model-based chemotherapy design has begun to address the specificity in drug-tumor pairs used in clinics. This is the first advancement in model-based chemotherapy design in an effort to bring its solution to the clinics.

Toxicity and efficacy drive patient chemotherapy schedule. Toxicity models are also included into patient models in model-based design in chemotherapy. Swan [81], Martin and Teo [77, 78], Costa *et al.* [71], Swierniak *et al.* [89], and Tse *et al.* [88] did not model the toxicity of chemotherapy explicitly. Swan used the maximum dose can be delivered as the place holder for patient toxicity [81]. Martin and Teo [77, 78], Costa *et al.* [71], Swierniak *et al.* [89], and Tse *et al.* [88] posted the implicit toxicity constraint by setting an upper limit in total drug exposure. These implicit toxicity constraints provided a convenience in modeling patient dynamics (no additional equations needed to capture patient toxicity). Clinically motivated toxicity measurements in chemotherapy can not be captured in the implicit models; therefore, explicit toxicity models were incorporated in later works by Iliadis and Barbolosi [74], Harrold *et al.* [76], and Pefani *et al.* [80]. Iliadis and Barbolosi developed a one equation model to capture the toxicity effect of etoposide in white blood cell dynamics [74]. Harrold *et al.* modeled weight loss as the toxicity effects in 9-NC chemotherapy. Normal cell population model with one equation was used as a toxicity model in the work of Pefeni *et al.* [80] in DNR and Ara-C combination chemotherapy. The change from

implicit toxicity models to explicit toxicity models in model-based chemotherapy design provides better representation of patient dynamics during chemotherapy;thus, bring the design algorithm solution closer to the clinical treatment schedule.

Beside improvements in patient dynamic models, chemotherapy design objective function and constraints have been changing in the past 30 years [65, 66, 67, 68, 69, 70, 71, 72, 73, 74, 75, 76, 77, 78, 81, 82]. Swan *et al.* objective is to achieve homeostasis with no logistical and toxicity constraints [81]. The algorithm yielded a continuous drug infusion which can lead to toxicity and become prohibitively expensive. The number of agents and clinical acceptability of continuous infusion are low. Nevertheless, Swan *et al.* work initiates the motivation of using engineering solution to aid clinicians in patient chemotherapy design.

A series of engineering chemotherapy treatment designs were published following Swan *et al.* [81] work [82, 84, 85]. These works did not provide any toxicity or logistical constraints in their problem formulation. Thus, the solutions of these problems yielded similar type of chemotherapy solution seen in Swan *et al.* [81], continuous drug infusion for a long period of time.

Realizing current chemotherapy clinical practice is cyclically and intermittently (with recovery intervals of up to week), Martin *et al.* assumed the drug administered weekly [77, 78]. The objective is also changed to minimize the tumor at the end of 52 weeks (1 year), without violating toxicity constraints (implicit toxicity limits on drug dose magnitude and total exposure),by determining the amount of drug to administer each week over a one year treatment horizon formulated as a an optimal control problem [77, 78]. Control vector parameterization was used to determine magnitude of the dose given weekly. The solution developed by Martin*et al.* suggested withholding treatment for a significant period of time after an initial dose, which was administered only because of a tumor volume constraint in the formulation. At the end of the treatment horizon, the algorithm delivered as much drug as possible without violating the toxicity constraints, would be given up to the total exposure constraints. This bang-bang treatment schedule at a critical point in the treatment horizon is a common characteristic of optimal control problems when the objective is to minimize or maximize states at the end of the horizon. The solution of this problem type is mathematical optimal but completely ignores clinical practice, where toxicity and efficacy drive treatment

[90, 91]. It would be unethical for a clinician to withhold treatment for a long period of time (up to six months, the calculated solution for a "high efficacy" drug) based on an engineering algorithm suggestion without any supporting evident.

The final point objective with implicit toxicity constraints formulation posted by Martin *et al.* [77, 78] were employed by other works by Costa *et al.* [71], Swierniak *et al.* [89], Ledzewicz and Schättler [86, 87], and Tse*et al.* [88]. The differences between the later works and Martin *et al.* work lay on the modeling of the cancer cell dynamics and the drug efficacy. Costa *et al.* divided cancer cells into a susceptible and a drug resistant cell populations [71]. Swierniak *et al.* considered the same two cancer cell populations with Costa *et al.*[71]. In this case, the drug resistant cells contained a distribution of drug resistances. A cell-cycle model of cancer tumor growth used in conjunction with cycle specific drugs were described in Ledzewicz and Schättler [86, 87]. Tse *et al.* extended the two drug algorithm [78] to capture the three drug dynamics [88] . Because there are almost no difference in the objective function formulation and implicit toxicity constraints (maximum drug exposure, maximum drug amount), the solution of these works gave a similar profile with Martin *et al.* dosing profile where drug is given toward the end of the treatment period [77, 78], not clinically applicable. Nevertheless, these works provided information to be considered in chemotherapy optimal design like drug resistance, cell cycle specific drug mechanism, and the generalizable structure of the algorithm.

The balance of efficacy and toxicity in chemotherapy scheduling optimization was considered by various authors for both theoretical and specific drug/tumor pairs [74, 66, 73, 92, 93, 94, 88, 95, 96, 97, 83] just like in the clinics where toxicity and efficacy drive chemotherapy schedule. Iliadis and Barbolosi were the first to consider explicit toxicity model in the chemotherapy [74]. They used one equation to describe white blood cell (WBC) concentration in plasma. The effect of the drug was captured by the bilinear kill term with a lag before the effect on the WBC population. The objective was minimized tumor cell population at the end of the treatment. The lower limit of WBC was used as a toxicity constraint. The solution yielded a several days infusion of etopside while WBC population remain at the lower limit for several days. The continuous infusion of etopside for several days are not practical in clinical setting due to a prolonged neutropenia grade 4 toxicity profile. Nevertheless, Il-

iadis and Barbolosi work is one of the first few considered explicit toxicity constraints. The inclusion of explicit toxicity constraints provide the chemotherapy schedule solution from the optimization problem becomes more clinically relevant.

Recognizing chemotherapy treatment end point is unknown in clinical practice, Harrold *et al.* [76] and Pefani *et al.* [80] reformulated the objective of the model based chemotherapy design to become more practical in clinical settings. Harrold et al. [76] posed the treatment scheduling problem with an engineering objective and clinically-relevant constraints. Minimization of tumor size every week along the treatment horizon, rather than just tumor size at the end of treatment, was the objective. Design of treatment was formulated as a receding horizon control problem [98], thereby allowing the algorithm to update its dosing schedule at intervals throughout the treatment. The drug considered was 9-nitrocamptothecin (9-NC), and the disease focus was a preclinical model of subcutaneous HT-29 colon carcinoma xenografts in severe combined immune deficient (SCID) mice. While the use of a preclinically relevant drug/tumor combination is an advantage, the drug was ultimately killed in Phase 2 clinical trials making translation to the clinic impossible. The toxicity model forthe drug was weight loss, modeled as being driven by 9-NC PK, due to the effect of 9-NC on intestinal mucosa (sloughing results from oral administration, which was used in the mice). The nonlinear PK model was converted to precalculated dynamic constraints as a result of not having dose-to-dose accumulation of the agent in the bloodstream. After a mathematical transformation, the PD model could be made linear; when combined with the linear toxicity model and the integer-programming constraints imposed by the PK, the resulting optimization problem was a mixed integer linear program (MILP). The work by Harrold *et al.* was able to move engineering approaches to cancer chemotherapy scheduling closer to clinical deployability in that the dosing decision is posed as the balance between efficacy and toxicity and the constraints limit 9-NC usage on toxicity and logistical grounds. The preclinical animal data testing the algorithm showed that the algorithm did well for the first cycle, but a more accurate toxicity model was needed for it to successfully design therapies of clinically-relevant duration (most mice were too sick to receive 9-NC doses on day 29, the first day of cycle 2 of therapy). Overall, the receding horizon formulation of the problem provides good clinical translatability for the algorithm; its key limitation were in the solution,

which required specialized transformations to address nonlinearities in PK and PD these are not generally applicable to arbitrary drug and tumor combinations thereby limiting the deployability of the algorithm.

Pefani *et al.* formulated the chemotherapy scheduling problem for acute myeloid leukemia (AML) using a combination chemotherapy of daunorubicin (DNR) and cytarabine (Ara-C), a standard drug combination used to treat AML [80]. Both DNR and Ara-C act on two different cell phases; therefore, a cell-cycle model is utilized to capture the tumor growth and drug effect dynamics. The PK model is a PBPK model with a bone marrow compartment in which the drug effects are captured by a sigmoid-Emax model: $\frac{E_{max}C(t)}{EC_{50}+C(t)}$; E_{max} is a maximum drug effectiveness rate, EC_{50} is the drug concentration at which the effectiveness is at its half maximum, and $C(t)$ is the drug concentration in the bone marrow compartment. The objective was the minimization of the number of leukemic cells over the treatment horizon. Constraints were posed such that the healthy cell population remained higher than the leukemic cell population at the end of each infusion. DNR is infused for one hour, and Ara-C is infused continuously for 24 hours are the optimal treatment schedule for their hypothesis patient dynamics without violating toxicity constraints. The optimal solutions yield better treatment with a less severe toxicity profile that current clinical practice; however, it is not clinically practical to implement continuous infusion of Ara-C when the standard of care in practice is two injections per day. The difference between Pefani *et al.* solution in the usage of Ara-C schedule and current clinical usage and the prolong toxicity profile with no recovery period are the discrepancies between the problem solution and clinical settings. Nevertheless, Pefani *et al.* work was able to target combination chemotherapy in optimal control with clinically relevant drugs and clinically motivated logistical and toxicity constraints.

Over the past 30 years, the improvement from in model-based chemotherapy in patient dynamic models (PK, efficacy, toxicity), problem formulation, and the inclusion of clinically relevant toxicity and logistical constraints has brought the solution of engineering optimal problem closer to clinical settings. The works in the past 30 years provide stepping stones for model-based chemotherapy design to be clinical ready and clinician friendly and to aid with patient dynamics to improve patient outcomes during chemotherapy.

1.3 THESIS OVERVIEW

Toxicity and efficacy drive chemotherapy treatment decisions, and treatment endpoints are not easily predicted in cancer chemotherapy. In chemotherapy, treatment is typically given in cycles, which allows clinicians to evaluate the response of patients and use the information as feedback to alter treatment accordingly. While the use of generic "drug and "tumor can provide some insight into engineering solutions for chemotherapy treatment design, such abstraction severely limits the clinical potential for impact of such work [76]. Therefore, drug/tumor combinations must be treated independently from a modeling perspective, and patient-specific parameters may have to be derived when developing treatment schedules.

While a clinically realizable formulation requires specific drug/tumor models for chemotherapy dosing optimization, a generalizable structure of the optimization problem would reduce the effort required to develop new algorithms for each drug/tumor pair. Linear models, though often used, cannot be assumed, and the toxicity effects must be captured specifically for clinically relevant measurements of the drug and its induced responses. The toxicity effect models are often nonlinear as well. A further challenge is the decision to dose or not (a discrete variable), coupled to a dose magnitude (a continuous variable) when drug is administered. As a result, a generalizable and clinically-relevant chemotherapy dosing optimization formulation is a mixed-integer nonlinear programming problem (MINLP). Solving the generalizable MINLP for chemotherapy dosing optimization is formidable, though successful solution could significantly impact drug development and (pre)clinical practice.

The remaining 4 chapters of this thesis entail the following. Chapter 2 presents a mathematical model of the neutrophil signaling cascade to capture its response to inflammation (an LPS challenge) and chemotherapy (absolute neutrophil count decrease as a result of docetaxel administration). Model reduction techniques and results for both linear and nonlinear models will be presented with examples of physiologically-based docetaxel pharmacokinetics and a nonlinear neutrophil-G-CSF model in Chapter 3. Chapter 4 presents the generalizable chemotherapy scheduling problem with docetaxel and its combination with cisplatin or carboplatin. The results of that include a treatment schedule for optimal tumor elimination without violating clinically-motivated toxicity constraints. The final chapter will

include perspectives and future research directions in neutrophils modeling to have a better mathematical representation of patient dynamics and in model-based chemotherapy design to bring the optimal solution to clinical settings and ultimately improve patient outcomes.

2.0 MODELING NEUTROPHIL RESPONSE TO AN INFLAMMATORY CHALLENGE AND CHEMOTHERAPY INDUCED MYELOSUPPRESSION

Understanding neutrophil dynamics through mathematical modeling can help predict the response to an inflammatory challenge as well as chemotherapy induced myelosuppression. The mathematical model can help to design timely intervention in the case of sepsis, or severe toxicity prevention in the case of chemotherapy. While the neutrophil response to an inflammatory challenge is rather fast, the impact of chemotherapy on neutrophil dynamics is on a slower timescale. To capture both of these dynamics, the biologically-based model of neutrophils and G-CSF dynamics is derived from the signaling cascade and available biological information. The model is calibrated using G-CSF injections, an LPS challenge and docetaxel induced myelosuppression.

2.1 BIOLOGICALLY-MOTIVATED MODEL OF NEUTROPHIL DYNAMICS

2.1.1 Friberg *el al.* Neutrophil Model [1]

Friberg *et al.* [1] developed a phenomenological model to capture neutrophil dynamics following marrow-toxic chemotherapy. The model was developed to capture patient neutrophils dynamics during different chemotherapy regimen [1].The model captures absolute neutrophil count (ANC) by using 5 differential equations and a nonlinear feedback mechanism, which depends on the ratio of plasma neutrophil concentration to its nominal value, to drive proliferation (see Figure 2, Equations (2.1)-(2.5), and Table 1). The model does not represent

G-CSF explicitly, though the authors note their feedback structure implicitly incorporates the effects of G-CSF among other activators [1, 37, 38]. The toxic effect of anticancer drugs on the progenitor cells is described using a sigmoid $Emax$ model [37], where progenitor cell elimination is a function of the drug concentration in the bone marrow ($\left(\frac{k_{37}}{k_{38}+D(t)}\right) Pr(t)$, as seen in Equation (2.6). The model captures neutrophil response data of several marrow-toxic chemotherapeutics (*e.g.*, paclitaxel, docetaxel, vinfluine) [1]. However, the dynamics of this

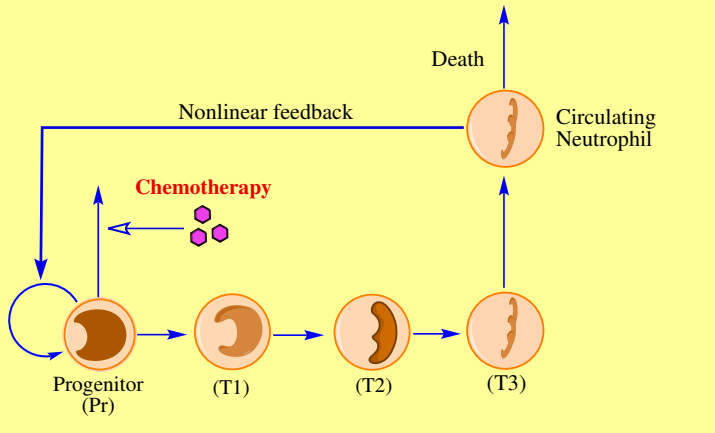

Figure 2: Friberg *et al.* [1] neutrophil model.

model are too slow to capture the neutrophil response to an inflammatory challenge. Neutrophils play an important role in inflammatory cascade [24]. Understanding the neutrophils dynamics during an infection would help to design an appropriate intervention to control its dynamics, especially for the case of sepsis, thereby motivating the construction of a unifying model of neutrophil dynamics applicable to multiple challenges.

$$\frac{dProl}{dt} = k_{prol} Prol \left(1 - \frac{E_{max}}{EC_{50} + D}\right) \left(\frac{Circ_0}{Circ}\right)^{\gamma} - k_{tr} Prol \tag{2.1}$$

$$\frac{dTransit1}{dt} = k_{tr} Prol - k_{tr} Transit1 \tag{2.2}$$

$$\frac{dTransit2}{dt} = k_{tr} Transit1 - k_{tr} Transit2 \tag{2.3}$$

$$\frac{dTransit3}{dt} = k_{tr} Transit2 - k_{tr} Transit3 \tag{2.4}$$

$$\frac{dCirc}{dt} = k_{tr} Transit3 - k_{circ} Circ \tag{2.5}$$

Table 1: Parameter values (P) for the Friberg *et al.* model [1]

P.	Value	Unit	P.	Value	Unit
k_{prol}	7.5×10^{-4}	$\frac{1}{min}$	E_{max}	83.9	–
EC_{50}	7.17	μM	γ	0.163	–
k_{tr}	7.5×10^{-4}	$\frac{1}{min}$	$Circ_0$	5.05×10^6	$cells/ml$
k_{circ}	7.5×10^{-4}	$\frac{1}{min}$	–	–	–

2.1.2 Maturation Chain Modification

The model developed herein retains the progenitor state, the maturation chain structure, and the circulating neutrophil pool from [1] ($Pr(t)$, $T1(t)$, $T2(t)$, $T3(t)$, and $Nc(t)$ respectively in Figure 2) . However, we expand the biology of the feedback regulation to explicitly incorporate the G-CSF signaling cascade. The production of the progenitor population becomes a function of G-CSF as shown in Equation (2.6).

$$\frac{dPr(t)}{dt} = \left(k_{41} + \frac{k_{32}G_{CSF}(t)}{k_{33} + G_{CSF}(t)}\right) S - k_{tr}Pr(t) - \left(\frac{k_{37}D(t)}{k_{38} + D(t)}\right) Pr(t) \tag{2.6}$$

Here k_{41} is the minimal production rate of progenitors when G-CSF concentration is low, k_{32} is the maximum G-CSF stimulation production rate of progenitors, and k_{33} is the G-CSF concentration at which inducible progenitor production is at half its maximum value. The chemotherapeutic drug toxicity is represented by the last term in Equation (2.6). In this term, k_{37} is the maximum toxicity rate corresponding to the E_{max} term in the Friberg model [1]. The drug concentration at which the toxicity is at its half maximum effect is k_{38}, and corresponds to the EC_{50} term in the Friberg model [1]. The drug plasma concentration is used as a driven force in the chemotherapeutic toxicity effect because there is no drug bone marrow concentration measurement available.

$$\frac{dT_1(t)}{dt} = k_{tr}Pr(t) - k_{tr}\left(1 + 1.5\frac{I_1(t)}{k_{36} + I_1(t)}\right)T_1(t) \tag{2.7}$$

$$\frac{dT_2(t)}{dt} = k_{tr}T_1(t) - k_{tr}\left(1 + 1.5\frac{I_1(t)}{k_{36} + I_1(t)}\right)T_2(t) \tag{2.8}$$

$$\frac{dT_3(t)}{dt} = k_{tr}T_2(t) - k_{tr}\left(1 + 1.5\frac{I_1(t)}{k_{36} + I_1(t)}\right)T_3(t) \tag{2.9}$$

where

$$k_{tr} = k_1\left(1 + k_2\frac{G_{CSF}(t)}{k_4 + G_{CSF}(t)}\frac{k_3}{k_3 + D(t)}\right) \tag{2.10}$$

The maturation chain structure is represented in Equations (2.7)- (2.9). In this case, the transport from one compartment to the next is dictated by the transport rate, k_{tr}, and the inflammatory response state, I_1. The transport rate k_{tr} (Equation (2.10)) includes a minimal constant, k_1, and a saturation function depending on G-CSF concentration with maximum rate, k_2, and half maximum G-CSF concentration, k_4. When affected by chemotherapy-induced myelosuppression, the maturation rate is slowed by the function $\frac{k_3}{k_3+D(t)}$ where k_3 is the drug concentration that inhibits the maturation rate by half. The inclusion of G-CSF, the inflammatory response, and drug toxicity should facilitate the use of the model not only in the case of chemotherapy-induced neutropenia but also to capture the dynamics of other challenges such as the immune response to sepsis.

2.1.3 Circulating Neutrophils and the Neutrophil Marginal Pool Model

$$\begin{aligned}\frac{dN_c(t)}{dt} = {} & k_{tr}T_3(t) - k_dN_c(t) + 1.5k_{tr}\left(\frac{I_1(t)}{k_{36} + I_1(t)}\right)(T_1(t) + T_2(t) + T_3(t)) \\ & -k_{tr}\left(1 - \frac{I_1(t)}{k_{36} + I_1(t)}\right)N_c(t) \\ & +k_{tr}\left(1 + 10\frac{I_1(t)}{k_{36} + I_1(t)} + k_{34}\frac{G_{CSF}(t)}{k_{35} + G_{CSF}(t)}\right)N_p(t)\end{aligned} \tag{2.11}$$

The circulating neutrophils are modeled by Equation (2.11).Here the first term is maturation of neutrophils from the T_3 state. The second term is the first order degradation rate of neutrophils as they undergo apoptosis. The third term in the equation is the recruitment of

young neutrophils to the circulation during an inflammatory response, induced by inflammatory signal $I_1(t)$. The two final terms are rates setting the equilibrium between circulating neutrophils and the marginal pool. The circulating neutrophil state is used to capture the absolute neutrophil count in plasma.

A neutrophil marginal pool has been included to capture rapid repletion dynamics for circulating neutrophil levels. The marginal pool is comparable in size to the circulating pool, and neutrophils from this pool are available for immediate mobilization in response to external stimuli (*i.e.*:infection, trauma) [37, 15, 16, 27]. The marginal pool is modeled using an equilibrium process, with the equilibrium constant heavily dependent on the external stimuli. The dynamics of the marginal pool are described in Equation (2.12).

$$\begin{aligned}\frac{dN_p(t)}{dt} &= k_{tr}\left(1-\frac{I_1(t)}{k_{36}+I_1(t)}\right)N_c(t) - k_{tr}\left(1+10\frac{I_1(t)}{k_{36}+I_1(t)}\right. \\ &\quad \left.+k_{34}\frac{G_{CSF}(t)}{k_{35}+G_{CSF}(t)}\right)N_p(t) \end{aligned} \tag{2.12}$$

Here the neutrophil equilibrium between the marginal pool and circulation is modeled by rate k_{tr} to create an equal amount of neutrophil count in marginal pool and in circulation [15, 16]. The equilibrium rate shifts from marginal pool to circulation in the presence of inflammatory signal or an increase in G-CSF concentration. The shift in equilibrium is modeled by the inhibition of neutrophil transport to the marginal pool and an increase in neutrophil migration rate from the marginal pool to circulation.

2.1.4 Biological Feedback in Neutrophil Production

G-CSF has been identified as the key stimulating factor that triggers neutrophil production and maturation [25, 29]. G-CSF production from stromal cells is the end product of an intricate signaling cascade (Figure 3). Neutrophil apoptosis and envelopment by macrophages is modeled by Equation (2.13):

$$\frac{dN_d(t)}{dt} = \frac{k_5 N_c(t)}{k_8+N_c(t)}\left(1-\frac{k_6 GCSF(t)}{k_7+GCSF(t)}\right)N(c) - k_9 N_d(t) \tag{2.13}$$

Here $N_d(t)$ represents the amount of neutrophils engulfed by macrophages. The rate of neutrophil elimination by macrophages is modeled with respect to $N_c(t)$ by a Michaelis-Menten saturating function with maximum rate k_5 and half maximum rate concentration k_8. The rate of neutrophils undergoing apoptosis decreases in the presence of G-CSF [25]. This effect is incorporated into the model by G-CSF inhibiting $N_d(t)$ degradation rate, $\left(1 - \frac{k_6 G_{CSF}(t)}{k_7 + G_{CSF}(t)}\right)$. The rate of $N_d(t)$ clearance is modeled using first order kinetics, with the clearance rate k_9. Interleukin-23 (IL-23) is secreted by macrophages. When the amount of circulating neutrophils engulfed by macrophages decreases, the rate of IL-23 released by macrophages increases [29]. Thus the rate of IL-23 production is modeled as a function of N_d as shown in Equation (2.14):

$$\frac{dIL_{23}(t)}{dt} = \left(k_{10} - \frac{k_{11} N_d(t)}{k_7 + N_d(t)}\right) - k_{12} IL_{23}(t) \tag{2.14}$$

In the absence of $N_d(t)$ or neutrophil depletion, IL-23 is produced by a zero order rate, k_{10}. When neutrophils are being replenished, the amount of $N_d(t)$ increases, which in turn decreases the IL-23 production through the function, $\left(\frac{k_{11} N_d(t)}{k_7 + N_d(t)}\right)$. IL-23 degradation is modeled using first order kinetics with rate constant, k_{12}. An increase in the amount of IL-23 activates T-cells. To capture the saturation effects of IL-23 on the T-cell population, the T-cell population is represented using two states: the activated state ($T_a(t)$) and the inactivated state ($T_i(t)$).

$$\frac{dT_a(t)}{dt} = \left(k_{15} + \frac{k_{16} IL_{23}(t)^2}{k_{17}^2 + IL_{23}(t)^2}\right) T_i(t) - \frac{k_{13} k_{14}^2}{k_{14}^2 + T_a(t)^2} T_a(t) \tag{2.15}$$

$$\frac{dT_i(t)}{dt} = \frac{k_{13} k_{14}^2}{k_{14}^2 + T_a(t)^2} T_a(t) - \left(k_{15} + \frac{k_{16} IL_{23}(t)^2}{k_{17}^2 + IL_{23}(t)^2}\right) T_i(t) \tag{2.16}$$

Equation (2.15) describes the dynamics of the activated T-cells, while Equation (2.16) shows the dynamics of inactive T-cells. The rate of T-cell conversion from inactive to active is modeled as basal rate k_{15} and a second-order Hill function depending on the concentration of IL-23 present with rate k_{16} and half maximum constant k_{17},. T-cell deactivation from an active to inactive state has the basal rate of k_{13}. When IL-23 concentration increases, the rate decreases, governed by the second order Hill function with half maximum constant k_{14}. Activated T-cells secrete IL-17 to increase the stromal cell production of G-CSF. The

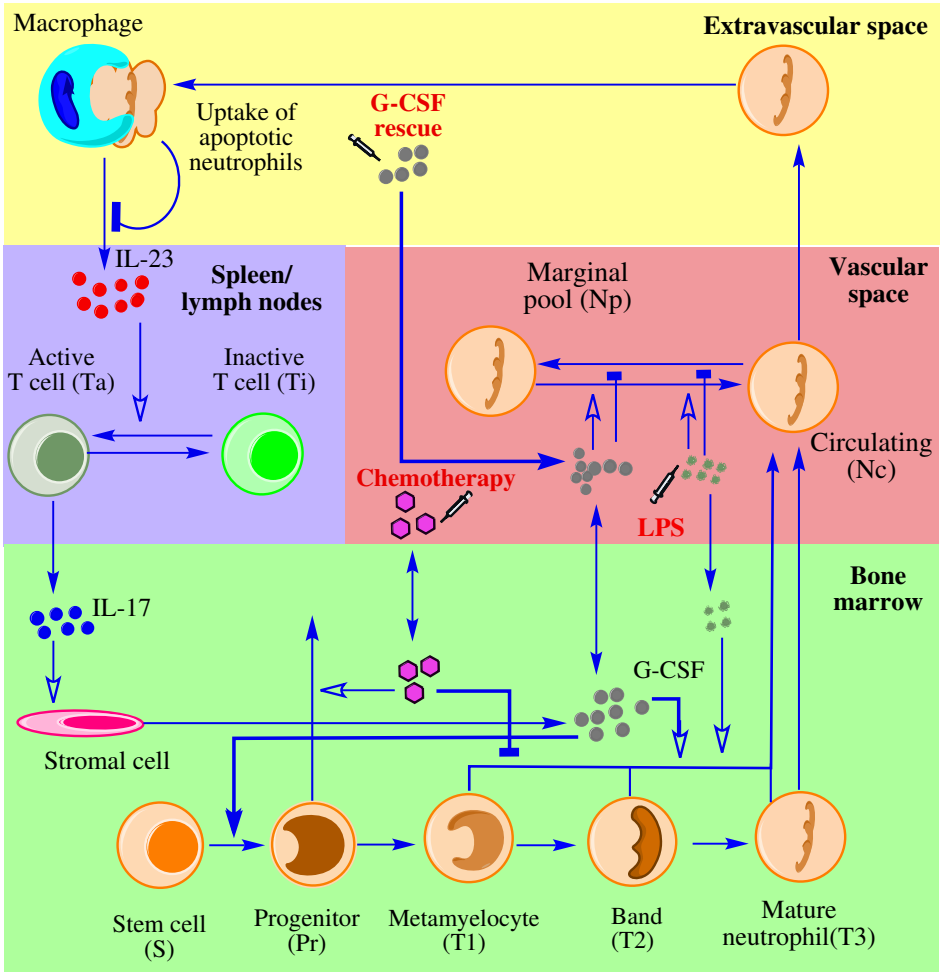

Figure 3: Neutrophil and G-CSF biologically-based model.

activated T-cells secrete IL-17 as shown in Equation (2.17).Production of IL-17 is modeled as first order with respect to the number of activated T-cells, with the rate k_{18}. The degradation of IL-17 is represented using first-order kinetics with the rate constant k_{19}. The increase in IL-17 triggers the activation of stromal cells, modeled in Equation (2.18).

$$\frac{dIL_{17}(t)}{dt} = k_{18}T_a(t) - k_{19}IL_{17}(t) \tag{2.17}$$

$$\frac{dS_c(t)}{dt} = \frac{k_{20}IL_{17}(t)}{k_{21} + IL_{17}(t)}IL_{17}(t) - \frac{k_{22}k_{23}}{k_{23} + S_c(t)}S_c(t) \tag{2.18}$$

Here a Michaelis-Menten function with maximum rate k_{20} and half maximum constant k_{21} is used to model the number of stromal cells being activated by IL-17. Stromal cell deactivation is also modeled as a saturating function of the number of activated stromal cells, with the half maximum constant k_{23} and maximum deactivation rate k_{22}. Activated stromal cells release G-CSF in order to increase neutrophil production and maturation. The G-CSF dynamics are modeled as a system of two equations to capture plasma dynamics as well as tissue dynamics when G-CSF is administered via subcutaneous injection, as shown in Equations (2.19)-(2.20):

$$\begin{aligned}\frac{dG_{CSF}(t)}{dt} &= \frac{k_{24}S_c(t)^2}{k_{25}^2 + S_c(t)^2}S_c(t) - \left(k_{26} + \frac{k_{27}N_c(t)}{k_{28} + N_c(t)}\right)G_{CSF}(t) \\ &\quad + k_{29}G_{CSF_T}(t) - k_{30}G_{CSF}(t) \qquad (2.19)\\ \frac{dG_{CSF_T}(t)}{dt} &= k_{30}G_{CSF}(t) - k_{29}G_{CSF_T}(t) - k_{31}G_{CSF_T}(t) \qquad (2.20)\end{aligned}$$

The production rate for G-CSF is a second order Hill function with maximum rate k_{24} and half maximum constant k_{25}, with respect to the number of activated stromal cells. The degradation rate of G-CSF is the sum of a basal rate k_{26} and a Michaelis-Menten function of circulating neutrophil concentration with maximum rate k_{27} and half maximum constant k_{28}. The G-CSF in the plasma is at equilibrium with the G-CSF in the tissue with forward rate k_{30} and reverse rate k_{29}. The G-CSF in the tissue is also metabolized at the constant rate k_{31} (Figure 3).

2.2 DISRUPTIONS TO CIRCULATING NEUTROPHIL DYNAMICS

Under external stimuli such as infection, endotoxin challenge, and myelosuppression chemotherapy, the homeostasis of circulating neutrophils is disrupted; thereby, the dynamics of the signaling cascade are changed. In the endotoxin challenge, the change in the neutrophils dynamics are within 24 hours after the induce of challenge [7]. In myelosuppression chemotherapy, the neutrophil dynamic change is occurred for a long period time (weeks) [1]. Using the two different dynamic challenges, the biological based neutrophil model will be calibrated and tested its ability to capture different dynamics.

2.2.1 Lipopolysaccharide (LPS) Challenge

LPS, an inflammatory challenge, has been used in healthy volunteers to activate the neutrophil response [7]. The LPS challenge is believed to trigger the inflammation cascade through the same mechanisms as those activated in sepsis [7]. Three dynamic elements are added to the model to capture the effects of LPS on the neutrophil response: (i) rapid mobilization of the neutrophil marginal pool (Equation (2.12) ;(ii) recruitment of immature neutrophils (T1, T2, T3) to the circulation (Equations (2.7)- (2.9); and (iii) LPS-induced clearance of neutrophil-LPS complexes (LPS bound to neutrophils)(Equation (2.11). LPS effects are modeled as two compartments to capture the temporally disparate effects of the challenge. The first compartment (Equation (2.21) represents circulating LPS after intravenous (IV) injection, which drives neutrophil-LPS clearance and neutrophil mobilization from the marginal pool. The second LPS compartment (Equation (2.22)) governs the slower inflammation dynamics that stimulate neutrophil migration from bone marrow. The clearance of LPS is modeled as first-order, as follows:

$$\frac{dLPS(t)}{dt} = -k_{39}LPS(t) \tag{2.21}$$

$$\frac{dI_1(t)}{dt} = k_{39}LPS(t) - k_{40}I_1(t) \tag{2.22}$$

2.2.2 Docetaxel Physiologically Based Pharmacokinetics Model (PBPK)

A PBPK model was developed by Florian *et al.* [5] with 35 linear differential equations to represent different tissues in the body. The model not only captures docetaxel plasma concentration, but also captures tissue concentrations and bound/unbound drug amounts with intracellular tissue in each tissue compartment. The schematic of the model is shown in Figure 4 and the model equations and parameters are shown in Appendix A.

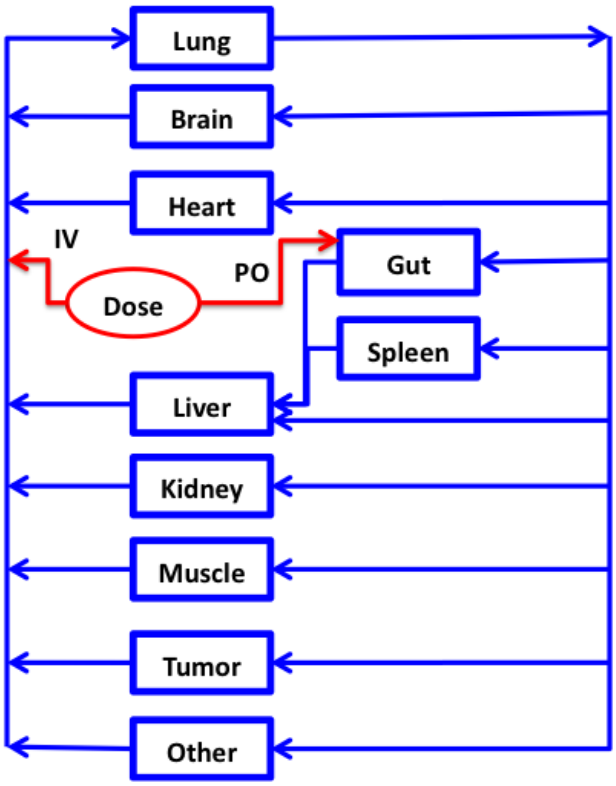

Figure 4: Docetaxel PBPK model [5].

2.3 PARAMETER ESTIMATION

Quality of fit is assessed by the sum of squared residuals between model predictions and experimental data, as follows:

$$J(p) = \sum_{i=1}^{N} \frac{1}{\sigma_i^2} \left(y(i) - y_{sim}(i,p)\right)^2 \tag{2.23}$$

Here, the sum is over the number of data points, N, in the experimental data set $y(i)$. Time-matched simulation data, $y_{sim}(i,p)$ is used to calibrate the parameters, p, that can be varied in order to reduce the error between predicted ($y_{sim}(i,p)$) and actual ($y(i)$) data. Weighting of data across time points is accomplished using the residual variance of the data, $\frac{1}{\sigma_i^2}$, at time points i. Numerically, the residual sum of squares minimization was implemented in MATLAB (©2014, The Mathworks, Natick, MA) using the *lsqnonlin* function. To mitigate the impact of finding a local minimum, multi-start optimization using different parameter vectors was employed to identify a "best fit parameter vector that provided good agreement between $y(i)$ and $y_{sim}(i,p)$ for each parameter vector-data set pair. Some parameter values were taken directly from the literature (see Table 2). In order to identify the remaining model parameters, the following procedure was implemented:

- using steady state levels of neutrophils [26], calculate parameters k_5, k_8, k_9, k_{10}, k_{12}, k_{13}, k_{15}, k_{17}, k_{18}, k_{19}, k_{20}, k_{21}, k_{22}, k_{23}, k_{24}, k_{25}, k_{26}, and k_{41}
- subcutaneous (SC) G-CSF injection data [6] are used to determine parameters k_2, k_4, k_6, k_7, k_{27}, k_{28}, k_{29}, k_{30}, k_{31}, k_{34} ,and k_{35}
- docetaxel chemotherapy challenge data [1] are used to calibrate parameters k_3, k_{11}, k_{14}, and k_{16}
- LPS challenge data [7] are fitted by adjusting parameters k_{36}, k_{39}, and k_{40}

Table 2 summarizes the model parameters, including a brief description of each parameter contribution, the state equation to which the parameter contributes, the value of the parameter, and the method by which the parameter value was established (literature or fitted). Table 3 provides a corresponding summary of the state equations in the model.

Table 2: Neutrophil model parameters (P). SS fitted: fitted to steady state data, Dyn. fitted: fitted to dynamic response data

P	Value	Unit	Description	Source
k_1	0.0006	$\frac{pg}{ml}$	Neutrophil maturation rate	[1]
k_2	14.5511	–	Neutrophil production and recruitment	Dyn. fitted
k_3	2.36×10^{-8}	$\frac{pg}{ml}$	Doxetacel concentration at half max rate	Dyn. fitted
k_4	8000	$\frac{pg}{ml}$	G-CSF concentration at half max rate	Dyn. fitted
k_5	0.0016	$\frac{1}{min}$	Apoptotic neutrophil at half max rate	SS fitted
k_6	0.25	–	G-CSF inhibited neutrophil apoptosis	Dyn. fitted
k_7	10^5	$\frac{pg}{ml}$	G-CSF concentration at half max rate	Dyn. fitted
k_8	10^7	$\frac{cell}{min}$	Neutrophil concentration at half max rate	SS fitted
k_9	0.0858	$\frac{1}{min}$	Apoptotic neutrophils clearance	SS fitted
k_{10}	0.11843	$\frac{1}{min}$	IL-23 production	SS fitted
k_{11}	0.1184	$\frac{1}{min}$	IL-23 production inhibition	Dyn. fitted
k_{12}	0.0253	$\frac{1}{min}$	IL-23 degradation	SS fitted
k_{13}	0.3603	$\frac{1}{min}$	T cell deactivation	SS fitted
k_{14}	10^6	$\frac{cell}{min}$	T cell at half max rate	Dyn. fitted
k_{15}	8.48×10^{-7}	$\frac{1}{min}$	basal T cell activation	SS fitted
k_{16}	24.9738	$\frac{1}{min}$	T cell activation	Dyn. fitted
k_{17}	50000	$\frac{pg}{ml}$	IL-23 concentration at half max rate	SS fitted
k_{18}	0.0062	$\frac{pg}{cell.ml}$	IL-17 production	SS fitted
k_{19}	0.0922	$\frac{pg}{ml}$	IL-17 degradation	SS fitted
k_{20}	0.002	$\frac{pg}{cell.ml}$	Stromal cell activation	SS fitted
k_{21}	5×10^4	$\frac{pg}{ml}$	IL-17 concentration at half max rate	SS fitted
k_{22}	0.0188	$\frac{1}{min}$	Stromal cell deactivation	SS fitted
k_{23}	3.2×10^4	$\frac{cell}{min}$	Stromal cell at half max rate	Dyn. fitted
k_{24}	0.0085	$\frac{pg}{cell.ml}$	G-CSF production	SS fitted
k_{25}	2.5×10^3	$\frac{cell}{min}$	Stromal cell at half max rate	SS fitted

Table 2 (continue)

k_{26}	0.001	$\frac{1}{min}$	G-CSF clearance	SS fitted
k_{27}	0.0066	$\frac{1}{min}$	G-CSF clearance by neutrophils	Dyn. fitted
k_{28}	10^7	$\frac{cell}{min}$	Neutrophil concentration at half max rate	Dyn. fitted
k_{29}	0.004	$\frac{1}{min}$	G-CSF transport from tissue to plasma	Dyn. fitted
k_{30}	9×10^{-11}	$\frac{1}{min}$	G-CSF transport from plasma to tissue	Dyn. fitted
k_{31}	0.00073	$\frac{1}{min}$	G-CSF tissue clearance	Dyn. fitted
k_{32}	0.00159	$\frac{1}{min}$	Progenitor cell production	[49]
k_{33}	6×10^4	$\frac{pg}{ml}$	G-CSF concentration at half max rate	[49]
k_{34}	8.4170	–	Marginal pool mobilization	Dyn. fitted
k_{35}	10^4	$\frac{pg}{ml}$	G-CSF concentration at half max rate	Dyn. fitted
k_{36}	3.5×10^9	$\frac{pg}{ml}$	neutrophil recruitment by IL-1	Dyn. fitted
k_{37}	77.5	$\frac{pg}{ml}$	Progenitor elimination	[1]
k_{38}	0.0015	$\frac{pg}{ml}$	drug concentration at half max rate	[1]
k_{39}	0.00045	$\frac{1}{min}$	LPS clearance	Dyn. fitted
k_{40}	0.0091	$\frac{1}{min}$	Inflammation clearance	Dyn. fitted
k_{41}	0.000035	$\frac{1}{min}$	Basal progenitor production	SS fitted

Table 3: Model equations and vorresponding biological states

Equation Number	**State**	**Biological Meaning**
(2.21)	LPS	Plasma LPS concentration
(2.22)	I_1	Inflammation dynamics activated by LPS
(2.6)	Pr	Progenitor population
(2.7)	T_1	Metamyelocyte population
(2.8)	T_2	Band population
(2.9)	T_3	Mature neutrophil population
(2.11)	N_c	Circulating neutrophil concentration
(2.12)	N_p	Marginal neutrophil pool
(2.13)	N_d	Apoptotic neutrophils
(2.14)	IL-23	IL-23 population
(2.15)	T_a	Activated T cells by IL-23
(2.16)	T_i	Inactive T cells
(2.17)	IL-17	IL-17 population
(2.18)	S_c	Active stromal cells
(2.19)	$GCSF$	Plasma G-CSF concentration
(2.20)	$GCSF_T$	Tissue G-CSF concentration

2.4 RESULTS

The overall model of the biologically-motivated neutrophil-G-CSF signaling cascade has 14 differential equations. This model can be used to capture the neutrophil-G-CSF dynamics during an inflammatory challenge (LPS) and docetaxel chemotherapy induced myelosuppression.

2.4.1 Response to Intravenous and Subcutaneous G-CSF Injections

The effects of G-CSF on neutrophil production and recruitment were studied in healthy human volunteers (n=16) by administering G-CSF subcutaneously (SC) or IV at doses of 375 μg and 750 μg [6]. Serial blood samples measured plasma neutrophil and G-CSF levels. Experimental data and simulation results for SC administration are shown in Figure 5. The model parameters were calibrated against data from the 750 μg SC dose, and the model fit in terms of both neutrophils and G-CSF was good. The model was then used to predict the G-CSF and neutrophil concentration profiles following a 375 μg SC dose. Although the model underpredicted the peak circulating neutrophil concentration, the model successfully captured the peak G-CSF concentration, as well as the dynamic response of G-CSF and neutrophils for the 375 μg dose. The ability of the model to be predictive for G-CSF effects on neutrophil production and recruitment was further evaluated with IV G-CSF administration. No parameters in the model were changed when simulating IV injections. Experimental data and simulation results are shown in Figure 6. For the 750 μg injection, the model overpredicted the average peak neutrophil concentration in the plasma and underpredicted the neutrophil clearance after peak concentration. However, the main neutrophil dynamics after G-CSF IV injection were captured by the model. The model also successfully captured G-CSF concentration after IV administration. For the 375 μg injection, the model predicted plasma neutrophil and G-CSF concentrations matching the experimental results. Overall, without additional adjustment in parameters, the effects of IV G-CSF administration on neutrophil production and recruitment were accurately captured by the model.

2.4.2 LPS Challenge

Neutrophils play an important role in the innate immune response. Understanding the recruitment and production of neutrophils during an infection or other inflammatory challenge could help in the design of treatments to combat sepsis and other inflammatory infections. To study human neutrophil dynamics under inflammatory challenge, Suffredini *et al.* [7] conducted a study in which endotoxin from *Escherichia coli* was administered IV (4 ng/kg of body weight, 6 human subjects) over 1 min. Serial blood samples measured plasma

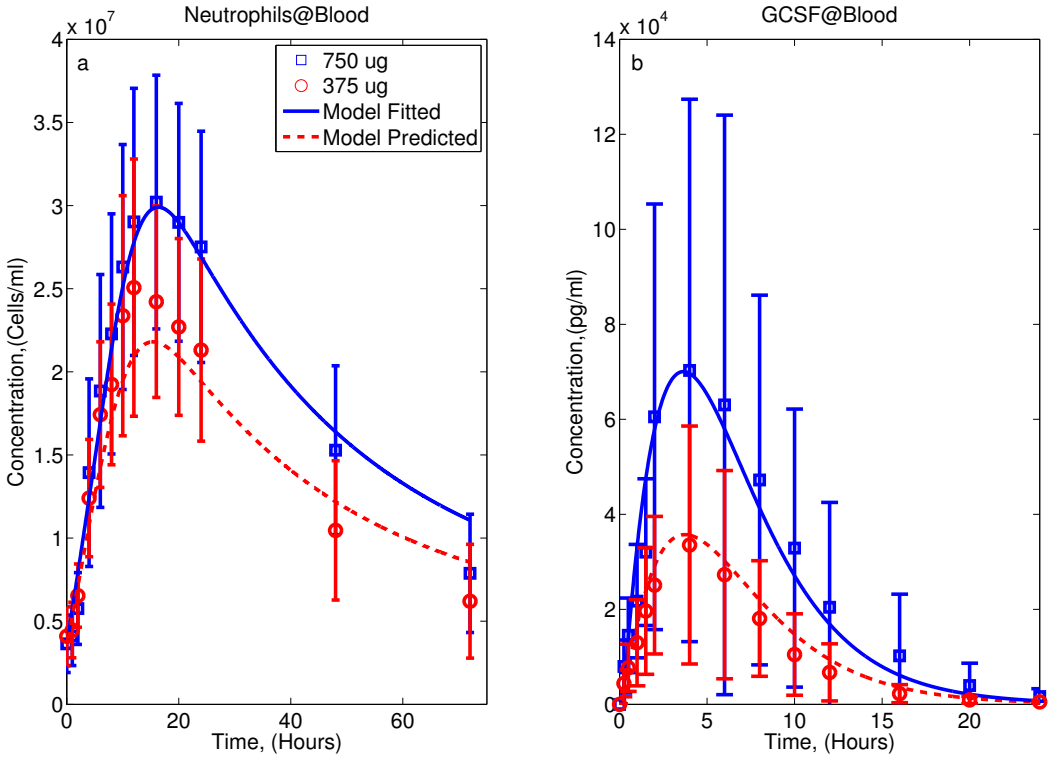

Figure 5: Published (mean ± std. dev., [6]) data and model fit of neutrophil and G-CSF concentrations in response to G-CSF SC injections.

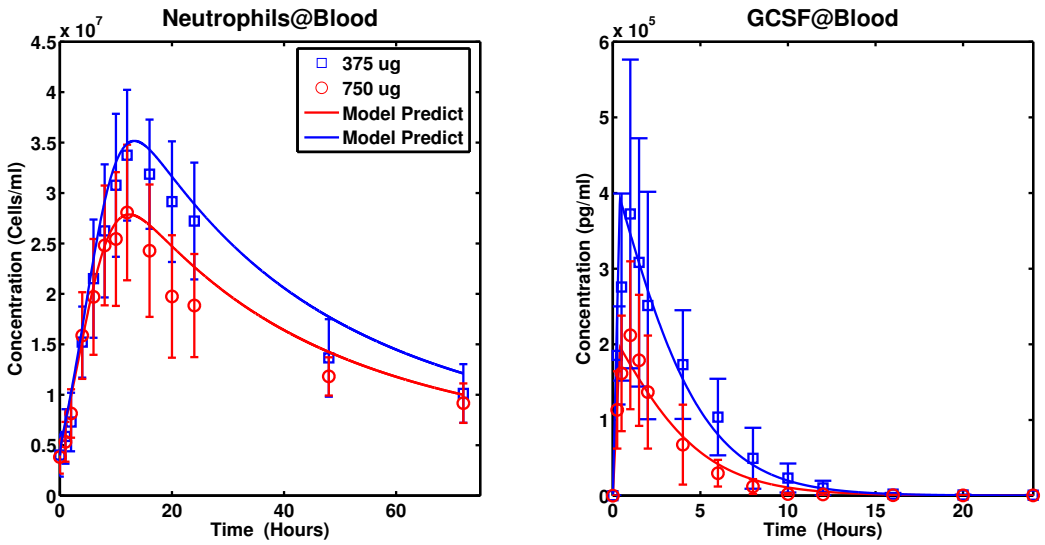

Figure 6: Published (mean ± std. dev., [6]) data and model fit of neutrophil and G-CSF concentrations in response to G-CSF IV injections.

neutrophils, G-CSF levels, and other inflammation-associated cytokines and chemokines. Experimental data and simulation results are shown in Figure 7. The observed neutrophil dynamics are captured well, although the model slightly underpredicts the neutrophil concentration at 2 hr, (Figure 7, left). Some discrepancy is also observed between the G-CSF experimental data and simulation results (Figure 7, right) in terms of peak timing, though the large error bars from the measurement data – likely a result of interpatient variability – reduce the confidence in the mean value of the 3 hr time point. Although the large error bars provide some uncertainty about how well the model is able to capture G-CSF concentration, the fast response of G-CSF in the LPS challenge (within 3 hours) is successfully predicted by the model. On the whole, the G-CSF model captures the experimental data.

The simulation results also provide insight into the complicated dynamics of the physiological inflammatory response, especially neutrophil production and recruitment dynamics. Figure 8 shows simulated LPS levels in the blood as well as the response of different neutrophil compartments. Although the LPS concentration is almost zero after 3 hours (Figure 8a), the effects of the LPS challenge on neutrophil production and recruitment continue for more than

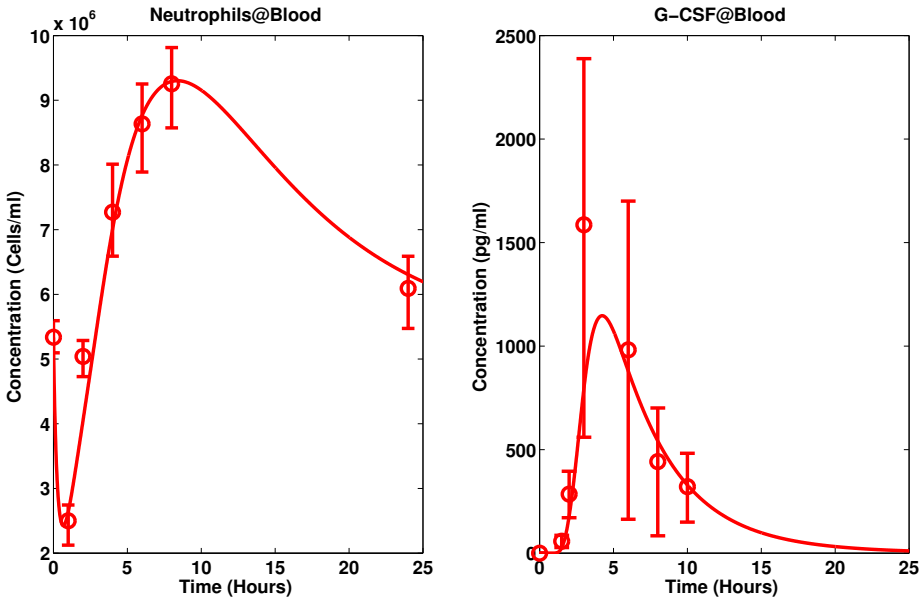

Figure 7: Published (mean ± std. dev., [7]) data and model fit of neutrophil and G-CSF concentration in response to an LPS challenge.

25 hours (Figure 8b and c). Under the LPS challenge, neutrophils quickly bind LPS leading to clearance; the resulting inflammation signal leads to the mobilization of neutrophils from the marginal pool (Figure 8d). The inflammation signal also triggers the recruitment of neutrophil precursors ($T_1(t)$-$T_3(t)$) to the circulation, which causes a drop from baseline of 10% ($T_1(t)$), 23% ($T_2(t)$), and 30% ($T_3(t)$) in their respective populations. The drop in circulating neutrophils leads to an increase in the population of progenitor cells through the G-CSF signaling cascade (Figure 8b). In response to the LPS challenge, homeostasis in neutrophil and precursor levels returns after 36 hours.

2.4.3 Docetaxel Chemotherapy

To study the effects of chemotherapy treatment on ANC, Friberg *et al.* [1] investigated ANC response to a variety of drugs that induce myelosuppresion; our study focuses on docetaxel. Pharmacokinetics (PK) are modeled using a physiologically-based PK model (PBPK) pre-

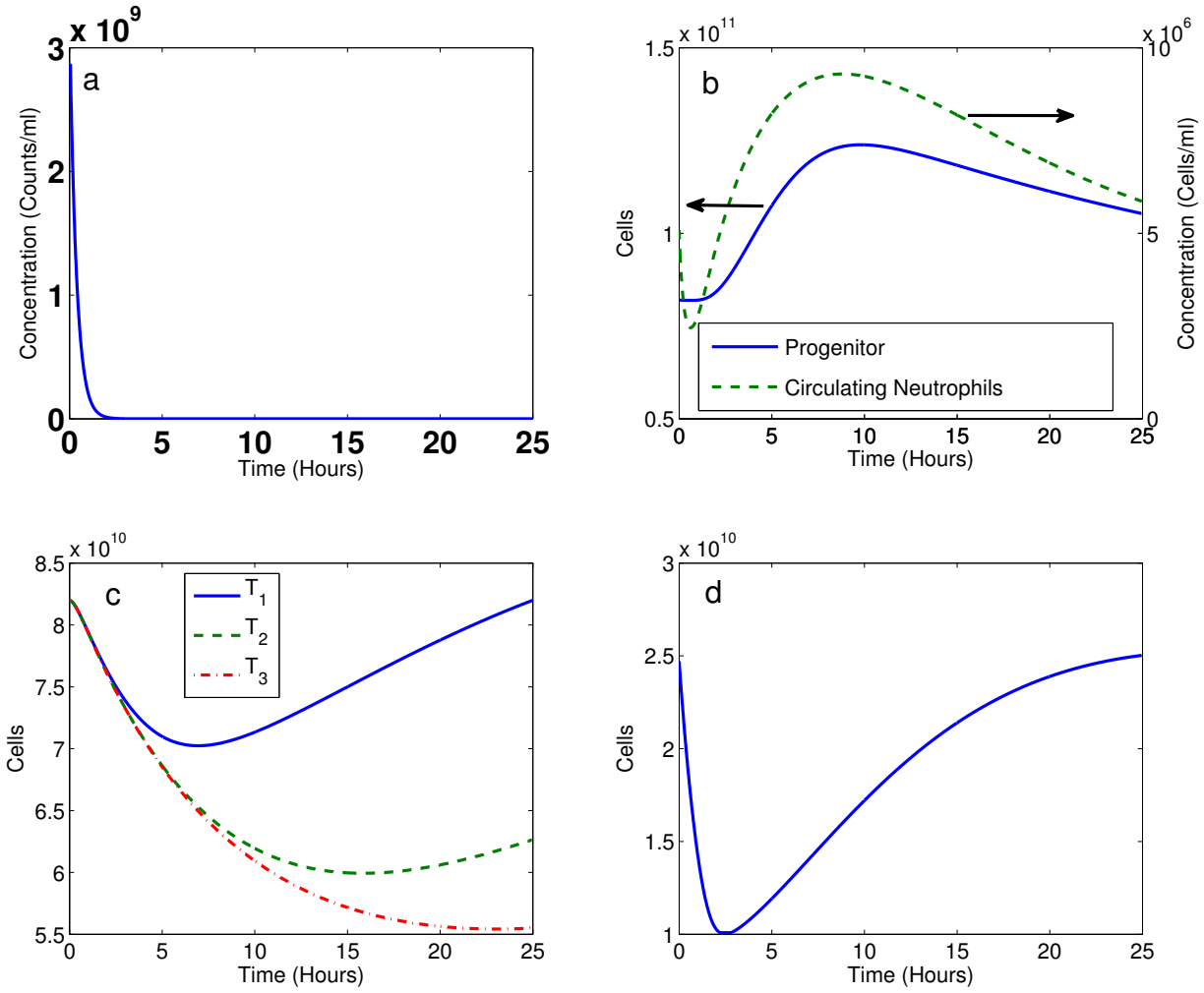

Figure 8: Dynamics of different neutrophil states and LPS. (a) LPS concentration, (b) progenitor population (left axis) and circulating neutrophil concentration (right axis), (c) maturation train population ($T_1(t)$, $T_2(t)$, and $T_3(t)$), (d) marginal pool population

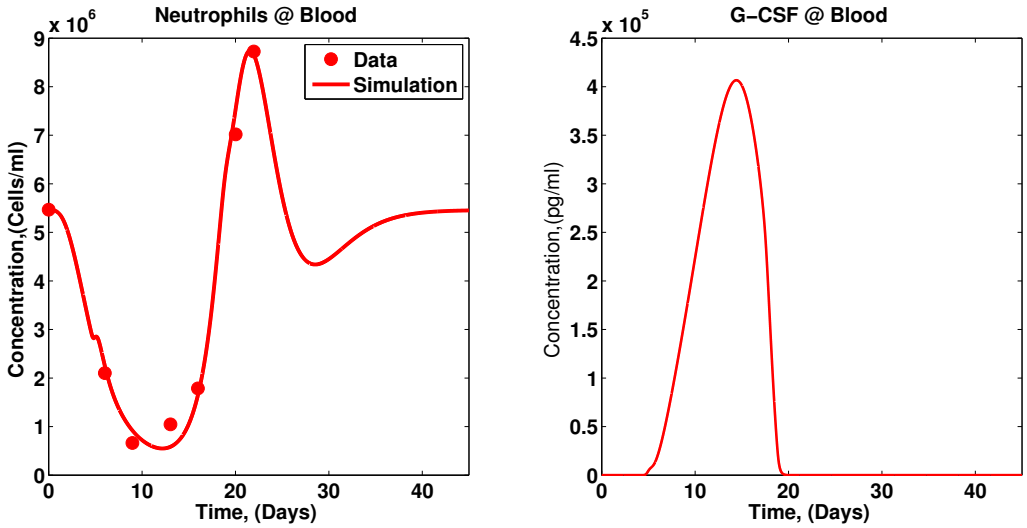

Figure 9: Data [1] and model fit of ANC after 1 hr docetaxel infusion at 100 mg/m^2.

viously developed in our lab [5]. Predictions of circulating docetaxel concentrations are identical to those produced by [99, 100], and docetaxel concentration is used to drive the neutrophil model. The neutrophil model prediction (simulation) is compared to docetaxel response data from patients receiving 100 mg/m^2 docetaxel by 1 hr infusion, as shown in Figure 9. Our model matches the experimental data, but it does not quite capture the nadir of ANC at day 8. The simulation results also show that the ANC level returns to baseline about one month after treatment. Comparing our model with the Friberg *et al.* model in response to 100 mg/m^2 docetaxel infusion, the Friberg *et al.* model was able to capture the nadir ANC but unable to capture the peak ANC. The average absolute error of our model compared to experimental data is 8% while the Friberg *et al.* model average absolute error is 12%. Moreover, our model explicitly includes the G-CSF effects on neutrophil dynamics rather than using the implicit nonlinear feedback observed in the Friberg *et al.* model (Figure 2). G-CSF has been used as a rescue agent for low ANC during chemotherapy. Our model has the ability to represent this effect without changing model parameters, while the Friberg *et al.* model would require an adjustment in the model parameters within the nonlinear feedback mechanism to capture the effect of G-CSF on ANC.

2.4.4 Docetaxel Schedule Comparison

Docetaxel is approved for administration at 60-100 mg/m^2, infused over one hour every three weeks (triweekly schedule) as either a single agent or in combination [101, 102]. An alternative schedule uses 30-45 mg/m^2 infused over 30 minutes every week for 6 weeks, followed by two weeks without treatment (the so-called weekly schedule) [103, 104]. These two schedules exhibit different toxicity profiles while having similar efficacy results [103, 105]. The percentage of patients experiencing grade 3 or 4 neutropenia is much lower on the weekly treatment (49%) compared to the triweekly schedule treatment (76%) [103, 104]. The simulated neutrophil and G-CSF profiles for triweekly docetaxel at 100 mg/m^2 (2 cycles) and weekly docetaxel at 33.3 mg/m^2 (1 cycle) are shown in Figure 10. The total docetaxel dose administered for both cases is 200 mg/m^2. The simulation results show that the nadir of neutrophil concentration is greater on the weekly schedule. After an initial nadir (1.5×10^6) at day 14, the plasma neutrophil concentration remains above 2×10^6 cells/ml through week 8 on the weekly schedule, while the neutrophil concentration drops to below 1×10^6 at both days 14 and 35 on the triweekly schedule.

2.4.5 G-CSF Rescue in Chemotherapy

G-CSF has been used to stimulate neutrophil production and maturation to mitigate neutropenia resulting from chemotherapy [106, 107]. G-CSF is administered via SC injection from days 2 to 12 for patients on the triweekly chemotherapy schedule; research has shown that delivery prior to day 2 or after day 12 does not provide significant benefit [108, 107]. One cycle of docetaxel therapy (100 mg/m^2, triweekly schedule) was simulated. Three G-CSF dose levels: 5, 10, and 15 μg/kg/day, were delivered from days 2 to 12. The simulation results are shown in Figure 11. G-CSF rescue successfully reduces the depth of the nadir – a key driver of treatment schedule changes for cancer chemotherapy patients. This effect appears to be saturable, however, as an increase from 5 to 10 μg/kg/day G-CSF led to a decrease in nadir depth, while a further increase to 15 μg/kg/day had no additional effect on nadir mitigation. This is at least partially driven by suppression of endogenous G-CSF production in the model; Figure 11 shows how circulating G-CSF increases with administration.

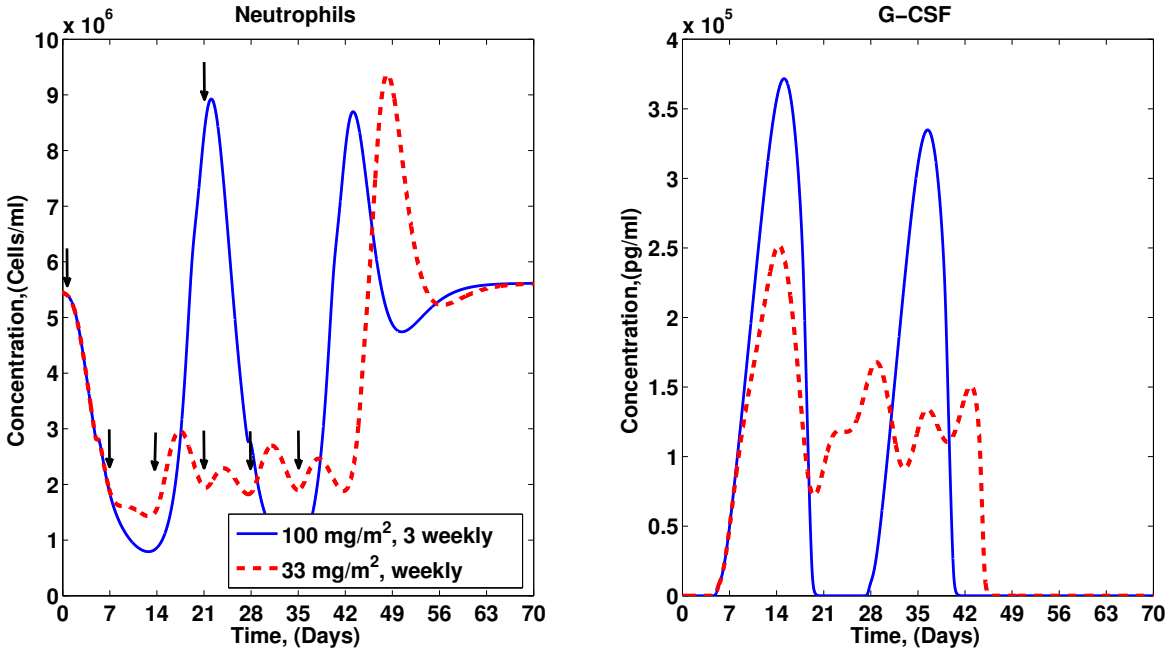

Figure 10: Neutrophil and G-CSF dynamics with different docetaxel schedules: 100 mg/m^2 every three weeks (blue solid) and 33.3 mg/m^2 weekly for six weeks (red dashed). Arrows indicate time of docetaxel administration (triweekly: days 0 and 28; weekly: days 0, 7, 14, 21, 28, 35)

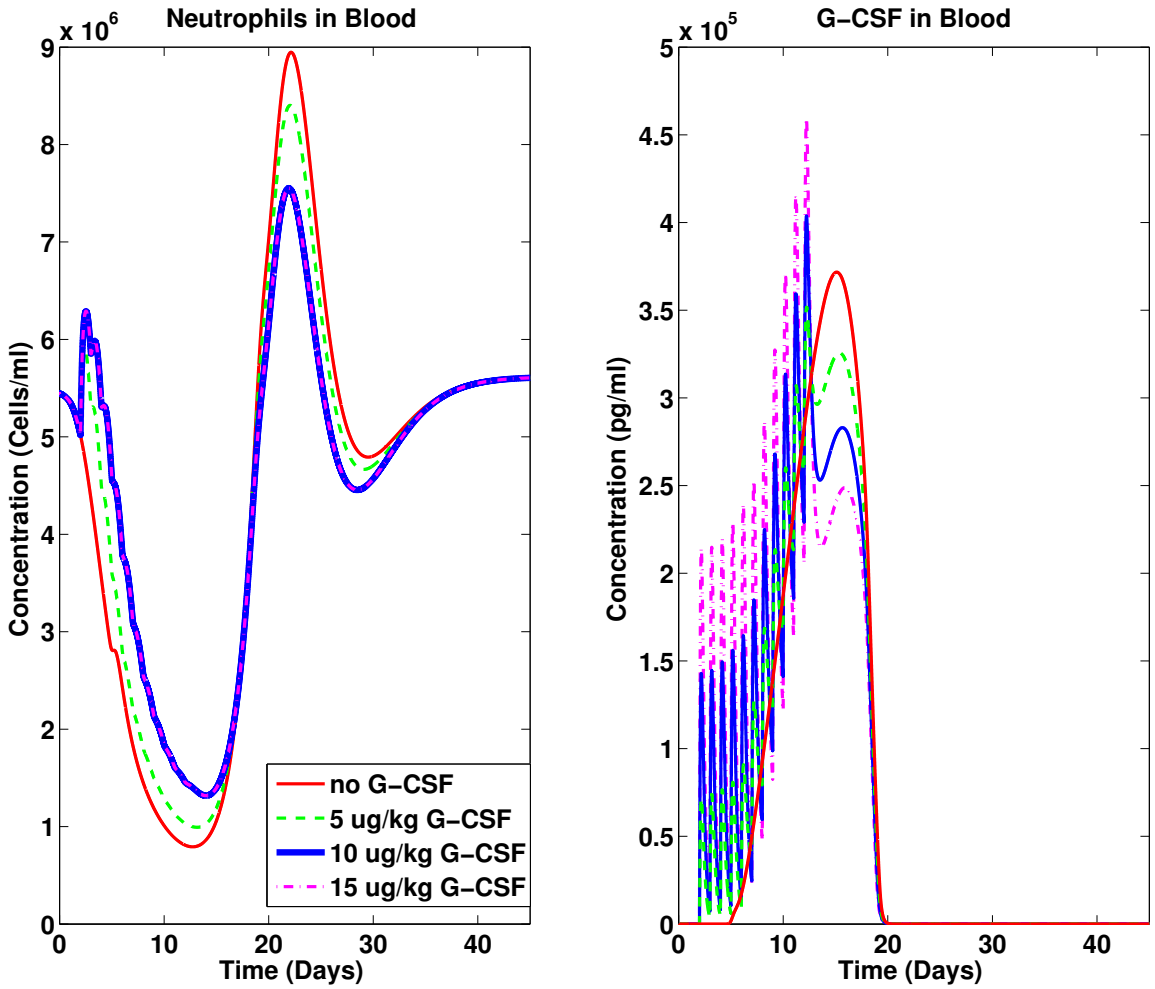

Figure 11: Neutrophil and G-CSF dynamics with different G-CSF dose levels in response to 100 mg/m^2 docetaxel administered at day 0.

The decreasing peak height around day 16, however, is evidence of decreased endogenous G-CSF production by stromal cells – a result of the increased number of circulating neutrophils and decreased feedback signal through the feedback cascade in Figure 3. In addition to the aforementioned saturation in observable effect of G-CSF on circulating neutrophil concentrations, the simulation results also suggest that higher doses may negatively impact recovery from chemotherapeutic challenges by suppressing endogenous production.

2.5 DISCUSSION

The neutrophil dynamic model is built from the identified signaling cascade of G-CSF and its effects on neutrophils. In order to capture the dynamics of the biological system, Michaelis-Menten and second-order Hill functions were used to represent saturation phenomena, characteristic of sensing and production limitations often encountered in biological systems. The key difference between these nonlinear functions is the linear initial region observed in the Michaelis-Menten kinetics versus the lag/switch-type response provided by the Hill function. The use of these well-understood structures aids biological understanding of the signals and responses, even though some parameters may be harder to estimate from available data (*e.g.*, Michaelis-Menten half-maximum values).

LPS challenge has been used to study the physiological inflammation response, and it is believed to provide some insight into sepsis response [7, 109]. The model captures neutrophil response to LPS challenge and the resulting G-CSF signal response. The depletion of immature neutrophils in the bone marrow compartments under inflammatory response, as in Figure 7, explains the rapid rise of circulating neutrophil levels and the experimental detection of "young" neutrophils in the blood [110, 111]. Coupling the physiological model with the neutrophil response to LPS may provide insight into both the migration and damage caused by activated neutrophils in healthy tissues as well as the systemic response to inflammation and sepsis. It should be noted that the uncertainty in the G-CSF concentrations at peak response to LPS challenge is significant, and though our model is within the error bars and approximates the mean data over the dynamic profile well, it does not capture the mean

value of the peak concentration. The implication is that there are a variety of model structures or parameter vectors that could capture this individual data set. With a focus on linear dynamics, we provide a comparatively simple representation that can capture the observed response. While this may, or may not, capture the mechanistic accuracy of the LPS-induced G-CSF response, further experiments would be required to elucidate these (in)accuracies.

Neutropenia/myelosuppression is a common chemotherapeutic toxicity. The ANC level categorizes neutropenia in increasing severities from grade 1 to grade 4 [112]. Simulations of the PBPK model of docetaxel, and the effect of this drug on neutrophil levels through the model, demonstrate the differences in toxicity resulting from triweekly and weekly docetaxel administration. Triweekly docetaxel results in grade 3 neutropenia (nadir between 0.5 to 1.0×10^6 cells/ml), which is consistent with observed clinical data [104, 103]. In contrast, the weekly schedule nadir only generates grade 2 neutropenia (nadir $<= 2\times10^6$ cells/ml), in agreement with literature [104, 113]. Recovery dynamics also differ, in that ANC is high on day 21 in response to triweekly docetaxel (so called "rebound"), which would return to baseline around day 30 if a second dose were not administered on day 21.

The ANC profile after weekly docetaxel administration can be explained by the endogenous G-CSF cascade. Day 0 and day 7 doses of docetaxel cause the neutrophil concentration to reach its nadir. The G-CSF production dynamics, neutrophil production response, and neutrophil maturation take 7-10 days from initial challenge [110, 111]. Hence, the innate recovery system of the body has begun to respond before the second dose, leading to a mitigated nadir depth; the magnitude of the drop in ANC after the second dose does not match that of dose 1. The second docetaxel dose also serves to further upregulate G-CSF. As a result of the increased neutrophil production already in the maturation chain (T_1-T_3), docetaxel dose 3 does not cause a drop to the same level as the single triweekly dose, even though an equivalent amount of docetaxel has been administered. The remaining doses on the weekly schedule show a small recovery of ANC due to the upregulated neutrophil production/maturation (a result of G-CSF signaling), a phenomenon unsustained in the triweekly schedule where a second grade 3 nadir is observed in cycle 2.

G-CSF rescue has been shown to decrease neutropenia grade [106, 107]. The model shows the effectiveness of exogenous G-CSF administration, while also indicating doses higher than

10 ug G-CSF/kg/day may be ineffective at further reducing neutropenia. A possible explanation of this observation is that at sufficiently high doses, the number of available unstimulated progenitor cells may become limiting. This explanation could be further studied and validated experimentally, and this could be a useful tool to optimize G-CSF dosing for neutropenia reduction. Another observation from the model is the reduction in endogenous G-CSF production due to exogenous G-CSF administration, as can be seen from the maximum G-CSF peak around day 16 (decreasing peak magnitude with increasing G-CSF daily dose). Although increasing dose from 10 μg G-CSF/kg/day to 15 μg /kg/day has no impact on neutrophil dynamics, this increment in dose causes a reduction in endogenous G-CSF production and circulating concentration after the final dose. One could imagine a scenario where this reduction may be detrimental, leading to a testable hypothesis from the model.

Although the model was built on the biological foundation of neutrophils and the G-CSF signaling cascade, the quality of the model parameters and structure in the feedback cascade can be debated due to the sparsity in supporting data for these states. However, the feedback G-CSF cascade is mainly driven by neutrophil apoptosis [114], and this is captured by the proposed model. Furthermore, the model captures both fast responses (inflammation) and slow dynamics (myelosuppressive therapeutic), lending credence to the structural choices. Finally, as more data is collected within the feedback signaling cascade, the physiological and biological framework can easily be (in)validated and refined.

2.6 SUMMARY

In this chapter, a model of neutrophil dynamics based on the biology of production and signaling through the G-CSF cascade was developed. The model was calibrated to an inflammatory LPS challenge for both neutrophil and G-CSF dynamics. The model was then tested with a myelosuppressive chemotherapy challenge, and it accurately predicted the much slower neutrophil dynamics following IV docetaxel administration. Finally, the model was used to study neutrophil dynamics after different chemotherapy schedules and G-CSF rescue during chemotherapy. The simulation results show that the model successfully captures

literature-reported dynamics for different chemotherapy schedules and for G-CSF rescue. This model of neutrophil dynamics, including the biologically-derived feedback of G-CSF on cell proliferation, provides a more detailed view of neutrophil dynamics in response to multiple disparate challenges. With its ability to capture both slow and fast neutrophil dynamics, the biologically-motivated model may be useful in studying neutrophil response and treatment design in a broad range of inflammatory and antineoplastic challenges, including sepsis and other myelosuppressive chemotherapy regimens, where neutrophils play a significant role in limiting treatment (cancer) or response (inflammation/sepsis).

3.0 LINEAR AND NONLINEAR MODEL REDUCTIONS FOR BIOLOGICALLY BASED MODELS

3.1 MODEL REDUCTION

Mathematical models, especially pharmacokinetic (PK) models, have been used in clinical practice to aid physicians in patient treatment [18, 99]. With simpler structures (often two or three compartments) and fewer parameters than mechanistic or physiological-bases models [8, 5], PK models are easy to use and able to capture patient drug dynamics [17, 18, 99]. Moreover, with as few as one parameter adjustment, PK models can successfully capture individual patient drug dynamics. For example, the three compartment model of docetaxel published in 2001 [99] captures docetaxel dynamics in 200 patients after a drug injection or infusion by adjusting only docetaxel clearance, which is a function of body surface area, age, α_1-acid glycoprotein, and albumin concentrations. Owing to their simple structures and ability to capture patient-specific drug dynamics, PK models are widely accepted in the clinical settings as tools to aid physicians in patient treatment.

However, the use of mathematical models in clinical settings is generally limited to PK models, despite the fact that mathematical models have been developed to capture the biological signaling cascades of different diseases [50, 115, 116], drug dynamics [117, 118], and their interactions [119, 120]. Although these models have successfully represented the biological information of various diseases and/or drug effects, the complex structure and large number of parameters make it difficult to tune these models to capture individual patient response without some guidelines or guidance regarding the impact of making adjustments to model parameters [116, 118, 120]. The complex model structures with large number of parameters discourage clinicians to apply these models in clinical settings.

To expand the use of mathematical models in clinical settings, model complexity needs to be reduced and key parameters identified so that clinicians will be able to efficiently implement the models and capture patient dynamics without needing to be an expert in the underlying model dynamics. In this work, we present a systematic method to reduce complexity in a biologically-based model, where complexity is measured as state and parameter quantity. Through sensitivity analysis and parameter correlation matrices, we utilize a technique developed by Daun *et al.* [23] to further reduce the parameter space to a key parameter set dictating the main model dynamics. Using our previously published model of the biological signaling cascade of neutrophils and Granulocyte-Colony Stimulating Factor (G-CSF) [8] as the case study, we reduce the model to a lower-order structure and identify the primary parameters necessary to capture the main dynamics of neutrophils and G-CSF in both an inflammatory challenge and in myelosuppression during chemotherapy.

3.2 PHYSIOLOGICAL BASED DOCETAXEL PHARMACOKINETIC MODEL REDUCTION

Although the docetaxel PBPK model is a linear model, 35 states could create difficulties in model simulation, if model speed is an issue as well as difficulties in optimization if model is used as dynamic constraints because number of constraints would scale with number of time steps in the optimization, which could be large[20, 21]. Therefore, reducing the model to a simpler structure would increase solution convergence rate and reduce the difficulty in model simulation and model-based optimization while the model dynamics of interest are preserved. The PBPK model is reduced by balanced truncation via the square root method [22] to retain the dynamics of docetaxel concentrations in plasma and in tumor. The general algorithm for this method can be outlined as the following for state space system (A,B,C,D) with a desired reduced order k [22]:

1. Find the single value decomposition (SVD) of the controllability (P) and observability (Q) grammians:

$$P = U_p \Sigma_p V_p^T \tag{3.1}$$

$$Q = U_q \Sigma_q V_q^T \tag{3.2}$$

2. Find the square root of the grammians (left/right eigenvectors)

$$L_p = U_p \Sigma_p^{1/2} \tag{3.3}$$

$$L_q = U_q \Sigma_q^{1/2} \tag{3.4}$$

3. Find the SVD of the grammian eigenvectors

$$L_q^T L_p = U \Sigma V^T \tag{3.5}$$

4. Compute the left (L) and right (R) transformation for final kth order reduced model

$$S_{L,BIG} = L_q U(;,1:k)\Sigma(1:k,1:k)^{-1/2} \tag{3.6}$$

$$S_{R,BIG} = L_p V(;,1:k)\Sigma(1:k,1:k)^{-1/2} \tag{3.7}$$

5. And then compute the A$_r$, B$_r$, C$_r$, D$_r$ matrix for the reduced the model

$$\left.\begin{array}{c|c} A_r & B_r \\ \hline C_r & D_r \end{array}\right. = \left.\begin{array}{c|c} S_{L,BIG}^T A S_{R,BIG} & S_{L,BIG}^T B \\ \hline C S_{R,BIG} & D \end{array}\right. \tag{3.8}$$

The algorithm is the built-in function *balancmr* from MATLAB. The detail of the algorithm and mathematical proof can be found in [22]. The PBPK model of docetaxel is reduced with plasma concentration as a single output, tumor concentration as a single output, and plasma and tumor concentrations as two simultaneous outputs. The reduced model error comparing to the original model is 2 times the sum of Hankel singular values of the truncated states. The reduced model with both plasma and tumor concentration as the output is also subjected to different docetaxel challenges to compare it to the original model result.

3.3 BIOLOGICALLY-BASED NEUTROPHIL MODEL REDUCTION

3.3.1 Parametric Sensitivity Analysis by the Finite Difference Method

The neutrophil-G-CSF signaling cascade is a set of $N_x = 14$ differential equations with N_x states and $M = 55$ parameters (denoted k_i). The sensitivity matrix $S = (s_{i,j})$ (dimension $N_x \times M$) is calculated using the finite difference method, in which the sensitivity coefficients, $s_{i,j}$ are calculated from the difference of nominal and perturbed solutions by [23, 121]:

$$s_{i,j}(t) = \frac{\partial x_i(t)}{\partial k_j} = \frac{x_i(t, k_j + \Delta k_j) - x_i(t, k_j)}{\Delta k_j} \tag{3.9}$$

where $i \in [1, N_x], j \in [1, M]$. To facilitate direct comparison of sensitivities between parameters having different nominal magnitudes, the sensitivity coefficients $s_{i,j}$ are normalized:

$$\overline{s_{i,j}}(t) = \frac{\partial x_i(t)}{\partial k_j} \frac{k_j}{x_i} \tag{3.10}$$

The normalized sensitivity matrices at different times t inform the dynamic effects of the parameters on the model outputs. If the sensitivity value is 1, then the output is highly sensitive to the parameter. If the sensitivity value is 0, the parameter is not sensitive (*e.g.*, the model output does not change if the parameter is changed). The normalized sensitivity matrices are used to cluster the parameters for model reduction and to reduce the parameter space.

3.3.2 Parameter Clustering via Sensitivity Analysis

We use the method developed by Chu *et al.* to compute the angle between the sensitivity vectors within the sensitivity matrix [20]

$$cos(\gamma_{i,j}) = \frac{s_i^T s_j}{s_{i_2}, s_{j_2}} \tag{3.11}$$

where s_i and s_j are sensitivity vectors associated with parameters k_i and k_j, respectively, and $\cos(\gamma_{i,j})$ is the cosine of the angle between the sensitivity vectors, which defines a similarity measure. If the similarity is equal to unity then the effects of the two parameters on the outputs are perfectly correlated. Parameter clustering via sensitivity analysis consists of the following steps [20]:

1. Calculate the sensitivity matrix using Equation (3.9)
2. Parameters that have sensitivity vector values less than 1% are removed from the analysis as these parameters have negligible effect on the output.
3. The parameters that have a small angle between their sensitivity vectors are grouped via agglomerative hierarchical clustering based on the similarity measurement given by Equation (3.11). The similarity measurement provides the proximity of the parameters to each other. The parameters close to each other (cosine value approximately equals to 1) are paired into binary clusters. The newly formed clusters are grouped into larger clusters until a hierarchical tree is formed. The clustering procedure results in a hierarchical tree represented in a dendrogram.
4. The hierarchical tree threshold is selected to determine the grouping of parameters [20]. Parameters in the same group have highly correlated effects on the outputs (*i.e.*, circulating neutrophil concentration and plasma G-CSF concentration in this case study).

The outcome of this procedure is that the parameters are clustered into distinctive groups where changes of a parameter in-group can be compensated for by changes of other parameters in the same group. Due to this correlation, it is only possible to estimate one parameter per group, which serves as an indicator that the model can be simplified without losing accuracy. However the correlation results do not provide guidance on how to simplify the model like in the case of linear model reduction. The information provides by clustering analysis is used to develop a guidance for nonlinear model reduction as described in Section 3.3.3.

3.3.3 Nonlinear Model Reduction Procedure

Nonlinear model reduction does not have a generalized procedure. In this thesis, we use the procedure of model reduction based on clustering analysis described by Chu*et al.* with the following steps [20]:

1. Only state variables involved in the signaling cascade containing the clustered parameters are considered for reduction or retention in the reduced model.
2. The components retained in the reduced model are chosen by the following rationale described by Chu *et al.* [20]: (a) at least one state is selected for each parameter cluster,

(b) state variables with the possibility of having experimental measurements should be retained. This step provides an general structure of the reduced model with dynamics of interests.

The structure of the reduced model is determined by linking the chosen variables from different clusters with the equations connecting these clusters or by lumping the reactions in the same cluster into one equation associated with the representative state variable [20]. It may be necessary to retain some states other than ones determined by this analysis in order to satisfy conservation laws [20].

3.4 PARAMETER SPACE REDUCTION VIA IDENTIFIABILITY ANALYSIS

3.4.1 Identifiability Analysis

A numerical method described by Jacquez and Greif is used to check *a priori* local identifiability of the parameters at a given time point [122]. Using the nominal values of parameter vector k, the N_x by M sensitivity matrices, $S(t_i)$, are calculated at all time points i at which measurements of neutrophils and G-CSF have been taken, using equation 3.9. The matrix G is then constructed by stacking the time dependent sensitivity matrices [23]:

$$G = \begin{bmatrix} S(t_1) \\ S(t_2) \\ S(t_3) \\ \vdots \\ S(t_n) \end{bmatrix} \tag{3.12}$$

The M by M parameter sensitivity-dependent correlation matrix R is calculated as follows:

$$C = cov(G) = G^T Q G \tag{3.13}$$

$$r_{i,j} = \frac{c_{i,j}}{\sqrt{c_{i,i} c_{j,j}}} \tag{3.14}$$

Here Q is generally a square matrix of weighting coefficients, allowing the weighting of matrix G depending on additional information available for this particular parameter or particular time point (e.g., biologically relevant, literature published parameter, available measurement at specific time). The remaining analyses herein employ Q as the identity matrix (equal weighting across parameters and time). The sensitivity-dependent correlation matrix is calculated via normalization of the matrix C with the geometric mean of its diagonal elements to scale the sensitivity matrix between -1 and +1. Each parameter that is locally identifiable has a correlation value between -1 and +1 with each of the other parameters. Parameters that are not locally identifiable have a correlation of exactly -1 or +1 with at least one other parameter. These parameters influence the model outcome in exactly the opposite or exactly the same ways, respectively. The parameter sensitivity-dependent correlation matrix, R is used to reduce the parameter space of the model.

3.4.2 Parameter Space Reduction Procedure

The number of free parameters in the K-reduced model is a K dimensional parameter set $\overline{\theta}$ that can be reduced using the following iterative process described by Daun *et al.* [23]:

1. Calculate the sensitivitydependent correlation matrix
2. Identify one highly correlated parameter pair (A,B)
3. If the model outcome is highly sensitive to both parameters, fix neither of them and restart with step 2. Else, fix to its nominal value the parameter in the pair that the model outcome is least sensitive to, and go back to step 1

The process continues until no more highly correlated, highly sensitive parameters remain. The calculations within this process are equivalent to:

1. calculating the sensitivity vectors for each parameter
2. calculating the angle between each pair, and for a pair with a sufficiency small angle between them,
3. calculating the magnitude of the vectors in the pair.

3.5 RESULTS

3.5.1 Docetaxel Pharmacokinetic Model Reduction

The docetaxel PBPK model (Section 2.2.2, and Appendix A) was reduced via the balanced truncation method of Section 3.2. Three reduced forms of the PBPK model, each characterized by its output variables, were generated:

- plasma docetaxel concentration as the only output
- tumor docetaxel concentration as the only output
- both plasma and tumor docetaxel concentrations as outputs

The Hankel singular values and their graphs were used to evaluate the accuracy of the reduced models with respect to the original model. When the docetaxel plasma concentration is the only output, the Hankel singular values with respect to the number of states in the truncated model are shown in Figure 12. Figure 12 suggests that the reduced model requires three or four states to accurately capture the docetaxel plasma concentration. The error bound ($2\sum_{i=1}^{N_T}\sigma_H(i)$) for three states is 2.610^{-2} while the error bound for four states is 8.410^{-3}. Since the normalized peak docetaxel concentration in plasma after an infusion is in order of 1, the three states model is used to capture docetaxel concentration in plasma. The current model used in the clinical setting to capture docetaxel pharmacokinetics has three compartments [99]. Our reduction shows that when only plasma dynamics are considered, the PBPK model can be reduced to a three state model that can capture the same dynamics as Bruno *et al.* [99].

The PBPK model is further evaluated under the same reduction technique when tumor tissue concentration is the only output. The Hankel singular values versus number of states in the truncated model are shown in Figure 13.

When tumor concentration is the only output of the model, Figure 13 suggests that a three or four state model can be used to accurately retain the dynamics of the drug inside the tumor. The error bound for the three state model is 7.2610^{-2} while the error bound for the four state model is $6.8e10^{-3}$. Peak normalized docetaxel tumor concentration after

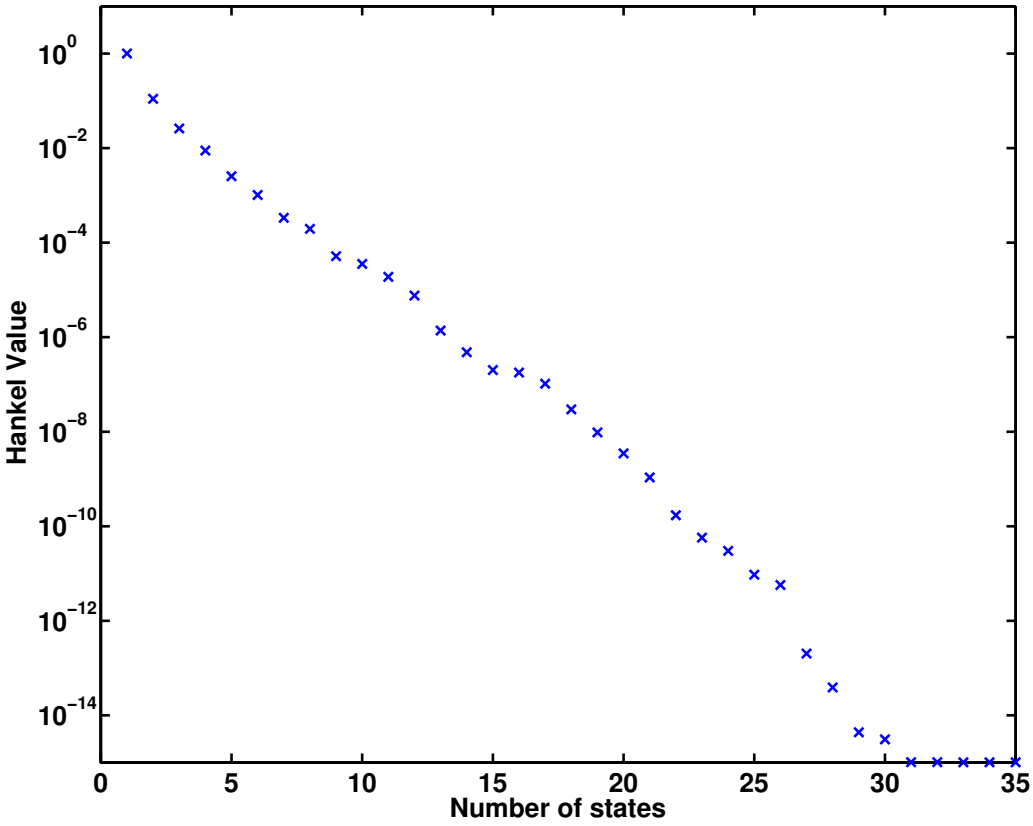

Figure 12: Hankel singular value versus number of states in the truncated model for docetaxel plasma concentration as output.

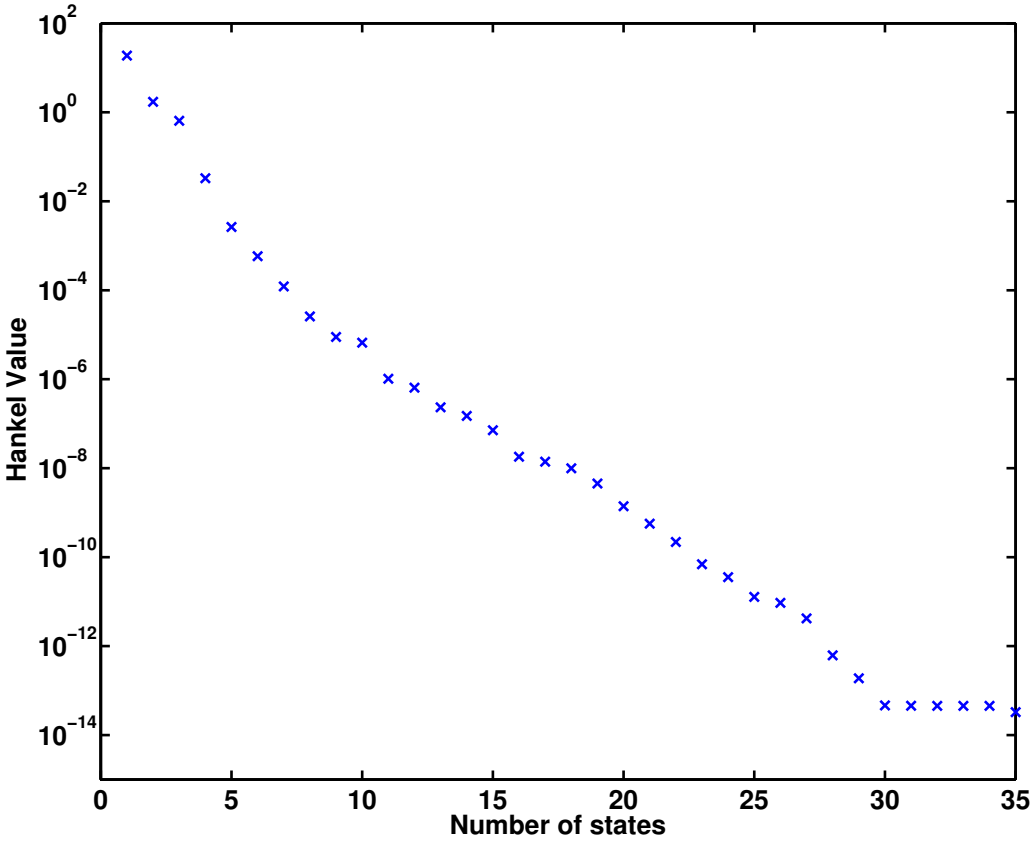

Figure 13: Hankel singular value versus number of states for docetaxel tumor concentration as output

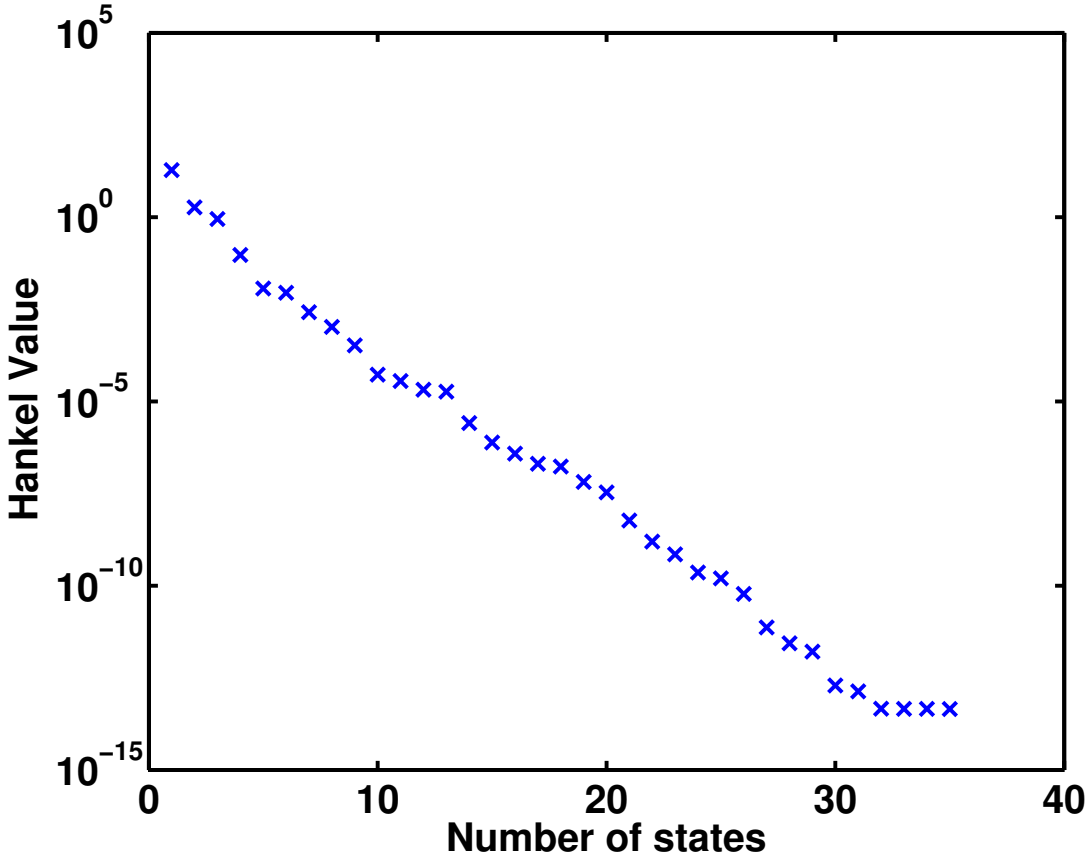

Figure 14: Hankel singular value versus number of states for docetaxel plasma and tumor concentrations as outputs

an infusion is in order of 1;therefore, the four states model is used to capture docetaxel concentration in tumor.

In the clinical setting, the drug plasma concentration is often the only available measurement. To evaluate drug efficacy, tumor concentration should be more informative, and therefore would need to be retained in the reduced model. In the models constructed in this dissertation, the plasma concentration drives toxicity while the tumor concentration drives drug efficacy. Therefore, the plasma and tumor concentrations are preserved as outputs for our reduced PK model. The Hankel singular values with respect to the number of states in the truncated model are shown in the Figure 14 for the case where both outputs need to be accurately captured upon reduction.

The Hankel singular values show that in order for the dynamics of the reduced model to accurately represent the plasma and tumor concentrations, the number of states in the reduced model should be between 3 and 5. The error bounds for 3,4, and 5 states are 0.23, 4.9010^{-2}, and 2.6010^{-2} respectively. Thus, 4 or 5 states would be able to capture the dynamics of interests. However, when the 4 states model is used, the docetaxel tumor concentration does not capture the peak concentration of the PBPK model, thus we use the five states model to capture both docetaxel concentrations in plasma and tumor. The final state space reduced model equations are shown in Equations (3.15) and (3.16)

$$\dot{x} = \underline{\underline{A}}x + \underline{B}u \tag{3.15}$$

$$y = \underline{\underline{C}}x \tag{3.16}$$

$$\underline{\underline{A}} = \begin{bmatrix} -1.258 \times 10^{-4} & -1.258 \times 10^{-4} & 5.422 \times 10^{-4} & -1.825 \times 10^{-5} & -1.147 \times 10^{-5} \\ 3.651 \times 10^{-4} & -1.133 \times 10^{-3} & -3.706 \times 10^{-4} & 2.44 \times 10^{-3} & 1.631 \times 10^{-3} \\ -8.15 \times 10^{-4} & 4.922 \times 10^{-3} & -1.027 \times 10^{-2} & -7.773 \times 10^{-3} & -5.653 \times 10^{-3} \\ -4.65 \times 10^{-4} & 2.67 \times 10^{-3} & 1.128 \times 10^{-2} & -3.372 \times 10^{-2} & -3.837 \times 10^{-2} \\ -2.971 \times 10^{-4} & 1.775 \times 10^{-3} & -7.655 \times 10^{-3} & -3.837 \times 10^{-2} & -0.1122 \end{bmatrix}$$

$$\underline{B} = \begin{bmatrix} 0.1104 \\ -6.455 \times 10^{-2} \\ 0.135 \\ 0.07957 \\ 0.05083 \end{bmatrix}$$

$$\underline{\underline{C}} = \begin{bmatrix} 3.1975 \times 10^{-4} & -1.529 \times 10^{-3} & 2.332 \times 10^{-3} & 1.984 \times 10^{-3} & -1.267 \times 10^{-3} \\ 7.672 \times 10^{-5} & -1.529 \times 10^{-3} & -6.8348 \times 10^{-5} & -4.0005 \times 10^{-6} & 2.7321 \times 10^{-6} \end{bmatrix}$$

The original model and the reduced model with two outputs (reduced PBPK model) were tested by challenging each with docetaxel infusions on two schedules, as follows:

- 100 mg/m^2, one hour infusion every three weeks
- 35 mg/m^2 thirty minute infusion three weeks on, one week off (or six weeks on two weeks off)

The simulated plasma and/or tumor concentrations for the original and reduced models are shown in Figures 15 and Figure 16, respectively. The reduced PBPK model and the PBPK model results for two different docetaxel infusions show that the reduced model retains the key dynamics of docetaxel for plasma and tumor concentrations. The sum of squared residuals between the original model and the reduced model are 3.1310^{-6} μM^2 and 9.2610^{-9} μM^2 for docetaxel concentration in plasma and docetaxel concentration in tumor for a 100 mg/m^2 IV infusion, respectively. For a 35 mg/m^2 IV infusion, the sum square of the residuals between the original model and the reduced model are $2.1210^{-6}\mu M^2$ and 2.30 10^{-10} μM^2

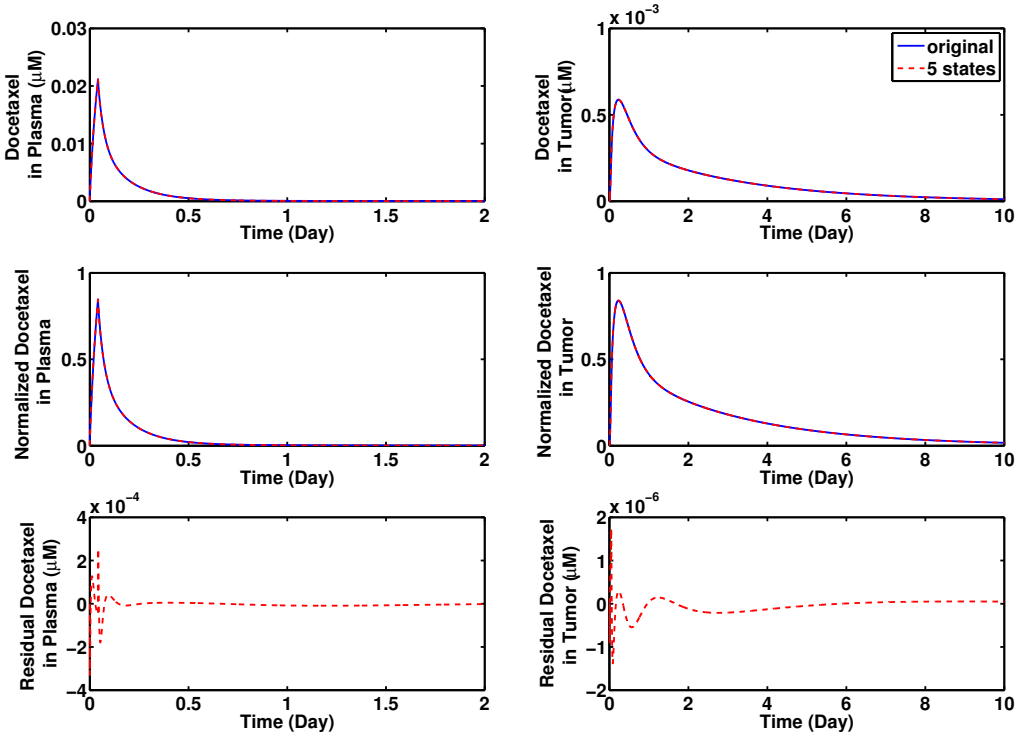

Figure 15: Docetaxel plasma concentration (top left) and tumor concentration (top right) for the original PBPK model (solid line, blue) and the reduced PBPK model (dashed line, red) for 100 mg/m^2 1 hour docetaxel IV infusion; docetaxel plasma concentration normalized with respect to maximum docetaxel plasma concentration (middle left) and docetaxel tumor concentration normalized with respect to maximum docetaxel tumor concentration (middle right). Also plotted are the residuals between the original model and the reduced model for plasma concentration (bottom left) and tumor concentration (bottom right). Note that x-axis spans differ by a factor of 5 between the plasma and tumor profiles.

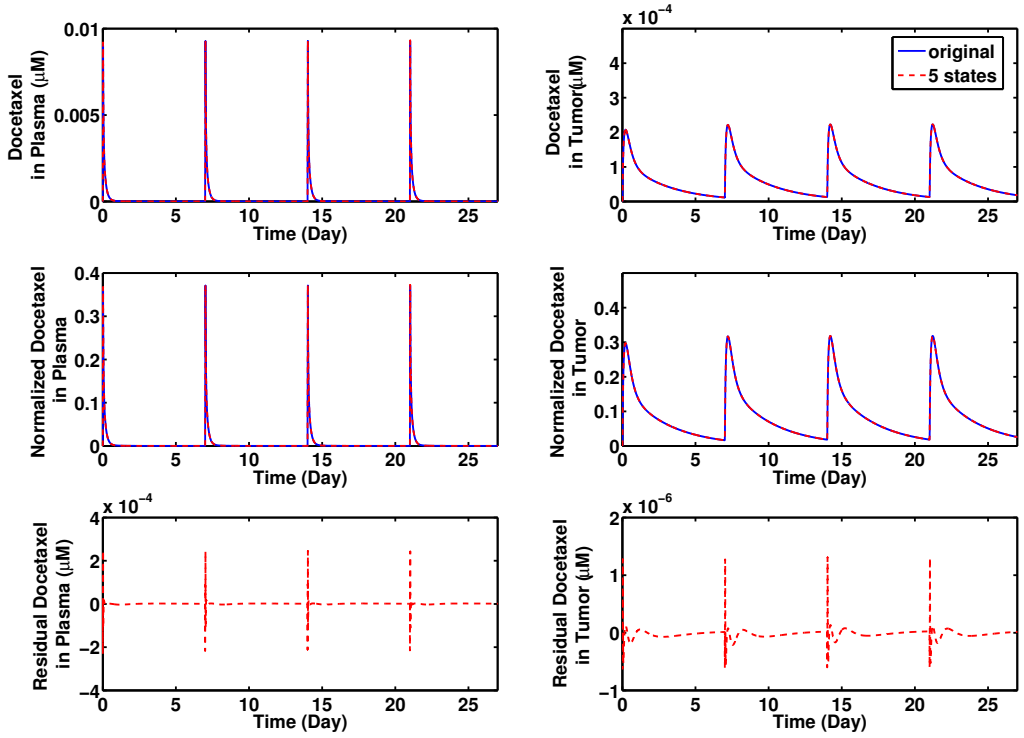

Figure 16: Docetaxel plasma concentration (top left) and tumor concentration (top right) for the original PBPK model (solid line, blue) and the reduced PBPK model (dashed line, red) for 35 mg/m^2 30 minutes docetaxel IV infusion; docetaxel plasma concentration normalized with respect to maximum docetaxel plasma concentration (middle left) and docetaxel tumor concentration normalized with respect to maximum docetaxel tumor concentration (middle right) Y-axis values are scaled to the peak plasma or tumor concentration, respectively, achieved after 100 mg/m^2 IV infusion. Also plotted are the residuals between the original model and the reduced model for plasma concentration (bottom left) and tumor concentration (bottom right).

for docetaxel concentration in plasma and docetaxel concentration in tumor, respectively. ,With the high level of dynamic agreement between the original model and reduced PBPK model, all further docetaxel PK simulations and optimizations herein use the reduced model.

3.5.2 Neutrophil Model Reduction

The clustering method via sensitivity analysis (section 3.3.2) for the G-CSF production (from N_c to G-CSF, as seen in Figure 3) yields a 20 parameter dendrogram, as seen in Figure 17. Using a cosine similarity cutoff of 0.9 yields two parameter clusters. The two parameter

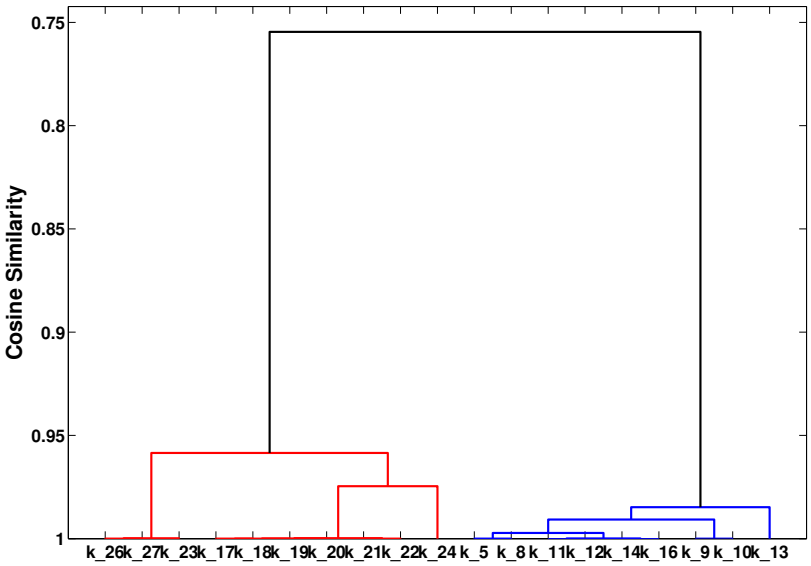

Figure 17: Dendrogram of 20 Parameter Clustering for G-CSF Production

clusters are related to the measurable states of Interleukin-17 (IL-17) [123] and Interleukin-23 (IL-23) [124], suggesting that two states can be used to capture the feedback mechanism of G-CSF production.

The original neutrophil-G-CSF model assumed the transit rates between compartments in the neutrophil maturation chain had the same value and mathematical representation [8]. To reduce the model further, we assume the transit rates in the maturation chain are independent of each other. The clustering method of parameters, revealed one cluster of

maturation chain parameters. One cluster reveals that the maturation chain can be reduced into one state. The final reduced neutrophil-G-CSF model is presented in Figure 18. Stem cells produce progenitors that mature into the neutrophil precursor population. Neutrophil precursor matures into circulating neutrophils, which are released to the vascular space. Decreasing circulating neutrophil counts cause IL-23 production to increase. An increase in IL-23 leads to IL-17 secretion. Increases in IL-17 cause more G-CSF to be produced. Thus, the production of progenitors and neutrophil precursors increases due to the increase in G-CSF concentration. The neutrophil and G-CSF dynamics are modeled by a set of states and ordinary differential equations as outlined below.

- **Stem cells (S):** Originating in the bone marrow niche, hematopoietic stem cells mature into progenitors in the presence of G-CSF [125, 126]. Stem cells in this model are assumed to be a constant population of cells that can differentiate into the progenitor population. The rate of differentiation from stem cells to progenitors is controlled by the G-CSF concentration.
- **Progenitor ($Pr(t)$):** progenitor is the population representing the first differentiated state of stem cells toward mature neutrophils [127]. The progenitor population is produced from stem cells, and the production rate is controlled by G-CSF concentration at the basal rate k_1 when G-CSF concentration is low, and at rate k_2 when G-CSF concentration is high. The maturation rate of the progenitor toward neutrophil precursors is also affected by the amount of G-CSF present [128].

$$\frac{dPr(t)}{dt} = \left(k_1 + \frac{k_2 GCSF(t)}{k_3 + GCSF(t)}\right) S - k_{tr} Pr(t) \tag{3.17}$$

where:

$$k_{tr} = k_{21}\left(1.0 + \frac{k_{22} GCSF(t)}{k_{23} + GCSF(t)}\right) \tag{3.18}$$

Here the basal maturation rate is k_{21}, and the increase in maturation rate is modeled using Michaelis-Menten kinetics with respect to G-CSF concentration having the maximum rate k_{22} and half maximum constant k_{23}.

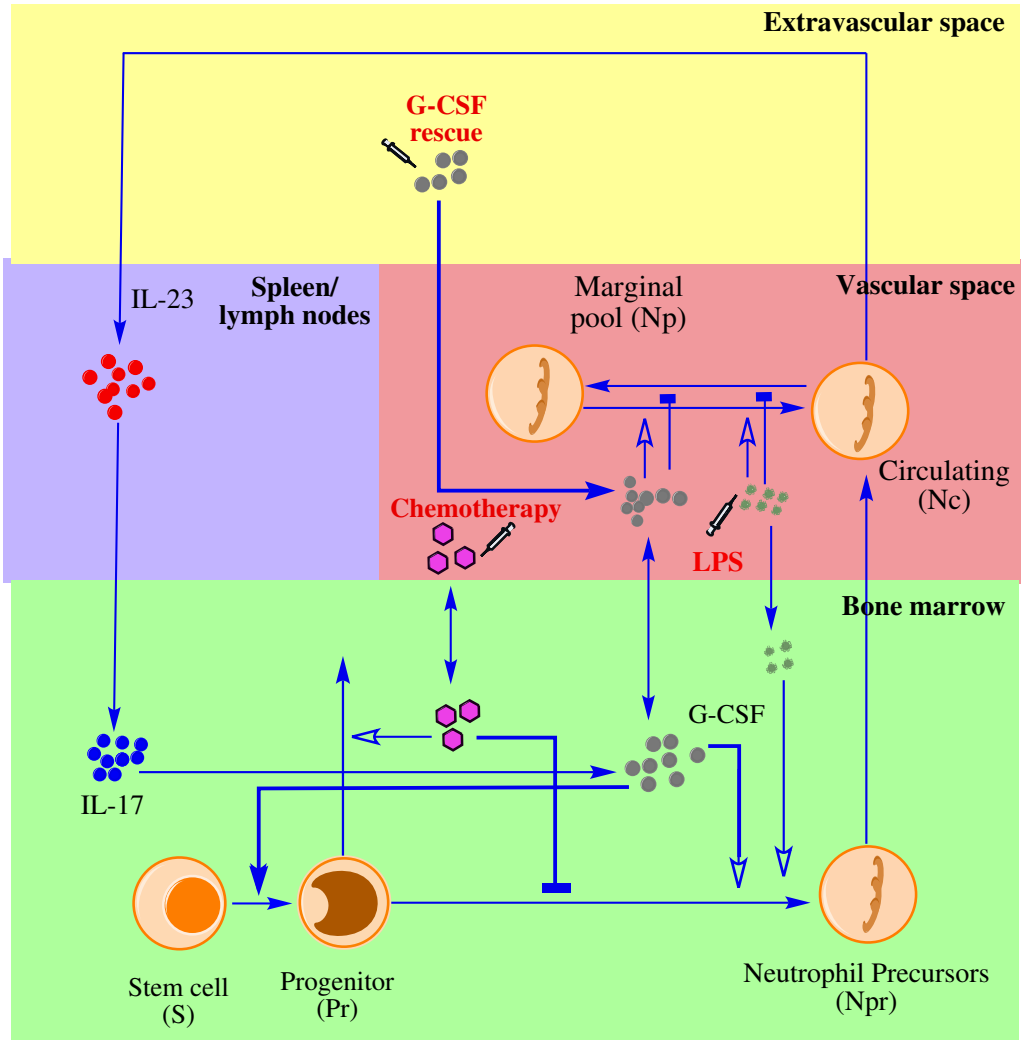

Figure 18: Reduced model of neutrophil-G-CSF signaling cascade

- **Neutrophil Precursors ($N_{pr}(t)$):** The $N_{pr}(t)$ state represents the population of premature neutrophils residing in the bone marrow [126, 127]. The maturation of precursors to circulating neutrophils depends on G-CSF concentration [128]. The maturation rates of $Pr(t)$ to $N_{pr}(t)$ and $N_{pr}(t)$ to circulating neutrophils are modeled as a function of G-CSF:

$$\frac{dN_{pr}(t)}{dt} = k_{tr}Pr(t) - \frac{k_{tr}}{3}N_{pr}(t) \tag{3.19}$$

  Here the rate of progenitors maturing to neutrophil precursors is k_{tr}, and the rate of neutrophil precursors migrating to the circulation is $\frac{k_{tr}}{3}$.

- **Marginal pool ($N_{pm}(t)$):** This is the portion of mature neutrophils residing within the body (non-circulating) that can immediately mobilize in response to external stimuli [129, 16]. The neutrophil marginal pool is comparable in size to the circulating pool [129, 16]. The marginal pool is modeled in equilibrium with the circulating neutrophils at rate k_{tr}, where the equilibrium parameters depend on G-CSF concentration modeled by using Michaelis-Menten kinetics having the maximum rate k_4 and half maximum constant k_5.

$$\frac{dN_{pm}(t)}{dt} = k_{tr}V_{Plasma}N_c(t) - k_{tr}\left(1.0 + \frac{k_4 GCSF(t)}{k_5 + GCSF(t)}\right)N_{pm}(t) \tag{3.20}$$

- **Circulating Neutrophils ($N_c(t)$):** The dynamics of circulating plasma neutrophils are captured by the state $N_c(t)$, which comes from the progenitor population. $N_c(t)$ is modeled in equilibrium with the $N_{pm}(t)$ state. Under external stimuli like trauma or infection, circulating neutrophils are recruited towards the site of the stimuli, an effect included in the model [129]. Circulating neutrophil degradation is modeled using first-order kinetics to maintain neutrophil homeostasis, where the degradation rate decreases with increasing G-CSF concentration (along a Michaelis-Menten kinetic)[130].

$$\begin{aligned}\frac{dN_c(t)}{dt} = & -k_{tr}N_c(t) + \frac{k_{tr}}{V_{plasma}}\left(1.0 + \frac{k_4 GCSF(t)}{k_5 + GCSF(t)}\right)N_p(t) \\ & + \frac{k_{tr}}{3V_{plasma}}N_{pr}(t) - k_d N_c(t)\end{aligned} \tag{3.21}$$

  where:

$$k_d = k_{24}\left(1.0 - \frac{k_{25}GCSF(t)}{k_{26} + GCSF(t)}\right) \tag{3.22}$$

- **Interleukin-23 ($IL_{23}(t)$):** IL-23 is produced by macrophage when the concentration of circulating neutrophils decreases below its normal level [124, 131]. IL-23 production is modeled as zero order production, k_9, with a second order Hill function inhibiting the effect of circulating neutrophils on IL-23 production with half maximum constant k_{10}. When circulating neutrophil concentration is high, IL-23 production is low. The degradation of IL-23 is modeled using first order kinetics with rate constant, k_{11}.

$$\frac{dIL_{23}(t)}{dt} = k_9\left(1.0 - \frac{N_c(t)^2}{k_{10}^2 + N_c(t)^2}\right) - k_{11}IL_{23}(t) \tag{3.23}$$

- **Interleukin-17 ($IL_{17}(t)$):** IL-17 is produced by activated T-cells in the presence of IL-23 [123, 132] . The production rate of IL-17 is modeled as a Hill function to capture the saturation of the production rate at high IL-23 concentration with rate constant k_{12} and half maximum constant k_{13}. The high order (4) of this term furthermore provides the fast response of IL-17 production to increased IL-23. However, IL-17 production is still small when IL-23 levels remain low. The degradation of IL-17 is also modeled as a Hill function with rate constant k_{14} and half maximum constant k_{15}. The rationale is that the clearance of IL-17 becomes zero order with excessive IL-17 to create in the saturating clearance effect observed in biological systems[133]:

$$\frac{dIL_{17}(t)}{dt} = \frac{k_{12}IL_{23}(t)^4}{k_{13}^4 + IL_{23}(t)^4} - \frac{k_{14}IL_{17}(t)^{1.5}}{k_{15}^{1.5} + IL_{17}(t)^{1.5}} \tag{3.24}$$

- **G-CSF ($G_{CSF}(t)$):** G-CSF is produced by stromal cells in the presence of IL-17 [134, 133]. The $G_{CSF}(t)$ in this model represents G-CSF concentration in the plasma. The G-CSF production rate is modeled as a second order Hill function in response to stimulation by IL-17, with rate constant k_6 and half maximum constant k_7 .The G-CSF clearance rate is modeled as first order with respect to G-CSF plasma concentration at rate k_8. The secondary clearance of G-CSF is driven by neutrophils. When the circulating neutrophil concentration is high, the clearance of G-CSF increases following a Michaelis-Menten function of circulating neutrophils with rate constant k_{16} and half maximum constant

k_{17}. The circulating G-CSF is in dynamic equilibrium with G-CSF in tissue ($GCSF_t(t)$) with forward rate constant k_{19} and reverse rate constant k_{18} to capture G-CSF dynamics after subcutaneous G-CSF administration [8].

$$\begin{aligned}\frac{dG_{CSF}(t)}{dt} &= \frac{k_6 IL_{17}(t)^2}{k_7^2 + IL_{17}(t)^2} IL_{17}(t) - \left(k_8 + \frac{k_{16}N_c(t)}{k_{17} + N_c(t)}\right) G_{CSF}(t) \\ &\quad + k_{18}G_{CSF_t}(t) - k_{19}G_{CSF}(t)\end{aligned} \tag{3.25}$$

- **G-CSF tissue ($G_{CSF_t}(t)$):** The G-CSF tissue state is in dynamic equilibrium with circulating G-CSF. The clearance of G-CSF in the tissue is modeled using first order kinetics with rate constant k_{20} to capture tissue clearance [8]:

$$\frac{dG_{CSF_t}(t)}{dt} = k_{19}G_{CSF}(t) - k_{18}G_{CSF_t}(t) - k_{20}G_{CSF_t}(t) \tag{3.26}$$

The reduced neutrophil model consists of 8 states and 26 parameters. A 43% state reduction and 54% parameter reduction is achieved via parameter clustering (section 3.3.2). The IL-23 and IL-17 states are retained as possible measurable states for further analysis if experimental measurements of those species become available. The reduced neutrophil model structure is used to capture the dynamics of neutrophils and G-CSF in LPS challenge and docetaxel chemotherapy.

3.5.3 Parameter Space Reduction

Although the reduced model contains 54% fewer parameters than the original model, it is still complex and difficult to fit all 26 remaining parameters. Among these parameters, some are less sensitive than others, and the majority of parameters are highly correlated with each other. As a result, sensitivity (Section (3.3.1)) and correlation analysis (Section (3.4.1)) are used to further decrease the parameter set to a small space for use in fitting patient-specific dynamics.

Examples of parameter sensitivity with respect to the plasma neutrophil concentration and plasma G-CSF concentration at day 4, 8, 12, 16, 21, and 30 after docetaxel infusion are shown in Figure (19). Most of the sensitive parameters are located between parameter k_9

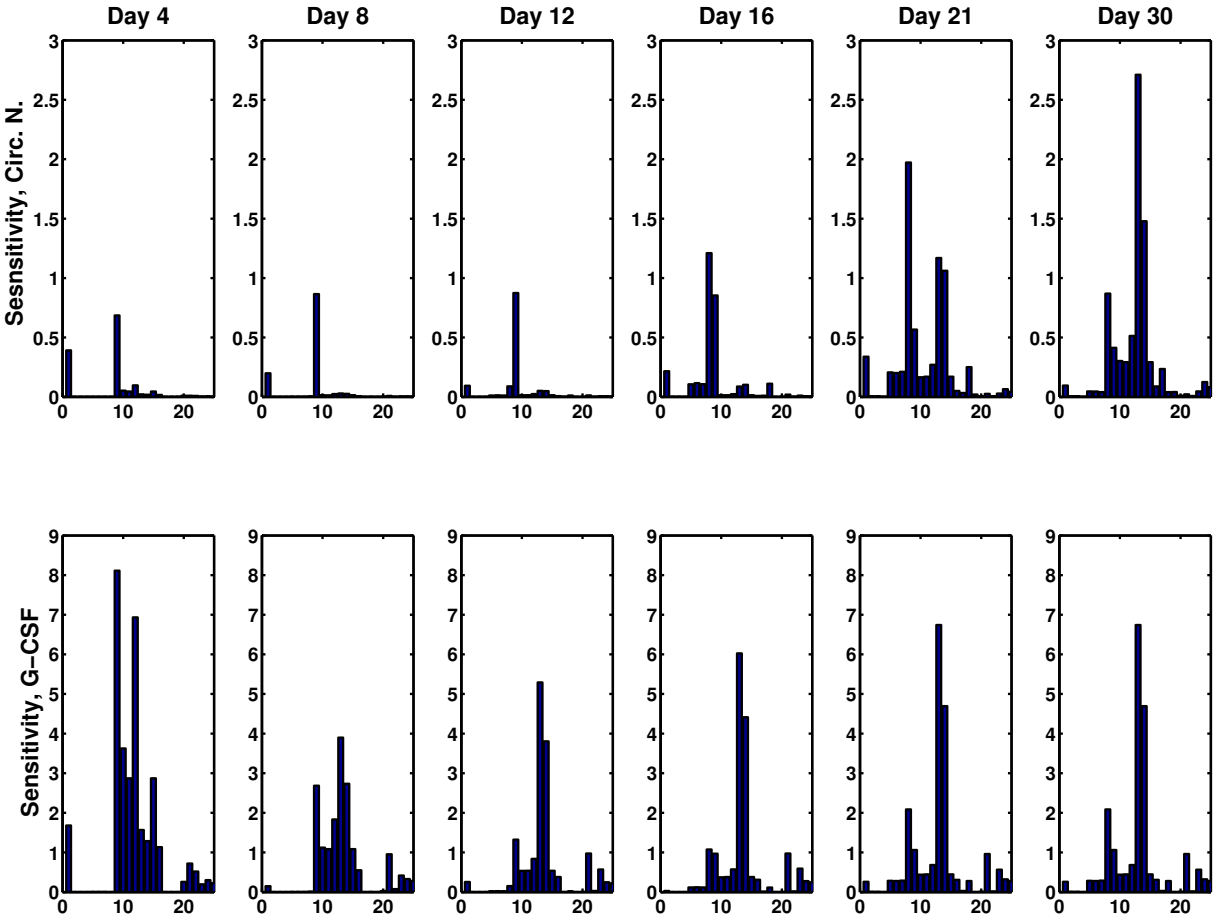

Figure 19: Normalized sensitivity of circulating neutrophils (Circ. N.) and G-CSF outputs at select time points versus parameters .

and parameter k_{15}, while the remaining parameters are generally less sensitive. Therefore, it is possible to remove the non-sensitive parameters from the parameter identification space.

The 27×27 correlation matrix of the parameters is shown in Figure 20. With at least 15 non-sensitive parameters and a correlated parameter matrix, the identifiability analysis described in Section (3.4.1) is used to reduce the parameter space of the model. The iterative process of removing one parameter at a time results in a 6×6 parameter correlation matrix

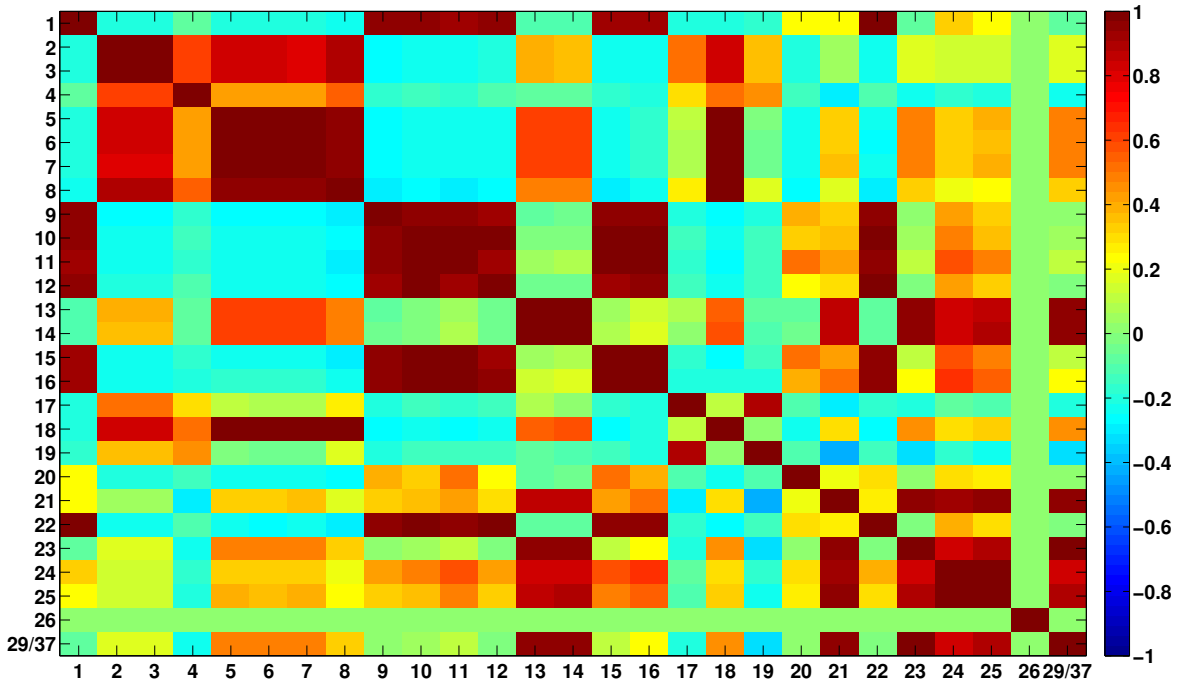

Figure 20: Parameter correlation matrix of all parameters in the reduced model

with the 6 most sensitive parameters associated with both the LPS challenge and docetaxel chemotherapy (Figure 21) where k_{29} and k_{37} are parameters associated with LPS challenge (Equation (2.22)) and docetaxel toxicity (Equation (2.11)), respectively. The roles of the six most sensitive parameters are examined in the context of neutrophil and G-CSF responses. 5 are consistent across challenges. Neutrophil and G-CSF dynamics are impacted by parameters k_9, k_{10}, and k_{11}, which are associated with IL-23 production and clearance (Equation (3.23)). Although these three parameters are highly correlated with each other (Figure 21), it is not possible to remove them from the parameter space due to their high sensitivity with respect to plasma neutrophil concentration and plasma G-CSF concentration. Parameters k_{14} and k_{15} (Figure 21) are associated with IL-17 clearance (Equation (3.24)). These two parameters are also highly correlated with each other; however, due to their sensitivity, the two parameters have to remain in the parameter space to capture neutrophil

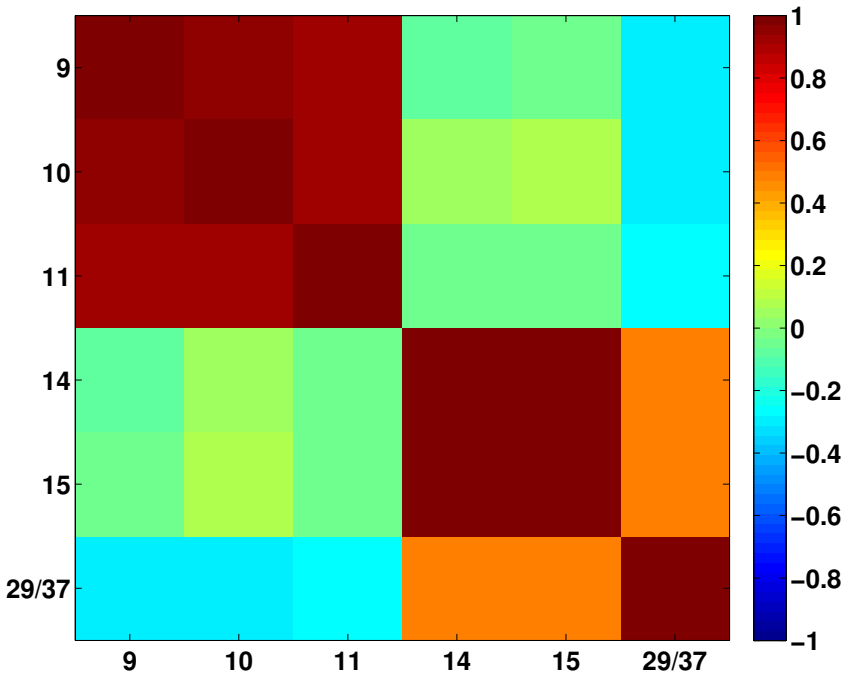

Figure 21: Parameter correlation matrix of 6 most sensitive parameters in the reduced model

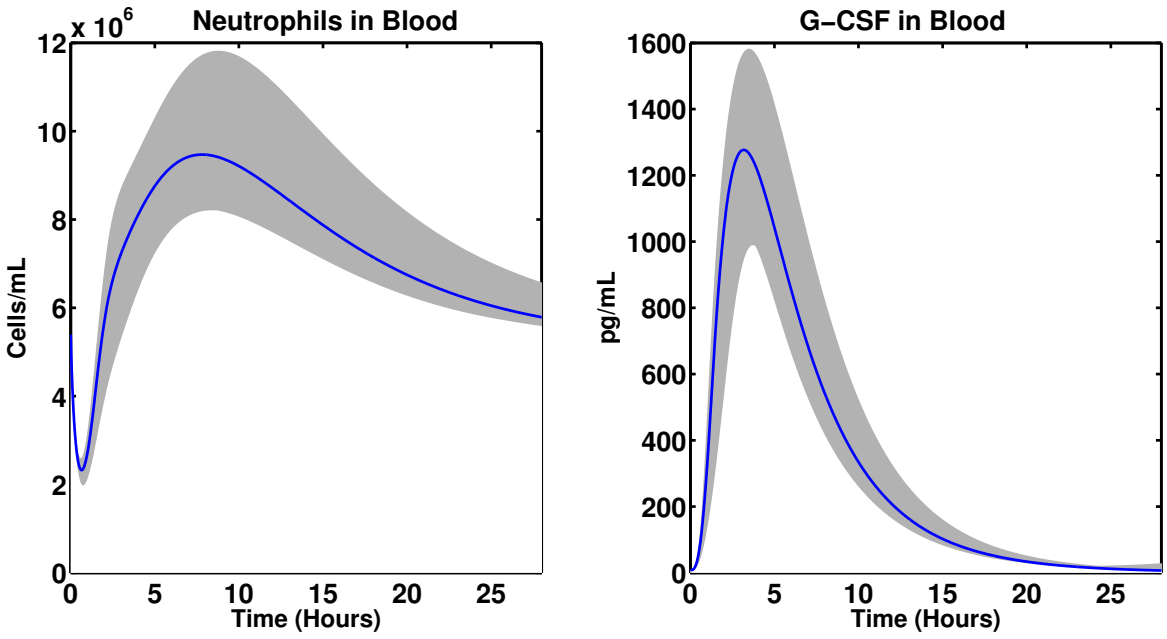

Figure 22: Neutrophil and G-CSF dynamics in response to 4 ng/kg LPS challenge. Nominal parameter value: solid line; ±50% variation of non-sensitive parameters: shaded area

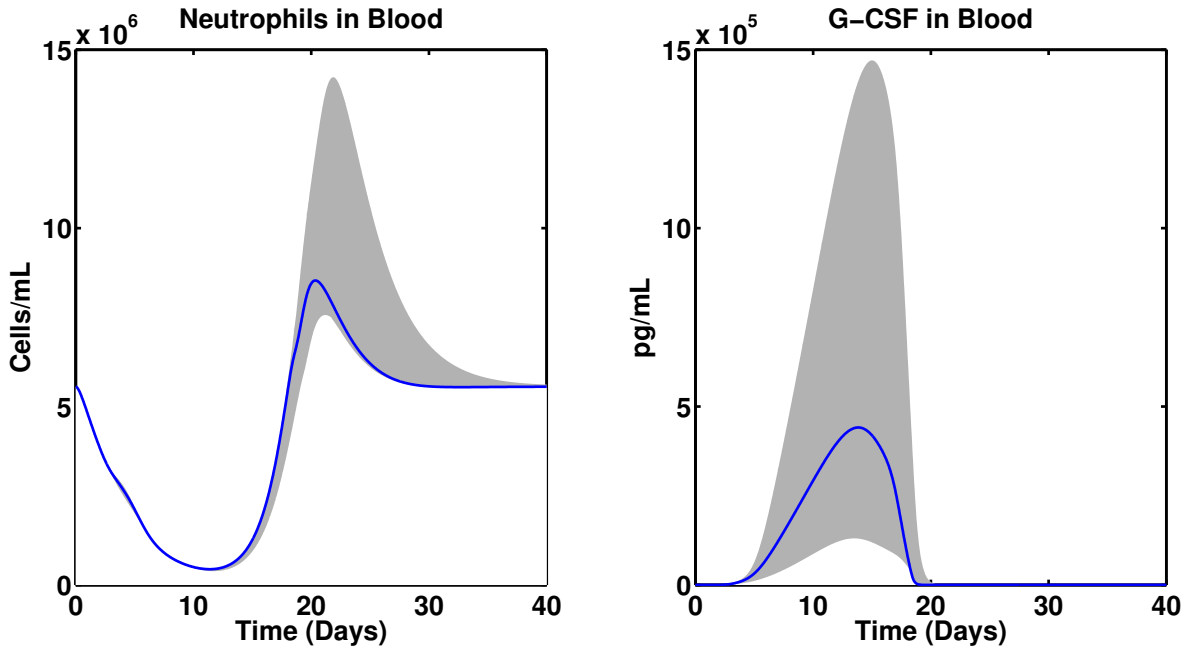

Figure 23: Neutrophil and G-CSF dynamics in response to 100 mg/m^2 docetaxel chemotherapy. Nominal parameter value: solid line; $\pm 50\%$ variation of non-sensitive parameters: shaded area

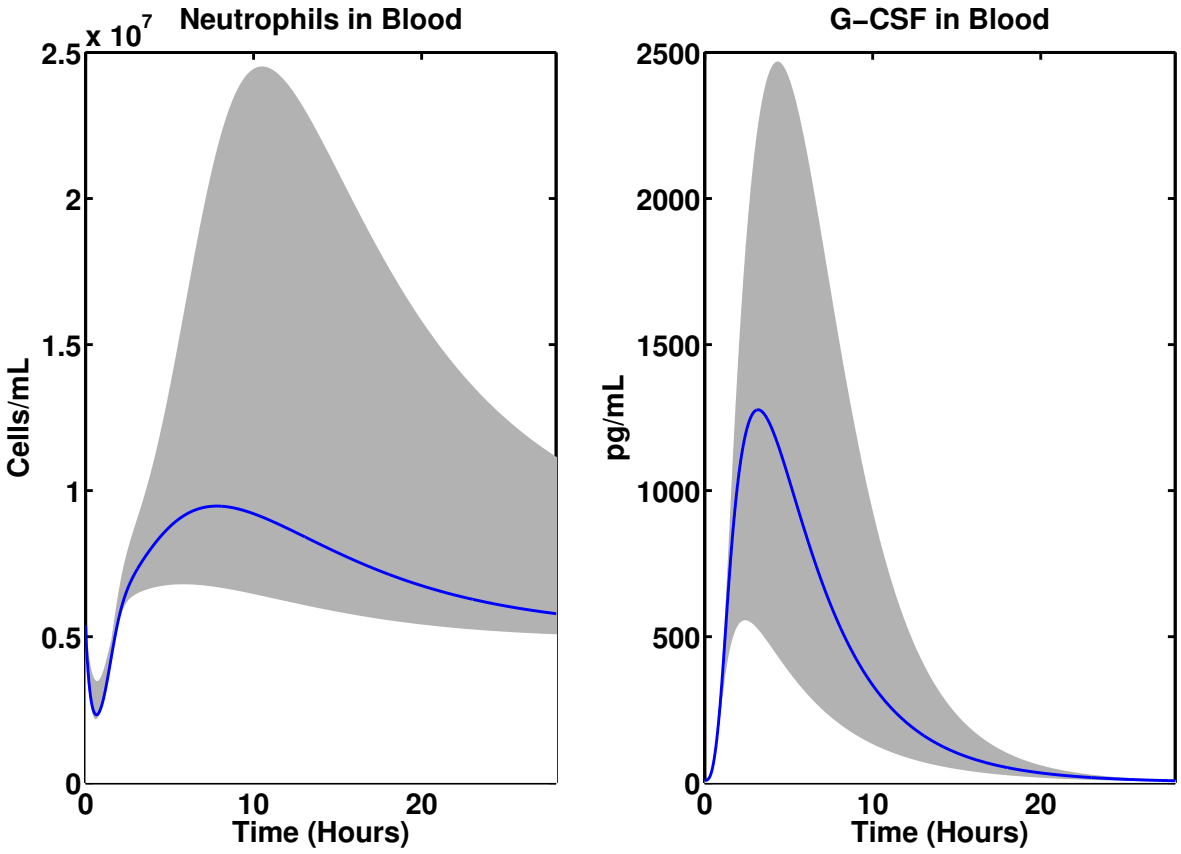

Figure 24: Neutrophil and G-CSF dynamics in response to 4 ng/kg LPS challenge. Nominal parameter value: solid line; ±50% variation in sensitive parameters: shaded area

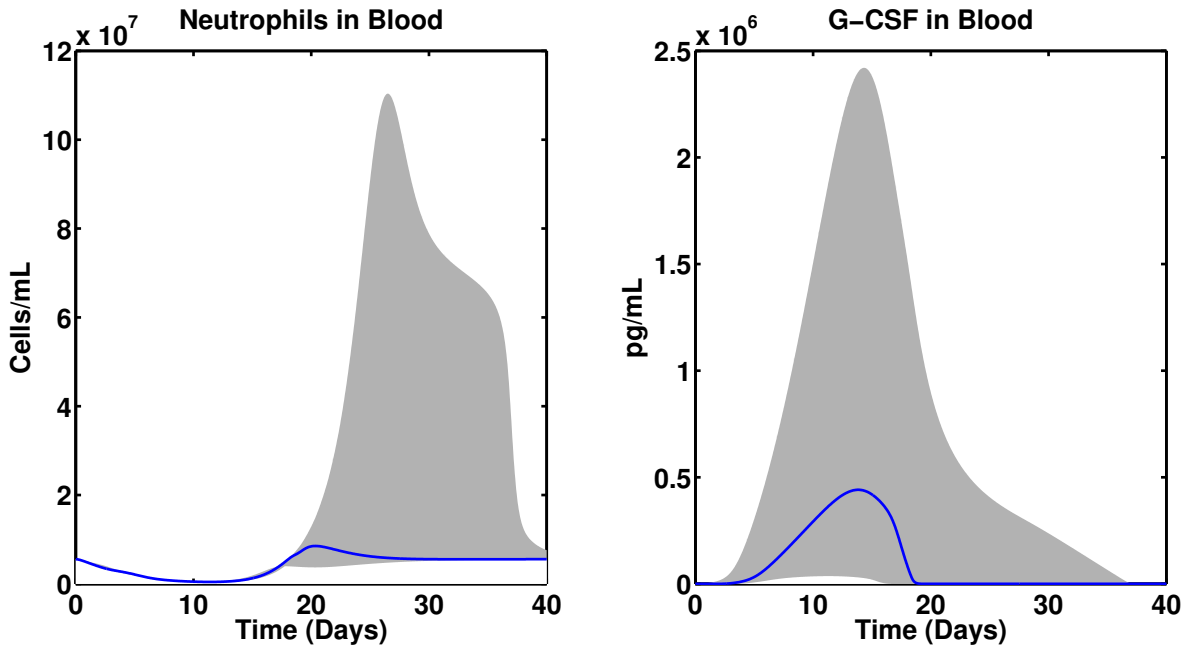

Figure 25: Neutrophil and G-CSF dynamics in response to 100 mg/m^2 docetaxel chemotherapy. Nominal parameter value: solid line; ±50% variation of sensitive parameters: shaded area

and G-CSF dynamics. The "sixth parameter is actually a challenge-dependent parameter pair, with clearance from the inflammation driven state (k_{29}) in the LPS challenge (Equation (2.22)) or the toxicity parameter (k_{37}) of docetaxel chemotherapy impacting neutrophil and G-CSF response for their respective challenges.

To verify that only non-sensitive parameters were removed, the 20 non-sensitive parameters were varied by $\pm 50\%$ from their nominal values. Changes were "directional, in that parameters were adjusted individually to maximize the increase or decrease in neutrophil counts and G-CSF concentrations observed. The simulation results of the varied parameters and the nominal values for 4ng/kg LPS challenges and 100 mg/m^2 of docetaxel chemotherapy are shown in Figure 22 and Figure 23, respectively.

The resulting comparison shows that the maximum difference in circulating neutrophil concentration between the nominal parameter set and the varied parameter set for LPS challenge is 30% and for docetaxel chemotherapy is 90%. The maximum difference in plasma G-CSF concentration between the nominal value parameter set and the varied parameter set is 15% for the LPS challenge and 180% for the docetaxel chemotherapy. Although 20 parameters from the model are varied 50% from their nominal values causing differences between the simulation results for the two parameter sets, these differences are much smaller than when sensitive parameters are varied. For example, a simultaneous 50% change in three sensitive parameters (k_{29} (LPS) or k_{37}(docetaxel), k_{11}, and k_{14}) yields a maximum change of 300% and 800% in neutrophil concentration for LPS challenge and docetaxel chemotherapy, respectively (Figures 24 and 25).

For G-CSF concentration, the results show a 120% and 500% maximum difference for LPS challenge and docetaxel chemotherapy, respectively. Hence, a small number of sensitive parameters can be effectively varied to capture individual patient dynamics using the reduced neutrophil model, rather than requiring the simultaneous estimation of 26 parameters a significant benefit in terms of computational cost and uniqueness of parameter estimation.

3.5.4 Model Parameter Estimation

As a result of the state and parameter reduction, re-calibration of the reduced neutrophil model parameters is required. In order to avoid estimating an entirely new parameter set, the following parameters from the original model are retained: k_1-k_8 and k_{16}-k_{26} (result from sensitivity analysis, Figure 19. Parameters k_9-k_{15}, associated with one point of reduction in the model, are calibrated with two different dynamic studies: inflammatory response to LPS challenge and myelosuppression resulting from docetaxel chemotherapy, using the method described in Section 2.3.

LPS Challenge: the LPS challenge uses endotoxin infusion to trigger the bodys inflammatory response and generates a similar response to that seen in sepsis. The study by Suffrendini *et al*, consisted of a 4ng/kg injection of *E. coli* endotoxin in six human volunteers [7]. The experiment measured the response of neutrophils and different cytokines at various time points. The reduced neutrophil model is used in combination with the LPS challenge (Section (2.2.1)) to capture the neutrophil response in the human body. The experimental and simulation results of the original model and reduced model are shown in Figure (26).

Right after the endotoxin injection, the plasma neutrophil concentration drops rapidly for the first 2 hours before beginning to increase and overshoot its nominal value at 7-10 hours. Plasma neutrophils finally return to homeostatic levels around 24 hours. The reduced neutrophil model is able to capture the early response (0-5 hours after challenge) better than the original model due to the removal of some of the states representing G-CSF production. The fast G-CSF response in the reduced model helps accelerate the recruitment of neutrophil precursors. After 5 hours, the performance of the two models vis-a-vis the data are comparable. However, the G-CSF response of the reduced model is faster than the data and the original model simulation in the first 2 hours after the challenge. The fast G-CSF response of the reduced model compared to the data and the original model is due to the removal of the intermediate states, which provide lag dynamics in the G-CSF response. However, the 2 hour dynamical difference does not impact or change the circulating neutrophil dynamics as seen in Figure 26. As the result of the 2 hour dynamical difference, the reduced neutrophil model is able to capture the maximum G-CSF concentration better,

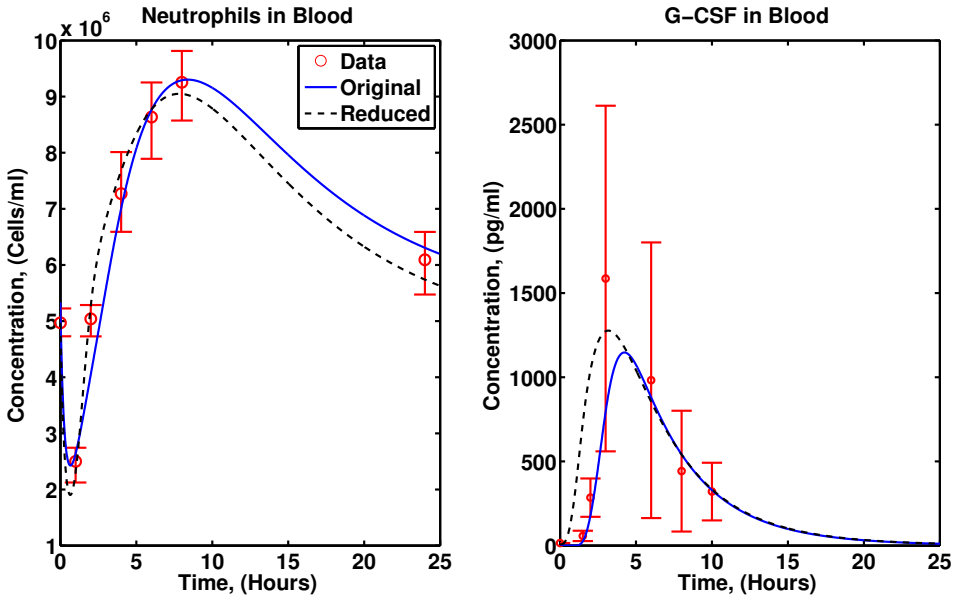

Figure 26: Published data (mean ± std. dev., [7]) and model fit of neutrophil and G-CSF concentrations in response to the LPS challenge. Original model (solid line)[8], reduced neutrophil model (dashed line)

Figure 26. The sum of squared error of the original model and the sum of squared error of the reduced neutrophil model with respect to G-CSF concentration data are 6.20×10^5 pg^2/ml^2 and 4.44×10^5 pg^2/ml^2, respectively Nevertheless, with the removal of 43% of states and 54% of parameters, the reduced model is able to capture the key dynamics of neutrophils and G-CSF in response to the LPS challenge in a similar manner to the original model with less complexity.

Docetaxel Chemotherapy: Experimental data from a 1 hour infusion of 100 mg/m^2 docetaxel [1] are used to evaluate the myelosuppressive effects of docetaxel on the model during chemotherapy. The reduced model, coupled with the reduced PBPK model (Equations (3.15)- (3.16)) is used to capture the neutrophil data. The experimental and simulation results of the original and reduced models are shown in Figure 27.

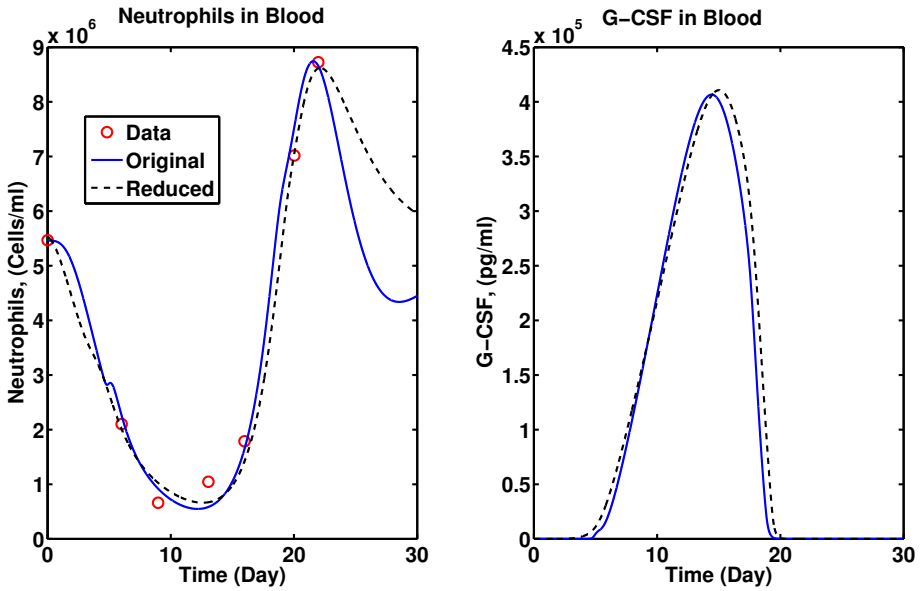

Figure 27: Data [1] (circles) and model fit of absolute neutrophil count after 1 hr docetaxel infusion at 100 mg/m^2. Original model (solid line), reduced model (dash line).

The reduced model follows the experimental data for the first 7 days. The original model contains many nonlinearities in its equations that cause the dip in circulating neutrophil dynamics observed around day 6. However, this phenomenon is not observed in the reduced neutrophil model because the nonlinear dynamics generating the dip were removed during model reduction. The model over-predicts the nadir neutrophil concentration (underpredicting the nadir magnitude) at day 9 and slowly reaches nadir concentration at day 14, similar to the original model. The models both capture the experimental data from day 14 to the end of the experiment. The difference in simulation results between the original model and the reduced model is pronounced after day 21. While the original model neutrophil count decreases rapidly and causes undershoot of the steady state neutrophil count, the reduced model neutrophil count slowly decreases toward its steady state value. Additional patient data beyond day 21, ideally in the absence of another docetaxel dose, would be required to (in)validate one of the model predictions/structures. Nevertheless, both models display similar dynamics from the beginning of chemotherapy to day 21, where the last data point is

available. G-CSF results from both models showed very similar dynamics and magnitude of G-CSF concentration, though no experimental data was available for comparison. To within the resolution of the data, the reduced model is able to capture experimental neutrophil dynamics after 1 hour infusion of 100 mg/m^2 of docetaxel. The final parameter set (Table 4) provides the reduced model the ability to capture the fast (LPS) and slow (docetaxel) response dynamics. Through the rigorous reduction of model states and parameters (43% and 54% respectively), the reduced model retains the key dynamics of the original model and maintains consistency with the experimental data. Given its simpler structure and a fewer number of parameters with key parameters identified, the model is used to implement into the model-based algorithm for chemotherapy scheduling optimization.

Table 4: Parameter values for the reduced model

Parameter	**Value**	**Unit**	**Parameter**	**Value**	**Unit**
k_1	3.14×10^{-4}	$\frac{1}{min}$	k_2	3.377×10^{-3}	$\frac{1}{min}$
k_3	1850	$\frac{pg}{ml}$	k_4	8.4170	–
k_5	1.0×10^5	$\frac{pg}{ml}$	k_6	8.35×10^{-4}	$\frac{1}{min}$
k_7	2.33×10^4	$\frac{pg}{ml}$	k_8	9.7×10^{-4}	$\frac{1}{min}$
k_9	3.56×10^6	$\frac{pg}{ml.min}$	k_{10}	1.18×10^6	$\frac{cells}{ml}$
k_{11}	179.3	$\frac{1}{min}$	k_{12}	437.0	$\frac{pg}{ml.min}$
k_{13}	2689	$\frac{pg}{ml}$	k_{14}	395	$\frac{pg}{ml.min}$
k_{15}	3.22×10^4	$\frac{pg}{ml}$	k_{16}	0.0066	$\frac{1}{min}$
k_{17}	1.0×10^7	$\frac{cells}{ml}$	k_{18}	0.004	$\frac{1}{min}$
k_{19}	9×10^{-11}	$\frac{1}{min}$	k_{20}	7.24×10^{-4}	$\frac{1}{min}$
k_{21}	5.9×10^{-3}	$\frac{1}{min}$	k_{22}	31.1862	–
k_{23}	1.52×10^3	$\frac{pg}{ml}$	k_{24}	0.00155	$\frac{1}{ml}$
k_{25}	0.2481	–	k_{26}	30900	$\frac{pg}{ml}$
S	1.5×10^9	$cells$	–	–	–

3.5.5 Parameter Adjustment Suggestions to Capture Patient Specific Neutrophil and G-CSF Dynamics

Capturing patient neutrophil and G-CSF dynamics during treatment in the case of chemotherapy or during an inflammatory response such as sepsis would help clinicians make more informed treatment decisions resulting in better patient outcome. Our reduced neutrophil model has the ability to capture the patient neutrophil and G-CSF dynamics by varying 6 parameters (k_{29} or k_{37}, k_9, k_{10}, k_{11}, k_{14}, and k_{15}). However, it is unnecessary to vary all 6 parameters since most of them are highly correlated with each other. Guidelines are provided to adjust parameters so that the model can capture the neutrophil response of an individual patient based on our experience with the model and its dynamic response:

1. Use the toxicity parameter, in the case of chemotherapy (k_{37}), or the inflammatory parameter (k_{29}), in the case of inflammation, as the primary parameter to capture the response. These parameters control how fast the neutrophil model will respond to challenges (*e.g.*, provide the downward slope and nadir neutrophil count). If the model is able to capture the patient dynamics then stop. If not, proceed to Step 2.

2. Vary parameters described in Step 1 simultaneously with parameters k_{11} and k_{14} to adjust the model dynamics to capture the change in patient neutrophil and G-CSF dynamics. These two parameters control the rate of neutrophil rebound and the peak of neutrophil count after challenges, providing additional dynamic response distal to the particular challenge.

3. If the fits are still not sufficiently accurate, parameter k_9 should be simultaneously estimated along with the parameters from the previous step that are appropriate to the challenge. In this case, k_9 will help to increase the rate of progenitor production through IL-23 and keeps this rate at elevated level to enhance the neutrophil rebound rate and the peak neutrophil count when varying k_{37} or k_{29} with k_{11} and k_{12} does not capture the dynamics of interest.

3.6 DISCUSSION

Mathematical modeling of biological systems provides great insight information about diseases, treatments, and patient dynamics [5, 8, 50]; however, due to their complexity, these models have not been widely used in model-based controls or model-based decision support systems. In this chapter, we provided a systematic approach to reduce a complex model to a simpler structure for both linear and nonlinear models using examples of a physiological based pharmacokinetic (PBPK) model of docetaxel and a biologically-based neutrophil-G-CSF model.

The PBPK model of docetaxel is a linear model capturing the docetaxel concentrations and dynamics in different organs after an IV drug dose. For a specific drug, concentrations and dynamics in certain organs are of concern due to toxicity or where tumors reside. Retaining the dynamics of interests without including all of the model equations would help to implement the model in model-based control or model-based decision support systems. For the case of docetaxel, the drug concentrations in plasma and inside the tumor are the key dynamics of the drug. While plasma concentration drives the toxicity profile of the drug (no bone marrow concentration measurement), the tumor concentration dictates the drug efficacy. Therefore, model reduction was applied to the PBPK model to decrease the number of equations and the computational complexity of the model while retaining the dynamics of plasma and tumor concentrations. The balanced truncation technique was applied to the 35 state PBPK model, yielding a 5 state linear model that conserves the dynamics of docetaxel in plasma and tumor. When plasma concentration is the only output of interest, the PBPK model can be reduced to a three states model. When tumor concentration is the only state of interest, The PBPK model can be reduced to four states.

While linear model reduction has been widely applied in engineering, there is not an existing generalized method for model reduction in nonlinear systems. Thus, reducing nonlinear models is not straightforward and requires the understanding of dynamic systems in general, as well as characteristics of the particular system under study. Sensitivity analysis was used to examine the parameters in the model and how they impact the model outputs. In our neutrophil-GCSF model, we are interested in circulating neutrophil concentration and

G-CSF concentration as outputs. The sensitive parameters were identified, and the states associated with those parameters are preserved during the model reduction. Using the clustering and reduction method developed by Chu *et al.*[20] suggests the possible number of states for the reduced neutrophil model is 5. Although model reduction through parameter sensitivity analysis and parameter clustering may suggest using fewer states, it may be difficult to achieve a full reduction to this number of states due to the potential loss of dynamics if too few of the states are preserved. Thus, for the neutrophil-GCSF model, we took a piecewise approach to nonlinear model reduction and were able to reduce the number of model states by 43%, and the number of parameters by 54%. The final reduced model contains 8 equations and 26 parameters without sacrificing its ability to capture neutrophil and G-CSF dynamics after an inflammatory challenge or docetaxel chemotherapy treatment.

Sensitivity analysis identifies the 6 key sensitive parameters in the reduced neutrophil model to be estimated to capture experimental data, Section 3.5.3. A key challenge in employing biologically-based models is the ability to quantitate the parameters of the model, some of which may be poorly informed by the data. Furthermore, when refining the model to match a specific data set, biologically-motivated models often have multiple parameters that can achieve an improvement in fit, leading to the possibility of overfitting. Parameter space reduction can identify the key parameters that establish the dynamics of the system. In our example (Section 3.3), the reduced neutrophil model was subjected to parameter space reduction where key parameters dictating the main dynamics of the neutrophil response in both chemotherapy and inflammatory challenge are retained. From 26 parameters, 6 key parameters in the reduced model were identified via sensitivity analysis. The results show that varying the 6 sensitive parameters changed the simulation outputs three-fold more than varying the 20 non-sensitive parameters for both challenges. These results provide guidance in which parameters to adjust in order to capture individual patient responses, in that the model dynamics can be adjusted by varying only the sensitive parameters.

3.7 SUMMARY

Although we are not able to reduce the number of key parameters to 1 or 2, the 6 most sensitive parameters are identified to capture data instead of varying 26 parameters total. Moreover, from our experience with the model, we provide guidelines for efficiently tuning the model to fit individual patient data. With systematic model reduction methods and key parameters identified, the model is more readily applicable to the clinical setting for monitoring patient toxicity response to chemotherapy, for example. Furthermore, the simplified structure of these mathematical models can be effectively used to aid clinicians with treatment decisions to improve patient outcome through implementation in a model-based decision support system, as we shall see in Chapter 4.

4.0 AN ALGORITHM FOR CLINICALLY-RELEVANT SOLID TUMOR CHEMOTHERAPY SCHEDULING

4.1 INTRODUCTION

Chemotherapy scheduling optimization problems have been posed and solved, primarily by engineers and mathematicians, with the goal of aiding clinicians in designing dose magnitudes and administration schedules that provide better patient outcomes in terms of tumor kill under toxicity constraints. The translation of these model-based algorithms to the clinic has generally not occurred to date due to some inconsistencies between the algorithm solutions and clinical chemotherapy treatment practice:

1. Treatment schedules: Algorithm solutions often administer drug continuously for a long period of time (more than 8 hours), while clinicians administer drug at higher rates over a shorter infusion period (30 minutes to a few hours) followed by a longer intervals for recovery.

2. Drug mechanism: Algorithms often calculate solutions based on administration of a general (nonspecific) "drug, which has the ability to kill tumor cells based on plasma concentration. In practice, chemotherapeutic agents are specific and their effect on different tumor cell types varies widely. Furthermore, the tumor concentration of drug is often lower the plasma concentration [5], due to diffusion or transport limitations for the particular drug, and the dynamics of drugs in tumor and plasma may occur over different timescales as a result [5]. Therefore, successful translation to clinical practice requires the use of models that are quantitatively accurate for the drug and tumor type employed, and how different drugs targeted different cell types when drug combination is

used; general solutions using nonspecific drugs and tumors can only provide a qualitative understanding of the interactions between the drug and tumor model types with the solution algorithm.

3. Toxicity measurements and constraints: Algorithm developers often pose adverse effects of chemotherapy either as implicit constraints on drug dose, administration rate, or interval (maximum drug concentration, maximum drug exposure) or as non-specific limitations (number of normal cells or healthy cells must be greater than a value). Toxicity measurements in clinical settings are explicit and drug specific (ANC, creatinine level, maximum tolerated dose, etc.). As was previously observed above, the use of a simple generalized equation and/or constraint to capture toxicity limits for the patient during chemotherapy is a clear departure from clinical practice where toxicities are measurable outcomes that limit treatment.

A few research teams have addressed this gap between engineering/mathematical theory and clinical practice by incorporating explicit detail of tumor type and treatment into their algorithms [76, 80]. A preclinical study by Harrold and Parker incorporated explicit drug and tumor information with clinically-relevant logistical constraints and a preclinical toxicity measure (body weight) to provide dosing recommendations for 9-nitrocamptothecin to SCID mice bearing human HT29 colon carcinoma xenografts [76]. While the algorithm returned a dosing regimen that was effective and in line with clinical practice, the toxicity model was insufficient to capture the side-effects of the algorithm-derived therapy, and the drug was killed in Phase 2 clinical trials.

Pefani *et al.* [80] developed an algorithm for treating acute myeloid leukemia (AML) using a combination chemotherapy of daunorubicin (DNR) and cytarabine (Ara-C), a standard drug combination used to treat AML [135]. While quite clinically-relevant, the AML study also uses implicit toxicity constraints that do not fully capture the measurable toxicity response to treatment. As patient toxicity is the main limit on aggressive therapy, the discrepancies between the models and practical settings are the primary hurdle to overcome in implementing a model-based decision support system to aid clinicians in chemotherapy schedule design.

A balance between drug efficacy and drug toxicity drives chemotherapy decision-making in the clinical setting. The goal of this chapter is to develop a clinically ready and generalizable treatment scheduling algorithm to design patient-specific chemotherapy schedules using both docetaxel as a mono-agent and in combination with cisplatin or carboplatin.

4.2 DOCETAXEL

Docetaxel, sold under the brand name Taxotere^{TM} produced by Sanofi had sales of $556 million in 2013 [136]. Docetaxel is produced by esterifying 10-deacetyl baccatin III, which is extracted from the leaves of the European yew tree [101]. Docetaxel is an anti-mitotic chemotherapeutic drug that interferes with cell division by binding to tubulin in the M-phase of cell growth [101]. Breast, ovarian, and prostate cancers are treated with docetaxel as a mono-agent [101, 105], and it is combined with platinum-based chemotherapy (*e.g.*, cisplatin) or cisplatin and 5-fluorouracil (5-FU) to treat non-small-cell lung cancer [137] and head-and-neck cancer [39], respectively.

Table 5: Myelosuppression toxicity grade corresponding to absolute neutrophil count (ANC) [2].

Neutropenia Grade	**ANC, $\times 10^6$ Cells/ml**
0 (No Toxicity)	ANC $\geq$ 2.0
1	1.5$\leq$ ANC $<$ 2.0
2	1.0 $\leq$ ANC $<$ 1.5
3	0.5 $\leq$ ANC $<$ 1.0
4	ANC $<$ 0.5

One of the main side effects of docetaxel is myelosuppression. Docetaxels interference in cell division does not just disrupt cancer cells; it also impacts the neutrophil progenitors in the bone marrow. Neutrophils are the main component of the white blood cell population and are part of the innate immune response. Low absolute neutrophil count (ANC) can

cause immune system breakdown and make the patient unable to fight off even low-level pathogenic infections. Toxicity, as measured by ANC, is categorized into different neutropenia levels as shown in Table 5. During docetaxel chemotherapy treatment, clinicians often try to eliminate tumor at without causing severe toxicity in patients. Despite these efforts, some patients exhibit grade 4 neutropenia because different patients have different efficacy and toxicity responses to treatment. In other words, patients that are highly sensitive to docetaxel chemotherapy could experience grade 4 neutropenia. When the ANC measurement shows grade 4 neutropenia, the chemotherapy is stopped and/or G-CSF is administered to bring patient ANC to 2.0 $\times 10^6$ cells/ml before the next docetaxel dose can be administered. Given the explicit primary toxicity of ANC for docetaxel, and the neutrophil model developed in Chapter 2, the remainder of this chapter addresses the synthesis of a chemotherapy scheduling optimization problem for minimizing tumor size via docetaxel administration under clinically-relevant constraints.

4.3 OPTIMIZATION PROBLEM FORMULATION

4.3.1 Objective Function

A common objective function in optimization-based problem formulations for chemotherapy scheduling is minimizing the number of tumor cells at the end of the treatment [77, 80]. However, in actual clinical practice, the final treatment time in chemotherapy is not set *a priori*. Efficacy of chemotherapy is evaluated along the course of the treatment, and adjustments are made to maximize efficacy while mitigating toxicity until the patient is, ideally, clinically cleared of cancer.

Harrold and Parker [76] were the first to pose a cancer treatment objective in a receding horizon control form that minimized tumor volume along the treatment trajectory rather than minimizing the tumor volume at the end point alone. Using this approach, we posed the objective function of the chemotherapy optimization problem as shown in Equation 4.1:

$$\min_{D_d(q)} \sum_{w=1}^{N_w} \Gamma(w)(N_d(w)) + \Gamma_u \sum_{q=1}^{m_q} D_d(q)^2 \tag{4.1}$$

The objective is to minimize the tumor volume, $N_d(w, D_d(q))$, every week, w, for N_w weeks; in the calculations below a horizon of $N_w = 24$ weeks was used. The weighting term $\Gamma(w)$ to design the drug administered early in the cycle; hence, eliminate the end point effect observed in Martin *et al.* solution [77, 78] . For this work, Γw =1 for all w in N_w. The input $D_d(q)$ is the amount of drug delivered at time q to achieve the minimal objective function value. Weeks, w, are the times that tumor size is evaluated (days 0, 7, 14, ...), while q is the time that drug is delivered (days 0, 1, 2, ...). The second term, weighted by Γ_u, is a penalty term that minimizes the utilization of small doses, which have little or no impact on tumor elimination [76]. Equation 4.1 is the main objective function for both docetaxel as a single agent treatment and when it is used in combination with other chemotherapeutics. The objective is posed and solved in a receding horizon control formulation, where the model in the algorithm has the ability to update its parameters to better match patient dynamics when data (*e.g.*, efficacy, ANC, etc.) becomes available.

4.3.2 Dynamic Constraints

Patient dynamics constrain the optimization algorithm used to design patient-specific chemotherapy schedules. To capture patient dynamics during chemotherapy, models of drug pharmacokinetics, drug pharmacodynamic efficacy (PD efficacy), and drug pharmacodynamic toxicity (PD toxicity) are developed. A schematic of the interactions between these key patient dynamics is shown in Figure 28. In our patient model, the pharmacokinetic (PK) model describes the drug concentration in a patient ofer time after drug administration. The PK model is utilized as the driving mechanism for the PD efficacy and PD toxicity models as seen in Figure 28. The PD efficacy model describes the cancer tumor growth process and the chemotherapeutic-driven tumor elimination and/or inhibited growth. The PD toxicity describes how chemotherapeutic agents induce toxic responses in the patient. In the patient model structure, the assumptions made are: i) the cancer tumor and the patient toxicity do not alter the drug clearance (*i.e.*, pharmacodynamics do not impact pharmacokinetics); ii) there is no interaction between cancer tumor growth and toxicity; iii) when two or more chemotherapeutic agents are used, the pharmacokinetic models of drugs do not interact

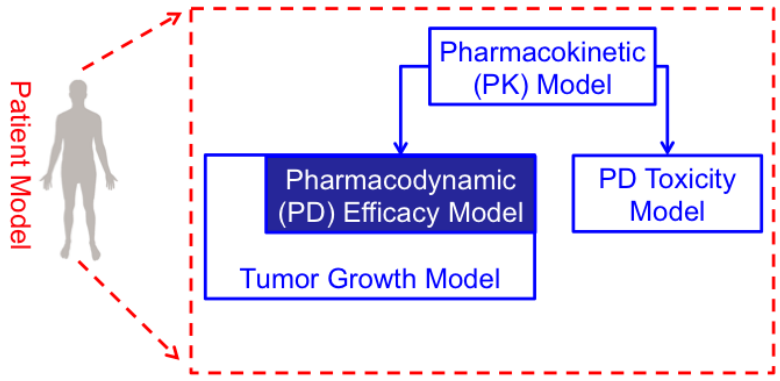

Figure 28: Schematic of models presenting patient dynamics in chemotherapy

(*i.e.*, the drugs used in combination do not have overlapping clearance mechanisms, meaning that the PK of a drug does not alter the concentration-vs-time profiles of any other drug(s) administered)

PK and PD models are often constructed using continuous-time ordinary differential equations, but the optimization in Equation (4.1) is computed in discrete time steps. The continuous-time differential equations in the models are therefore discretized using orthogonal collocation on finite elements [138] into:

$$x_i(k+1) \quad = \quad F(x(k), D(k)) \tag{4.2}$$

$$\begin{aligned} \textit{Objective} \quad &: \quad (4.1) \\ \textit{s.t.} \quad &: \quad \text{PK, PD efficacy, and PD toxicity models} \\ &\quad\quad\; \text{clinically-motivated logistical constraints} \end{aligned} \tag{4.3}$$

where $x_i(k+1)$, $i \in N$, is the state x_i at time $k+1$, and it is updated as a function of states x and drug D at time k. These dynamic constraints are utilized in the optimization problem to represent the patient dynamics during chemotherapy. The resulting generalized

cancer chemotherapy scheduling problem can be formulated as Problem 4.3. Mathematically posing and solving this problem requires explicit definition of the models, and their related constraints. This is the topic of the remainder of this chapter.

4.4 TUMOR GROWTH MODELS

4.4.1 Self-Seeding Tumor Growth Model

Small tumors (*e.g.* those with a volume less than 1 mm^3) grow exponentially. As tumor size increases, the growth rate decreases due to a lack of space, increase in pressure (due to tumor expanding into existing tissue space), and nutrient deprivation because of irregular vasculature development inside the tumor. Norton *et al.* introduced a Gompertzian model (Equation (4.4)), which was able to capture the progression of tumor size in breast cancer patients and has since been widely used to describe tumor growth [139]. In Equation (4.4), τg =$1.0\times10^{-3}h^{-1}$ is the doubling time during experimental growth, ρg =10^{12} cells is the plateau cancerous cell population, N_o =1.0×10^{10} cells is initial cancerous cell population , and $N_g(t)$ is tumor cell population at time t [139]. The Gompertzian model captures exponential growth of tumor at short times and growth rate slows to zero as tumor volume reach a maximum carrying capacity above the tumor volume generally accepted to result in the death of a patient (1L, or 10^12 cells) [139]. An alternative model, also proposed by Norton *et al.*, hypothesized the concept of cancer self-seeding and used this concept to explain the dynamics of tumor growth and metastasis. In this hypothesis, the tumor size is described as a fractal geometry where the tumor mass increases due to an imbalance in two power-law processes. This new tumor growth model is as follows [140]:

$$\frac{dN_g(t)}{dt} = frac1\tau gln\left[\frac{(ln(\rho g/N_o)}{\rho_g/2N_o}\right]N_g ln\left[\frac{r}{h}o_g/N_g(t)\right] \tag{4.4}$$

$$\frac{dN(t)}{dt} = k_{growth}N(t)^{a/c} - k_{death}N(t)^{b/c} \tag{4.5}$$

$N(t)$ is the number of cancer cells, k_{growth} and k_{death} are tumor growth and death rates, respectively, and a, b, and c are constants satisfying $3 \geq b \geq c > a \geq 2$ (proliferation

occurs in a mass region having lower fractal dimension than the region where apoptosis occurs) [140]. The values for a/c and b/c deployed in our model are 0.9026 and 1.1079 respectively. The values for k_{growth} and k_{death} are 4.30×10^{-5} cells$^{0.974}$/min and 1.4583×10^{-7} cells$^{-0.1079}$/min. This power law tumor growth equation displays the same dynamics of tumor growth represented by the Gompertzian model. Since there is no logarithmic function in the power law model, it is easier to implement numerically, and the power law model is used to capture the tumor dynamics in our single agent chemotherapy scheduling optimization.

4.4.2 Saturating Rate Cell-Cycle Model

Biologically motivated cell-cycle models provide greater insight into cell growth by capturing the individual phases of growth [85]. The standard cell cycle has five total phases, as shown in Figure 29; however, experimental techniques without extensive and destructive evaluation (cells broken down to evaluate for RNAs [5]) prevent unique quantification of quiescence (G_0) and growth (G_1) phases, in addition to the mitotic preparation (G_2) and mitosis (M) phases. These models are often exponential in structure, however, and the linear equations fail to capture the saturating tumor growth dynamics observed clinically. Recognizing the difficulties in uniquely quantifying each cell phase population, but wanting to keep the saturating growth rate behavior observed clinically, Florian *et al.* developed a three state saturating-rate cell cycle model to capture the growth of cancer cells in different phases of the cell cycle (Equations (4.6)- (4.9), Table 6) [5].

$$\frac{dX_G(t)}{dt} = -k_{GS}X_G(t)ln\left(\frac{\theta}{N(t)}\right) + 2k_{MG}X_M(t)\left(\frac{\theta}{N(t)}\right) \tag{4.6}$$

$$\frac{dX_S(t)}{dt} = -k_{SM}X_S(t) + k_{GS}X_G(t)\left(\frac{\theta}{N(t)}\right) \tag{4.7}$$

$$\frac{dX_M(t)}{dt} = -k_{MG}X_M(t)\left(\frac{\theta}{N(t)}\right) + k_{SM}X_S(t) \tag{4.8}$$

$$N(t) = X_G(t) + X_S(t) + X_M(t) \tag{4.9}$$

Thus, in the model, $G(t)$ represents the quiescence and growth phases, $S(t)$ represents the DNA synthesis phase, and $M(t)$ represents the mitotic preparation and mitosis phases. As in the Gompertzian tumor growth model, the cell-cycle model contains a saturation effect that provides slower tumor growth as the size of the tumor increases.

Table 6: Modified cell-cycle model parameters.

Parameters	Value	Units	Parameters	Value	Units
k_{GS}	$1.30\times10^{-}3$	1/hr	k_{MG}	$1.69\times\ 10^{-}2$	1/hr
k_{SM}	3.90×10^{-2}	1/hr	θ	1.00×10^{12}	cells

4.4.3 Modified Cell-Cycle Model with Self Seeding Hypothesis

Using the same power law hypothesis as in the tumor growth model of Equation (4.5), the saturating-rate cell-cycle model is modified to a similar structure as the power law model. The modified cell-cycle model is shown in Equations (4.10)-(4.13).

$$\frac{dX_G(t)}{dt} = -k_{GS}X_G(t)^{a/c} + 2k_{MG}X_M(t) \tag{4.10}$$

$$\frac{dX_S(t)}{dt} = -k_{SM}X_S(t) + k_{GS}X_G(t)^{a/c} \tag{4.11}$$

$$\frac{dX_M(t)}{dt} = -k_{MG}X_M(t) + k_{SM}X_S(t) - k_{death}N(t)^{b/c} \tag{4.12}$$

$$N(t) = X_G(t) + X_S(t) + X_M(t) \tag{4.13}$$

In the modified cell-cycle model, $X_i(t)$ ($i \in \{G, S, M\}$)) corresponds to the number of cells (or equivalently volume using 10^{12} cells = 1 L) in G (growth), S (DNA synthesis), or M (mitosis) phases, k_j ($j \in \{GS, SM, MG\}$) are the interphase transfer rate constants for each phase, and a/c and b/c are the fractal constants associated with growth rate and apoptosis rate. While it is rigorously correct to replace every transfer term between compartments in the saturating cell-cycle model [5] with the fractal growth and death terms, additional analysis of the model structure (i.e., sensitivity analysis) demonstrated that the fractal growth term transitioning cells from the G to S states controls the overall dynamics of cell-cycle growth. Therefore, we only incorporate the fractal growth term in the transition between G and S phase (Equations (4.10) and (4.11). Moreover, the apoptosis rate is only included in the M phase dynamics (Equation (4.12)) as a function of the total cancer cell population, rather than the M phase fraction. The parameters for the modified cell-cycle model are shown in Table 7

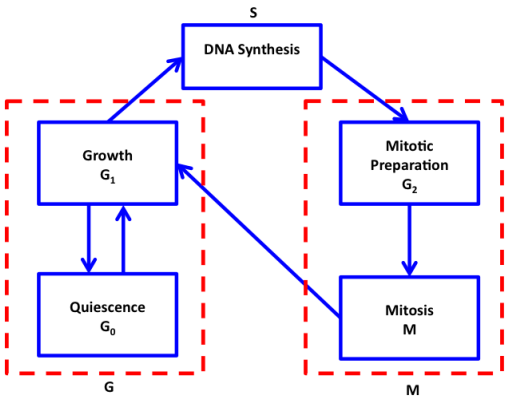

Figure 29: The five phases of cell cycle. Lumped G ($G_0 + G_1$) and M ($G_2 + M$) compartments capture the easily resolvable cell cycle phases, forming a lower-order cell cycle model.

4.5 DOCETAXEL AS SINGLE AGENT CHEMOTHERAPY

4.5.1 Docetaxel PD Efficacy Model

Docetaxel is an M-phase active antitumor agent, when tumor growth is represented as cell cycle specific. Alternatively, lumped tumor approximations (total number of cells) can be used to describe cancer cell growth and death in aggregate. Under single chemotherapy treatment, the tumor growth model in Equation (4.5) becomes:

$$\frac{dN(t)}{dt} = k_{growth}N(t)^{a/c} - k_{death}N(t)^{b/c} - k_{eff}D(t)N(t) \tag{4.14}$$

Here k_{eff} is the tumor cell elimination rate constant and $D(t)$ is the drug concentration inside the tumor described in Section 3.2. The bilinear kill term, $k_{eff}D(t)N(t)$, depends on drug concentration as well as the number of cancerous cells and captures the effect of a drug on cancer cell growth during single agent chemotherapy *in vitro* [76, 78]. It is assumed that this functionality scales to the *in vivo* scenario, though there exist alternate formulations, with solid biological justification, for *in vivo* cell kill by chemotherapeutics [141, 142]. In

Table 7: Modified cell-cycle model parameters.

Parameters	Value	Units	Parameters	Value	Units
k_{GS}	$4.4139\times10^{-}5$	cells$^{0.974}$/min	k_{MG}	$1.4\times\ 10^{-}3$	min^{-1}
k_{SM}	5.8681×10^{-4}	min^{-1}	k_{death}	7.583×10^{-8}	cells$^{-0.1079}$/min
a/c	0.9026	-	b/c	1.1079	-

the absence of a generally accepted mathematical structure for drug-induced cell death, the bilinear kill relationship is employed herein for both single agent chemotherapy and combination chemotherapy.

4.5.2 Docetaxel Neutropenic Toxicity Model

When docetaxel is used as a single agent, the drug concentration in the plasma (Section 3.2) affects the progenitor population (Equation (3.17)) through a dynamic lag, Equation (4.15). Here, state $C_{b_i}(t)(i$: docetaxel) represents the effect of the drug on bone marrow dynamics, as driven by transport from the plasma compartment, $C_{p_i}(t)$ at the rate k_{vbm_i} (Section 3.2). The effect state is degraded follow the inhibition Michaelis-Menten kinetics with the half maximum constant, k_{40} and the maximum degradation rate constant k_{bmv_i}. Progenitor cells are killed by drug in $C_{b_i}(t)$ following sigmoid-Emax kinetics with a maximum rate E_{max_i} and half maximum constant EC_{50_i}, the parameter values are shown in Table 8.

$$\frac{dC_{b_i}(t)}{dt} = k_{vbm_i}C_{p_i}(t) - k_{bmv_i}\left(1.0 - \frac{C_{b_i}(t)}{k_{40_i} + C_{b_i}(t)}\right)C_{b_i}(t) \tag{4.15}$$

$$\frac{dPr(t)}{dt} = \left(k_1 + \frac{k_2 GCSF(t)}{k_3 + GCSF(t)}\right)S - k_{tr}Pr(t) - \frac{E_{max_i}C_{b_i}(t)}{EC_{50_i} + C_{b_i}(t)}Pr(t) \tag{4.16}$$

Table 8: Docetaxel (D) neutropenia model parameters

Parameters	Value	Unit	Parameters	Value	Unit
k_{vbm_D}	0.3017	min^{-1}	k_{bmv_D}	0.0802	min^{-1}
k_{40_D}	0.0005	μM	E_{max_D}	0.0130	min^{-1}
EC_{50_D}	0.7873	μM	-	-	-

4.5.3 Docetaxel Chemotherapy Optimization Problem

4.5.3.1 Toxicity Constraints: The limiting factor in chemotherapy dosing is the clinically-observed toxicity of the administered drugs. When the toxicity profile is too severe, the chemotherapy schedule is interrupted or delayed until patient health improves (*i.e.*, toxicity measures return to within acceptable limits). To prevent patients from experiencing severe toxicity-induced side-effects, toxicity constraints are considered in the optimization problem.

When docetaxel is administered, ANC is used as the primary toxicity measurement. In a clinical setting, a blood sample is drawn and analyzed prior to the patient receiving their next treatment dose. If ANC is within acceptable limits, drug is administered. Otherwise, the chemotherapy schedule is delayed until the ANC of the patient reaches a safe level. Equation (4.17) stipulates that a patient not suffer a grade 3 toxicity:

$$N_c(k) \geq 1 \times 10^6 \; cells/ml \tag{4.17}$$

$$\sum_{q}^{7+q} N_c(q) \geq 10.5 \times 10^6 \; cells/ml \; \forall q \in 1, 2..., 21 \tag{4.18}$$

$$N_c(q) + N_c(q+8) \geq 3.0 \times 10^6 \; cells/ml \; \forall q \in 1, 2..., 21 \tag{4.19}$$

Here $N_c(k)$ is the ANC count at time step k through the discretization of the continuous-time model (Equation (4.2), Section 4.3.2). The discrepancy between discrete-time and

continuous-time model could cause the optimization solution violating the toxicity constraints when using the continuous-time model. To resolve this discrepancy between the two models, the time step k has to be predetermined to ensure the simulation results between the discrete-time model and the continuous-time model are the same. To avoid a treatment schedule that maintains a low ANC throughout the treatment, a further toxicity constraint is imposed such that the ANC measurements 7 days apart must always have 1 that is better than grade 2 (*i.e.*, the patient cannot spend a full week suffering from a grade 2 or more severe ANC toxicity) as shown in Equations (4.18)- (4.19).

In Equation (4.18), sum of ANC over seven days must be greater than or equal to the sum of 7 times the ANC upper limit for grade 2 toxicity (1.5×10^6 cells/ml). This constraint is applied over every 7-day window in the therapeutic optimization problem. Equation (4.19) ensure the ANC measurements 7 days apart must have 1 better than grade 2. Equations (4.17)- (4.19) are used in combination with the neutropenia model of Equations (3.18)-(3.26) and Equations (4.15)-(4.16) to constrain the optimization problem away from treatments that would induce acute severe, or longer-duration depressed, ANC.

4.5.3.2 Logistical Constraints: Logistical constraints are incorporated into the current formulation to ensure the clinical applicability of the algorithm and improve the patient treatment outcome. Drug infusion rate is held constant over the duration of a one-hour infusion. The number of doses delivered, or the number of patient visits, per week is fixed at one to limit patient hospital visits (implicitly improving patient quality of life). To alleviate the burden on clinicians and hospitals, treatments are only administered during business hours, Monday-Friday (8 AM-5 PM). The binary variable $b_d(k)$ is introduced to denote when the drug is delivered at time step k, with delivery indicated by $b_d(k) = 1$, and $b_d(k) = 0$ denoting no drug administration on a given day. The sum of b_d over seven days must be less than or equal to 1 as shown in Equation 4.20:

$$\sum_{k=1}^{168} b_d(24 * k + 1) \quad \leq \quad 1 \tag{4.20}$$

This constraint is repeated for every week in the treatment scheduling problem. The total amount of drug that can be administered is different for docetaxel, cisplatin, and carboplatin.

For docetaxel, the maximum recommended amount of drug that can be intravenously delivered per three week period is 105 mg/m^2 [103, 101]. The drug dose recommendation is used as the upper bound on the amount of drug that can be administered in every 3 weeks period by the algorithm:

$$\sum_{q=1}^{21} D_d(q) \quad \leq \quad 105\ mg/m^2 \tag{4.21}$$

Here $D_j(k)$ is the amount of drug j infused on day k. These logistical constraints are coupled with the dynamic and toxicity constraints in the chemotherapy scheduling problem for single agent docetaxel.

4.5.3.3 Scheduling Problem for Single-Agent Docetaxel: The problem formulation for scheduling single-agent docetaxel chemotherapy is as follows:

$$\begin{aligned} \textit{Objective} \quad &: \quad (4.1) \\ s.t. \quad &: \quad \text{PK:} \quad (3.15) - (3.16) \\ &\quad\ \ \text{PD Efficacy:} \quad (4.14) \\ &\quad\ \ \text{PD Toxicity:} \quad (3.18) - (3.26),\ (4.15) - (4.16) \\ &\quad\ \ \text{Toxicity Constraints:} \quad (4.17) - (4.19) \\ &\quad\ \ \text{Logistics:} \quad (4.20),\ \textit{and}\ (4.21) \end{aligned} \tag{4.22}$$

The objective in Problem 4.22 is the minimization of tumor volume along a treatment horizon of 24 weeks with penalties for small drug dose usage. Problem 4.22 contains 408,000 variables and 408,200 constraints respectively.

G-CSF is often used as a rescue agent when the patient experiences grade 4 neutropenia. Allowing G-CSF usage for ten consecutive days during a 21 day docetaxel chemotherapy cycle (consistent with clinical practice), we examined the impact of allowing G-CSF administration on optimal docetaxel administration schedules. The G-CSF usage constraint can be added to Problem 4.22 as follows:

$$\sum_{k=1}^{10} b_g(k) \quad = \quad 10 \tag{4.23}$$

In Equation (4.23), the binary variable, $b_g(k)$ is 1 when G-CSF is used, and 0 when no G-CSF is administered. The sum of the number of G-CSF doses is set to be equal to 10 for 10 consecutive days over each 21 days docetaxel cycle. When G-CSF is used, the optimization Problem 4.22 becomes:

$$\begin{aligned} \textit{Objective} \quad &: \quad (4.1) \\ s.t. \quad &: \quad \text{PK:} \quad (3.15) - (3.16) \\ &\quad \text{PD Efficacy:} \quad (4.14) \\ &\quad \text{PD Toxicity:} \quad (3.18) - (3.26),\ (4.15) - (4.16) \\ &\quad \text{Toxicity Constraints:} \quad (4.17) - (4.19) \\ &\quad \text{Logistics:} \quad (4.20),\ (4.21),\ \textit{and}\ (4.23) \end{aligned} \tag{4.24}$$

4.5.4 Solution Methodology

The chemotherapy scheduling Problems (4.22) and (4.24) are formulated as mixed integer nonlinear programming (MINLP) problems with a large number of variables and constraints (up 585,000 variables and 850,000 constraints). MINLPs cannot be guaranteed to return an optimal solution, and they are often difficult to solve for even local optima when the number of variables and constraints are large (convergence is not guaranteed) [21, 143, 144]. To overcome these challenges, we repose the problem into an enumeration step addressing the binary variable problem followed by a continuous nonlinear programming problem. A two-step optimization is used to solve these problems:

1. Enumeration: the possible combinations of the binary variables in the logistical constraints, coupled with an integer variable grid of possible dose magnitudes (5 mg/m^2 increment), are examined to determine the best time (days) to infuse the drug such that the objective function would be minimized given the grid of dose magnitudes (large dose

step size). The enumeration step is deployed in the C++ programming language with an explicit Euler method as our ordinary differential equation integrator (Equation (4.25)):

$$x(k+h) \quad = \quad x(k) + h * dx(f(x(k), D(k))) \tag{4.25}$$

Here the state $x(k+h)$ at time step $k+h$ is updated by summing the state at previous time step k and a product of step h and the state derivative at time k, $dx(k)$, the time step used in this integrator is 1 (h=1 min). The result of the enumeration step is a chemotherapy schedule with an estimate dose magnitude at each infusion that yields desirable objective function value

2. Dynamic optimization: The solution from the enumeration step is then used as the initialization for the dynamic optimization where the exact dose magnitudes (0.1 mg/m^2 precision) are determined for the optimal treatment schedule. The dynamic optimization is modeled and solved in Pyomo (https://software.sandia.gov/trac/coopr/wiki/Pyomo). Pyomo is a Python based modeling language that is part of the Coopr package developed by the Sandia National Lab [145]. The discretization method used for the dynamic optimization is orthogonal collocation on finite elements [138]:

$$x(k+1, m) \quad = \quad x(k, ncp) + h \sum_{i=1}^{ncp} (a(i, m) dx(k+1, i)) \tag{4.26}$$

$$a \quad = \quad \begin{pmatrix} 0.1968 & 0.3944 & 0.3764 \\ -0.0655 & 0.2921 & 0.5125 \\ 0.0238 & -0.0415 & 0.1111 \end{pmatrix} \tag{4.27}$$

Here the state x at finite element, k+1, and collocation point, m is calculated based on the value of x at element k and the last last collocation point, ncp, following Equation (4.26). The finite element step size is defined at h, a is a $ncp \times ncp$ parameters matrix, and $dx(f(x(k+1, i), D(k+1)))$ is the derivative of state x at finite element $k+1$. In our optimization problem, h=60 minutes step size, the number of collocation points ncp=3, and parameter values for a are shown in Equation (4.27). Ipopt (https://projects.coin-or.org/Ipopt) is used as the nonlinear program solver. The solution of the two-step optimization is a set of drug infusion schedules that minimizes tumor size without causing severe patient toxicity.

4.5.5 Results

4.5.5.1 Clinical Standard of Practice Schedules vs. the Algorithm Optimal Schedule The treatment schedule for nominal problem dynamics with single-agent docetaxel chemotherapy, as posed in Equation (4.22) contains 408,000 variables and 408,200 constraints respectively. The optimization algorithm takes 40 minutes to find an optimal treatment schedule. The result is compared to clinically-administered docetaxel schedules, as seen in Figure 30. Two clinically-standard docetaxel schedules are considered in the comparison: 100 mg/m^2 every 3 weeks (q3w) and 35 mg/m^2 every week for 3 weeks followed by 1 week off (qw 3 of 4). Under the q3w schedule, the nominal patient is predicted to experience grade 3 neutropenia during every cycle of treatment (Figure 30b). Dosing qw 3 of 4, the nominal patient only experiences grade 2 neutropenia. The optimal treatment for the nominal patient, as generated by solution of Problem (4.22), administered 3 doses on days 1, 11, and 15 of a 21-day period with doses of 57 mg/m^2, 25 mg/m^2, and 23 mg/m^2, respectively (Figure 30a). Under the optimal treatment schedule, this patient only experiences grade 2 neutropenia, which is the same toxicity grade as the qw 3 of 4 schedule.

The drug efficacy results for the three schedules are shown in Figure 30d. For the 100 mg/m^2 q3w schedule, the tumor size is reduced to the detection limit, which is 10^5 cells (horizontal dashed line), in 64 days, while for the 35 mg/m^2 qw 3 of 4 schedule, the tumor size reaches the detection limit after 96 days of treatment. The optimal solution is able to reduce the tumor size to the detection limit by day 85, the same time to complete clinical response (tumor size undetectable) as with the 100 mg/m^2 q3w schedule. A summary of treatment details for the nominal patient is shown in Table 9.

The 100 mg/m^2 q3w schedule decreased tumor size at the fastest rate with the least amount of drug administered among the three schedules, but it also causes increased neutropenia toxicity. Although the nominal patient is similar to the population description [1], we expect that individuals will have variable toxicity in response to treatment. Thus, an explicit way to mitigate toxicity during the treatment would be a significant advantage. The 35 mg/m^2 qw3 of 4 schedule decreases the severity of the toxicity, however, the treatment duration until the tumor shrinks below the detection limit is longer. The algorithm suggests

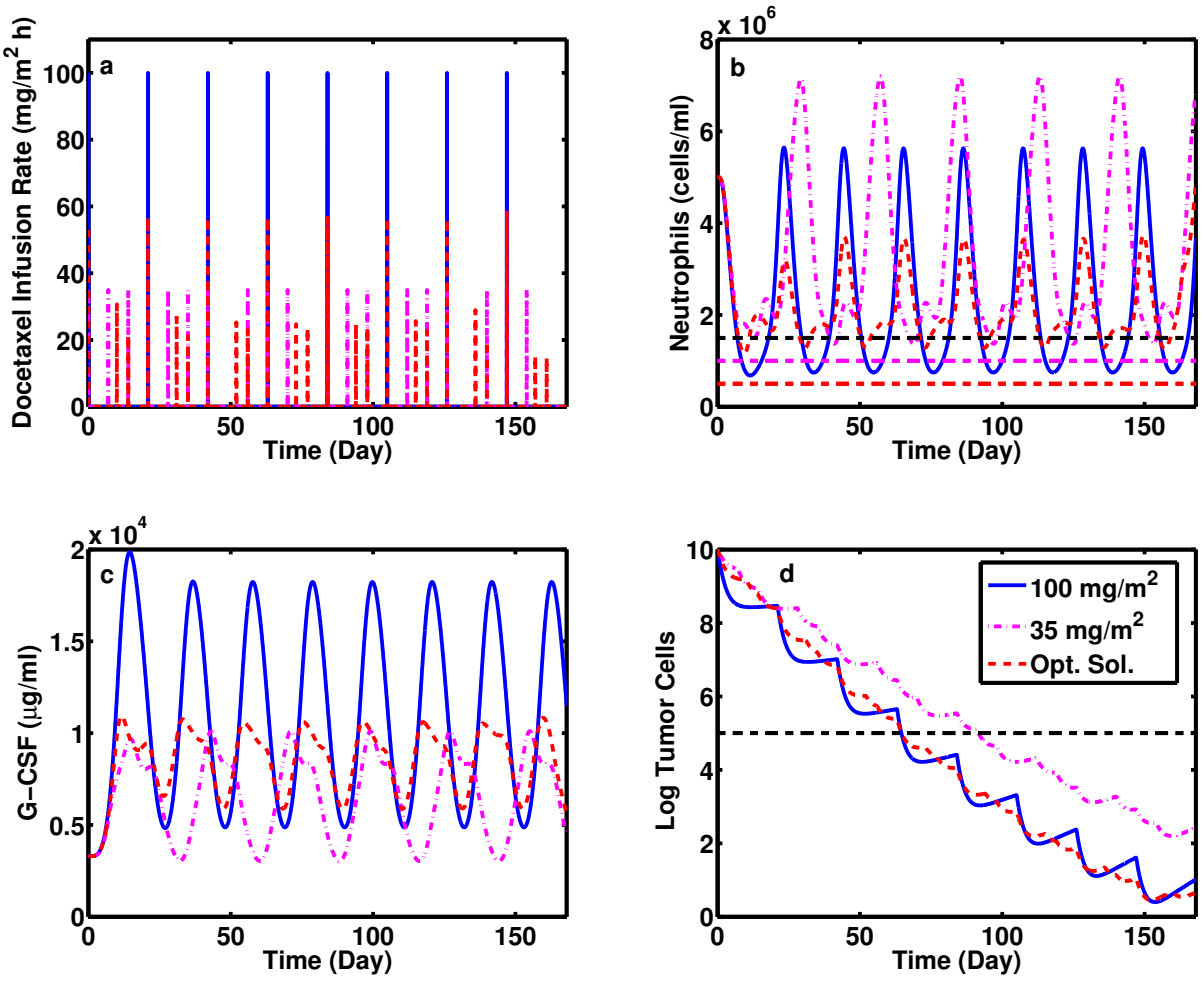

Figure 30: Comparison of clinical standard-of-practice docetaxel administration schedules versus the solution of Problem (4.22). Dashed line: 100mg/m^2 every 3 weeks; dashed-dotted line: 35 mg/m^2 every week for 3 weeks followed by 1 week off; solid line: optimal treatment schedule as provided by the algorithm. Panel a: drug infusion rate; panel b: ANC (horizontal dashed lines: neutropenia grades 2, 3, and 4 from top to bottom); panel c: G-CSF plasma concentration; panel d: log of number of cancer cells (horizontal dashed line: clinical detection limit).

Table 9: Summary of treatment results for different chemotherapy schedules.

Treatment Schedule	**Total Drug Delivered (mg/m^2/21 Days)**	**Neutropenia Grade**	**Detection Limit Reached (Day)**
100 mg/m^2 (q3w)	100	3	64
35 mg/m^2 (qw 3 of 4)	105	2	96
Optimal	105	2	64

a treatment schedule for the patient that is able to reduce the tumor size at the same rate as the 100 mg/m^2 q3w schedule without causing the patient to experience grade 3 neutropenia. The optimization posed in Problem 4.22 produces the treatment schedule that maximizes tumor elimination without inducing a severe toxicity profile.

4.5.5.2 Personalized Treatment Schedule for Different Patient Toxicity Profiles:

Interpatient variability is expected in pharmacokinetics as well as sensitivity to treatment in terms of both efficacy (tumor kill) and toxicity. The ability of the algorithm to adapt to individual patients is tested against simulated patients having different toxicity sensitivities to treatment. The patient-specific dynamics in chemotherapy optimization are the drug efficacy and the drug toxicity.

The drug toxicity profile is the limiting factor when it comes to patient response during chemotherapy, because toxicity can lead to delays in administration. In the optimization algorithm, the toxicity constraints often limit the amount of drug that can be administered to the patient. Therefore, the patient toxicity profiles are varied by changing parameter k_{vbm_D} (Equation (4.15) to test the ability of the algorithm to tailor chemotherapy schedules to individual patient response. As k_{vbm_D} increases, the patient becomes more sensitive to docetaxel; hence, docetaxel causes more neutropenic toxicity to the patient, leading to depressed ANC levels. Three representative patient toxicity profiles are chosen: patients who are insensitive to docetaxel (k_{vbm_D}=0.3017 min^{-1}, nominal patient), sensitive to doctaxel

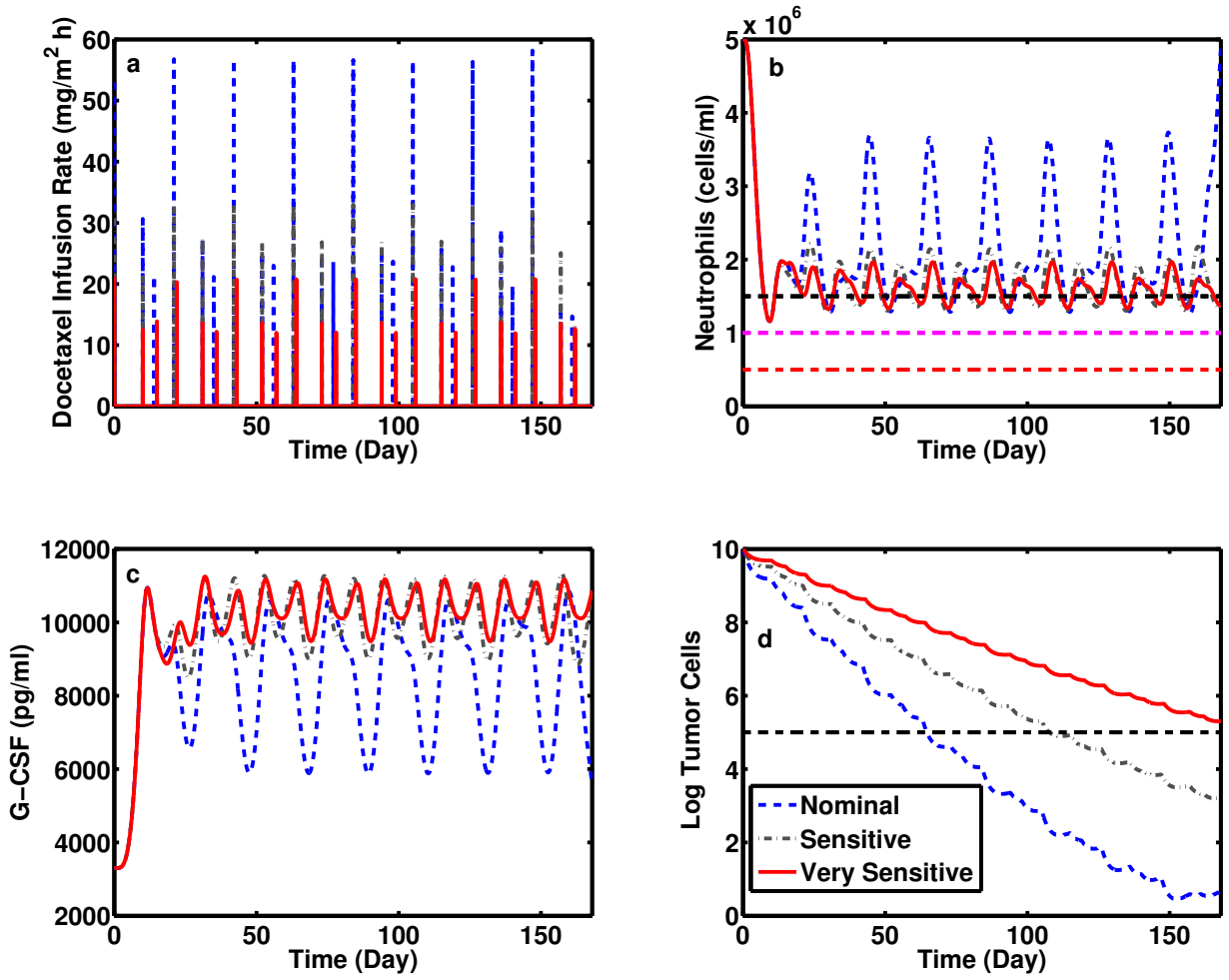

Figure 31: Comparison of docetaxel schedules for different patient toxicity profiles for Problem (4.22). Dashed line: insensitive to docetaxel (k_{vbm_D}=0.3017 min^{-1}, nominal patient); dash-dotted line: sensitive to docetaxel (k_{vbm_D}=0.5028 min^{-1}); solid line: very sensitive to docetaxel (k_{vbm_D}=0.7542 min^{-1}). Panel a: drug infusion rate; panel b: ANC (horizontal dashed lines: neutropenia levels 2, 3, and 4 from top to bottom); panel c: G-CSF plasma concentration; panel d: log of number of cancer cells (horizontal dashed line: clinical detection limit)

Table 10: Summary of treatment results for different patient toxicity profiles

Treatment Schedule	**Total Drug Delivered (mg/m^2/21 Days)**	**Neutropenia Grade**	**Detection Limit Reached (Day)**
Not Sensitive (Nominal)	105	2	64
Sensitive	69	2	109
Very Sensitive	47	2	172

(k_{vbm_D}=0.5028 min^{-1}), and very sensitive to docetaxel (k_{vbm_D}=0.7542 min^{-1}). Simulation results are shown in Figure 31. The algorithm is able to scale the drug dose to account for changes in sensitivity (Figure 31a). For the insensitive patient, the algorithm delivered the maximum amount of drug that can be delivered in a 3 week period (105 mg/m^2); clinically, this amount might have been increased after several cycles of low toxicity in order to potentially increase cell kill while keeping the patient at manageable toxicity. For the sensitive patient, the algorithm scaled down the amount of drug delivered over 3 weeks to 69 mg/m^2. Finally, the very sensitive patient could be administered only 47 mg/m^2 of docetaxel over a three week period. A summary of the treatment plans for the three different toxicity profiles is shown in Table 10.

None of the simulated patients treated by the algorithm experienced grade 3 neutropenia (Figure 31b and Table 10). As the toxicity increases, the total amount of drug administered per 21 days decreases (Figure 31a and Table 10). Since less drug can be administered, as patients become more sensitive to the toxic side-effects of the drug, the number of days of treatment until the tumor size decreases to the clinical detection limit increases from 64 (non-sensitive, low toxicity patient) to 172 (very sensitive, high-toxicity patient) (Figure 31d and Table 10). The advantage of the algorithm is the ability to tailor dose to the expected toxicity, while still maximizing tumor kill at various fixed sensitivities to the toxic effects of docetaxel.

Table 11: Summary of treatment results for different toxicity constraints.

Treatment Schedule	**Total Drug Delivered (mg/m^2/21 Days)**	**Neutropenia Grade**	**Detection Limit Reached (Day)**
Less Restrictive Constraints	105	2	64
More Restrictive Constraints	91	1	81

4.5.5.3 More Conservative Toxicity Constraints: The flexibility of the algorithm is further tested by adjusting the toxicity constraints of ANC to enforce lower toxicity grades. Equations(4.17) and (4.18) are modified to become:

$$N_c(k) \geq 2.0 \times 10^6 \; cells/ml \tag{4.28}$$

$$\sum_{i=1}^{7} N_c(i) \geq 17.5 \times 10^6 \; cells/ml \tag{4.29}$$

$$N_c(1) + N_c(8) \geq 5.0 \times 10^6 \; cells/ml \tag{4.30}$$

Equation (4.28) ensures the ANC does not drop below $2\times$ 10^6 (*i.e.*, no grade 1 toxicity), and Equation (4.29) forces the week to week neutrophil count level to be greater or equal to 2.5×10^6 cells/ml (no week-to-week toxicity of any grade). These two toxicity constraints then replace Equations 4.17 and 4.18 in Problem 4.22 to become Problem 4.31. A revised docetaxel treatment schedule is calculated by solving Problem 4.31. The optimal treatment schedules for the less restrictive and more restrictive toxicity constraints and the nominal patient response are shown in Figure 32 and Table 11. As the toxicity constraints become more restrictive, the amount of total docetaxel infused is decreased from 105 mg/m^2 every 3 weeks to 91 mg/m^2 every 3 weeks (Figure 32a and Table 11) in order to satisfy the new toxicity constraints (32b). The duration of the treatment prior to reaching the detection limit also increases from 64 days to 81 days. (Figure 32d and Table 11). The simulation results demonstrate the flexibility provided by the algorithm in incorporating or modifying constraints and the resulting changes to the treatment design.

$$
\begin{aligned}
\textit{Objective} \quad &: \quad (4.1) \\
\textit{s.t.} \quad &: \quad \text{PK:} \quad (3.15) - (3.16) \\
&\quad\;\; \text{PD Efficacy:} \quad (4.14) \\
&\quad\;\; \text{PD Toxicity:} \quad (3.18) - (3.26),\ (4.15) - (4.16) \\
&\quad\;\; \text{Toxicity Constraints:} \quad (4.28) - (4.30) \\
&\quad\;\; \text{Logistics:} \quad (4.20),\ \textit{and}\ (4.21)
\end{aligned} \tag{4.31}
$$

4.5.5.4 Targeted Tumor Size Control: Periodic feedback is used by clinicians to evaluate the efficacy of treatment and to adjust treatment as necessary to mitigate side effects. After a patient is treated and "cured by chemotherapy, that patient often comes back periodically to ensure that neither the tumor, nor any metastases, have (re)appeared [146]. Using assumption that we can control the patient tumor size to target size for a long period of time to avoid complication, we evaluate the algorithm in scheduling target tumor tracking [147]. In the docetaxel chemotherapy problem, we set the target tumor size to be 10^3 cells (10^6 cells= 1 mm^3) which is below the current detection limit. The objective for the tumor volume tracking problem is:

$$
\min_{D_d(q)} \sum_{w=1}^{96} (N_d(w) - 3)^2 + \Gamma_u \sum_{q=1}^{m_q} D_d(q)^2 \tag{4.32}
$$

Here the first term in Equation (4.32) is the sum of squared differences between the tumor size and the targeted tumor size, minimized every week over 96 weeks. The second term in Equation (4.32) is the penalty term for small drug doses (that typically contribute to toxicity

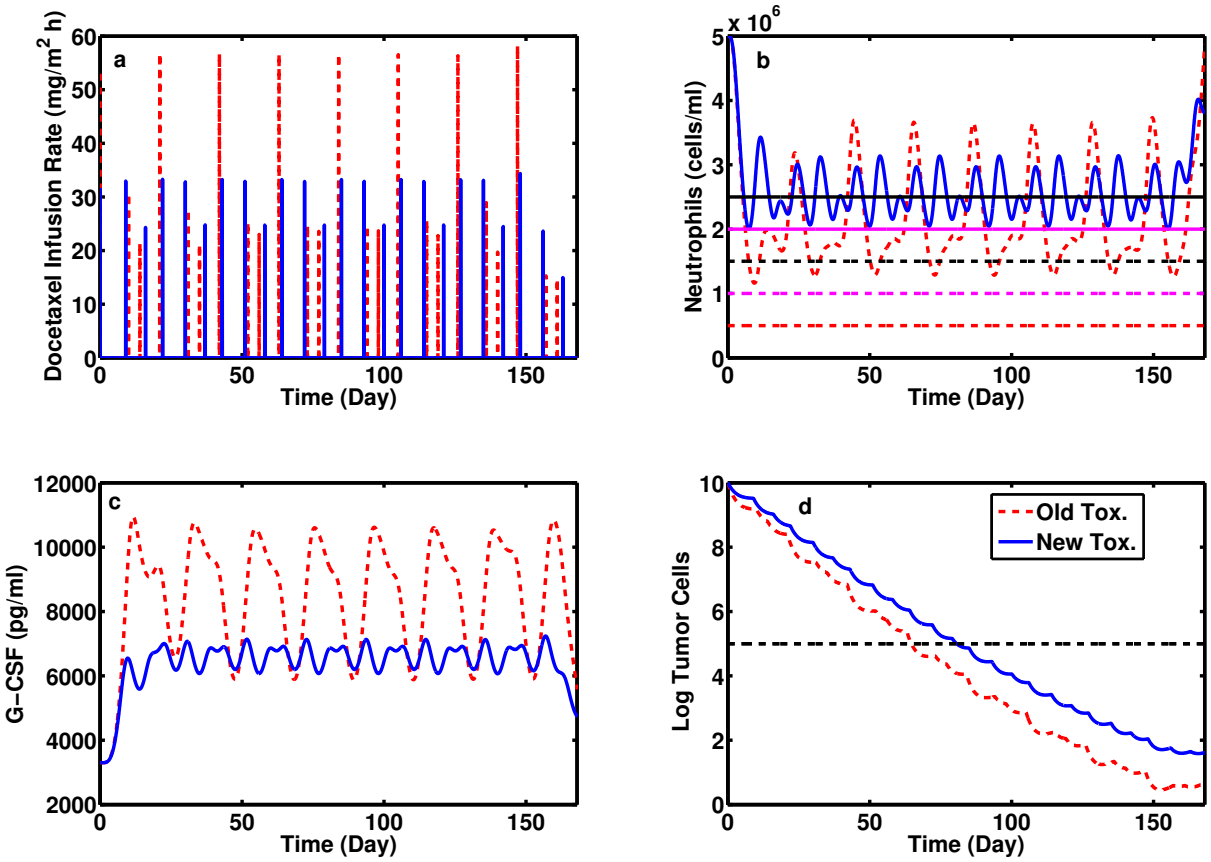

Figure 32: Comparison of docetaxel schedules for different toxicity constraints for Problem (4.31). Dashed line: more restrictive toxicity constraints; solid line: less restrictive toxicity constraints. Panel a: drug infusion rate; panel b:ANC (horizontal dashed lines: less restrictive toxicity constraints, horizontal solid line: more restrictive toxicity constraints); panel c: G-CSF plasma concentration; panel d: log of number of cancer cells (horizontal dashed line: clinical detection limit)

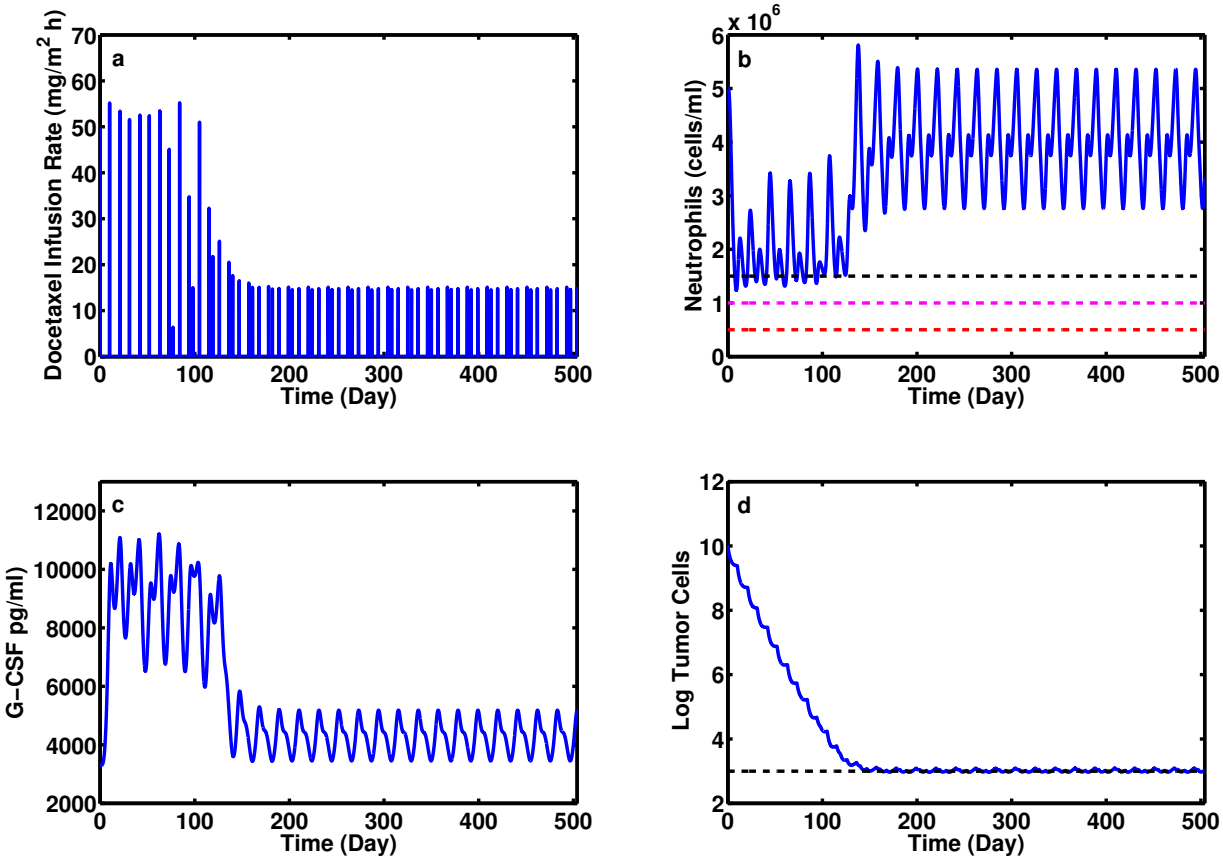

Figure 33: Targeted tumor size for Problem (4.33). Panel a: drug infusion rate; panel b: ANC (horizontal dashed lines: neutropenia levels 2, 3, and 4 from top to bottom); panel c: G-CSF plasma concentration; panel d: log of number of cancer cells (horizontal dashed line: targeted tumor size).

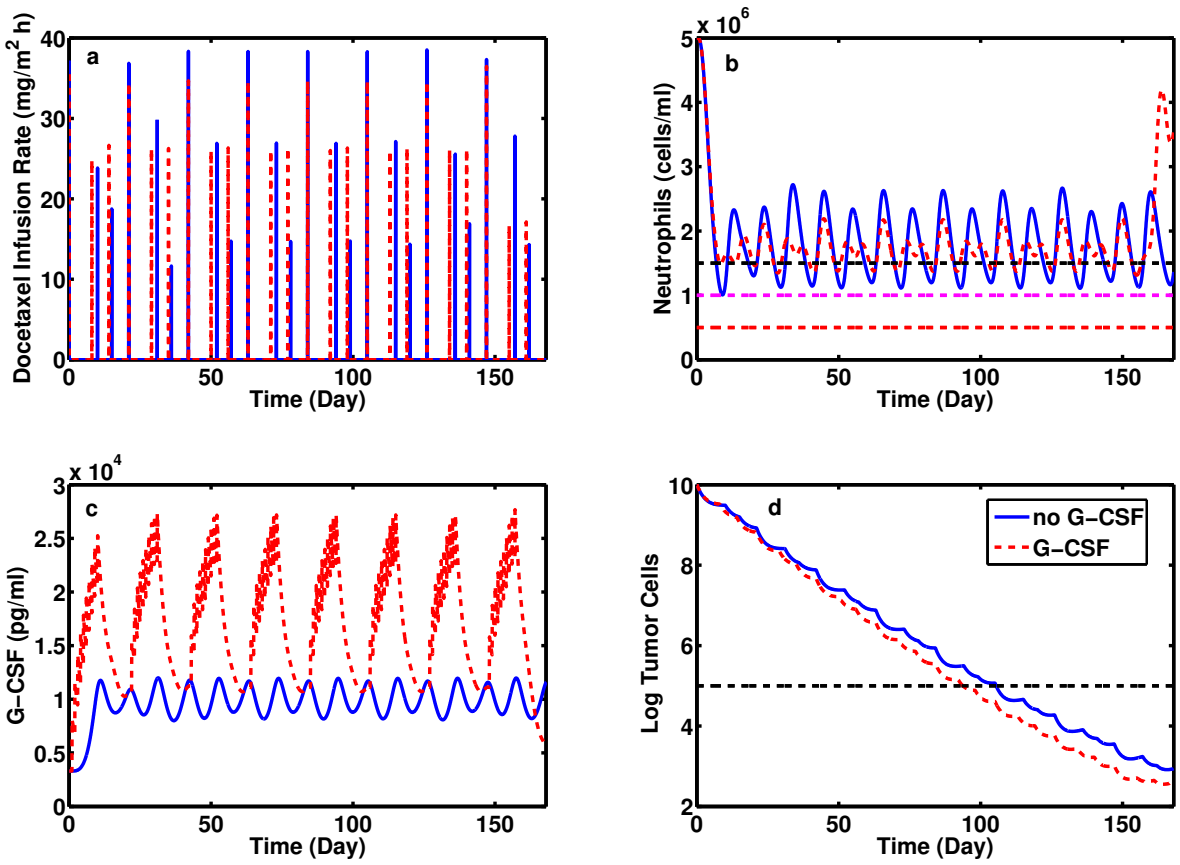

Figure 34: Comparison of docetaxel schedules and patient outcome to treatment without (solid) and with (dashed) G-CSF administration. Panel a: drug infusion rate; panel b: ANC (horizontal dashed lines: neutropenia levels 2, 3, and 4 from top to bottom); panel c: G-CSF plasma concentration; panel d: log of the number of cancer cells (horizontal dashed line: clinical detection limit).

Table 12: Summary of treatment results without and with G-CSF administration.

Treatment Schedule	**Total Drug Delivered (mg/m^2/21 Days)**	**Neutropenia Grade**	**Detection Limit Reached (Day)**
No-GCSF	80	2	107
G-CSF	87	1	95

but have little or no effect on tumor size). With the new objective function, the optimization problem becomes:

$$
\begin{aligned}
\textit{Objective} \quad &: \quad (4.32) \\
s.t. \quad &: \quad \text{PK:} \quad (3.15) - (3.16) \\
&\quad\;\; \text{PD Efficacy:} \quad (4.14) \\
&\quad\;\; \text{PD Toxicity:} \quad (3.18) - (3.26),\ (4.15) - (4.16) \\
&\quad\;\; \text{Toxicity Constraints:} \quad (4.28) - (4.30) \\
&\quad\;\; \text{Logistics:} \quad (4.20),\ \textit{and}\ (4.21)
\end{aligned}
\tag{4.33}
$$

The solution for the targeted tracking problem is shown in Figure 33. The algorithm results show that, the maximum drug dose (without violating toxicity constraints) is administered at the beginning of treatment when the tumor size (Figure 33d) is bigger than the targeted size . This lasts for 7 cycles (Days 0-147 in Figure 33a) and reduces the tumor size at a maximal rate, constrained by toxicity. When the difference between the actual tumor size and the targeted tumor size is approaching the target (Days 140-170 in Figure 33d), the amount of drug delivered is reduced, as seen in Figure 33a, to ensure that tumor size reaches the target. After the target tumor size is reached (day 170 onward in Figure 33d), the drug dose is further decreased to a maintenance amount that keeps the tumor size at the targeted value, on average.

4.5.5.5 Docetaxel and G-CSF Rescue: G-CSF is often used as a rescue agent when patient ANC drops to very low levels (*e.g.*, grade 4 neutropenia) and it can be designed into treatment in advance if the drug is known to exhibit highly toxic responses in patients (E_{max}=0.026 1/min , k_{vbm}=0.377 1/min). The algorithm can be further enhanced to employ G-CSF as an additional administered agent that mitigates neutropenia, thereby leading to more aggressive docetaxel administration. When administered, G-CSF is dosed once a day for 10 consecutive days per cycle, as seen in Equation 4.23. Optimization problems 4.22 and 4.24 are solved for the nominal patient to evaluate the impact of G-CSF on docetaxel schedules and patient outcome. The optimization results are shown in Figure 34 and Table 12.

Comparing the results between schedules utilizing G-CSF and schedules not administering G-CSF, G-CSF allows an increase in the amount of docetaxel administered from 80 to 87 mg/m^2 every 21 days for the nominal patient (Figure 34a and Table 12). The increase in the amount of drug that can be administered per cycle leads to a shorter treatment time until the tumor is clinically not detectable when using G-CSF (95 days) as compared to treatments not utilizing G-CSF (107 days), as shown in Figure 34d and Table 12. The optimal G-CSF usage, when administration is limited to 10 consecutive days, is to begin treatment on day 2 (finishing on day 11) after the first dose of docetaxel in a 21 day cycle. Although the patient toxicity profiles satisfy the toxicity constraints in both cases, the patient treated with G-CSF has a higher nadir neutrophil count (1.45×10^6 cells/ml) compared to the patient without G-CSF treatment (1.13×10^6 cells/ml). Thus, the use of G-CSF in docetaxel chemotherapy allows an increase in the amount of the drug infused and decreases the neutropenia experienced by patients.

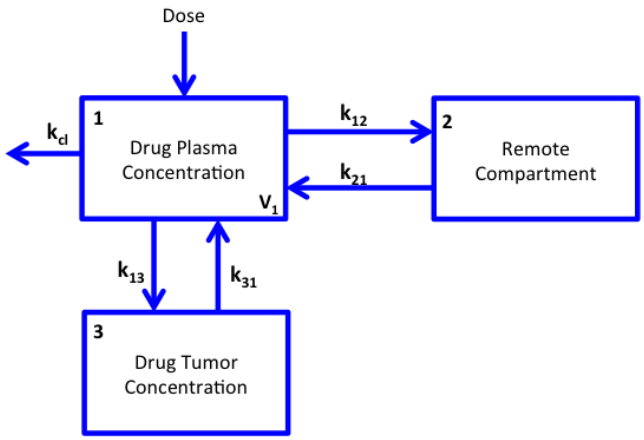

Figure 35: Compartmental-based pharmacokinetic model structure for cisplatin and carboplatin.

4.6 DOCETAXEL COMBINATION CHEMOTHERAPY WITH CISPLATIN OR CARBOPLATIN

4.6.1 Cisplatin and Carboplatin Pharmacokinetic Models

Compartmental PK models are often used to capture drug concentration in plasma after dosing. Each compartment is governed by an ordinary differential equation to capture the observed response of drug concentration over time. Compartments are added – as necessary – to improve the quality of fit, such that drug concentration profiles with biphasic (two time constants) elimination require the addition of a remote compartment to capture the plasma profile using Compartment 1 [148, 3, 4]. A compartmental model, as shown in Figure 35, is used to capture the dynamics of cisplatin [148, 3, 149] or carboplatin pas13,van91. A third compartment is added to the existing model structure to represent the drug concentration in the tumor.

Mathematically, this model is represented using the ordinary differential equation description in Equations (4.34)-(4.36) and their corresponding parameters for cisplatin or carboplatin, as shown in Tables 13 and 14, respectively. The drug plasma concentration in mg/L is represented by compartment 1, with distribution volume V_1. The right-hand side terms capture: (i) drug infusion (rate $u(t)$, in mg/min); (ii) drug clearance via a first order rate mechanism with rate constant k_{cl}; (iii) drug transport in dynamic equilibrium (2 terms, rate constants k_{12} and k_{21}) with remote compartment 2; and (iv) drug transport in dynamic equilibrium (2 terms, rate constants k_{13} and k_{31}) with remote compartment 3, which represents the tumor in this compartmental model structure. These models will be used to represent cisplatin or carboplatin concentration dynamics in the patient.

$$\frac{dC_p(t)}{dt} = \frac{u(t)}{V_1} - k_{cl}C_p(t) - k_{12}C_p(t) + k_{21}C_2(t) - k_{13}C_p(t) + k_{31}C_t(t) \tag{4.34}$$

$$\frac{dC_2(t)}{dt} = k_{12}C_p(t) - k_{21}C_2(t) \tag{4.35}$$

$$\frac{dC_t(t)}{dt} = k_{13}C_p(t) - k_{31}C_t(t) \tag{4.36}$$

Table 13: Cisplatin PK model parameters [3]

Parameters	**Value**	**Unit**	**Parameters**	**Value**	**Unit**
V_1	41.87	L	k_{cl}	2.29×10^{-4}	min^{-1}
k_{12}	0.0034	min^{-1}	k_{21}	0.0018	min^{-1}
k_{13}	0.012	min^{-1}	k_{31}	0.015	min^{-1}

4.6.2 Combination Chemotherapy Efficacy Model

When combination chemotherapy is utilized, drugs may target different phases of the cell growth cycle; therefore, the modified cell-cycle model should accurately capture how combination chemotherapy affects the tumor growth dynamics through their respective mechanisms of action. For docetaxel in combination with cisplatin or carboplatin, these drugs

Table 14: Carboplatin PK model parameters [4]

Parameters	**Value**	**Unit**	**Parameters**	**Value**	**Unit**
V_1	5.07	L	k_{cl}	0.20	min^{-1}
k_{12}	0.12	min^{-1}	k_{21}	0.027	min^{-1}
k_{13}	0.012	min^{-1}	k_{31}	0.015	min^{-1}

target different cell phases in the cell cycle. While cisplatin/carboplatin target S-phase cells, docetaxel acts in the M-phase of growth. Thus, the modified cell-cycle model is used to capture the cycle-specific kill mechanisms of each drug, as shown in Equations (4.37)-(4.40):

$$\frac{dX_G(t)}{dt} = -k_{GS}\left[X_G(t)\right]^{a/c} + 2k_{MG}X_M(t) \tag{4.37}$$

$$\frac{dX_S(t)}{dt} = -k_{SM}X_S(t) + k_{GS}\left[X_G(t)\right]^{a/c} - k_{eff_1}D_1(t)X_S(t) \tag{4.38}$$

$$\frac{dX_M(t)}{dt} = -k_{MG}X_M(t) + k_{SM}X_S(t) - k_{death} * \left[N(t)\right]^{b/c} - k_{eff_2}D_2(t)X_M(t) \tag{4.39}$$

$$N(t) = X_G(t) + X_S(t) + X_M(t) \tag{4.40}$$

The two bilinear kill terms, $k_{eff_1}D_1(t)X_S(t)$ and $k_{eff_2}D_2(t)X_M(t)$, are used to model the tumor elimination rate in the S- and M- phases when drugs are administered. The bilinear kill terms are derived from *in vitro* cell study data, which might not completely capture the dynamics of drug distribution and action *in vivo*; however, the bilinear kill terms are widely employed as mathematical approximations for anticancer action of chemotherapeutics.

4.6.3 Cisplatin Nephrotoxicity Model

The main adverse effect of cisplatin is kidney damage (nephrotoxicity) [150, 151, 152]. A toxicity model to capture this effect is necessary for the cisplatin chemotherapy scheduling problem. During a cisplatin chemotherapy regimen, the concentration of creatinine in plasma increases due to inhibited renal clearance [153, 154, 152]. Before each cisplatin cycle, the concentration of plasma creatinine and its clearance rate are measured to make sure the

patient does not have nephrotoxicity that would preclude cisplatin administration. In a typical healthy subject, the plasma creatinine concentration normally ranges between 0.5-1.0 mg/dl, and the clearance rate is 97-137 ml/min. When the plasma concentration of creatinine is $\geq$1.2 mg/dl and/or creatinine clearance is $\leq$60 ml/min, cisplatin chemotherapy is withheld until the creatinine level in the patient decreases and their clearance rate increases to less toxic levels [153, 155]. For this study, creatinine plasma concentration and clearance rate will be used as the toxicity markers.

One equation will be used to describe the creatinine concentration, $Cr(t)$, in the plasma [156]:

$$\frac{dCr(t)}{dt} = k_{1cr} - \frac{CL(C(t))}{V_d} Cr(t) \tag{4.41}$$

where k_{1cr} is the rate of endogenous creatinine production and $CL(C(t))$ is the creatinine clearance rate, which is dependent on the cisplatin concentration, $C(t)$, and V_d is a distribution volume. The clearance of creatinine is defined as:

$$CL(C(t)) = k_{cl_{cis}} - k_{clred} \frac{C(t)}{C_{50} + C(t)} \tag{4.42}$$

Here $k_{cl_{cis}}$ is the nominal clearance rate of plasma creatinine, k_{clred} is the maximum inhibition in creatinine clearance rate, C_{50} is the cisplatin concentration at which the rate of creatinine clearance inhibition is at half its maximum value, and $C(t)$ is the cisplatin plasma concentration. Equations (4.41) and (4.42) are coupled with the pharmacokinetic model of cisplatin (Equations (4.34)-(4.36)) to establish a nephrotoxicity constraint when using cisplatin in both single-agent and combination chemotherapy treatments.

4.6.4 Docetaxel and Carboplatin Neutropenic Toxicity Model

Both docetaxel and carboplatin have a myelosuppressive effect. The reduced neutropenia model, in the form from Section 3.5.2, is used to represent the patient neutrophil response to docetaxel and carboplatin chemotherapy as single agents and in combination. When docetaxel and carboplatin are used in combination, the effects of these drugs on the progenitor population is modeled as:

$$\begin{aligned}\frac{dPr(t)}{dt} &= \left(k_1 + \frac{k_2 GCSF(t)}{k_3 + GCSF(t)}\right) S - k_{tr} Pr(t) - \frac{E_{max_D} C_{b_D}(t)}{EC_{50_D} + C_{b_D}(t)} Pr(t) \\ &\quad - \frac{E_{max_C} C_{b_C}(t)}{EC_{50_C} + C_{b_C}(t)} Pr(t) + \frac{E_{max_D} C_{b_D}(t)}{EC_{50_D} + C_{b_D}(t)} \frac{E_{max_C} C_{b_C}(t)}{EC_{50_C} + C_{b_C}(t)} Pr(t) \quad (4.43)\end{aligned}$$

Here each drug affects progenitors at the rate E_{max_i} and half maximum constant EC_{50_i}. The combination effect is corrected by the product of the two Michaelis-Menten functions, which is the last term in Equation (4.43). The parameters for the toxicity effects of docetaxel and carboplatin on neutrophil dynamics are shown in Table 15

Table 15: Docetaxel (D) and carboplatin (C) neutropenia model parameters for Equations (4.15)- (4.43.

Parameters	Value	Unit	Parameters	Value	Unit
k_{vbm_D}	0.3017	min^{-1}	k_{vbm_C}	0.1819	min^{-1}
k_{bmv_D}	0.0802	min^{-1}	k_{bmv_C}	0.4369	min^{-1}
k_{40_D}	0.0005	μM	k_{40_C}	0.0005	μM
E_{max_D}	0.0130	min^{-1}	E_{max_C}	0.0053	min^{-1}
EC_{50_D}	0.7873	μM	EC_{50_C}	0.7873	μM

4.6.5 Nephrotoxicity Constraints

In the case where cisplatin is used as an anticancer agent, kidney damage must be considered in the patient toxicity profile. Treatment elevates creatinine concentration and simultaneously decreases creatinine clearance rate. The creatinine concentration and its clearance

rate are posed as toxicity constraints for cisplatin chemotherapy following Equations (4.44) and (4.45). Here k is a discretization step. Equation (4.44) constrains the creatinine concentration, $Cr(k)$, beneath the maximum allowable level, which is 1.2 mg/dL. Equation (4.45) constrains the creatinine clearance rate, $CL_{Cr}(k)$, such that it does not drop below the clinically allowed rate.

$$Cr(k) \leq 1.2\ mg/dl \tag{4.44}$$

$$CL_{Cr}(k) \geq 60\ ml/min \tag{4.45}$$

4.6.6 Additional Logistical Constraints

The recommended dose for cisplatin is 100 mg/m^2 via IV infusion every three weeks [39, 137]. The carboplatin dose recommendation is 900 mg/m^2 via IV infusion every three weeks [4, 157]. These drug dose recommendations are used as the upper bound on the amount of drug that can be administered in every 3 week period (Equations (4.46) and (4.47)). Here $D_j(k)$ is the amount of drug j ($j \in \{cis, car\}$), infused on day k. These logistical constraints are coupled with the dynamic and toxicity constraints in the chemotherapy scheduling problem for single agent docetaxel and for combination chemotherapy in the cases of docetaxel-cisplatin and docetaxel-carboplatin combinations.

$$\sum_{q=1}^{21} D_{cis}(q) \leq 100\ mg/m^2 \tag{4.46}$$

$$\sum_{q=1}^{21} D_{car}(q) \leq 900\ mg/m^2 \tag{4.47}$$

4.6.7 Combination Chemotherapy Problem Formulation

4.6.7.1 Docetaxel-Cisplatin Combination: When docetaxel and cisplatin are used in combination, the optimization Problem 4.22 is modified to become:

$$
\begin{aligned}
\textit{Objective} \quad &: \quad (4.1) \\
\textit{s.t.} \quad &: \quad \text{Docetaxel PK:} \quad (3.15) - (3.16) \\
&\qquad\quad \text{Cisplatin PK:} \quad (4.34) - (4.36) \\
&\qquad\quad \text{Combination PD Efficacy:} \quad (4.37) - (4.40) \\
&\qquad\quad \text{Docetaxel PD Toxicity:} \quad (3.18) - (3.26),\ (4.15) - (4.16) \\
&\qquad\quad \text{Cisplatin PD Toxicity:} \quad (4.41),\quad (4.45) \\
&\qquad\quad \text{Docetaxel Toxicity Constraints:} \quad (4.28) - (4.30) \\
&\qquad\quad \text{Cisplatin Toxicity Constraints:} \quad (4.44),\ (4.45) \\
&\qquad\quad \text{Logistics:} \quad (4.20),\ (4.21),\ \textit{and}\ (4.46)
\end{aligned}
\tag{4.48}
$$

Problem 4.48 contains 585,000 variables and 885,000 constraints, which is an increase of 20% in the number of variables and 110% in the number of constraints when compared to optimizing docetaxel treatment alone (Problem 4.22). Problem 4.48 is solved using the method described in Section 4.5.4.

4.6.7.2 Docetaxel-Carboplatin Combination: When docetaxel and carboplatin are used in combination, the optimization Problem 4.22 is modified to become:

$$
\begin{aligned}
\textit{Objective} \quad &: \quad (4.1) \\
\textit{s.t.} \quad &: \quad \text{Docetaxel PK:} \quad (3.15) - (3.16) \\
&\qquad\quad \text{Carboplatin PK:} \quad (4.34) - (4.36) \\
&\qquad\quad \text{Combination PD Efficacy:} \quad (4.37) - (4.40) \\
&\qquad\quad \text{Combination PD Toxicity:} \quad (3.18) - (3.26),\ (4.15) - (4.43) \\
&\qquad\quad \text{Combination Toxicity Constraints:} \quad (4.28) - (4.30) \\
&\qquad\quad \text{Logistics:} \quad (4.20),\ (4.21),\ \textit{and}\ (4.47)
\end{aligned}
\tag{4.49}
$$

Problem 4.49 contains 585,000 variables and 598,000 constraints which is an increase in 20% number of variable and 48% number of constraints in comparing to optimize docetaxel treatment alone. As above, the method described in Section 4.5.4 is used to solve this problem.

4.6.8 Results

4.6.8.1 Docetaxel and Cisplatin Combination: The docetaxel-cisplatin scheduling optimization in Problem (4.48) is solved for two different sets of nephrotoxicity dynamics, one with high creatinine production (Patient 1) and one with low clearance rate (Patient 2), by changing toxicity model parameters in Equations (4.41) and (4.42). The parameter values for the nephrotoxicity for these two patients are shown in Table 16. Problem 4.48 contains 585,000 variables and 885,000 constraints, and the algorithm takes 2 hours to find the optimal treatment schedules for both docetaxel and cisplatin. The treatment schedules and patient response during 8 cycles of treatment are shown in Figure 36 and Table 17.

Table 16: Parameter values for two different patient nephrotoxicity dynamics in Equations (4.41) and (4.45).

Patient	k_{1cr} **mg/dL/min**	$k_{cl_{cis}}$ **ml/min**	k_{clred} **ml/min**	C_{50} **mg/ml**	V_d **ml**
1	0.128	230	660	2.14	1000
2	0.654	109	230	2.14	1000

The total amount of docetaxel infused to both patients is 67 mg/m^2 per 21 days (Figure 36a and Table 17), because they have the same neutropenic toxicity profile (Figure 36b). When cisplatin is infused, the plasma creatinine level increases (Figure 36e) due to a decrease in the creatinine clearance rate (Figure 36f). For Patient 1 (high creatinine production), the plasma creatinine level reaches an upper limit of 1.2 mg/dL, at which point cisplatin infusion is stopped. For Patient 2 (low creatinine clearance rate), the clearance rate drops to a lower limit of 60 ml/min, which sets the maximum amount of cisplatin that can be infused

Table 17: Summary of treatment results for Docetaxel and Cisplatin combination

Treatment Schedule	**Docetaxel Delivered (mg/m^2/21 Days)**	**Cisplatin Delivered (mg/m^2/21 Days)**	**Detection Limit Reached (Day)**
Patient 1	67	100	106
Patient 2	67	100	101

(Figure 36d). In both patients, tumor size is reduced to the detection limit 101-106 days after treatment (Figure 36g and Table 17). As in the case of docetaxel used as a single agent, the docetaxel-cisplatin combination schedules and dose magnitudes are governed by patient toxicity profiles; neutropenia for docetaxel and nephrotoxicity for cisplatin. For this drug comination, with no overlapping toxicities, administration schedules are optimized by the algorithm such that toxicity and logistical constraints are satisfied.

4.6.8.2 Docetaxel and Carboplatin Combination: Combination chemotherapy does not often utilize two or more drugs with the same adverse effects, even though these drugs have different mechanisms of action. Clinicians are often concerned that drug combinations with overlapping toxicities may cause severe side-effects that could interrupt treatment schedules and negatively impact the patient. We hypothesize that the algorithm can optimally dose two or more effective drugs with overlapping toxicities in combination without inducing severe toxic side-effects.

Docetaxel and carboplatin have the same myelosuppressive effects on patients during chemotherapy. While docetaxel effect targets the M-phase in the cell cycle, carboplatin targets the S-phase. Both drugs are effective as single-agent chemotherapeutics. A docetaxel-carboplatin combination is used to test the ability of the algorithm to administer two drugs with overlapping toxicities while satisfying toxicity constraints and maximizing treatment effect. The optimization Problem 4.49 is solved for docetaxel, carboplatin, and their combination, in order to compare single-agent and combination effects.

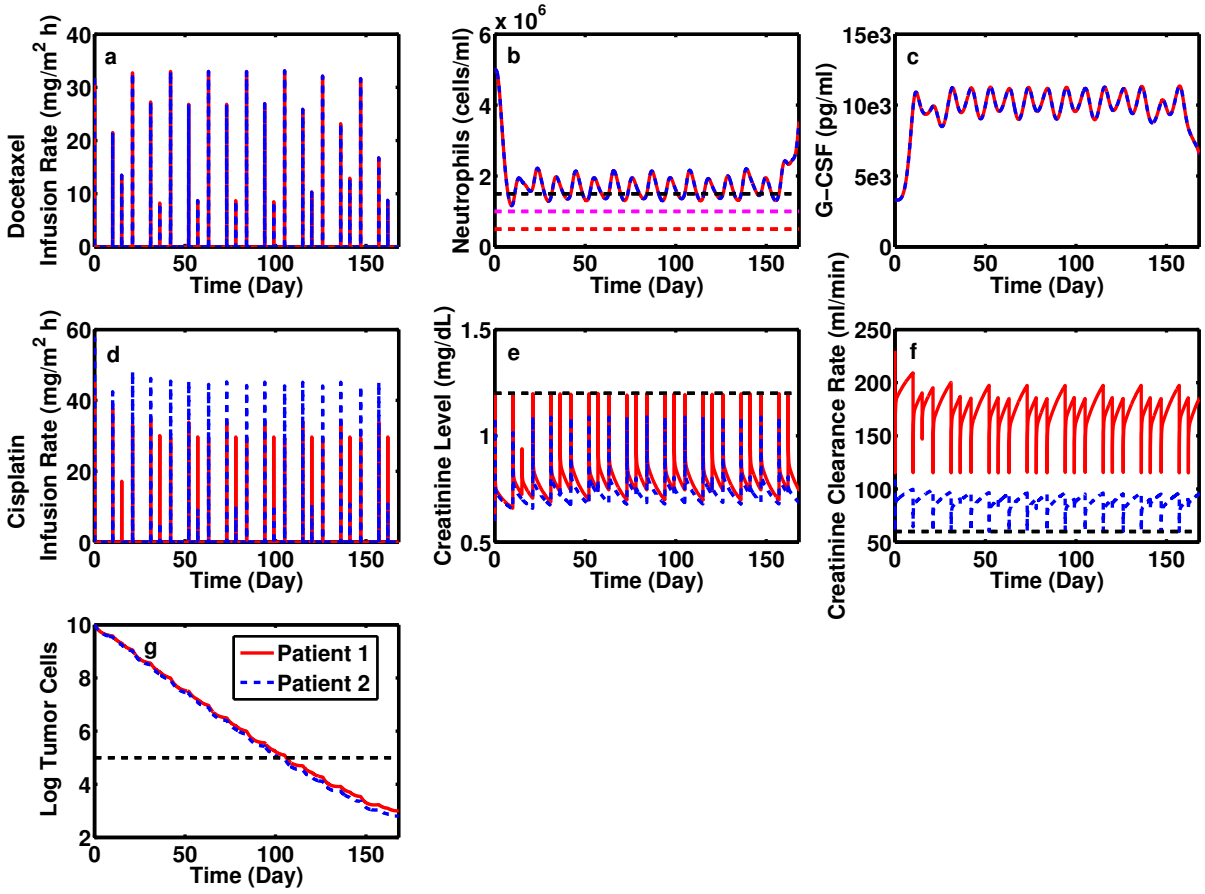

Figure 36: Docetaxel-cisplatin schedules for different nephrotoxic patient parameters. Solid line: Patient 1 (high creatinine production rate); dashed line: Patient 2 (low creatinine clearance rate). Panel a: docetaxel infusion rate; panel b: ANC (horizontal dashed lines: neutropenia levels 2, 3, and 4 from top to bottom); panel c: G-CSF plasma concentration; panel d: cisplatin infusion rate; panel e: creatinine plasma concentration (horizontal dashed line: creatinine level upper limit, 1.2 mg/dL); panel f: creatinine clearance rate (horizontal dashed line: lower limit in clearance rate, 60 ml/min); panel g: log of number of cancer cells (horizontal dashed line: detection limit).

Table 18: Patient 3 parameter values (docetaxel (D) and carboplatin (C))

Parameters	**Value**	**Unit**	**Parameters**	**Value**	**Unit**
k_{vbm_D}	**0.5028**	min^{-1}	k_{vbm_C}	**0.1819**	min^{-1}
k_{bmv_D}	0.0802	min^{-1}	k_{bmv_C}	0.4369	min^{-1}
k_{40_D}	0.0005	μM	k_{40_C}	0.0005	μM
E_{max_D}	0.0130	min^{-1}	E_{max_C}	0.0053	min^{-1}
EC_{50_D}	0.7873	μM	EC_{50_C}	0.7873	μM
k_{eff_D}	**0.806**	$\mu M.min^{-1}$	k_{eff_C}	0.0108	$\mu M.min^{-1}$

Table 19: Patient 4 parameter values (docetaxel (D) and carboplatin (C))

Parameters	**Value**	**Unit**	**Parameters**	**Value**	**Unit**
k_{vbm_D}	**0.2514**	min^{-1}	k_{vbm_C}	**0.0905**	min^{-1}
k_{bmv_D}	0.0802	min^{-1}	k_{bmv_C}	0.4369	min^{-1}
k_{40_D}	0.0005	μM	k_{40_C}	0.0005	μM
E_{max_D}	0.0130	min^{-1}	E_{max_C}	0.0053	min^{-1}
EC_{50_D}	0.7873	μM	EC_{50_C}	0.7873	μM
k_{eff_D}	**0.3636**	$\mu M.min^{-1}$	k_{eff_C}	0.0108	$\mu M.min^{-1}$

Table 20: Summary of treatment results for docetaxel and carboplatin combination therapy where docetaxel is more effective than carboplatin.

Treatment Schedule	**Docetaxel Delivered (mg/m^2/21 Days)**	**Carboplatin Delivered (mg/m^2/21 Days)**	**Day Reached Detection Limit**
Docetaxel (Doc.)	68.7	0	84
Carbopalatin(Car.)	0	452.7	130
Doc.+ Car.	63.4	369.1	53

Two patient cases, and their associated parameter values relating to drug toxicity in Equations (4.15)-(4.43) and drug efficacy in Equations (4.37)-(4.40) are shown in Tables 18 and 19. The differences in their dynamics are bold in Tables 18 and 19 (bold parameters). The optimal treatment design results for Patient 3 are shown in Table 20 and Figure 37e while the optimal treatment design for Patient 4 is shown Table 21 and Figure 38e.

For Patient 3 starting from the same initial tumor size, 84 days are required to reach the tumor size detection limit when 68.7 mg/m^2/ 21 days of docetaxel is used as a single-agent. Carboplatin alone requires 130 days to reach the detection limit with of 452.7 mg/m^2/21 days of carboplatin infusion. When docetaxel and carboplatin are used in combination, the optimal treatment schedule is able to reduce the tumor size to the detection limit 53 days after treatment starts. The dose magnitudes are optimized by balancing the drug efficacy and toxicity effects as seen in Table 20 and Figures 37a and d, where 63.4 mg/m^2 of docetaxel in combination with 269.1 mg/m^2 of caborplatin are infused per 21 days. The doses are adjusted by the algorithm to ensure that neutropenia constraints are not violated as shown in Figure 37b.

To test the algorithm flexibility, Patient 4 dynamics were tested. In this patient, the toxicity of carboplatin and docetaxel parameters, k_{vbm_C} and k_{vbm_D}, respectively, are reduced by 50% comparing to Patient 3 parameters. Docetaxel efficacy in Patient 4 is also reduced

Table 21: Summary of treatment results for docetaxel and carboplatin combination where carboplatin is more effective than docetaxel.

Treatment Schedule	**Docetaxel Delivered (mg/m^2/21 Days)**	**Carboplatin Delivered (mg/m^2/21 Days)**	**Day Reached Detection Limit**
Docetaxel (Doc.)	105.0	0	127
Carbopalatin (Car.)	0	900.0	77
Doc.+ Car.	104.8	885.24	43

by 45% comparing to Patient 3. The optimal treatment algorithm results for Patient 4 are presented in Table 21 and Figure 38e.

For Patient 4, it takes 127 days of treatment with docetaxel as a single-agent for the tumor size to reach the detection limit at the dose level of 105 mg/m^2/21 days, while only 77 days are needed for carboplatin alone to reduce the tumor size below the detection limit at a dose rate of 900 mg/m^2/21 days (Table 21 and Figures 38a and d). Increased amounts of docetaxel and carboplatin can be delivered due to the reduction in the toxicity parameter values (k_{vbm_D} and k_{vbm_C}) in Patient 2 (50% reduction in value versus Patient 1). Docetaxel efficacy is also reduced by 45% in Patient 2. Therefore, we see an increase the amount of docetaxel and carboplatin delivered to Patient 2 (the maximum amount of single-agent drug can be delivered over 21 days: 105 mg/m^2 docetaxel or 900 mg/m^2 carboplatin). The reduction in docetaxel efficacy causes the treatment using docetaxel alone to take 43 days longer to reach the detection limit than Patient 1, even though more drug is administered.

When used in combination to treat Patient 4, docetaxel and carboplatin doses are scaled down to 104.8 mg/m^2 and 885.24 mg/m^2, respectively on day 1, 10, and 15 from the treatment to satisfy the toxicity constraints. Since more drugs were administered in combination therapy, Patient 4 spent 9 days out of 21 days in grade 2 neutropenia while only 5 days out of 21 days in grade 2 neutropenia when single agent was used. Patient 4 is not sensitive to these

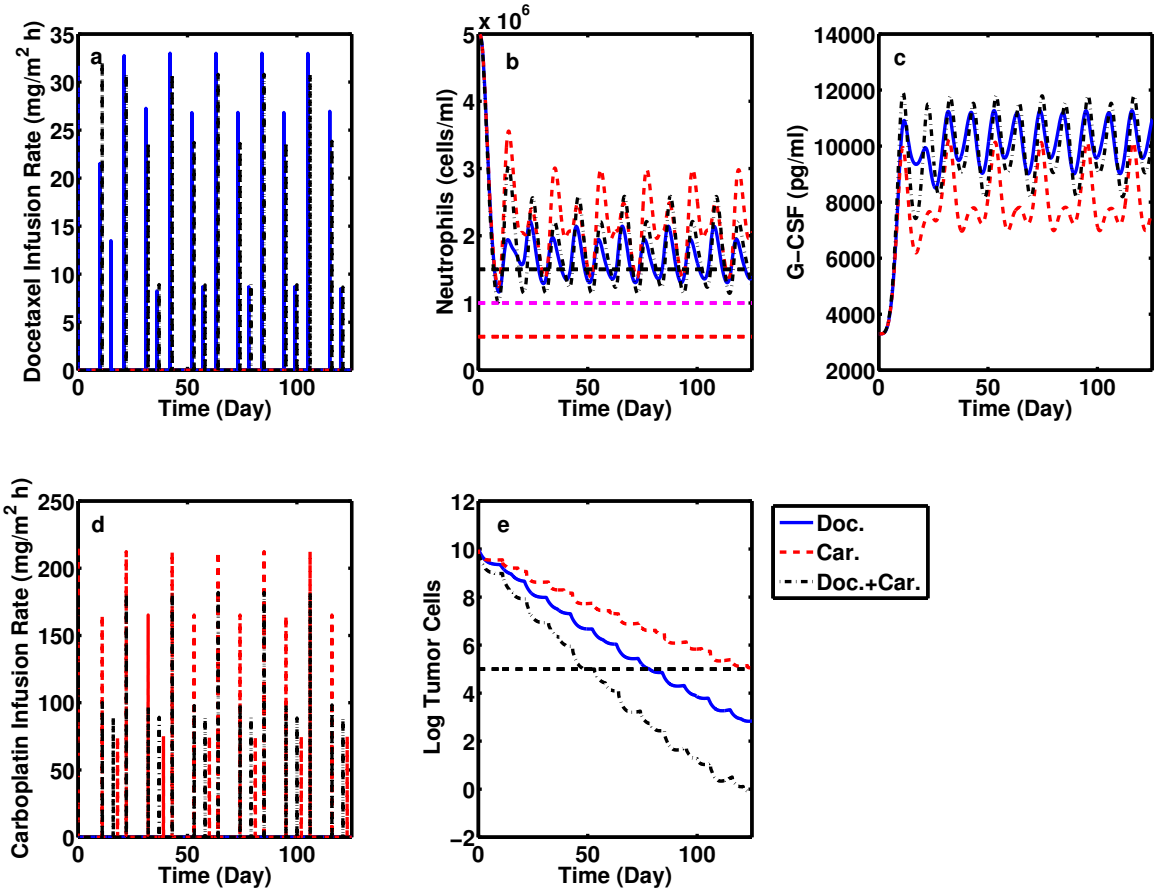

Figure 37: Optimal docetaxel-carboplatin treatment for Patient 3, high sensitivity to chemotherapeutic agents. Solid line: docetaxel as a single agent; dashed line: carboplatin as a single agent; dashed-dotted line: docetaxel and carboplatin combination. Panel a: docetaxel infusion rate; panel b: ANC (horizontal dashed lines: neutropenia levels 2, 3, and 4 from top to bottom); panel c: G-CSF plasma concentration; panel d: carboplatin infusion rate; panel e: log of number of cancer cells (horizontal dashed line: detection limit)

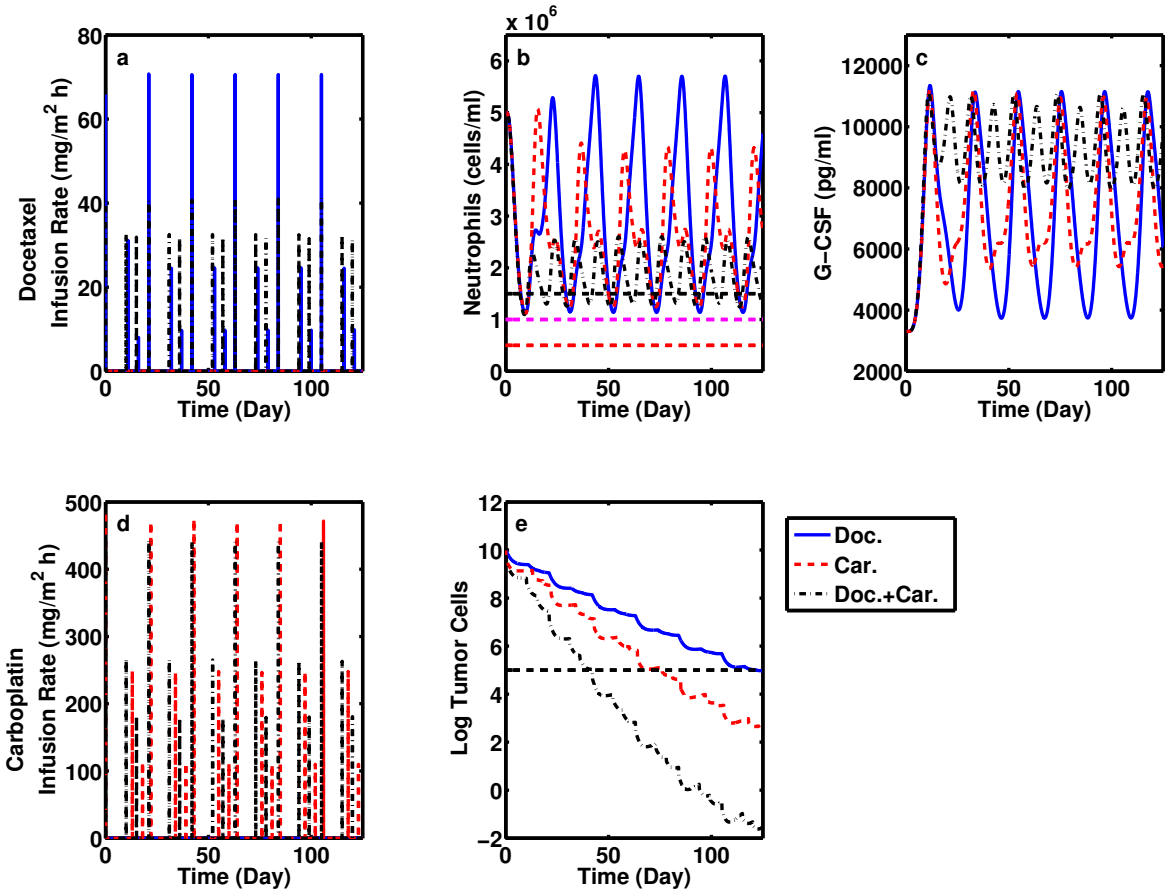

Figure 38: Optimal docetaxel-carboplatin treatment for Patient 4, low sensitivity to chemotherapeutic agents. Solid line: docetaxel as a single agent; dashed line: carboplatin as a single agent; dashed-dotted line: docetaxel and carboplatin combination. Panel a: docetaxel infusion rate; panel b: ANC (horizontal dashed lines: neutropenia levels 2, 3, and 4 from top to bottom); panel c: G-CSF plasma concentration; panel d: carboplatin infusion rate; panel e: log of number of cancer cells (horizontal dashed line: detection limit)

drug toxicities due to the 50% reduction in toxicity parameters (k_{vbm_D} and k_{vbm_C}); hence, there is only a small reduction in drug amount compared to the single agent therapy. When docetaxel and carboplatin are used in combination for Patient 3, the tumor size reaches the detection limit after 43 days. These combination therapy treatment schedules show that the algorithm is able to adjust the drug doses in combination in order to maximize tumor elimination without violating toxicity constraints.

4.6.8.3 Combination Therapy to Track a Tumor Volume Target: The ability of the optimization algorithm to regulate tumor size (*i.e.*, control to target size) is tested using docetaxel and carboplatin in combination. Conceptually, this is related to metronomic chemotherapy [147] , where it is postulated that a small dose of drug can keep cancer in check over long periods of time without toxicity. This alternative formulation instead identifies a therapy that will control the tumor volume to a target size less than the detection limit and hold it there over time using the lowest dose of drug possible. The target tumor volume is set to be 10^3 cells; the resulting problem formulation is shown in Problem 4.50. The algorithm results are shown in Figure 39.

$$
\begin{aligned}
\textit{Objective} \quad &: \quad (4.32) \\
s.t. \quad &: \quad \text{Docetaxel PK:} \quad (3.15) - (3.16) \\
&\qquad \text{Carboplatin PK:} \quad (4.34) - (4.36) \\
&\qquad \text{Combination PD Efficacy:} \quad (4.37) - (4.40) \\
&\qquad \text{Combination PD Toxicity:} \quad (3.18) - (3.26),\ (4.15) - (4.43) \\
&\qquad \text{Combination Toxicity Constraints:} \quad (4.28) - (4.30) \\
&\qquad \text{Logistics:} \quad (4.20),\ (4.21),\ \textit{and}\ (4.47)
\end{aligned}
\tag{4.50}
$$

When the tumor size is significantly greater than the targeted tumor size, the algorithm delivers the maximum allowable drug dose (Figures 39a and d) that does not violate toxicity constraints (Figures 39b) in order to reduce the difference between the tumor size and target (Figures 39e). When the tumor size reaches the target, the algorithm reduces the drug doses

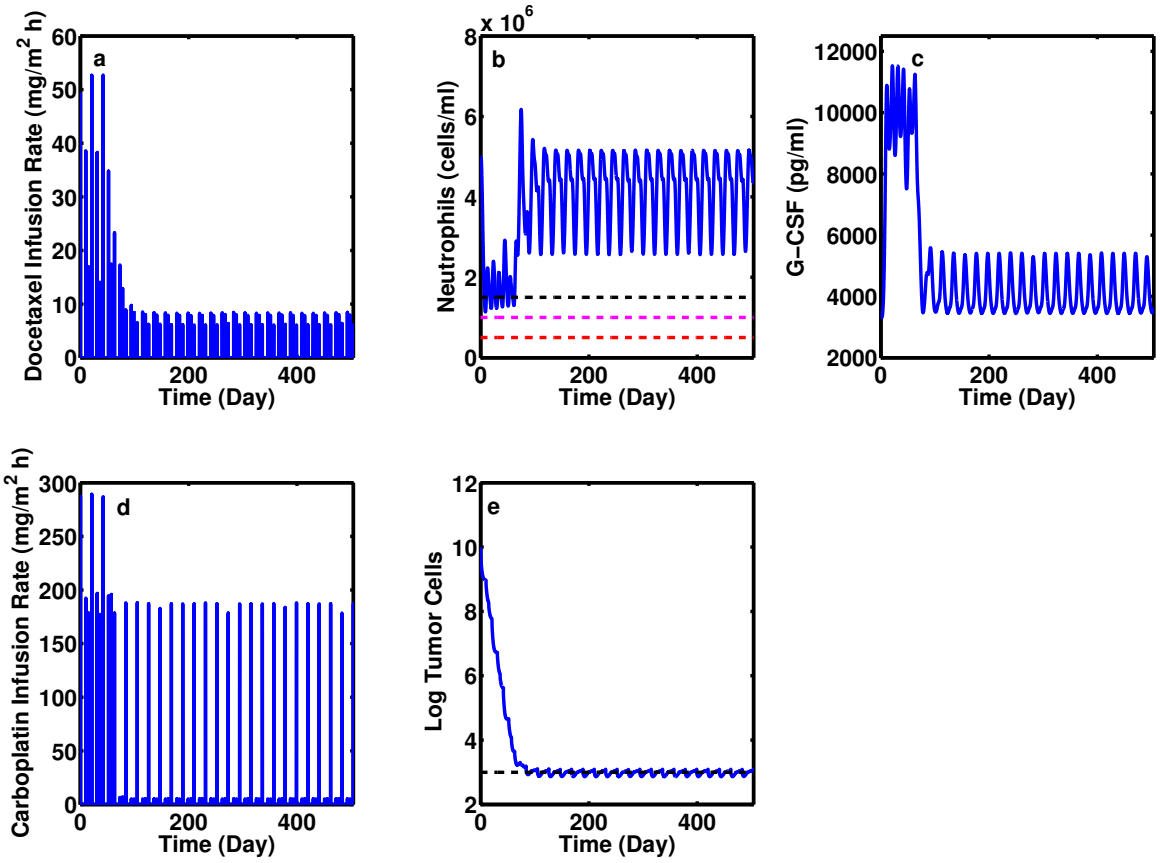

Figure 39: Docetaxel-carboplatin combination schedule for tracking a target tumor volume. Panel a: docetaxel infusion rate; panel b: ANC (horizontal dashed lines: neutropenia levels 2, 3, and 4 from top to bottom); panel c: G-CSF plasma concentration; panel d: carboplatin infusion rate; panel e: log of number of cancer cells (horizontal dashed line: target tumor volume = 10^3 cells)

for both docetaxel and carboplatin so as to maintain the tumor size at target (Figure 39e). Throughout the 500 days of treatment, the ANC level of the patient does not violate the toxicity constraints, as observed in Figure 39b. With the ability to track target tumor sizes using combination chemotherapy, the algorithm demonstrates the flexibility needed to handle different objectives for the design of combination chemotherapy treatments.

4.6.8.4 Drug Resistance in Combination Chemotherapy: The ability of the algorithm to adapt to potential drug resistance is tested by changing the efficacy of docetaxel throughout the treatment. A decrease in docetaxel efficacy, potentially related to the cancer cells developing a resistance to docetaxel, can be achieved by decreasing k_{eff_2} of Equation (eq:XMK) stepwise in 20% increments every 2 cycles starting after cycle 4. The results are shown in Figure 40. The algorithm implementation recalculates a revised optimal treatment schedule after every cycle. The efficacy model parameters for docetaxel are re-estimated cycle-wise, and modifications to the treatment schedule are made to maintain efficacy in the presence of drug resistance. The efficacy of docetaxel changes begin at cycle 5, as shown in Figure 40f. The docetaxel efficacy used by the algorithm is always one cycle behind the patient response to treatment because the algorithm needs a "measurement" (the tumor size deviating above the expected response to treatment, Figure 40e) in order to update the model and alter treatment for the next cycle.

When docetaxel efficacy decreases, the docetaxel and carboplatin schedules are changed in order to maximize tumor elimination rate. In this case, the amount of docetaxel administered is decreased from cycle 5 to cycle 9 with decreasing efficacy of the drug, and no docetaxel is infused when the drug no longer has any effect on tumor elimination (Figure 40a). As the amount of docetaxel infused decreases, the amount of carboplatin infused increases, eventually reaching the maximum single-agent amount that can be administered without violating toxicity constraints, Figures 40b and d.

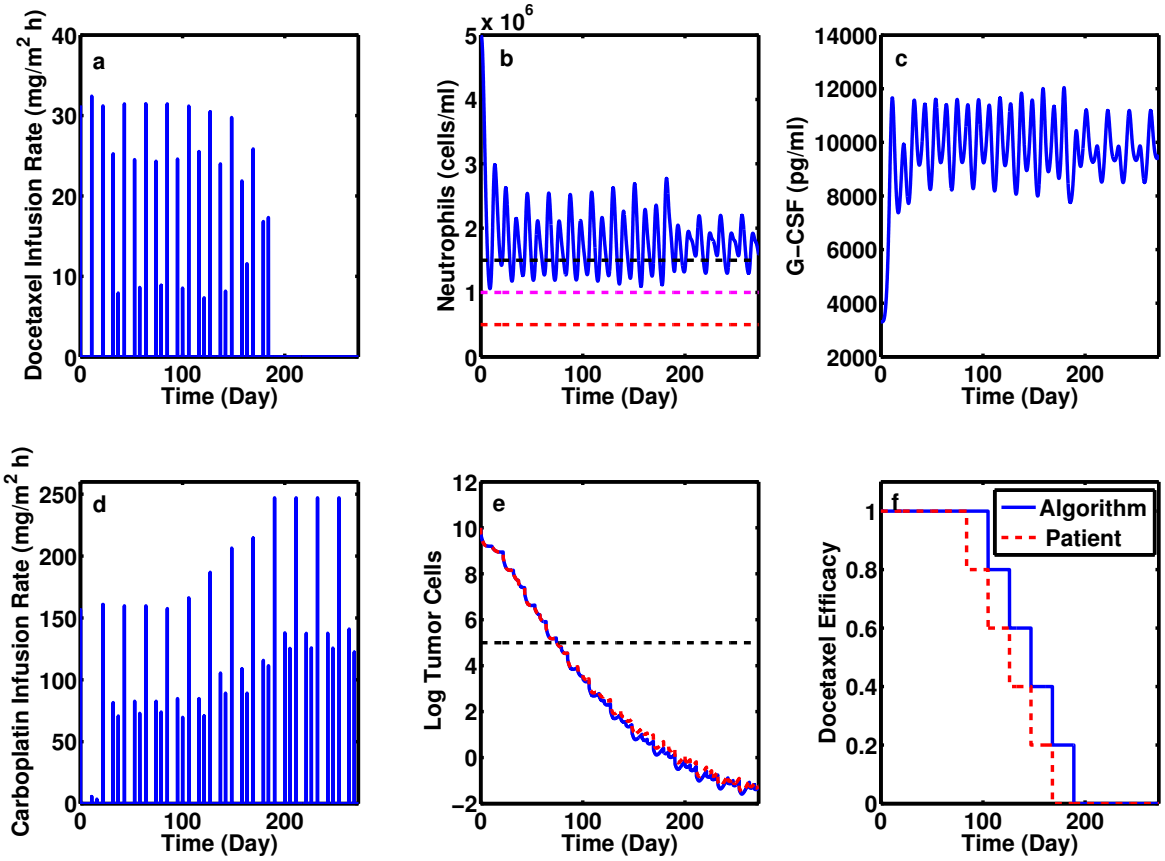

Figure 40: Docetaxel-carboplatin combination schedule with docetaxel resistance. Panel a: docetaxel infusion rate; panel b: ANC (horizontal dashed lines: neutropenia levels 2, 3, and 4 from top to bottom; panel c: G-CSF plasma concentration; panel d: carboplatin infusion rate; panel e: log of number of cancer cells (solid line: algorithm prediction; dashed line: actual patient dynamics; horizontal dashed line: detection limit); panel f: normalized docetaxel efficacy (solid line: algorithm prediction; dashed line: actual patient dynamics)

4.7 DISCUSSION

Chemotherapy scheduling optimization problems have been developed with the goal of aiding clinicians in achieving the best patient outcomes. Using docetaxel as a specific case of a widely utilized chemotherapy agent (both as single-agent and in combination chemotherapies), we posed a generalizable chemotherapy scheduling optimization problem that addresses not only explicit toxicity limits but also other differences between theoretical treatment algorithms and clinical practice. The main adverse effect of docetaxel is myelosuppression resulting in neutropenia. Docetaxel pharmacokinetic, pharmacodynamic, and neutropenia models are incorporated into the optimization algorithm with toxicity constraints of no worse than grade 3 neutropenia acutely, and a week-to-week ANC not worse than neutropenia grade 2. The results shown in Figure 30 and Table 9 demonstrate that the algorithm balances efficacy with the toxicity of docetaxel to yield the same treatment efficacy as current clinical schedules. While simulated patients do not experience grade 3 neutropenia as a result of treatment using our algorithm, patients following the actual clinical schedules experience grade 3 or worse neutropenia (100 mg/m^2 every 3 weeks) or sacrifice some efficacy to avoid severe toxicity (35 mg/m^2 weekly). With clinically motivated constraints, our algorithm has the ability to produce an optimal docetaxel schedule balancing efficacy and toxicity.

Patients respond to chemotherapy differently; therefore an algorithm must have the ability to adjust chemotherapy schedules to capture individual dynamics and design optimal patient-specific treatment schedules. Toxicity constraints limit the amount of drug that can be administered in our algorithm. Therefore, patient toxicity profiles were varied for docetaxel, cisplatin, and carboplatin to test the ability of the algorithm to perform as toxicity constraints were tightened or relaxed over time. When patient toxicity profiles change (Figures 31, 36, 37, and 38), the algorithm maximizes tumor elimination rate for each patient by changing the dosing schedules while ensuring that the toxicity constraints are not violated. The adjustment of drug dosing schedules to balance efficacy with toxicity for patient-specific dynamics will allow the algorithm to design individual patient schedules and update the schedules if patient dynamics change during treatment.

The problem structure is formulated for ease of implementation and computational efficiency. Pharmacokinetic, pharmacodynamic, and toxicity models are explicitly incorporated into the algorithm to optimize the patient chemotherapy schedule. The generalizability of the algorithm is tested with two different combination chemotherapies: docetaxel-cisplatin and docetaxel-carboplatin. Docetaxel and cisplatin have different toxicity profiles, which increases the number of variables and constraints (20% and 110% respectively) in the algorithm – a numerical challenge. As a result, the algorithm takes 2 hours to solve for the docetaxel-cisplatin combination schedule rather than just 1 hour for the docetaxel schedule alone. Docetaxel and carboplatin demonstrate overlapping toxicity, which creates a challenge for the algorithm in finely tuning the treatment schedule by balancing between toxicity and efficacy to achieve the smallest objective function during treatment. The suggested treatment schedules provided by the algorithm for both combinations with different patient dynamics (Figures 36, 37, and 38) confirm that the algorithm can be used to schedule different drug treatments when models of these drugs are available.

Figures 37 and 38 show that when drug efficacy and toxicity are known, the algorithm can design a schedule for each drug to minimize patient treatment time without violating modeled toxicity constraints. In current clinical settings, drugs with overlapping toxicities are avoided in combination chemotherapy so that patients are prevented from experiencing severe toxicities. If two drugs with different mechanisms of action have overlapping toxicities, the algorithm is able to adjust the schedules to ensure that the treatment benefits from the optimal effects of the two drugs. This generalizability and adaptability opens the door for clinicians and scientists to evaluate new combination schedules for drugs with overlapping toxicities that maximize tumor elimination rate. Moreover, when one drug begins to develop drug resistance, the algorithm is able to update the efficacy of the drug to maximize the elimination of the tumor without violating toxicity constraints.

4.8 SUMMARY

Discrepancies between algorithm solutions and clinical practice have prevented scheduling algorithms from becoming helpful aids for the design of chemotherapy schedules. Here we have developed a generalizable and clinically-relevant chemotherapy scheduling algorithm and have shown through docetaxel, docetaxel-cisplatin, and docetaxel-carboplatin examples that it is applicable to current clinical settings. The algorithm is ready to be tested in a clinical environment and assist clinicians in understanding individual patient dynamics and tailoring treatment design to achieve the best patient outcome (short-duration effective treatment without dose-limiting toxicity). With clinical data, the algorithm and models can be validated, extended, and improved into a powerful decision support system for the design of personalized chemotherapy schedules based on individual patient dynamics.

5.0 SUMMARY AND FUTURE RESEARCH

Mathematical models can be utilized to understand disease and patient dynamics. In this thesis, different mathematical models are presented for different diseases ranging from inflammation to chemotherapy-induced myelosuppression. Mathematical models are developed from knowledge of biology resulting in in both detailed mathematical descriptions of biology such as in the case of the neutrophil signaling cascade and simple model structures as seen in the case of the pharmacokinetic model for carboplatin and cisplatin. These models with information about disease dynamics, drug dynamics, and patient responses to treatments can be implemented into model-based control or model-based optimization to help clinicians with patient treatment decision.

Most biologically-based models are limited in implementation in model-based control and model-based optimization due to their complex structures (*e.g.*, large state dimension, large highly-correlated parameter space). However, the advantages of these complex biologically based models are their flexibility in capturing different disease dynamics through the inclusion of different mechanisms acting on the different model states. Using a neutrophil signaling cascade and two different acting mechanisms of the two challenges on the cascade, inflammatory acting on circulating neutrophils and chemotherapy acting on progenitors, the biological-based model of neutrophil signaling cascade was developed and successfully captured the two different dynamics created by inflammatory challenge and chemotherapy induced myelosuppression. The biologically-based model of neutrophils shows that a biologically-based model has a capacity to capture different challenge dynamics basing on their acting mechanisms on the biological cascade.

The large of number states and large number of parameters of biologically-based models often prevent these models from being utilized in model-based control and model-based op-

timization. Depending on the disease of interest, the model reduction method used in this thesis can be applied to reduce a complex biological based model to a simpler structure while still capturing the important dynamics without a loss in accuracy. Moreover, when two or more dynamics are studied in one biological signaling cascade, the reduction method can still be applied to produce a model that preserves all of the dynamics of interests. Through a biologically-based model of neutrophils, we demonstrated that model order reduction and parameter space reduction techniques will result a lower order model with key parameters identified to reserve dynamics of neutrophils after an inflammatory challenge or chemotherapy induced myelosuppression. The simpler model structure with key dynamic parameters identified will make the reduced model to be more easily implemented in model-based control and model-based optimization.

With their predictive ability, mathematical models can be used to aid clinicians in patient specific treatment design through model-based control or model-based optimization. To demonstrate how mathematical models can be utilized for treatment design, a generalizable model-based chemotherapy optimization algorithm is developed to design a clinically relevant dosing schedule with clinically motivated toxic and logistical constraints for docetaxel and its combinations as examples. The algorithm can be extended to different drug and drug combination dynamics to design a variety of patient specific chemotherapy schedules.

This research demonstrates a method for building mathematical models from biological information, reducing them into simpler forms, and utilizing them for optimal patient specific treatment design. This thesis provides an advanced step toward a clinically useful form of a decision support system; however, further research is needed to advance the development of these mathematical models and gain the acceptance of clinicians in using computers to aid treatment design.

5.1 BIOLOGICALLY BASED MODEL DEVELOPMENT AND REDUCTION

An example of a biologically based neutrophil-G-CSF model and its reduced structure shows that biologically based models have the flexibility to capture different dynamical challenges (LPS for fast dynamics and docetaxel for slow dynamics). However, challenges in building biologically based models are the lack of experimental data and an incomplete understanding of the relevant signaling cascades. For instance, we use a simple differential equation to capture the inflammatory response after an LPS challenge. However, this is not the case for the inflammatory signaling cascade. Instead, it is a complex response of inflammatory and anti-inflammatory cytokines that activates neutrophils and returns the immune response to homeostasis. Modeling the biological response of cytokines is a significant challenge due to the incomplete understanding of the role and function of each cytokine in the cascade, the overlapping roles of the cytokines, and a lack of detailed time series data for these cytokines. Moreover, biologically-based models often contain a large number of equations and parameters and identifying these parameter values is difficult. Although biologically-based models are powerful tools to capture different dynamical challenges, there are challenges in building those models due to their complex structures and lack of supporting data.

In our biologically based neutrophil model, we assume that all neutrophil precursors have the same functionality as mature neutrophils. However, studies have shown that neutrophil precursors have different migration and phagocytic properties during an infection [50]. Thus, to apply the model for local infection like in the case of sepsis, different neutrophil populations and their functionality should be considered to accurately capture neutrophil dynamics during a non-LPS inflammatory challenge.

Neutrophil migration and recruitment following an LPS challenge is modeled as a single term, as shown in Equation 2.21, since there is no inflammation causing organ damage like in the case of sepsis. To expand our model to capture patient dynamics during sepsis, neutrophil migration and recruitment have to be considered in greater detail. In sepsis, in addition to recruitment to the site of infection, neutrophils are misdirected toward the lungs, kidneys, and the liver, where they cause organ damage that can eventually lead to patient mortality

if no intervention action is taken. One of the difficulties in modeling sepsis is accounting for tissue damage. Most of the current techniques model damage as a heuristic function of neutrophils and cytokines present in the local tissue. When this heuristic function value is larger than some threshold then local tissue damage occurs. Although these heuristic models are able to represent certain sepsis dynamics, they are unable to explain why certain patients survive and why othersdie as a result ofsepsis. Understanding why neutrophils are misdirected to select organs and how they cause local tissue damage would increase the accuracy in capturing the dynamics of sepsis.

Neutrophil dynamics are the only consideration in our model for an LPS challenge. Although neutrophils are one of the key players in innate immune response, neutrophil dynamics are not the only factor that should be considered when trying to capture the biological response to sepsis. Other immune response dynamics also contribute to the mechanism of sepsis and play roles in the patient recovery process. The activation of macrophages and their associated cytokine secreting mechanisms are important during the initial phase of a local infection. The migration of cytokines and their activation of the endothelial layer are important factors in describing the neutrophil migration mechanism to different organs. The neutrophil (over-)activation by cytokines during sepsis also contributes to the outcome. These processes and mechanisms can be added to our current neutrophil model to better represent the systemic inflammatory response of sepsis and to better capture patient dynamics during sepsis. Ultimately, a detailed biologically-based model of the innate response should be able to predict patient outcome and to be used as a tool for sepsis treatment design.

5.2 CLINICALLY RELEVANT CHEMOTHERAPY SCHEDULING OPTIMIZATION

The chemotherapy optimization algorithm develops clinically-relevant personalized chemotherapy schedules for docetaxel as a single-agent and its use in combination with carboplatin or cisplatin. The schedules returned by the algorithm retain the same efficacy as current clinical schedules with fewer adverse effects. For treatments involving two drugs with different

toxicities, the algorithm solves these schedules without violating either logistical constraints or drug toxicity constraints. For treatments with two drugs having the same toxicity, the algorithm is able to maximize tumor elimination by finely tuning each drug dose without violating constraints. The current algorithm brings a computer aided chemotherapy treatment system closer to the clinical setting without significantly modifying current standard treatment practices.

The current algorithm explicitly includes clinically-motivated toxicity constraints as represented by measurable quantities, which is a departure from many previously developed chemotherapy scheduling algorithms. This improvement helps aid acceptance of computer-aided chemotherapy scheduling by current clinical practitioners. Further improvements can be made in the current algorithm by increasing its accuracy in capturing tumor dynamics and (dis)validating the generalizability and the performance of the algorithm. The algorithm applicability should be extended to different drugs and drug combinations beyond those examined in this thesis. For instance, a three-drug combination should be studied to test the algorithm for its extensibility. A simple three drug combination test could be docetaxel, cisplatin, and 5-fluorouracil (5-FU), since docetaxel and cisplatin dynamics are built into the current algorithm. Examining alternate drug combinations with different toxicities would help to test the algorithms extensibility and robustness. In our algorithm, the toxicity constraints are set at low toxicity grades to prevent patients from experiencing severe toxicities. However to design the specific toxicity constraints for each drug, a detailed study is needed to evaluate the cost of high toxicity constraints, the extent of treatment, and patient quality of life after the treatment (survial rate, remission rate, and recurrence rate). These analyses will help to design improved toxicity constraints for the best patient outcomes.

Our algorithm currently uses clinically-relevant toxicities for each drug to impose toxicity constraints. The results show that in most patients, toxicity restricts the amount of drug that can be delivered and the timing of administration (as determined by patient neutrophil recovery dynamics). Most of currently used chemotherapeutic drugs have more than one toxic effect on patients during chemotherapy. For instance, docetaxel and carboplatin induce both anemia and thrombocytopenia. Cisplatin also causes nerve damage in addition to kidney damage. Including additional clinically-relevant toxicity models and constraints

would allow the algorithm to more accurately predict toxic effects and produce a scheduling solution that maintains a high degree of efficacy while limiting or avoiding toxicity-induced side-effects.

Drug effects on the tumor term in the current algorithm are modeled as a bilinear function with respect to tumor size and drug concentration inside the tumor. The bilinear kill term is derived from *in vivo* experiments, where cancer cells are incubated in petri dishes at different drug concentrations. The drug concentration that kills 50% of the cells in 24 hours is called the half maximal inhibitory concentration IC-50 level. The IC-50 data are used to calculate the rate constant for tumor elimination when the drugs are present within the tumor. While .descriptive, the bilinear kill term is not an ideal functionality for modeling drug effects on tumor size in a system of ordinary different equations, especially for *in vitro* system , because the drug concentration changes with time in animal or human body. Improvements in the tumor elimination term can increase the accuracy of the algorithm in capturing patient dynamics. Understanding the drug acting mechanism on tumor cells and developing a detail model to capture this mechanism will increase the accuracy of the algorithm in capturing tumor dynamics during chemotherapy

Cancer cells often develop drug resistance during chemotherapy, and the current tumor elimination model does not account for this effect. Understanding how cancer cells respond to chemotherapy and eventually become resistant to chemotherapeutic drugs would increase the model accuracy in predicting tumor dynamics compared to actual tumor dynamics.

The continuity assumption is made in this current algorithm to model tumor growth dynamics. This assumption is valid when tumor size is larger than 10^4 cells. However, when the tumor size is smaller than 10^3 cells, this assumption is no longer valid [158]. At this size, tumor growth follows a stochastic process. The tumor can grow to be larger (recurrence), or can be eliminated from the body (cure). The stochastic tumor growth process for small tumors can be further examined to explain the different cancer responses observed in patients.

In addition to improvements of the models within the algorithm and a deeper understanding of the biological dynamics of tumors and their interaction with chemotherapeutic drugs, the validation of the algorithm with actual clinical data is necessary to bring the algorithm forward to deployment in clinical settings. The first validation step is the comparison

of tumor growth dynamics and chemotherapeutic effects to actual clinical data. Current published data do not include the time series data of tumor decrease during chemotherapy. Obtaining tumor size time series data for different chemotherapeutic drugs will help to calibrate the tumor model and develop a suitable function for the tumor elimination rate.

The second validation step is to ensure that patient toxicity profiles match the toxicity model predictions produced by the optimization algorithm. Most of the clinical data currently reported in the literature are the overall nadir toxicity of the patient during chemotherapy. However, patients experience different toxicity levels throughout their treatments. Patient toxicity time series measurements can be used to update patient toxicity models and design the next treatment based on the available dynamics.

The first and second validation steps can be performed without additional clinical trials. Data previously and currently obtained can be reformatted per patient treatment and be used to calibrate the algorithm and evaluate its performance. Drug concentration inside a tumor is an important factor in determining the efficacy of the drug. A clinical trial with head and neck cancer patients can be run to measure drug concentration in tumors, because biopsies of the head-and-neck can be performed less invasively in these patients. These measurements will explain drug transport from plasma to tumor and increase the accuracy of the tumor elimination rate prediction of the model.

A final validation step is to compare the algorithm with current clinical treatment schedules in performance for both efficacy and toxicity measures. The efficacy of the algorithm should be not inferior to the current clinical schedules while decreasing the number and/or frequency of adverse effects compared to current clinical schedules. When the algorithm schedules have comparable efficacy and superior toxicity profiles than current clinical standards, a graphical user interface (GUI) needs to be developed to aid clinicians in deploying this computer-aided treatment design tool. The GUI should include, but not be limited to, patient information (sex, age, height, weight, medical history, etc.), tumor volume, toxicity measurement data (ANC, creatinine level, etc.), and other relevant information. The output of the GUI should be the recommended drug dosage and the predicted tumor and toxicity profiles of the patient. The GUI with the underlying optimization algorithm will help clinicians visualize the patient dynamics throughout chemotherapy and suggest the next

treatment schedule that maximizes the tumor elimination rate without causing severe toxicity. The clinically ready, clinician friendly and patient tailorable chemotherapy scheduling algorithm will help clinicians to design patient-specific treatments with the hope of improving patient outcomes during chemotherapy.

APPENDIX A

FLORIAN *ET AL.* DOCETAXEL PBPK MODEL AND PARAMETERS

The complete set of equations for the docetaxel PBPK model are shown below [5]: Venous Blood:

$$\begin{aligned}\frac{dC_{ven}}{dt} &= \frac{1}{V_{ven}(1-f_{hem})}(F_{in}C_{in} - F_{tot}C_{ven}) + \frac{f_{hem}}{(1-f_{hem})}k_{rbcplas}C_{rbcv} \\ &\quad -k_{plasrbc}f_{unb}C_{ven} + \frac{u(t)}{V_{ven}(1-f_{hem})} \qquad (A.1)\\ \frac{dC_{rbcv}}{dt} &= -k_{rbcplas}C_{rbcv} + \frac{(1-f_{hem})}{f_{hem}}k_{plasrbc}f_{unb}C_{ven} \qquad (A.2)\end{aligned}$$

Lung:

$$\begin{aligned}\frac{dC_{lv}}{dt} &= \frac{F_{tot}}{V_{lv}}(C_{ven} - C_{lv}) - k_{lve}f_{unb}C_{lv} + \frac{V_{le}}{V_{lv}}k_{lev}C_{le} \qquad (A.3)\\ \frac{dC_{le}}{dt} &= \frac{V_{lv}}{V_{le}}k_{lve}f_{unb}C_{lv} - k_{lev}C_{le} + k_{bind_{out}}C_{lb} - k_{bind_{in}}C_{le} \qquad (A.4)\\ \frac{dC_{lb}}{dt} &= -k_{bind_{out}}C_{lb} + k_{bind_{in}}C_{le} \qquad (A.5)\end{aligned}$$

Arterial Blood:

$$\begin{aligned}\frac{dC_{art}}{dt} &= \frac{1}{V_{art}(1-f_{hem})}(F_{tot}C_{lv} - F_{tot}C_{art}) + \frac{f_{hem}}{(1-f_{hem})}k_{rbcplas}C_{rbca} \\ &\quad -k_{plasrbc}f_{unb}C_{art} \qquad (A.6)\\ \frac{dC_{rbca}}{dt} &= -k_{rbcplas}C_{rbca} + \frac{(1-f_{hem})}{f_{hem}}k_{plasrbc}f_{unb}C_{art} \qquad (A.7)\end{aligned}$$

Gut:

$$\frac{dC_{gv}}{dt} = \frac{F_g}{V_{gv}}(C_{art} - C_{gv}) \tag{A.8}$$

Brain:

$$\frac{dC_{bv}}{dt} = \frac{F_b}{V_{bv}}(C_{art} - C_{bv}) - k_{bve}f_{unb}C_{bv} + \frac{V_{be}}{V_{bv}}k_{bev}C_{be} \tag{A.9}$$

$$\frac{dC_{be}}{dt} = \frac{V_{bv}}{V_{be}}k_{bve}f_{unb}C_{bv} - k_{lev}C_{be} + k_{bind_{out}}C_{bb} - k_{bind_{in}}C_{be} \tag{A.10}$$

$$\frac{dC_{bb}}{dt} = -k_{bind_{out}}C_{bb} + k_{bind_{in}}C_{be} \tag{A.11}$$

Spleen:

$$\frac{dC_{sv}}{dt} = \frac{F_s}{V_{sv}}(C_{art} - C_{sv}) - k_{sve}f_{unb}C_{sv} + \frac{V_{se}}{V_{sv}}k_{sev}C_{se} \tag{A.12}$$

$$\frac{dC_{se}}{dt} = \frac{V_{sv}}{V_{se}}k_{sve}f_{unb}C_{sv} - k_{sev}C_{se} + k_{bind_{out}}C_{sb} - k_{bind_{in}}C_{se} \tag{A.13}$$

$$\frac{dC_{sb}}{dt} = -k_{bind_{out}}C_{sb} + k_{bind_{in}}C_{se} \tag{A.14}$$

Liver:

$$\begin{aligned}\frac{dC_{liv}}{dt} &= \frac{1}{V_{liv}}(F_{li}C_{art} + F_gV_{gv} + F_sC_{sv} - (F_g + F_s + F_{li})C_{liv}) - k_{live}f_{unb}C_{liv} \\ &\quad + \frac{V_{lie}}{V_{liv}}k_{liev}C_{lie}\end{aligned} \tag{A.15}$$

$$\frac{dC_{lie}}{dt} = \frac{V_{liv}}{V_{lie}}k_{live}f_{unb}C_{liv} - k_{liev}C_{lie} + k_{bind_{out}}C_{lib} - k_{bind_{in}}C_{lie} - k_{clli}C_{lie} \tag{A.16}$$

$$\frac{dC_{lib}}{dt} = -k_{bind_{out}}C_{lib} + k_{bind_{in}}C_{lie} \tag{A.17}$$

Kidney:

$$\frac{dC_{kv}}{dt} = \frac{F_k}{V_{kv}}(C_{art} - C_{kv}) - k_{kve}f_{unb}C_{kv} + \frac{V_{ke}}{V_{kv}}k_{kev}C_{ke} \tag{A.18}$$

$$\frac{dC_{ke}}{dt} = \frac{V_{kv}}{V_{ke}}k_{kve}f_{unb}C_{sv} - k_{kev}C_{ke} + k_{bind_{out}}C_{kb} - k_{bind_{in}}C_{ke} \tag{A.19}$$

$$\frac{dC_{kb}}{dt} = -k_{bind_{out}}C_{kb} + k_{bind_{in}}C_{ke} \tag{A.20}$$

Muscle:

$$\frac{dC_{mv}}{dt} = \frac{F_m}{V_{mv}}(C_{art} - C_{mv}) - k_{mve}f_{unb}C_{mv} + \frac{V_{me}}{V_{mv}}k_{mev}C_{me} \quad (A.21)$$

$$\frac{dC_{me}}{dt} = \frac{V_{mv}}{V_{me}}k_{mve}f_{unb}C_{mv} - k_{mev}C_{me} + k_{bind_{out}}C_{mb} - k_{bind_{in}}C_{me} \quad (A.22)$$

$$\frac{dC_{mb}}{dt} = -k_{bind_{out}}C_{mb} + k_{bind_{in}}C_{me} \quad (A.23)$$

Fat:

$$\frac{dC_{fv}}{dt} = \frac{F_f}{V_{fv}}(C_{art} - C_{fv}) - k_{fve}f_{unb}C_{fv} + \frac{V_{fe}}{V_{fv}}k_{fev}C_{fe} \quad (A.24)$$

$$\frac{dC_{fe}}{dt} = \frac{V_{fv}}{V_{fe}}k_{fve}f_{unb}C_{fv} - k_{fev}C_{fe} + k_{bind_{out}}C_{fb} - k_{bind_{in}}C_{fe} \quad (A.25)$$

$$\frac{dC_{fb}}{dt} = -k_{bind_{out}}C_{fb} + k_{bind_{in}}C_{fe} \quad (A.26)$$

Tumor:

$$\frac{dC_{tv}}{dt} = \frac{F_t}{V_{tv}}(C_{art} - C_{tv}) - k_{tve}f_{unb}C_{tv} + \frac{V_{te}}{V_{tv}}k_{tev}C_{te} \quad (A.27)$$

$$\frac{dC_{te}}{dt} = \frac{V_{tv}}{V_{te}}k_{tve}f_{unb}C_{tv} - k_{tev}C_{te} + k_{bind_{out}}C_{tb} - k_{bind_{in}}C_{te} \quad (A.28)$$

$$\frac{dC_{tb}}{dt} = -k_{bind_{out}}C_{tb} + k_{bind_{in}}C_{te} \quad (A.29)$$

Heart:

$$\frac{dC_{hv}}{dt} = \frac{F_t}{V_{hv}}(C_{art} - C_{hv}) - k_{hve}f_{unb}C_{hv} + \frac{V_{he}}{V_{hv}}k_{hev}C_{he} \quad (A.30)$$

$$\frac{dC_{he}}{dt} = \frac{V_{hv}}{V_{he}}k_{hve}f_{unb}C_{hv} - k_{hev}C_{he} + k_{bind_{out}}C_{hb} - k_{bind_{in}}C_{he} \quad (A.31)$$

$$\frac{dC_{hb}}{dt} = -k_{bind_{out}}C_{hb} + k_{bind_{in}}C_{he} \quad (A.32)$$

Other:

$$\frac{dC_{ov}}{dt} = \frac{F_o}{V_{ov}}(C_{art} - C_{ov}) - k_{ove}f_{unb}C_{ov} + \frac{V_{oe}}{V_{ov}}k_{oev}C_{oe} \quad (A.33)$$

$$\frac{dC_{oe}}{dt} = \frac{V_{ov}}{V_{oe}}k_{ove}f_{unb}C_{ov} - k_{oev}C_{oe} + k_{bind_{out}}C_{ob} - k_{bind_{in}}C_{oe} \quad (A.34)$$

$$\frac{dC_{ob}}{dt} = -k_{bind_{out}}C_{ob} + k_{bind_{in}}C_{oe} \quad (A.35)$$

Table A.1: Parameter values (P) for the PBPK model [5]

P.	Value	Unit	P.	Value	Unit
k_{live}	10.253	min^{-}1	k_{liev}	0.0965	min^{-}1
k_{clli}	0.1023	min^{-}1	k_{lve}	0.2662	min^{-}1
k_{lev}	0.0365	min^{-}1	k_{tve}	0.110	min^{-}1
k_{tev}	0.0006	min^{-}1	k_{mve}	0.5952	min^{-}1
k_{mev}	0.0158	min^{-}1	k_{sve}	1.8667	min^{-}1
k_{sev}	0.0445	min^{-}1	k_{hve}	2.246	min^{-}1
k_{hev}	0.0495	min^{-}1	k_{fve}	0.2162	min^{-}1
k_{fev}	0.0079	min^{-}1	k_{kve}	2.924	min^{-}1
k_{kev}	0.1859	min^{-}1	k_{bve}	0.0547	min^{-}1
k_{bev}	0.0573	min^{-}1	k_{ove}	0.7451	min^{-}1
k_{oev}	0.0099	min^{-}1	$k_{rbcplas}$	0.00128	min^{-}1
$k_{plasrbc}$	0.000348	min^{-}1	$k_{bind_{in}}$	0.001015	min^{-}1
$k_{bind_{out}}$	0.000895	min^{-}1	f_{unb}	0.05	-
f_{hem}	0.45	-	F_{li}	0.45	L/min
V_{li}	1.80	L	f_{li}	0.16	-
F_l	5.60	L/min	V_l	0.53	L
f_l	0.30	-	F_t	0.03	L/min
V_t	0.2	L	f_t	0.05	-
F_g	1.13	L	V_g1.13	L	
F_m	0.59	L/min	V_m	28.0	L
f_m	0.03	-	F_s	0.02	L/min
V_s	0.18	L	f_s	0.20	-
F_h	0.26	L/min	V_h	0.33	L
f_h	0.02	-	F_f	0.74	L/min
V_f	15.0	L	f_f	0.03	-
F_k	1.24	L/min	V_k	0.31	L

Table A.1 (continue)

f_k	0.24	-	F_b	0.78	L/min
V_b	1.40	L	f_b	0.04	-
F_o	0.36	L/min	V_o	15.8	L
f_o	0.05	-	F_tot	5.60	L/min
V_{ven}	3.318	L	V_art	2.212	L

APPENDIX B

ADDITIONAL OPTIMIZATION ALGORITHM RESULTS

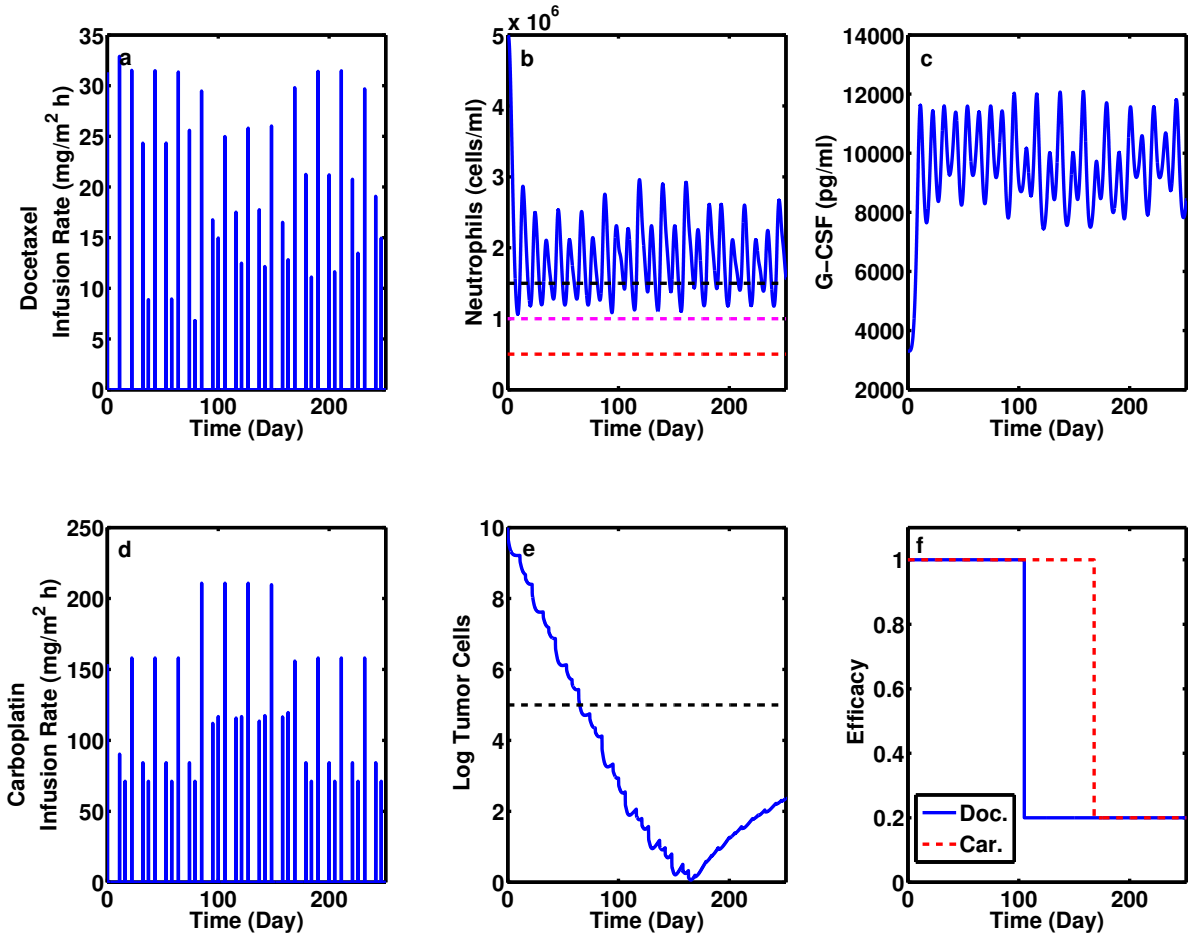

Figure B.1: Algorithm treatment schedule for changing drug efficacy during treatment.Panel a: docetaxel infusion rate; panel b: ANC neutrophil count (horizontal dashed lines: neutropenia levels 2,3,and 4 from top to bottom); panel c: G-CSF plasma concentration; panel d:carboplatin infusion rate; panel e: log of number of cancer cells (horizontal dashed line: tracking target); pane f: normalized drug efficacy (solid line: docetaxel, dashed line: carboplatin)

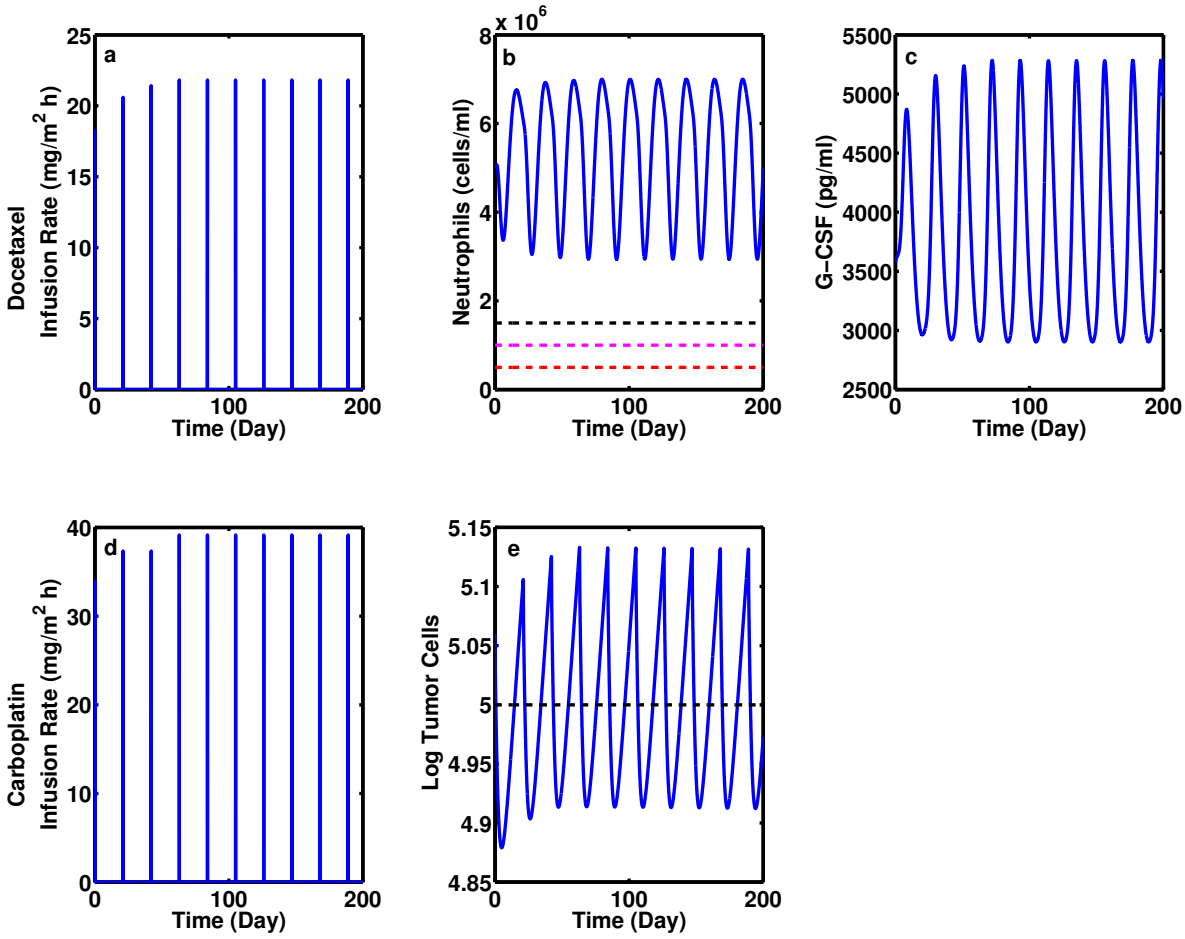

Figure B.2: Docetaxel-carboplatin combination schedule per 3 weeks for targeted tumor tracking. Panel a: docetaxel infusion rate; panel b: ANC neutrophil count (horizontal dashed lines: neutropenia levels 2,3,and 4 from top to bottom); panel c: G-CSF plasma concentration; panel d:carboplatin infusion rate; panel e: log of number of cancer cells (horizontal dashed line: tracking target)

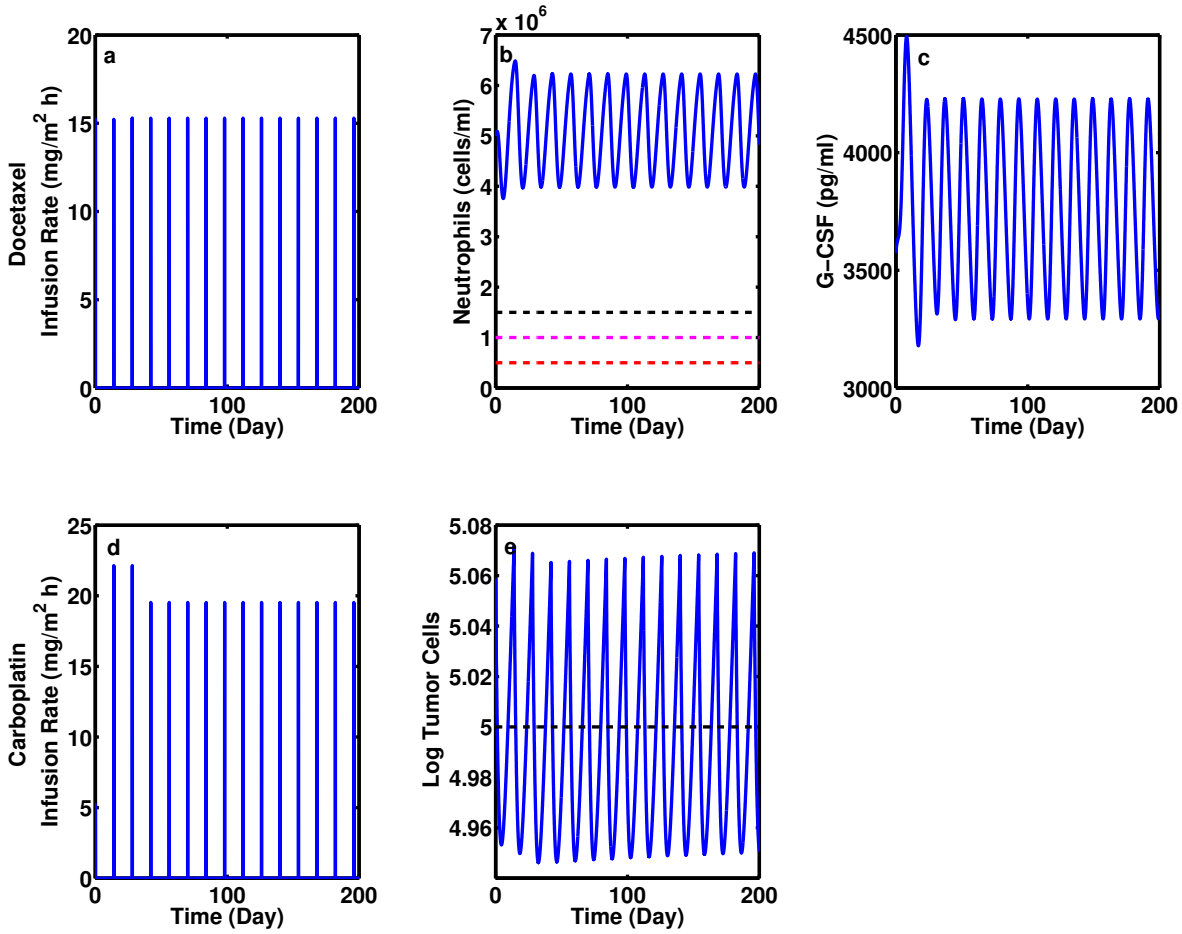

Figure B.3: Docetaxel-carboplatin combination schedule per 2 weeks for targeted tumor tracking. Panel a: docetaxel infusion rate; panel b: ANC neutrophil count (horizontal dashed lines: neutropenia levels 2,3,and 4 from top to bottom); panel c: G-CSF plasma concentration; panel d:carboplatin infusion rate; panel e: log of number of cancer cells (horizontal dashed line: tracking target)

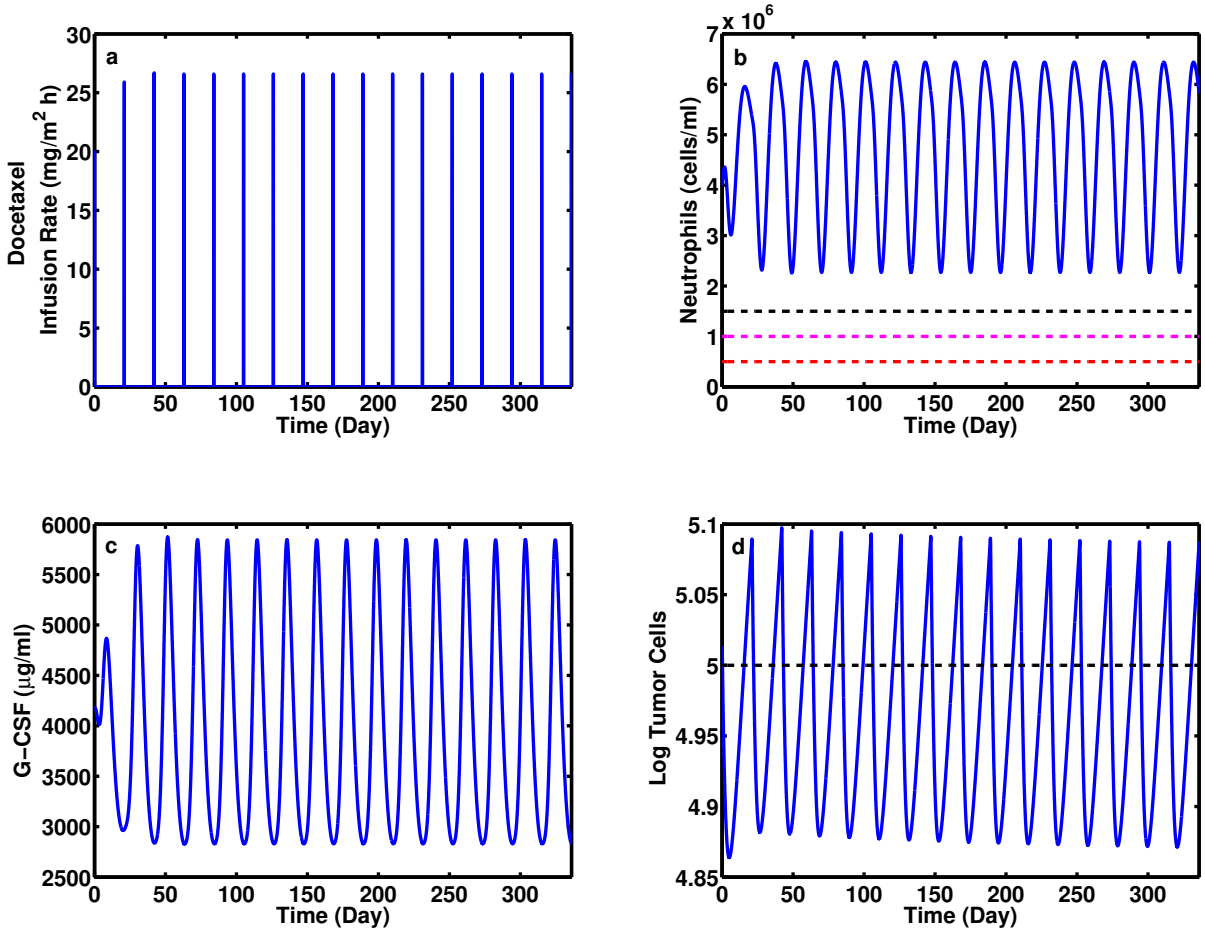

Figure B.4: Docetaxel schedule per 3 weeks for targeted tumor tracking. Panel a: drug infusion rate; panel b: ANC neutrophil count (horizontal dashed lines: neutropenia levels 2,3,and 4 from top to bottom); panel c: G-CSF plasma concentration; panel d: log of number of cancer cells (horizontal dashed line: tracking target)

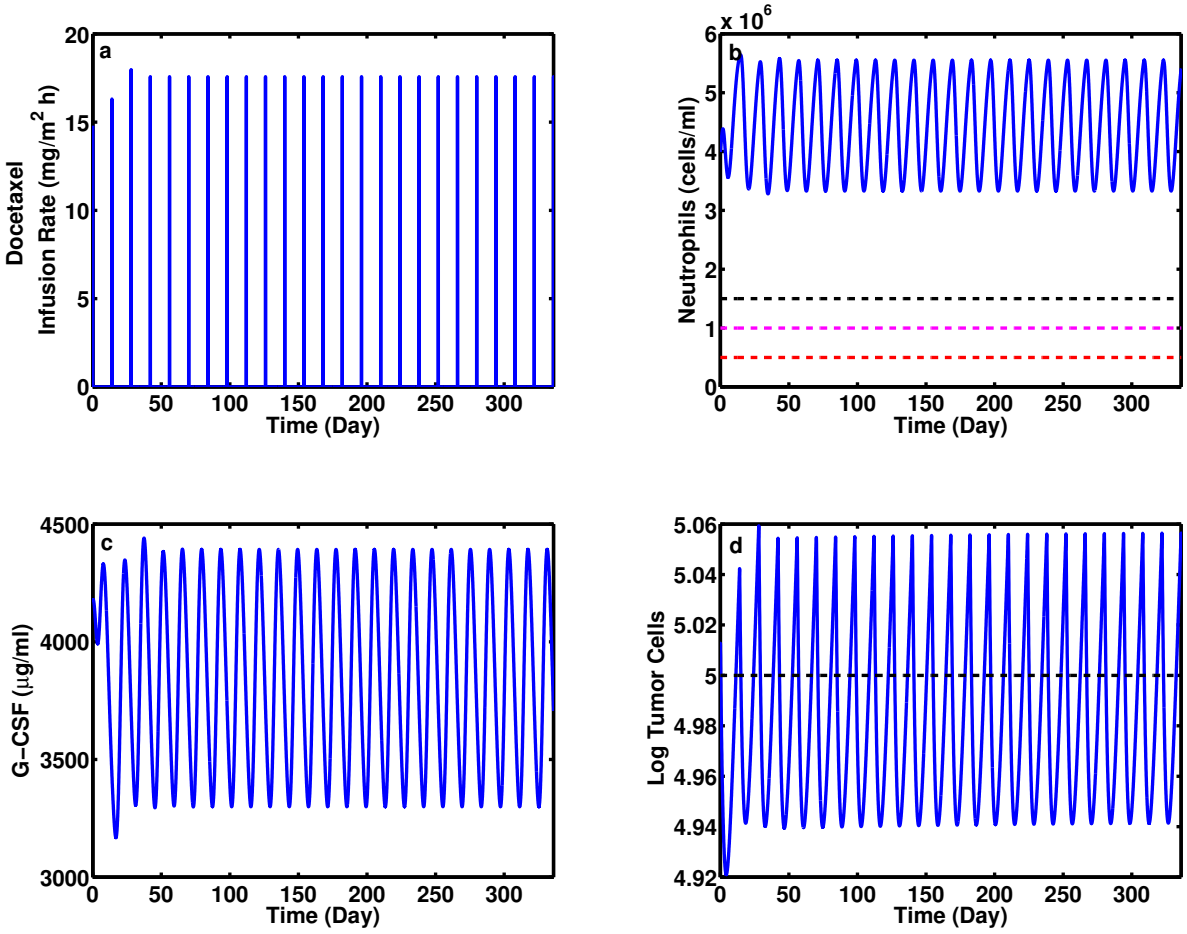

Figure B.5: Docetaxel schedule per 2 weeks for targeted tumor tracking. Panel a: drug infusion rate; panel b: ANC neutrophil count (horizontal dashed lines: neutropenia levels 2,3,and 4 from top to bottom); panel c: G-CSF plasma concentration; panel d: log of number of cancer cells (horizontal dashed line: tracking target)

APPENDIX C

DATA DRIVEN GLUCOSE-INSULIN DYNAMICS MODELING FOR CRITICALLY ILL PATIENT

C.1 GLUCOSE-INSULIN DYNAMICS IN CRITICALLY ILL PATIENTS REVIEW

Patients in intensive care units (ICUs) often exhibit irregular blood glucose levels due to the changing of the bodys dynamics in response to stress[159]. In critically ill patients glucose dynamics are altered by changes in hormone responses, inflammatory responses to an injury or surgery, and external medication [160, 161, 162]. These internal and external stimuli cause decreasing insulin sensitivity in the body[163], decreasing insulin production[160], and increasing endogenous glucose production [164]. The irregular glucose-insulin dynamics exhibited by these patients requires clinicians to intervene and tightly control patient glucose within a specific range.

In a healthy person, blood glucose is homeostatically regulated between 70 mg/dL and 120 mg/dL which is defined as the normoglycemic range [159]. In the ICU, patient blood glucose is often controlled between 180 mg/dL and 200 mg/dL which is defined as the hyperglycemic range [159]. Controlling patients blood glucose in the hyperglycemic range decreases the risk of moderate and severe hypoglycemia. When blood glucose drops to hypoglycemic ranges morbidity and mortality rates increase in the ICU. Bellomo *et al.* showed that of 4946 patients in their study, 1109 patients experienced hypoglycemia, and hospital mortality was 36.6 % for these patient compared with 19.7% in those did not experience hypoglycemia

[165]. Moreover, a study by Egi *et al.* showed that decreased blood glucose variability also decreased the risk of death [166]. Thus, controlling patients blood glucose in a specific range would help to reduce mortality and morbidity, especially when hypoglycemia can be avoided.

C.1.1 Targeted Glucose Control in ICUs

Targeted glucose control in the ICU was first introduced by Van den Bergh *et al.* in 2001 [159]. In this study, a total of 1548 patients were randomly distributed between two treatments: intensive insulin therapy, where blood glucose levels were maintained between 80 mg/dL and 110 mg/dL or conventional treatment where blood glucose levels were maintained between 180 mg/dL and 200 mg/dL. The results showed that intensive insulin therapy reduced mortality in the ICU from 8.0% with conventional treatment to 4.6% with intensive treatment. The benefit of intensive insulin therapy showed the greatest value in reducing mortality associated with death due to multi-organ failure with a proven septic focus. The authors concluded that maintaining blood glucose between 80 mg/dL and 110 mg/dL reduced morbidity and mortality among critically ill patients in ICUs.

Since 2001, various authors have been studying targeted glucose in critically ill patients and how it impacts patient outcomes in ICUs [167, 168, 169]. Van den Bergh *et al.* performed a similar trial, in 2006 in the ICU of the same hospital [170]. The results show that there is no significant reduction in hospital mortality. However, a reduction in morbidity was shown through a reduction of mechanical ventilation usage time, acute kidney injury, and of patient stay duration in the ICU and hospital.

The first multicenter trial to study the impact of targeted glucose control in patients with severe sepsis was undertaken in 18 academic hospitals in Germany and was publish by Brunkhorst *et al.* [167]. The trial was stopped early because the number hypoglycemic incidents increased in patients who underwent targeted glucose control. There was no significant evident of improved mortality on either the 28th or 90th day mortality evaluation among two groups. Despite this result, in 2008 Dellinger *et al.* published an international guidelines for management of severe sepsis and septic shock in which targeted glucose control is recommended[168].

Another multicenter study was published by Preiser *et al.* in 2009 [169]. The study compared the effect of targeted glucose control and conventional glucose control (140-180 mg/dL) on the mortality of patients admitted to 21 medical surgical ICUs. The original study design was to recruit 3500 patients; however, the study was stopped at 1078 patients due to the high number of protocol violations. The trial also reported no significant difference in ICU mortality between the two groups. An increase in hypoglycemic incident rates was observed in the targeted glucose control group.

The Normal Glycemia in Intensive Care Evaluation-Survival Using Glucose Algorithm Regulation (NICE-SUGAR) study was published in 2009 and changed the recommendation for glucose control [171]. The NICE-SUGAR study evaluated the 90-day mortality rate in 6104 critically ill patients from 42 hospitals in Australia, New Zealand, Canada, and the United States. Among 6022 available patient outcomes, targeted glucose control showed an increased in risk of death (27.5% vs. 24.9%).

These clinical trials show contradicting results in targeted glucose controls impact on mortality. However, these studies agree that there is a risk of increasing hypoglycemic incidents when patients undergo targeted glucose control. Patients who experienced hypoglycemic incidents have been shown to have an increased mortality rate compared to patients that did not experience hypoglycemic incidents. Blood glucose variability also showed an association in patient outcome. Increased blood glucose variability increased the risk of death. With better glucose control systems where hypoglycemia can be avoided and patient blood glucose variability can be reduced, targeted glucose control can be beneficial in improving patient outcome by reducing mortality and morbidity.

C.1.2 Glucose-Insulin Dynamics Models

Mathematical models proposed in the literature have attempted to capture glucose-insulin dynamics, including the Intravenous Gluocse Tolerance Test (IVGTT), Oral Glucose Test (OGTT), and Frequently Sampled Intravenous Glucose Tolerance Test (FSIGT) [172, 173, 174, 175]. Bergman *et al.* were the first to model glucose-insulin dynamics using a minimal model structure, in the early eighties [9]. The three states model describes the dynamics

of glucose and insulin after an IVGTT. In this model, the authors introduced the idea of insulin sensitivity which was varied to capture the differences in glucose and insulin dynamics among healthy and obese populations. The same authors have further published papers to complete, test, and validate the results of the minimal model [174, 176, 175]. The model has been a benchmark for mathematical models of glucose-insulin dynamics.

Different variations and extensions of the minimal model have been published to capture glucose-insulin dynamics for both diabetic and non-diabetic population. According the Bergman *et al.*, in their perspective in 2007, there are approximately 50 major studies published per year and more than 500 papers can be found in the literature which involve the minimal model [176]. Tolić *et al.* extended the minimal model to a six-state model to capture the delay effect of insulin on hepatic glucose production [177]. Moreover, the insulin release is broken down into two states to represent the delay effects of glucose on insulin production. The model simulated circadian insulin secretion oscillation.

Gaetano *et al.* proposed a two-state delay differential equation model where remote compartments which mediate the insulin-dependent glucose uptake were removed. In the model, the endogenous insulin release is proportional to the average glucose concentration over b minutes following time t [172]. The model was calibrated and validated by means of real data from a standard IVGTT procedure. After the Gaetano *et al.* model, subsequent models with similar structure have been published and validated for different data sets. These DDE models claim superior performance during IVGTT but have limited extensibility to long term glucose-insulin dynamics.

The Bergman minimal model structure has been widely used to capture glucose-insulin dynamics for both diabetic and non-diabetic patient populations. Roy and Parker published the extend minimal model to include the dynamics of free fatty acid (FFA) for type I diabetic patients[178]. There is no endogenous insulin production in the model; the only insulin source is intravenous insulin delivery. The model included two new remote states to represent the insulin effect on FFA dynamics and FFA effect on glucose dynamics. The model captured *in vivo* data published from different studies. By incorporating the FFA dynamics and its effects on plasma glucose, the models ability to predict glucose concentration dynamics after a mixed meal (carbohydrate and fat) were increased.

Using the extended minimal model as the core structure for glucose-insulin dynamics, Roy and Parker extended the model to capture mixed meals as a disturbance [179]. The model has three additional states to represent the input from a meal: proteins, fats, and carbohydrates. In the model, protein is converted to a glucose equivalent to evaluate its impact on glucose-insulin dynamics. The model was validated with experimental data from mixed meal tolerance test. The model was then subjected to a controller algorithm to evaluate the linear control performance with mixed meal disturbance rejection. With a long term goal of developing closed-loop controllers to regulate blood glucose, it is necessary to develop accurate models with easily identifiable parameters. The extended minimal model with mixed meal model could be extended toward the development of wearable pancreas due to its detailed structure and easily identifiable parameters.

Glucose-insulin mathematical models have been used to develop *in silico* patients to test glucose control algorithm performance for type I diabetic patients [180, 181, 182]. An *in silico* simulator was approved by the FDA in 2008 as a substitute for animal trials in preclinical testing of control strategies during artificial pancreas studies [183]. The simulator includes 300 simulated subjects in three age groups: 100 adults, 100 adolescents, and 100 children. Within the simulator, a mathematical model of glucose-insulin dynamics is constructed as a glucose subsystem and insulin subsystem linked together by the control of insulin on glucose utilization and endogenous production. The glucose subsystem consists of a two-compartment model of glucose kinetics. The insulin subsystem has two compartments to represent the liver and plasma. Endogenous glucose production, rate of glucose appearance, and glucose utilization are the most important model processes. An *in silico* simulator is the preclinical benchmark to test control algorithms in glucose regulator in type I diabetic patients.

Glucose-insulin mathematical models are also implemented in model predictive control algorithms to regulate type I diabetic patient blood glucose in artificial pancreases[184, 185, 186]. Heusden *et al.* published a third order model to capture the glucose response to insulin [184]. The input of the model is the insulin being delivered and the output variable is the blood glucose concentration (deviation from the steady state). The model has a patient-specific gain and a safety factor to capture an individuals glucose-insulin response.

The model is then deployed in a zone model predictive control algorithm and tested on 100 *in silico* patients from the FDA type I diabetic patient simulator. The control algorithm was able to control the plasma glucose and handle meal disturbance without hypoglycemic incidents. The simple model structure allowed model implementation into control algorithm with minimal parameter adjustment to easily capture individual patients glucose-insulin dynamics.

Glucose-insulin mathematical models have been widely applied toward glucose control for type I diabetic patients [184, 185, 186]. The concept of applying mathematical models to regulate glucose in critically ill patients began to develop after the benefits of targeted glucose control were published by Van den Bergh *et al.* [159]. Wong *et al.* published a model-based insulin and nutrient delivery controller to regulate glucose in critically ill patients [187]. The glucose-insulin model embedded in the controller is a three-state model with a similar structure to that of Bergman *et al.* model [174]. The glucose uptake in the model is a saturating function of the remote insulin compartment. The endogenous insulin production is a function of plasma insulin by itself and not dependent on the glucose concentration. The model is then used to capture and regulate blood glucose for 8 different patients.

The same group published an Intensive Control Insulin-Nutrient-Glucose (ICING) model in 2011 [188]. The model was an extension of the previously published model. In the glucose equation, the model included a constant glucose uptake from the central nervous system, and a constant basal glucose production was also incorporated into the model. The insulin dynamics were extended to include a first order kidney clearance rate and saturating liver clearance rate. The endogenous insulin production was retained as a function of blood insulin. The model was able to capture insulin and glucose dynamics for critically ill patients whose blood glucose was measured hourly and regulated between 4.0 and 6.0 mmol/L. The ICING model was able to reduce the fitting error between model value and measurement by 50% compared to the previously published model.

Hovorka *et al.* developed a nonlinear model for type I diabetic patients that contained two compartments to represent glucose dynamics and four compartments to represent insulin dynamics[189]. The two glucose compartments are the glucose gut compartment and plasma glucose compartment. The four insulin compartments are the plasma insulin compartment

and three remote insulin compartments. The three remote compartments control the glucose uptake rate, endogenous glucose production, and the glucose transport rate from the gut to plasma. The model was extended for use in a model predict control algorithm to regulate plasma glucose in critically ill patients in subsequent papers. The use of the model in the authors control algorithm resulted in regulated plasma glucose in the target range better than without use of the control algorithm. There were no hypoglycemic incidents in 220 patients both with and without controller implementation.

A simulated model of glucose regulation was published in 2008 by Hovorka *et al.* [190]. The model is a combined model of five submodels: a submodel of endogenous insulin secretion, a submodel of insulin kinetics, a submodel of enteral glucose absorption, a submodel of insulin action, and a submodel of glucose kinetics. The model also included a time varying insulin sensitivity parameter to capture the glucose-insulin dynamics of critically ill patients. In the model, the insulin sensitivity controls glucose uptake and endogenous glucose production. The model was evaluated against data from 6 critically ill patients. The average difference between the model predictions and measured blood glucose was 1.9% for the best fit patient. The model was then used to regenerate one patients dynamics using the control algorithm. The authors acknowledged that a time varying insulin sensitivity parameter is essential to capture the physiologic response of critically ill patients.

Models play an important role in model based control for glucose regulation in critically ill patients. Although there are previously published models in the literature, these models only capture a narrow range of plasma glucose concentrations due to the availability of the data. Using the available models from Roy *et al.* [178, 179], this thesis will extend the model to capture non diabetic critically ill patient glucose dynamics using data available from the HIDENIC dataset [191].

C.2 INTRODUCTION

Critically ill patients often lose their ability to regulate glucose due to injury and/or trauma [159]. Critically ill patients blood glucose levels are often controlled by clinicians in inten-

sive care unit (ICU). Normally, clinicians regulate patient blood glucose levels between the hyperglycemic range of 180-200 mg/dL defined as standard care of practice [159]. Controlling patient blood glucose in the hyperglycemic range would prevent patient blood glucose from dropping into the hypoglycemic range of below 70 mg/dL. Hypoglycemia decreases patient survival rate and increases mortality rate [192, 193, 194]. In a 2001 single center trial with 1,546 patients, Van den Berghe *et al.* concluded that compared to standard care, targeted glucose control between 80 mg/dL and 110 mg/dL resulted in a mortality reduction from (8.0% to 4.6%) [159]. However, subsequent single and multi-center studies were not able to reproduce the same results, that targeted glucose control decreases mortality [169, 170, 171, 192, 193, 195, 196, 197]. This is evident in the largest trial of targeted glucose control in ICU, the Normaglycemia in Intensive Care Evaluation-Survival Using Glucose Algorithm Regulation (NICE-SUGAR) trial, conducted with 6,104 patients in across 42 centers [198]. The targeted glucose control group in this trial had a 2.6% increase in mortality rate compared to the control group [198]. Although different conclusions are drawn about whether targeted glucose control improves patient outcome, all of the trial results show that severe hypoglycemic incidence (<40 mg/dL) increase in the targeted glucose control group by up to 28% [159, 170, 198]. This is crucial because hypoglycemia in critically ill patients increase morbidity and mortality [192, 193, 194]. The inability to avoid hypoglycemia may affect the benefits of targeted glucose control in patient outcome. Thus, targeted glucose control benefits could be fairly evaluated by avoiding hypoglycemia. Hypoglycemia can be eliminated during targeted glucose with the aid of mathematical modeling and a control algorithm. Mathematical modeling captures the patient glucose-insulin dynamics while a control algorithm uses glucose or insulin to regulate blood glucose levels within the targeted range.

The concept of using mathematical models and control algorithms to regulate blood glucose has been widely applied in type-I diabetic patients. These models and their respective control algorithms have advanced to several successful clinical trials for outpatient supports [182, 199, 200, 201, 202, 203]. The FDA approved an *in silico* patient simulator, which has contributed to the success of these models and control algorithms [183]. The simulator contains 100 virtual adults, 100 adolescents, and 100 children. These 300 patients represent

variability present in the type-I diabetic population observed *in vivo* [183]. The simulator helps to bench mark the performance of models and control algorithms for type-I diabetic insulin treatment before clinical trials.

A similar *in silico* simulator for critically ill patients would enable the use of mathematical models and control algorithms for targeted glucose control without hypoglycemia. Mathematical models capturing glucose-insulin dynamics in the ICU have been created toward developing a virtual patient bank to help with glucose control in critically ill patients. For instance, Lin *et al.* developed a glucose insulin model to capture 173 patients glucose-insulin dynamics under glycemic range between 4.4 to 6.1 mmol/L. The average patient fitting error was 2.8% (1.18-6.41%)[188]. The model was able to capture a normal glycemic range in critically ill patients. It was one of the few that confirmed the use of mathematical models to capture the complex dynamics of glucose and insulin in critically ill patients.

Hovorka *et al.* examined the effectiveness of using an enhanced model predictive control algorithm (eMPC) in targeted glucose control compared to a routine glucose management protocol (RMP) in cardiac surgery patients [190]. There were 60 patients 30 for each case - subjected to glucose control to maintain euglycemia (target range 4.4-6.1 mmol/liter). The mean blood glucose, percentage of time in target range, and hypoglycemia events were used as performance measurable outcomes. The mean blood glucose was 6.2 mmol/liter in the eMPC group versus 7.2 mmol/liter in the RMP group. The percentage of time in the target range was 60.4 % for the eMPC group versus 27.5% for the RMP group. No severe hypoglycemia occurred in either group. The eMPC was able to control patient blood glucose levels closer to the target range compared to RMP. Hovorka *et al.* proved that MPC can help to maintain patient blood glucose within a targeted range without hypoglycemia.

Mathematical modeling of glucose-insulin dynamics in critically ill patients would help create a virtual patient bank to test glucose control algorithms. It could also be used in targeted glucose control algorithms for better patient glucose regulation. In this chapter, we present a data driven-glucose insulin dynamic model capturing the dynamics of 200 critically ill patients from the University of Pittsburgh Medical Center Database. The model can be coupled with future high frequency patient data to create a virtual patient bank of glucose-insulin dynamics in critically ill patients. The virtual patient bank can be used to test

glucose control algorithm in its ability to regulate critically ill patient glucose within a targeted range. The model can also be coupled with a control algorithm to help regulate patient blood glucose within a targeted range with the hope of decreasing morbidity and improving patient outcome.

C.3 METHODS

C.3.1 Intravenous Glucose Tolerance Test (IVGTT)

The Intravenous Glucose Tolerance Test (IVGTT) is used to evaluate patient insulin sensitivity. The IVGTT protocol includes intravenously injecting glucose into the patient and subsequently measuring plasma glucose and insulin concentrations. These insulin and glucose concentrations are used to estimate the patient insulin sensitivity. The IVGTT is often used in the healthy patient population. The IVGTT data is obtained from Bergman *et al.*[9] where the volunteers (n=6) are injected with 300 mg/kg of glucose over 60 seconds at t=20 minutes. Glucose and insulin concentrations are reported subsequently to capture the change in glucose-insulin dynamics. The IVGTT test data are used to calibrate the endogenous insulin release profile in healthy volunteers in our model.

C.3.2 Patient Selection

The HIgh-DENsity Intensive Care (HIDENIC) database contains patient data from ICU admissions at the University of Pittsburgh Medical Center [191]. The database is an extensive electronic medical record of 46,169 patients from 1991-2008, with $> 97\%$ of care collected after 2001. All data are de-identified. The HIDENIC database includes ICU information (observations, measurements, interventions, and daily notes from all services except physicians) and hospital medical information (laboratory results, medication prescribed, and hospital discharge summaries).

The database query includes all patients older than 18 years without the diagnosis of diabetic ketoacidosis or a non-ketonic hyperosmolar state. Complete electronic records be-

Table C.1: Patient Information.

Information	**Average(Min-Max)**
Number of Patients	200(119M)
Age	63.3(18-98)
Height (m)	1.71 (1.47-1.99)
Weight(kg)	82.3(40-181)
Hospital Duration (days)	5(2-25)

tween 2005-2008 in the surgical ICU are included for patient query. Patients who stayed in the surgical ICU between 48 hours and 2 weeks are selected to have a representative pool of ICU patient dynamics. A Python script automatically extracts patient data from the database via MySQL.

The data between 2005 and 2008 in the surgical ICU allows us to extract a group of 200 patients with detailed records for use in the study. A summary of the patient information is shown in Table C.1.

C.3.3 Glucose-Insulin Dynamic Model for Critically Ill Patients

An extended type I diabetic glucose-insulin dynamic model developed by Roy *et al.* [178] is used as the main structure to capture critically ill patient dynamics. The model consists of 6 equations of 15 parameters (Equations (D.1)- (D.6), Table D.1). The structure of the model and the interactions between glucose, insulin, and free fatty acid (FFA) are shown in Figure C.1. In this model, insulin and FFA impact glucose uptake by peripheral tissues and the liver through their remote states, X and Z respectively from Figure C.1. Insulin affects glucose and FFA transport rates to adipose and peripheral tissues through its remote states, X and Y respectively from Figure C.1. The model does not have the effect of glucose on insulin release or production because it is a type I diabetic patient model.

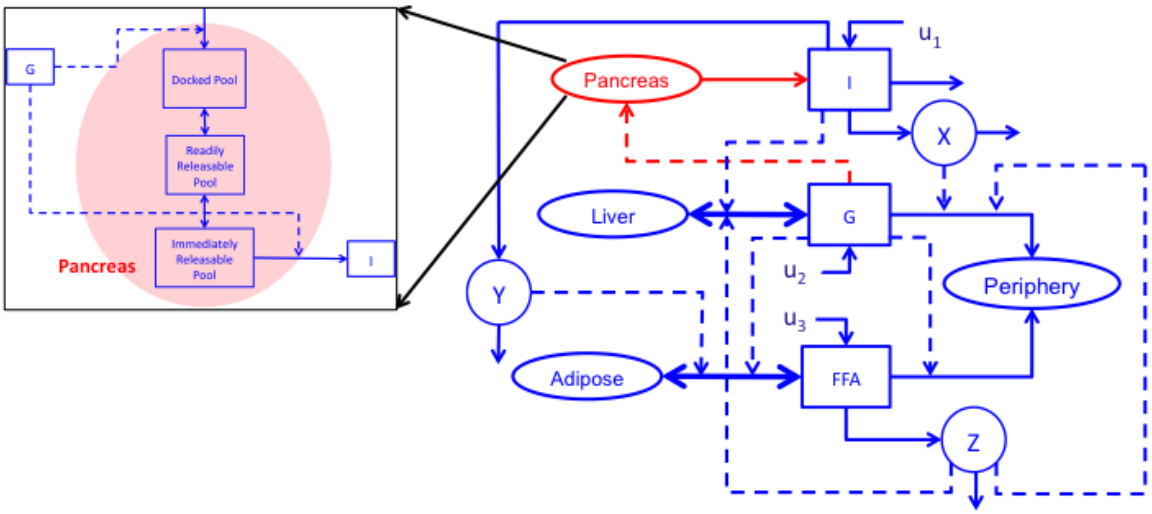

Figure C.1: Block diagram of glucose-insulin dynamics model with insulin release model built in. The original model is in blue and the addition for this study is in red with a zoomed in view

The mixed meal model [179] (Equations (D.7)- (D.9)) is incorporated into the extended minimal model to capture oral nutrient administration to the patient. The mixed meal model uses the nutrient intake in terms of carbohydrates, protein, and fat and captures their effects on glucose, insulin, and FFA dynamics in the type I diabetic patient. Additional details about the extended minimal model and the mixed meal model can be found in the references section [178, 179].The full extended minimal model with the mixed meal model and their parameters are shown in Appendix D.

The model also has the capability to handle intravenous delivery of nutrients and insulin (u_1, u_2, and u_3). Endogenous insulin release and exogenous insulin help to regulate plasma glucose in critically ill patients. Therefore, an endogenous insulin release model is needed to capture non-diabetic glucose-insulin dynamics of critically ill patients. In a healthy person, endogenous insulin release has a biphasic profile under glucose stimuli [204, 205, 206]. The first phase of insulin release is the fast pulse response. When plasma glucose concentration rises, the pancreas releases insulin immediately to lower blood glucose[206]. This first pulse response causes a fast rise in insulin concentration within the plasma. If plasma glucose concentration remains above the normal glycemic range, then the pancreas synthesizes more insulin and releases it into the plasma to lower blood glucose concentration [206]. Insulin synthesis and release after the fast pulse response accounts for the second phase of the insulin release profile.

Insulin resides in different pools as suggested by biological experiments [207, 208] and recent mathematical models [209, 210, 211]. The increase in glucose concentration triggers the release of insulin from the intermediately releasable pool via messengers such as Ca^{+2} and ATP [210]. The intermediately releasable pool is responsible for the first phase of the endogenous release pool [210]. The increase of plasma glucose triggers the biosynthesis of insulin in β cells and the mobilization of insulin in the reserve pool toward the docked pool and to the readily releasable pool [211]. The insulin then migrates toward the intermediately releasable pool [211]. The synthesis of new insulin and migration of insulin from the reserve pool to different pools before being released accounts for the second phase of the insulin release [211].

A three compartment model representing the three biological states of insulin in the pancreas are inserted into the glucose-insulin dynamic model to capture the biphasic response of the endogenous insulin release profile as shown in Figure C.1. Insulin is produced and located in three different pools: the docked pool, the readily releasable pool, and the immediately releasable pool [206].

$$\frac{dI_D}{dt} = p_{I1}(G(t) - G_b) - p_{I2}I_D(t) + p_{I3}I_{RR}(t) \tag{C.1}$$

$$\frac{dI_{RR}}{dt} = p_{I2}I_D(t) - p_{I3}I_{RR}(t) - p_{I4}I_{RR}(t) + p_{I5}I_{IR}(t) \tag{C.2}$$

$$\frac{dI_{IR}}{dt} = p_{I4}I_{RR}(t) - p_{I5}I_{IR}(t) - p_{I6}(G)I_{IR}(t) - p_{I7}I_{IR}(t) \tag{C.3}$$

$$Where$$

$$p_{I6}(G) = p_{I8}\frac{G(t)^n}{p_{I9}^n + G(t)^n} \tag{C.4}$$

In our model, the docked pool represents the process of insulin synthesis and migration from the reserve pool to the docked pool. When plasma glucose elevates ($G(t)$) higher than the basal glucose concentration,G_b, the docked pool produces insulin at the p_{I1} rate. Insulin can transport back and forth between the docked pool and readily releasable pool at the rates p_{I2} and p_3 respectively. Equation (C.1) describes the docked pool insulin dynamics. In addition, to equilibrate with the docked pool, the readily releasable pool is also in equilibrium with the intermediately releasable pool at the forward rate p_{I4} and reverse rate p_{I5}. Equation (C.2) shows the insulin dynamics in the readily releasable pool. The intermediately releasable pool insulin dynamics are shown in Equation (C.3. Besides being in equilibrium with the readily releasable pool, the intermediately releasable pool secretes insulin into the plasma at the basal rate p_{I7}. When plasma glucose concentration is high, the intermediately releasable pool increases its insulin release through $p_{I6}(G)$, where $p_{I6}(G)$ is the Hill function described in Equation (C.4). The parameter, p_{I8} is the maximum insulin release rate, and p_{I9} is the glucose concentration where insulin rate is at its half maximum. Equation (C.3) describes the insulin dynamics in the intermediately releasable pool. The endogenous insulin release model is shown in Equations (C.1) - (C.4).

C.3.4 Parameter Estimation Capturing Changes in Glucose-Insulin Dynamics

Critically ill patients glucose and insulin dynamics change throughout their time in the ICU. To capture the variations in patient glucose-insulin dynamics, the insulin dependent glucose uptake (Insulin sensitivity, SI in Equation (D.3)) and basal glucose production (EGP_0 in Equation (D.3)) are changed throughout the patients stay in the ICU. The changes in SI and EGP_0 impacts the model dynamics through a first order filter for each parameter (Equations (C.5) and (C.6)) to avoid sharp changes in glucose-insulin dynamics.

$$\frac{dSI}{dt} = k_f(p_{e1} - SI(t)) \tag{C.5}$$

$$\frac{dEGP_0}{dt} = k_f(p_{e2} - EGP_0(t)) \tag{C.6}$$

Parameters p_{e1} and p_{e2} in Equations (C.5) and (C.6) are updated, respectively, when blood glucose is measured to minimize the sum of squared error between the model glucose simulation and patient glucose measurement data (Equation (C.7)):

$$J(p) = \sum_{i=1}^{N} (y(i) - y_{sim}(i,p))^2 \tag{C.7}$$

In Equation (C.7), the sum is over the number of data points, N, in the experimental data set, $y(i)$. Time-matched simulation data, $y_{sim}(i,p)$ is used to calibrate the parameter set, p, those can be used to reduce the error between predicted ($y_{sim}(i,p)$) and actual ($y(i)$) data. The objective, $J(p)$, is the sum of the squared difference between the experimental measurement and simulation result. In this work, the difference between the blood glucose measurements and blood glucose simulation was minimized via the changes of parameters, p_{e1} and p_{e2}. Parameters p_{e1} and p_{e2} impact the glucose-insulin model dynamics via the insulin sensitivity (SI) and endogenous glucose production (EGP_0) through Equations (C.5) and (C.6), respectively. Numerically, the residual sum of squares minimization is implemented in MATLAB (©2013, The Mathworks, Natick, MA) using the *lsqnonlin* function.

Model performance is evaluated by calculating the Model Absolute Relative Error (MARE):

$$MARE = \frac{\sum_{i=1}^{N} |y(i) - y_{sim}(i)|}{N \sum_{i=1}^{N} y(i)} \tag{C.8}$$

Here the absolute difference between experimental data set, $y(i)$ and model result, $y_{sim}(i)$ are summed over the number of data points, N. The difference is then divided by the product of the experimental data sum and number of data points, N. Equation (C.8) is used to calculate the MARE for 200 patients to establish the mean and the range of the error.

C.4 RESULTS

C.4.1 Insulin Release Calibration

The endogenous insulin release model is calibrated with the IVGTT test. The results of model fitting and experimental data for both insulin and glucose are shown in Figure C.2. The model is able to represent the fast rise in insulin response due to the sudden spike in blood glucose concentration. While blood glucose concentration remains high, the secondary response of insulin was shown around t=20 minutes after glucose was injected into the body. When blood glucose began to approach the normal glycemic range (80-110 mg/dL), insulin secretion slowed down and insulin concentration returned to its nominal value. The summary of parameters of the insulin release model is shown in Table C.2.

C.4.2 Critically Ill Patients Glucose-Insulin Dynamics

An example of the model and experimental data are shown in Figures C.3 and C.4 for patients number 4 and 55 out of 200 patients, respectively. Figures C.3a and C.4a show the glucose measurements of experimental data (x) and simulation results (solid line). With the inputs of insulin infusion (Figures C.3b and C.4b), intravenous nutrient infusion (Figures C.3c and C.4c), and oral nutrient intake (Figures C.3d and C.4d), the model is able to capture the experimental data with the residual error (the difference between model and data), shown in Figures C.3e and C.4e. Figures C.3f and C.4f and Figures C.3g and C.4g show

Table C.2: Model Parameters

Parameters	Value	Unit	Parameters	Value	Unit
p_{I1}	$0.65*10^{-3}$	$\frac{mU*dL}{mg*min}$	p_{I8}	0.33	min^{-1}
p_{I2}	0.11	min^{-1}	p_{I9}	100	$\frac{mg}{dL}$
p_{I3}	0.02	min^{-1}	k_i	0.49	-
p_{I4}	0.025	min^{-1}	G_b	85	$\frac{mg}{dL}$
p_{I5}	0.005	min^{-1}	n	4	-
p_{I7}	0.003	min^{-1}	p_f	0.06	min^{-1}

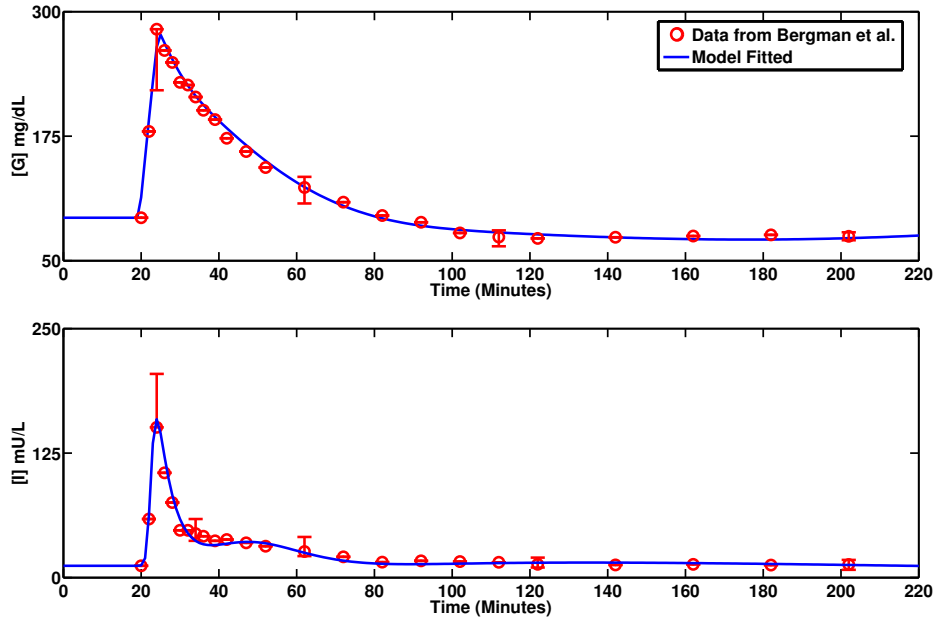

Figure C.2: Intravenous glucose tolerance test data (circle, from Bergman *et al.* [9]) and the model fits of glucose and insulin. IVGTT data of 6 healthy volunteer with 300 mg/kg of glucose injection over 60 seconds.

how the SI and EGP_0 parameters are changed accordingly for each individual patient via Equations (C.5)- (C.6). 200 different patient profiles of glucose-insulin dynamics in the first 48 hours after admission are evaluated individually. The model absolute relative error came out to be 2.14% for 200 patients (5000 glucose measurement), with a minimum error of 0.014% and maximum of 8.31% per patient.

In order to evaluate how well the model performs against the experimental data, Clarke error grid analysis (EGA) [212, 213] is used to plot the model results versus the experimental measurements. The Clarke error grid is divided into 5 zones, A-E, with shifts from A to E indicating performance losses between the model and patient data. The desired result of a good model performance is that the model results, when plotted with the patient glucose data or with the rate of glucose change, show $\geq$ 80% of the points fall into zone A. Using Clarke EGA, we evaluate the performance of our model against 200 patients glucose data. The results of the point-EGA (p-EGA) and the rate-EGA (r-EGA) are shown in Figures C.5 and C.6 respectively. The p-EGA is the plot of the model blood glucose level versus the actual glucose measurement. The r-EGA is the plot of the rate of the change in blood glucose between two data points of simulation versus the actual measurement. The summaries of percentage of data per zone for both p-EGA and r-EGA are shown in Table C.3. From this result, the model captures the patient dynamics in the ICU (96.0% zone A agreement with the experimental measurement). The model is able to capture not only the glucose value of the measurement but also the rate of change of the glucose between the two measurement values with the same confidence (98.57% zone A agreement).

C.5 DISCUSSION AND SUMMARY

The insulin release model coupled with the glucose-insulin dynamic model is calibrated with its insulin release profile via IVGTT (Figure C.2). It is able to capture both insulin and glucose dynamics after glucose injection. There are models developed to capture endogenous insulin release in healthy volunteers or in β-cells. However, the insulin dynamic models in healthy volunteers often capture the second phase of insulin release, like in the case of

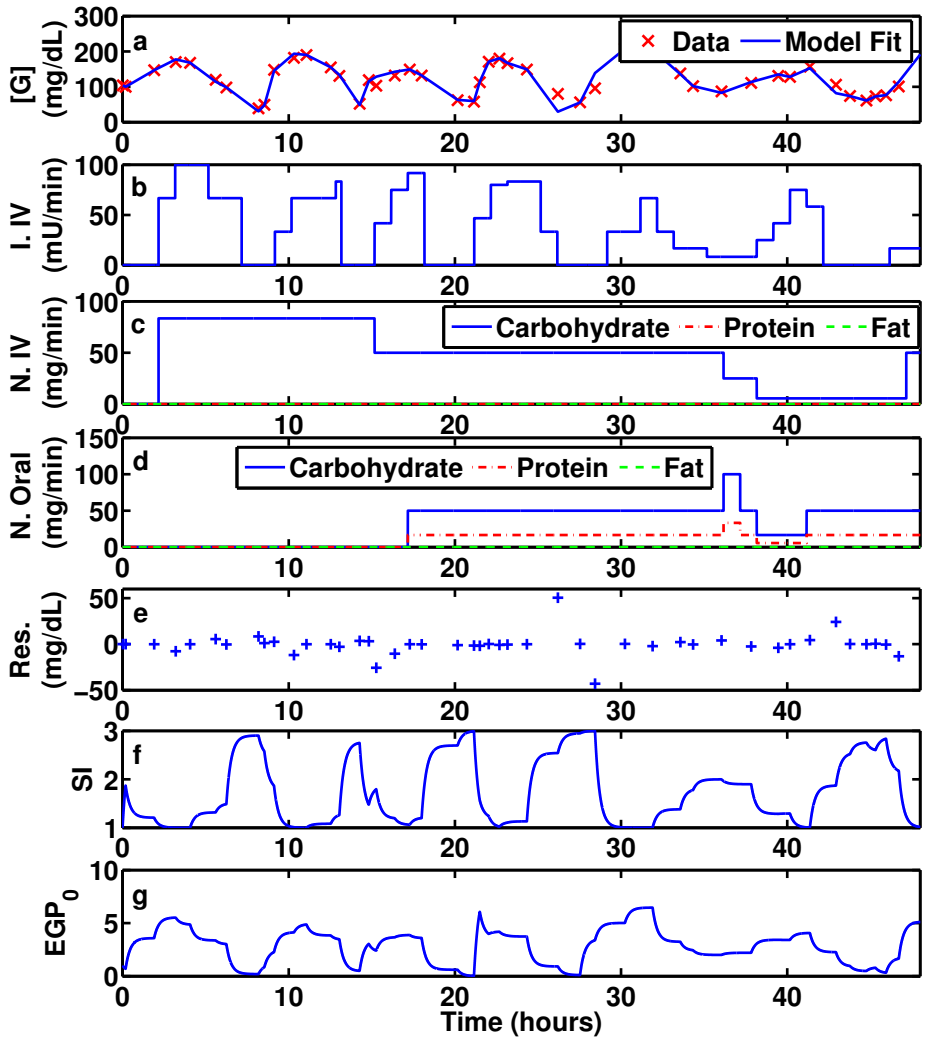

Figure C.3: Patient number 4 glucose-insulin dynamics captured by the model. N IV: intravenous nutrient infusion, N OR: nutrient intake orally, I IV: intravenous insulin infusion, Res: residual error between model and experimental data. Panel a: glucose measurement(x) and simulation result (solid line); panel b: intravenous insulin infusion rate; panel c: intravenous nutrient infusion; panel d: oral nutrition intake; panel e: residual error between model and patient glucose measurement; panel f: change in insulin sensitivity; panel g: change in endogenous glucose production

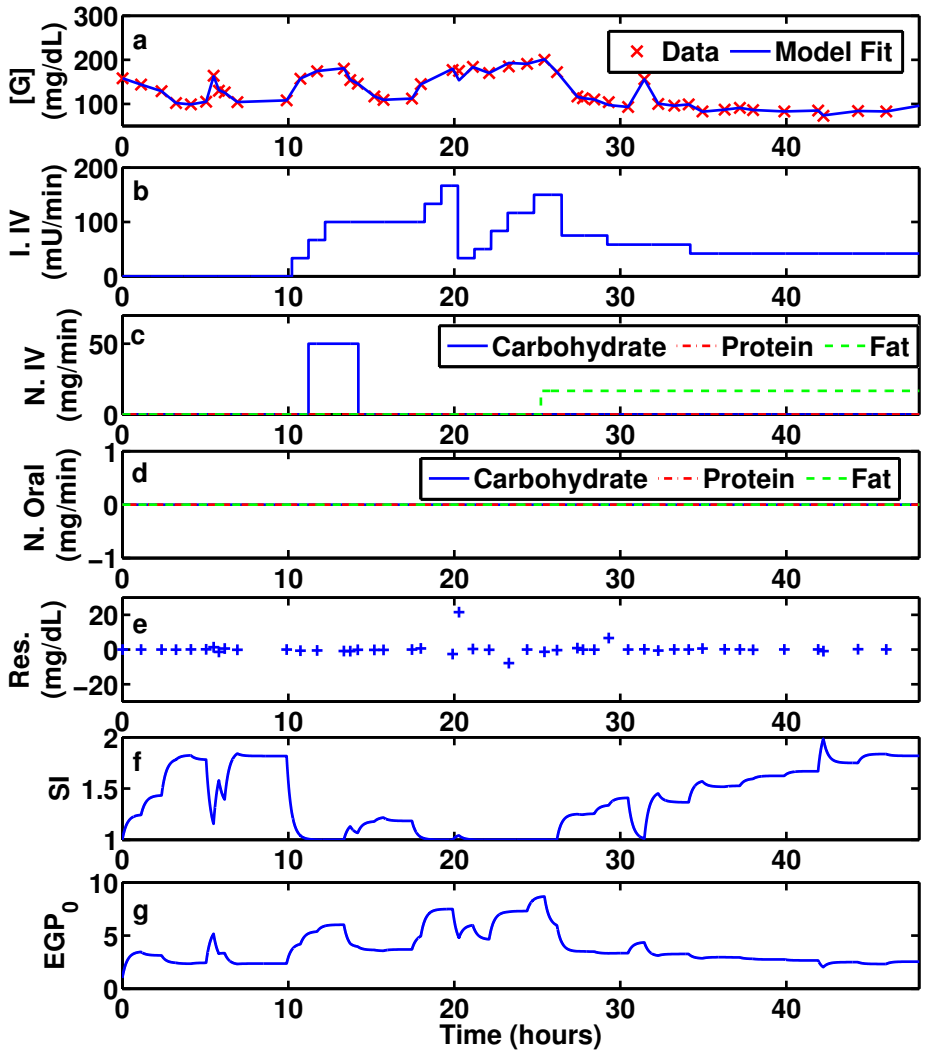

Figure C.4: Patient number 55 glucose-insulin dynamics captured by the model. N IV: intravenous nutrient infusion, N OR: nutrient intake orally, I IV: intravenous insulin infusion, Res: residual error between model and experimental data. Panel a: glucose measurement(x) and simulation result (solid line); panel b: intravenous insulin infusion rate; panel c: intravenous nutrient infusion; panel d: oral nutrition intake; panel e: residual error between model and patient glucose measurement; panel f: change in insulin sensitivity; panel g: change in endogenous glucose production

Table C.3: The summary of Clarke's EGA results (percentage of data in a zone).

Zone	p-EGA	r-EGA
A	96.00 %	98.57 %
B	3.65 %	1.20 %
C	0.00 %	0.04 %
D	0.35 %	0.12 %
E	0.00 %	0.07 %

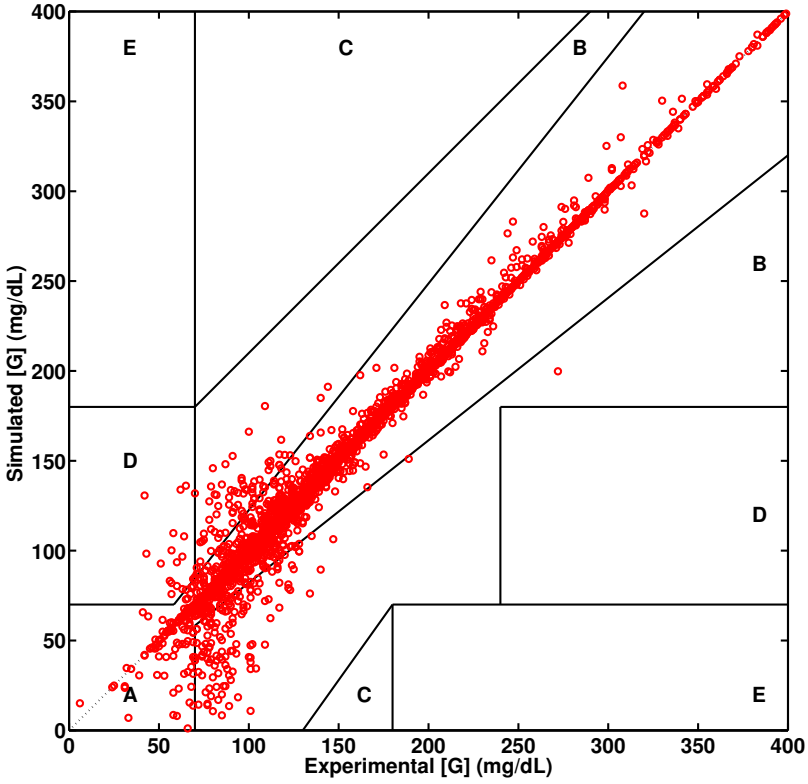

Figure C.5: Clarke's Error Grid Analysis of blood glucose(BG) level (p-EGA)

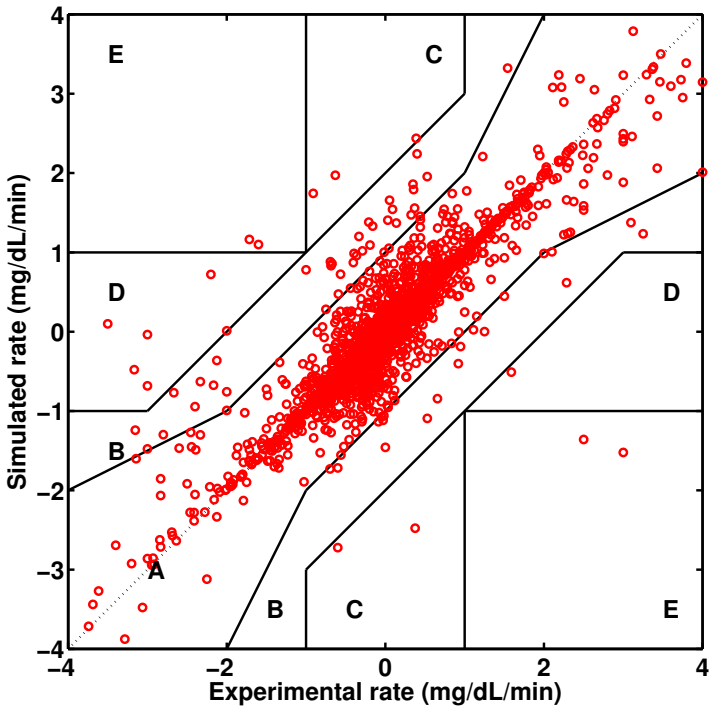

Figure C.6: Clarke's Error Grid Analysis of the change in blood glucose (r-EGA)

the Bergman model. On the other hand, the β-cell insulin release models often focus on the first fast pool release of insulin. However, in critically ill patients, the plasma glucose concentration often remains in the hyperglycemic range for a long period time. Both fast and slow insulin release dynamics contribute to the overall patient glucose-insulin dynamics. The insulin release model is developed by using a three compartmental model in order to capture both phases of the insulin release profile in healthy volunteers after IVGTT. The insulin release model is incorporation into the current existing glucose-insulin dynamic model for type I diabetic patients and helps to extend the model capability to capture the critically ill patient population.

The glucose data from The HIDENIC data set is used to represent critically ill patients glucose and insulin dynamics to evaluate the model performance [191]. The HIDENIC data set contains 46,169 patients information during their time in the hospital. The challenge of patient information extraction is that not all patient information is in one table. Therefore, cross reference between different tables is needed to get the patient data. For instance, the patient blood glucose measurements are in the glucose table, while the amount of glucose delivered is in the nutrient table. Most of the drug and nutrient information delivered to the patients are written in the product branch names. We develop a Python script that uses the patient admission number to cross reference and extract the information of the patient out of the database. The Python script also recognizes different nutrient information and their branch names to put them into appropriate columns in the final patient table. The columns include glucose, free fatty acids, and protein. The Python script automatically queries 200 patients out of the surgical ICU with hospital stays between 48 hours and 2 weeks to carefully fit the model of glucose-insulin dynamics. For the purpose of this study, we are only interested in the information pertaining to glucose-insulin dynamics. However, this Python script can be also extended to extract patient information for different studies.

The information from 200 patients with different hospital lengths of stay (48 hours to 2 weeks), ages, sexes, and outcomes (survived or deceased non-survived), is used to calibrate the model performance. We limit the model performance calibration to the first 48 hours of the patient duration in the hospital because the patient data in the HIDENIC is not specifically designed for this study. First, the patients glucose measurements are often missed

after a long period of time ($\geq$ 8 hours), especially after the first 48 hours if the patient is recovering. Moreover, after the first 48 hours of recovery, patients often receive subcutaneous infusion of insulin, whose dynamics the current model could not capture. Finally, information regarding nutrients delivered orally after 48 hours is also often missing from the database. Therefore, we decided to calibrate and evaluate the model performance using the first 48 hours after admission. This ensures the models ability to capture the patient glucose-insulin dynamics with known external stimuli.

Glucose-insulin dynamics of ICU patients vary widely due to different factors such as stress-induced hormone concentration [214, 215], cytokine concentration [216, 217], and surgery or trauma [218, 219, 220]. These factors cause the insulin sensitivity (SI) and endogenous glucose production (EGP_0) to change in critically ill patients. Therefore, two parameters associated with insulin sensitivity (SI) and endogenous glucose production (EGP_0) are estimated in our model via (Equation (C.5)- (C.6)). These two parameters allow the models blood glucose concentration to span the patient range (blood glucose level less than 400 mg/dL). Although one parameter variation is preferred to capture patient dynamics, when only SIor EGP_0 is varied to capture the patient plasma concentration, the models absolute relative errors are 19% (8%-30%) and 15% (10%-29%), respectively. One parameter estimation can not capture plasma glucose concentration when it is higher than 250 mg/dL. Therefore, the variation of SI and EGP_0 simultaneously is used to capture high plasma glucose concentrations and accurately represent ICU patient glucose dynamics.

The model was used to fit 200 patients individually. The two examples of patient glucose profiles are shown in Figures C.3 and C.4. The model takes insulin infusion rates and nutrients (intravenous and oral) as inputs, and varies insulin sensitivity and endogenous glucose production to fit the patient glucose dynamics. The model was able to capture the patient glucose dynamics with 2.14% (0.01%-8.31%) model absolute relative error. The Clarke's point and rate EGAs are used to visually show how well the model performs against the measurement data. In theory, the model and data would match perfectly with the experimental data; in the EGA graphs, the simulation results plotted against the experimental results would lie perfectly on the 45-degree line. However, discrepancies between model prediction and measurement data often occurs. The EGAs allow us to evaluate the model

performance in terms of whether the discrepancies between model and data are acceptable for this work. The Clarkes EGA analyses of 200 patients are shown in Figures C.5 and C.6 for the blood glucose measurement and for the rate of change accordingly, the model was able to capture more than 95% of the blood glucose measurements in zone A, and 99.6% of the rates in zones A and B.

The glucose model results predict the concentration lower than the experimental measurement when plasma glucose concentration is below 100 mg/dL, as seen in Figure C.5, and in patient 4 dynamics around 26 hours (Figure C.3). The model often under predicts glucose concentration when patient glucose concentration is in the hypoglycemic range. However, the difference between the model and the patient data only accounts for 0.4% of unacceptable performance in Zones C,D, and E. For perspective, a good continuous glucose sensor, when plotting sensor measurement versus actual blood glucose, has 97.9% of data in both zones A and B (70.4% in zone A and 27.5% in zone B)[221]. From this pEGA result, the model has the ability to successfully capture the patient plasma concentrations.

For the rate- EGA, the model was able to capture most of the rates of the experimental results in Zones A and B (99.7%), and only 0.3% of the rate results are in zones C, D, and E, as shown in Figure C.5 and Table C.3. A good glucose sensor, when plotting the sensor rate versus the measurement rate, has 91.7% of the rate in both zones A and B (70.0% in zone A, and 21.7% in zone B) [221]. From both pEGA and rEGA, the model is able to accurately capture both blood glucose measurements and blood glucose rate of change in critically ill patients.

Lin *et al.* published the ICING model, which is also calibrated against our 200 patients data [188]. The p-EGA and r-EGA for the Lin *et al.* model results are shown in Table C.4. The results show that the Lin *et al.* model is able to capture measurement glucose data with 96.07% of the data falling in Zones A and B for p-EGA and with 98.69% of the rate date falling in Zones A and B for r-EGA. The model absolute relative error is 5% (0.023%-12.22%). The EGAs and the model absolute errors from the Lin *et al.* model showed that our model has slightly better performance in capturing the critically ill patient glucose-insulin dynamics.

Table C.4: Summary of Clarke EGA results for Lin *et al.* model (percentage of data in a zone).

Zone	**p-EGA**	**r-EGA**
A	92.00 %	96.44 %
B	4.07 %	2.25 %
C	2.20 %	1.04 %
D	1.73%	0.17 %
E	0.00 %	0.10 %

Fitting glucose-insulin dynamics is often followed by the assumption of glucose following the straight-line interpolation between the two data points. This method allows the model to capture the plasma glucose concentration accurately since the dynamics of the patient glucose is a straight line between two data points. This assumption is valid when patient blood glucose levels are measured frequently. In our 200 patient dataset, the patient blood glucose measurements are rather sparse, and sometimes, the duration between two measurements is greater than 90 minutes. Thus, this assumption is not the best way to fit patient glucose dynamics for our 200 patients. Instead, we decided to vary the patient SI and EGP_0 using first order filter dynamics, and allow the patient glucose dynamics to vary following the natural course of the model dynamics. Although some accuracy is sacrificed by fitting the patient glucose dynamics by using our method, the model is still one of the better models capturing glucose-insulin dynamics for critically ill patients.

Using the available glucose-insulin dynamic mathematical models for type I diabetic patients, we extend the model to capture the glucose and insulin responses after an IVGTT by incorporating the insulin release model. The final glucose-insulin model is then used to capture the critically ill patient glucose-insulin dynamics. 200 surgical ICU patients information from the HIDENIC data set are extracted to calibrate the glucose-insulin model performance. The patient glucose-insulin dynamics change throughout their time in the

hospital; therefore, the parameters associated with insulin sensitivity and endogenous glucose production are varied to capture these dynamic changes. The model accurately captures 200 patients glucose data.

Glucose control in critically ill patients could potentially improve patient survival rates and reduce morbidity when hypoglycemia can be avoided. In this work, we develop a glucose-insulin dynamics model that has an ability to capture critically ill patient glucose-insulin dynamics. The final model can be used with appropriate data to develop a virtual patient bank for glucose dynamics in critically ill patients. Moreover, the model can also be used in the controller for targeted glucose control without hypoglycemia.

C.6 FUTURE RESEARCH RECOMMENDATIONS

A model of glucose-insulin dynamics has been developed from an existing model for type I diabetic patients and is able to capture glucose data from surgical ICU patients in the HIDENIC database. The two parameters associated with insulin sensitivity and endogenous glucose production are varied in the model to represent the impacts of different factors on patient-specific glucose-insulin dynamics. Improvements can be made to accurately capture glucose-insulin dynamics in critical care patients. Free fatty acids (FFAs) play a role in regulating glucose in humans, Roy *et al.*[178] is able to capture how FFAs interact with glucose and insulin in healthy type I diabetic patients. However, little information is available explaining how these interactions change in critical care patients and how they contribute to the overall glucose-insulin dynamics. Examining FFA interaction with glucose and insulin and how it changes in critical care patients will increase the model accuracy in capturing patient glucose-insulin dynamics.

Changes in critical care patients glucose-insulin dynamics are attributed to different internal and external factors. Endogenous stress-induced hormones: glucorticoids, epinephrine, and cortisol alter plasma glucose levels by interfering with endogenous glucose production and insulin driven glucose uptake. Moreover, glucorticoids, epinephrine, and cortisol are also exogenously administered in the ICU to help patient recovery. These hormones contribute to

plasma glucose fluctuations and increase the chance of hyperglycemia. Incorporating these hormone dynamics and their effects onto glucose-insulin dynamics in the current existing model will help to explain and capture the changes in a patients glucose levels during their time in the ICU.

The inflammatory cytokines IL-1, IL-6, and TNF-α also play roles in the glucose-insulin dynamics of critically ill patients. TNF-α and IL-1 interfere with insulin sensitivity by decreasing the effect of insulin driven glucose uptake and IL-6 increases the effect of insulin driven glucose uptake. Understanding these cytokine dynamics and how they interact with the insulin driven glucose uptake signaling cascade would help explain the change in glucose-insulin dynamics in critical care patients and aid glucose control algorithms in better regulating patient glucose levels.

In addition to a deeper understanding at the biological level of the changes in glucose-insulin dynamics in ICU patients, model improvements can also be made to increase model accuracy in representing patient glucose dynamics. The current model does not capture subcutaneously delivered insulin dynamics. Subcutaneously delivered insulin is often used in patients recovering from injury or disease in the ICU. Subcutaneous insulin may have fast or slow acting dynamics based on the chemical structure of the delivered insulin. Capturing these different subcutaneous insulin dynamics will help to build better virtual patient dynamics used to test glucose control algorithms for critical care patients.

Patient glucose databases should be improved to build a better glucose-insulin dynamic model and better virtual patients to test glucose control algorithm. Although the HIDENIC database contains critically ill patient data, the time between glucose measurements is rather large. Moreover, nutrient information is often missing in the database. The data scarcity and missing information present a difficulty in accurately determine patient glucose dynamics. With better data glucose measurements (continuous glucose measurement or high frequency glucose measurement) and nutrient intake records, the virtual patient database can be built and utilized as a tool for testing and validating glucose control algorithms for critically ill patients resulting in better glucose regulation without hypoglycemia.

The current model of glucose-insulin dynamics contains 14 equations with nonlinear terms to capture patient data, Appendix D. The large number of equations and nonlinear

terms create difficulties in implementing the model in a model-based control algorithm. Model reduction can be applied to the current model of glucose-insulin dynamics to reduce the number of states and nonlinear terms for ease of implementation. Moreover, during the model reduction step, sensitivity analysis identifies the key parameter(s) that govern model dynamics. The controller can estimate these sensitive parameters to capture patient dynamics and by predicting future outcomes using these dynamics better regulate patient glucose levels. As a result of research to advance a deeper understanding of the causes of variation in glucose-insulin dynamics to the development of models and subsequent reduction to simple forms for control algorithms, targeted glucose control can be achieved without hypoglycemia to help improve patient outcomes and reduce patient morbidity in the ICU.

APPENDIX D

EXTENDED MINIMAL MODEL WITH MIXED MEAL MODEL EQUATIONS AND PARAMETERS

Extended Minimal Model:

$$\frac{dI(t)}{dt} = -nI(t) + p_5 u_1(t) + p_{I6}(G) I_{IR}(t) + p_{I7} I_{IR}(t) \tag{D.1}$$

$$\frac{dX(t)}{dt} = -p_2 X(t) + p_3 I(t) \tag{D.2}$$

$$\frac{dG(t)}{dt} = -p_1 G(t) + p_1 EGP_0(t)(1 - k_i SI(t))(t) G_b - p_4 SI(t) X(t) G(t) + p_6 (G(t) Z(t) - G_b Z_b) + \frac{u_2(t)}{Vol_G} \tag{D.3}$$

$$\frac{dY(t)}{dt} = -p_{F2} Y(t) + p_{F3} I(t) \tag{D.4}$$

$$\frac{dF(t)}{dt} = -p_7 (F(t) - F_b) - p_8 Y(t) F(t) + p_9(G)(F(t)G(t) - F_b G_b) + \frac{u3(t)}{Vol_F} \tag{D.5}$$

$$\frac{dZ(t)}{dt} = -k_2 Z(t) + k_1 F(t) \tag{D.6}$$

Mixed Meal Model:

$$\frac{dN_G(t)}{dt} = x_G G_{emp}(t) - k_G N_G(t) \tag{D.7}$$

$$\frac{dN_P(t)}{dt} = x_P G_{emp}(t) - k_p N_P(t) \tag{D.8}$$

$$\frac{dN_F(t)}{dt} = x_F G_{emp}(t) - k_F N_F(t) \tag{D.9}$$

$$u_2(t) = k_G N_G(t) + 0.6 k_P N_P(t) + u_{GI}(t) + 0.6 u_{PI}(t) \quad \text{(D.10)}$$

$$u_3(t) = k_F N_F(t) + u_{FI}(t) \quad \text{(D.11)}$$

Table D.1: Extended minimal model with mixed meal model parameters

Parameters	**Value**	**Unit**	**Parameters**	**Value**	**Unit**
p_1	0.06	min^{-1}	p_{F1}	0.17	min^{-1}
p_2	0.037	min^{-1}	p_{F2}	10^{-5}	min^{-1}
p_3	$0.12 * 10^{-4}$	min^{-1}	n	0.142	min^{-1}
p_4	1.3	$\frac{ml}{min*\mu U}$	G_b	98	$\frac{mg}{dL}$
p_5	$0.568 * 10^{-3}$	mL^{-1}	F_b	380	$\frac{\mu mol}{L}$
p_6	$0.6 * 10^{-4}$	$(min * \mu mol)^{-1}$	Vol_G	117	dL
p_7	0.03	min^{-1}	Vol_F	11.7	L
p_8	4.5	$\frac{ml}{min*\mu U}$	k_G	0.022	min^{-1}
$k_9(G)$	$0.00021e^{0.0055G}$	$\frac{dL}{min*mg}$	k_p	0.0097	min^{-1}
k_1	0.02	min^{-1}	k_F	0.015	min^{-1}
k_2	0.03	min^{-1}	-	-	-

APPENDIX E

CHEMOTHERAPY OPTIMIZATION CODE

E.1 ENUMERATION CODE

```
/*  Thang Ho
 * University of Pittsburgh
 * March 04 2014
 */
//#define min(a,b) ((a) < (b) ? (a) : (b))
//##define max(a,b) ((a) >= (b) ? (a) : (b))
#include "stdio.h"
#include "math.h"
#include<fstream>
#include<iostream>
#include <ctime>
#include<omp.h>

const int NUM_THREADS= 16;
using namespace std;
static void mdlDerivativesNL(double *dx, double *x, double *u)
{
```

```
double C_tumor, C_plasma;
double r_cell, V_cell, A_tumor, V_tumor, e_porosity, k_growth_1,
    k_death, ratio;
double E_max, EC_50, k_vbm, k_bmv, k_sc_bl, k_bl_sc, k_dgcsf,
    k_d;
double V_ven, Bmin, Bmax, kG, BGmax, DGr, DGn, k_tr, kN;
/* This a cancer therapeutic model for Docetaxel with G-CSF
    rescue*/
/* u[0]: Docetaxel Intravenous infusion*/
dx[0]=0.0;
dx[1]=0.0;
dx[2]=0.0;
dx[3]=0.0;
/* PYOMO ONLY USES FROM X[4] TO X[17] */
/*drug concentration in Plasma and tumor*/
C_plasma=(0.01279*x[5]    -0.06116*x[6]    +0.09328*x[7]
    +0.07936*x[8]    +0.05068*x[9])*0.025;
C_tumor=(0.1096*x[5]    -0.02064*x[6]    -0.09764*x[7]
    -0.005715*x[8]    -0.003903*x[9])*0.0007;


V_cell=1.0*pow(10.0,-3.0);/*ml, basing the hypothesis 10^6
    cells =1 L;*/
r_cell=1.0*pow((3.0/(4.0*3.14)*V_cell),(1.0/3.0)); /*mm*,
    Radius of the cell*/
e_porosity=53.57;
A_tumor=4.0*3.14*r_cell*r_cell;
V_tumor=V_cell*e_porosity;
k_growth_1=.061/24.0/60.0;/*1/min*/
k_death=0.00020/24.0/60.0; /*1/min*/
```

```
ratio=A_tumor/V_tumor;
dx[4]=k_growth_1*ratio*pow(10.0,(ratio-1.0)/ratio*x[4])-
    k_death*ratio*pow(10.0,(1.0-ratio)/(ratio*ratio)*x[4])
    -1.212*ratio*C_tumor;
/*Docetaxel Five states reduction model from Florian et al
    physiologically based model*/

dx[5]=-0.0003227*x[5] -0.0001258*x[6] +0.0005422*x[7]
    -1.825*pow(10.0,-5.0)*x[8] -1.147*pow(10.0,-5.0)*x[9]
      +0.1104*u[0];
dx[6]=0.0003651*x[5] -0.001133*x[6] -0.0003706*x[7]
    +0.00244*x[8] +0.001631*x[9] -0.06455*u[0];
dx[7]=-0.000815*x[5] +0.004922*x[6] -0.01027*x[7]
    -0.007773*x[8] -0.005653*x[9] +0.135*u[0];
dx[8]=-0.0004651*x[5] +0.00267*x[6] -0.01128*x[7]
    -0.03372*x[8] -0.03837*x[9] +0.07957*u[0];
dx[9]= -0.0002971*x[5] +0.001775*x[6] -0.007655*x[7]
    -0.03837*x[8] -0.1122*x[9] +0.05083*u[0];

/*Neutrophil Models */
k_sc_bl=0.004;
k_bl_sc=9.5779*pow(10.0,-11.0);
k_dgcsf=7.2434*pow(10.0, -4.0);
k_tr=0.00043;
E_max=0.0130*2.0;
EC_50=0.7873;
k_vbm=0.2514*1.5;
k_bmv=0.0802*(1.0-x[17]/(0.0005+x[17]));
k_d=0.00155;
Bmin =0.0002;
```

```
    Bmax= Bmin*1400.0;
    kG=1.0;
    kN=0.05;
    BGmax=0.1;
    DGr=0.00061297;
    DGn=0.0015;
    V_ven=5.53/2.0*1000.0;

    /*Maturation Train*/
    /*IL_17*/
    dx[10]=BGmax*kN/(kN+x[16]) -0.0014*x[10];
    /*GCSF Plasma*/
    dx[11]=0.00092174*x[10]-0.00022174*x[11]+k_sc_bl*x[18];
    /*Pr*/
    dx[12]=(Bmin*kG + Bmax*x[11])/(kG+x[11])-E_max*x[17]/(EC_50+x
        [17])*x[12]-k_tr*x[12];
    /*T_1*/
    dx[13]=k_tr*x[12]-(k_tr)*x[13];
    /*T_2*/
    dx[14]=k_tr*x[13]-k_tr*x[14];
    /*T_3*/
    dx[15]=k_tr*x[14]-k_tr*x[15];
    /*Neutrophils*/
    dx[16]=k_tr*x[15]-k_d*x[16];
    /*Bone Marrow*/
    dx[17]=-k_bmv*x[17]+k_vbm*C_plasma;
    /*G-CSF-tissue*/ /* Not used in Pyomo code*/
    dx[18]=-k_sc_bl*x[18]-k_dgcsf*x[18];//+u[1]/V_venus;
}
```

```
int main()
{
    double start_time = omp_get_wtime();
    double Pr=161.945448133839;
    double Train=161.945448133839;
    double IL_17=0.0794060143983421;
    double GCSF=0.330078919631521;
    double NC=44.9268017917568;

    double* x0 = new double[19];
    x0[0] = 0.0;
    x0[1] = 0.0;
    x0[2] = 10000.0;
    x0[3] = 10000.0;
    x0[4] = 10.0;
    x0[5] = 0.0;
    x0[6] = 0.0;
    x0[7] = 0.0;
    x0[8] = 0.0;
    x0[9] = 0.0;
    x0[10] = IL_17;
    x0[11] = GCSF;
    x0[12] = Pr;
    x0[13] = Train;
    x0[14] = Train;
    x0[15] = Train;
    x0[16] = NC;
    x0[17] = 0.0;
    x0[18] = 0.0;
```

```
int h = 1; // minutes
long int nSteps = 24*7*27*60/h;
fstream file;
file.open("Result_long_3.txt", ios::out);

double d1_start = 0;
double d1_end = 1.05;
double d1_interval = 0.05;
unsigned long long d1_point = (d1_end - d1_start)/d1_interval
   +1;

double d2_start = 0;
double d2_end = 1.05;
double d2_interval = 0.05;
unsigned long long d2_point = (d2_end - d2_start)/d2_interval
   +1;

double d3_start = 0;
double d3_end = 1.05;
double d3_interval = 0.05;
unsigned long long d3_point = (d3_end - d3_start)/d3_interval
   +1;

int ts1_start = 0;
int ts1_end = 10080;
int ts1_interval = 1440;
unsigned long long ts1_point = (ts1_end - ts1_start)/
   ts1_interval+1;
```

```
int ts2_start = 0;
int ts2_end = 10080;
int ts2_interval = 1440;
unsigned long long ts2_point = (ts2_end - ts2_start)/
   ts2_interval+1;

    int ts3_start = 0;
int ts3_end = 10080;
int ts3_interval = 1440;
unsigned long long ts3_point = (ts2_end - ts2_start)/
   ts2_interval+1;



unsigned long long N_simulation = d1_point*d2_point*d3_point*
   ts1_point*ts2_point*ts3_point;

double d1_store[NUM_THREADS];
double d2_store[NUM_THREADS];
double d3_store[NUM_THREADS];
double ts1_store[NUM_THREADS];
double ts2_store[NUM_THREADS];
    double ts3_store[NUM_THREADS];
double obj_store[NUM_THREADS];

for (int i = 0; i< NUM_THREADS; i++)
  {
    d1_store[i]=0;
    d2_store[i]=0;
    d3_store[i]=0;
```

```
        ts1_store[i]=0;
        ts2_store[i]=0;
        ts3_store[i]=0;
        obj_store[i]=1e8;
      }
    omp_set_num_threads(NUM_THREADS);


#pragma omp parallel for shared(x0, d1_store, d2_store, d3_store,
    ts1_store, ts2_store, ts3_store, obj_store) firstprivate(nSteps
    , h, N_simulation, d1_start, d1_end, d1_interval,d1_point,
    d2_start, d2_end, d2_interval,d2_point, d3_start, d3_end,
    d3_interval,d3_point, ts1_start, ts1_end, ts1_interval,
    ts1_point,ts2_start, ts2_end, ts2_interval,ts2_point,ts3_start,
     ts3_end, ts3_interval,ts3_point) schedule(dynamic)
     for ( unsigned long long sindex = 0; sindex < N_simulation;
         sindex++){

       int TID = omp_get_thread_num();

       double d1 = d1_start + d1_interval* floor((sindex%(d1_point*
           d2_point*d3_point*ts1_point*ts2_point*ts3_point))/(
           d2_point*d3_point*ts1_point*ts2_point*ts3_point));
       double d2 = d2_start + d2_interval* floor((sindex%(d2_point*
           d3_point*ts1_point*ts2_point*ts3_point))/(d3_point*
           ts1_point*ts2_point*ts3_point));
       double d3 = d3_start + d3_interval* floor((sindex%(d3_point*
           ts1_point*ts2_point*ts3_point))/(ts1_point*ts2_point*
           ts3_point));
```

```
double ts1 = ts1_start + ts1_interval* floor((sindex%(
    ts1_point*ts2_point*ts3_point))/(ts2_point*ts3_point));
     double ts2 =  ts2_start + ts2_interval* floor((sindex%(
        ts2_point*ts3_point))/ts3_point);
     double ts3 = ts3_start + ts3_interval* floor(sindex%(
        ts3_point));



double* dx = new double[19];
double* x = new double[19];
double* u = new double[1];
double* x16_day_end = new double[30*7]; // the value of x
    [16] at the end of each day, added by yankai

u[0] = 1.0;
for (int j=0; j<19; j++) {
     x[j] = x0[j];
}

bool constraint_violated = false;
long int consecutive_steps_below_13p5 = 0;
double obj=0.0;

for (int i=0; i<nSteps; i++) {
              if (i < 60||(i>=30240+ts1 && i<30300+ts1)||(i
                 >=60480+ts1&&i<60540+ts1)||(i>=30240*3+ts1 &&
                 i<30240*3+60+ts1)||
                        (i>=30240*4+ts1 &&i<30240*4+60+ts1)||(i
                           >=30240*5+ts1 &&i<30240*5+60+ts1)||(i
                           >=30240*6+ts1 &&i<30240*6+60+ts1)||
```

```
        (i>=30240*7+ts1 &&i<30240*7+60+ts1)){
        u[0] = d1;
}
else if ((i >= 10080+ts2 && i < 10140+ts2)||(i
    >=30240+10080+ts2 && i < 30240+10140+ts2)||(i
     >=30240*2+10080+ts2 && i < 30240*2+10140+ts2
    )||
                    (i >=30240*3+10080+ts2 && i <
                        30240*3+10140+ts2)||(i
                        >=30240*4+10080+ts2 && i <
                        30240*4+10140+ts2)||(i
                        >=30240*5+10080+ts2 && i <
                        30240*5+10140+ts2)||
                    (i >=30240*6+10080+ts2 && i <
                        30240*6+10140+ts2)||(i
                        >=30240*7+10080+ts2 && i <
                        30240*7+10140+ts2)    ){
        u[0] = d2;
}
else if ((i >= 20160+ts3 && i < 20220+ts3)||(i
    >= 30240+20160+ts3 && i < 30240+20220+ts3)||(
    i >= 30240*2+20160+ts3 && i < 30240*2+20220+
    ts3)||
                    (i >= 30240*3+20160+ts3 && i <
                        30240*3+20220+ts3)||(i >=
                        30240*4+20160+ts3 && i <
                        30240*4+20220+ts3)||(i >=
                        30240*5+20160+ts3 && i <
                        30240*5+20220+ts3)||
```

```
                    (i >= 30240*6+20160+ts3 && i <
                        30240*6+20220+ts3)||(i >=
                        30240*7+20160+ts3 && i <
                        30240*7+20220+ts3)){
            u[0] = d3;
}
else {
            u[0] = 0.0;
}

mdlDerivativesNL(dx, x, u);
for (int j=0; j<19; j++) {
            x[j] += h*dx[j];
}
if((i==3000)||i==(3000+30240)||(i==3000+30240*2)
    ||(i==3000+302040*3)||(i==3000+30240*4)||(i
    ==3000+30240*5)||(i==3000+30240*6)||(i
    ==3000+30240*7)){
            obj=obj+10.0*x[4];
}
if(i==10080||i==20160||i==30240||i
    ==10080+30240||i==20160+30240||i
    ==30240+30240||i==10080+30240*2||i
    ==20160+30240*2||i==30240+30240*2||
          i==10080+30240*3||i==20160+30240*3||i
              ==30240+30240*3||i==10080+30240*4||i
              ==20160+30240*4||i==30240+30240*4||i
              ==10080+30240*5||i==20160+30240*5||i
              ==30240+30240*5||
```

```
                i==10080+30240*6||i==20160+30240*6||i
                  ==30240+30240*6||i==10080+30240*7||i
                  ==20160+30240*7||i==30240+30240*7) {
                obj=obj+x[4];
            }

        //   if (x[16] < 13.47) {
              // commented by yankai
        ////        consecutive_steps_below_13p5++;
        //  }
// else {
          //        consecutive_steps_below_13p5 = 0;
         // }
 int day_number = i / 1440;     // for i=0,1,...1439, it
    is day 0
 if((i+1) % 1440 == 0 )  // if i = 1439 1439+1440.... at
    the end of day, added by yankai
 {
     x16_day_end[day_number] = x[16];
     if( day_number >=6)
     {
         double x16_week_sum = x16_day_end[day_number] +
            x16_day_end[day_number-1] + x16_day_end[
            day_number-2] + x16_day_end[day_number-3] +
            x16_day_end[day_number-4] + x16_day_end[
            day_number-5] + x16_day_end[day_number-6];
         if(x16_week_sum<4.49*3.0*7.0)
         {
             // week_week_con constraint violated
             constraint_violated = true;
```

```
                break;
            }
        }
        if( day_number >=7)
        {
            double x16_plus_week_ago = x16_day_end[
               day_number] + x16_day_end[day_number-7];
            if(x16_plus_week_ago < 4.49*3.0*2.0)
            {
                // week_week_con constraint violated
                constraint_violated = true;
                break;
            }
        }
    }


            if (x[16] < 8.98 || (d1+d2+d3)>1.05) {
                    // constraint violated
                    constraint_violated = true;
                    break;
            }


    }
if (constraint_violated) {
  //          printf("[%lf,%lf,%lf]: Constraint Violated\n",
     d1, d2, d3);
}
else {
          obj=obj+5.0*8.0*(d1*d1+d2*d2+d3*d3);
```

```
            if( obj < obj_store[TID]){
              d1_store[TID]=d1;
              d2_store[TID]=d2;
              d3_store[TID]=d3;
              ts1_store[TID]=ts1;
              ts2_store[TID]=ts2;
              ts3_store[TID]=ts3;
              obj_store[TID] = obj;
            }
            /*
            file<<ts1;
            file<<"      ";
            file<<ts2;
            file<<"      ";
            file<< d1;
            file<<"      ";
            file<<d2;
            file<<"      ";
            file<<d3;
            file<<"      ";
            file<<obj<<endl;
            */// I want this to output to a txt or dat file//
  }

  delete []dx;
  delete []x;
  delete []u;
}// printf("%lf,%lf,%lf, %lf\n", d1, d2, d3, x[4]);

for (int i =0; i< NUM_THREADS; i++){
```

```
        file<<ts1_store[i];
        file<<"     ";
        file<<ts2_store[i];
        file<<"     ";
            file<< ts3_store[i];
            file<<"     ";
            file<<d1_store[i];
        file<<"     ";
        file<<d2_store[i];
        file<<"     ";
        file<<d3_store[i];
        file<<"     ";
        file<<obj_store[i]<<endl;
    }

    file.close();
    delete []x0;
    printf("yep\n");
    double end_time = omp_get_wtime();

    std::cout << "time: " << (end_time-start_time)<<" (s)"<< std::
       endl;
    return 0;

}
```

E.2 GENERATE DATA FILE FOR PYOMO

```
clc
clear all
close all
tic
warning off
 A=load('Result_long_3.txt');
 [Obj,index]=min(A(:,7));
 B=A(index,:);
mex Cancer_version_1.c

Pr=161.945448133839;
Train=161.945448133839;
IL_17=0.0794060143983421;
GCSF=0.330078919631521;
NC=44.9268017917568;
%Initial conditions
x0=[0.0,0.0,10000,10000,10,0,0,0,0,0,IL_17,GCSF, Pr, Train, Train,
    Train,NC,0,0];


%tspan=[0:60:24*60*21]';

tspan=zeros(24*21*9+1,1);
tspan(1)=0;
for i=1:1:504*9
      tspan(i*3-1)=(0.155+i-1)*60;
      tspan(i*3)=(0.645+i-1)*60;
```

```
    tspan(i*3+1)=i*60;
end

tsim=tspan;
u1=zeros(size(tspan),1);

for i=1:1:3
    for j=1:8
        if j==1
            u1(i+504*3*(j-1))=B(4);
        else
        u1(i+504*3*(j-1)+B(1)/60*3)=B(4);
        end
    u1(i+168*3+504*3*(j-1)+B(2)/60*3)=B(5);
    u1(i+168*2*3+504*3*(j-1)+B(3)/60*3)=B(6);
    end
end

PARAMETERS=simset('InitialState',x0,'Solver','ode15s','MaxStep',1,
    'OutputPoints','specified');
u=[tspan,u1];


%whos
%pause
%u=[tspan,dose,constant_dose];



[t,x,y]=    sim('sim_Cancer',tsim,PARAMETERS,u);
```

```
y(:,13);

fid = fopen('data.py', 'w');

fprintf(fid, 'x={');

for i=1:1:504*9
    for j = 5:1:18
        if ((i ~= 504*9) || (j ~= 18))
            fprintf(fid, '(%d,%d,0):%f,',j-1, i-1, y(i*3-1,j));
            fprintf(fid, '(%d,%d,1):%f,',j-1, i-1, y(i*3,j));
            fprintf(fid, '(%d,%d,2):%f,',j-1, i-1, y(i*3+1,j));
        else
            fprintf(fid, '(%d,%d,0):%f,',j-1, i-1, y(i*3-1,j));
            fprintf(fid, '(%d,%d,1):%f,',j-1, i-1, y(i*3,j));
            fprintf(fid, '(%d,%d,2):%f',j-1, i-1, y(i*3+1,j));
        end
    end
end
fprintf(fid, '}\n');

fprintf(fid, 'C_plasma={');
for i=1:1:504*9
    if i ~= 504*9
        fprintf(fid, '(%d,0):%f,',i-1, y(i*3-1,20));
        fprintf(fid, '(%d,1):%f,',i-1, y(i*3,20));
        fprintf(fid, '(%d,2):%f,',i-1, y(i*3+1,20));
    else
        fprintf(fid, '(%d,0):%f,',i-1, y(i*3-1,20));
```

```
        fprintf(fid, '(%d,1):%f,',i-1, y(i*3,20));
        fprintf(fid, '(%d,2):%f',i-1, y(i*3+1,20));
    end
end
fprintf(fid, '}\n');

fprintf(fid, 'C_tumor={');
for i = 1:1:504*9
    if i ~= 504*9
        fprintf(fid, '(%d,0):%f,',i-1, y(i*3-1,21));
        fprintf(fid, '(%d,1):%f,',i-1, y(i*3,21));
        fprintf(fid, '(%d,2):%f,',i-1, y(i*3+1,21));
    else
        fprintf(fid, '(%d,0):%f,',i-1, y(i*3-1,21));
        fprintf(fid, '(%d,1):%f,',i-1, y(i*3,21));
        fprintf(fid, '(%d,2):%f',i-1, y(i*3+1,21));
    end
end
fprintf(fid, '}\n');
fclose(fid);
```

E.3 PYOMO SIMULATION

```
from coopr.pyomo import *
from coopr.opt import SolverFactory
import data
########
### Model Definition
# Parameter
# Number of finite elements
```

```
nfe= 252*2*9
# Number of collocation points
ncp=3
FE=range(nfe)
CP=range(ncp)
# Total simulation time
time=30240*9
V_cell=1.0*10.0**-3.0 #ml, basing the hypothesis 10^6 cells =1 L;
r_cell=(3.0/(4.0*3.14)*V_cell)**(1.0/3.0) # mm*, Radius of the
    cell
e_porosity=53.57
A_tumor=4.0*3.14*r_cell*r_cell
V_tumor=V_cell*e_porosity
k_growth_1=0.062/24.0/60.0   #1/day
k_death=0.00021/24.0/60.0    #1/day
ratio=A_tumor/V_tumor
k_eff=1.212*ratio
EC_50=0.7873
E_max=0.0130*2.0
k_sc_bl=0.004
k_dgcsf=0.00072434
k_tr=0.00043
k_d=0.00155
Bmin =0.0002
Bmax= Bmin*1400.0
kG=1.0
kN=0.05
BGmax=0.1
DGr=0.00061297
DGn=0.0015
```

```
V_ven=5.53/2.0*1000.0
k_vbm=0.2514*1.5
Week_range=range(1,21*9-5)
S_xRange=range(4,18)
#Week_1_range=range(1,168+72+24)
#Week_2_range=range(169+72+24,168+168*2)
#Week_3_range=range(168+168+1,168+168*2)



#Setting up objective sampling vector
Weeks_6=[167,167+168,167+168*2,167+168*3,167+168*4,167+168*5,
    167+168*6, 167+168*7, 167+168*8,167+168*9, 167+168*10,
    167+168*11, 167+168*12, 167+168*13, 167+168*14, 167+168*15,
    167+168*16, 167+168*17, 167+168*18, 167+168*19, 167+168*20,
    167+168*21, 167+168*22, 167+168*23]
Days_21=[50, 50+504, 50+504*2, 50+504*3, 50+504*4, 50+504*5,
    50+504*6, 50+504*7]

#Setting up the toxicity sampling vector
Weeks_range_dose={}
for i in range(9):
     Weeks_range_dose[i]=range(504*i,504*(i+1))
Week={}
for i in Week_range:
     Week[i]=[24*i-1, 24*(i+1)-1, 24*(i+2)-1, 24*(i+3)-1, 24*(i+4)
         -1, 24*(i+5)-1, 24*(i+6)-1]

Day_range_7=range(1,21*9-5)
Day={}
for i in Day_range_7:
```

```
    Day[i]=[24*i-1,24*(6+i)-1]

# Initial Condition
for k in Week_range:
    if value(sum(data.x[16,i,ncp-1] for i in Week[k]))
        <4.49*3.0*7.0:
         print 'Week_range[',k,']:'

for k in Day_range_7:
    if value(sum(data.x[16,i,ncp-1] for i in Day[k]))
        <4.49*3.0*2.0:
         print 'Day_range[',k,']:'
x0={}
x0[4]=10.0
x0[5]=0.0
x0[6]=0.0
x0[7]=0.0
x0[8]=0.0
x0[9]=0.0
x0[10]=0.0794060143983421
x0[11]=0.330078919631521
x0[12]=161.945448133839
x0[13]=161.945448133839
x0[14]=161.945448133839
x0[15]=161.945448133839
x0[16]=44.9268017917568
x0[17]=0.0


model=ConcreteModel()
```

```
a_init = {}
a_init[0,0] = 0.19681547722366
a_init[0,1] = 0.39442431473909
a_init[0,2] = 0.37640306270047
a_init[1,0] = -0.06553542585020
a_init[1,1] = 0.29207341166523
a_init[1,2] = 0.51248582618842
a_init[2,0] = 0.02377097434822
a_init[2,1] = -0.04154875212600
a_init[2,2] = 0.11111111111111
model.a = Param(FE,CP, initialize=a_init)

h = [60.0]*nfe

def _init_x(m,n,i,j):
    return x0[n]
x_l_bound={}
x_u_bound={}

# Setting up the bounds
for i in S_xRange:
    if i <10:
        x_l_bound[i]=None
        x_u_bound[i]=None
    else:
      x_l_bound[i]=0.0
      x_u_bound[i]=None
    if i == 16:
        x_l_bound[i]=4.49*2.0
        x_u_bound[i]=None
```

```
def _bound_x(m,n,i,j):
#     return [None,None]
    return [x_l_bound[n],x_u_bound[n]]

model.x=Var(S_xRange,FE,CP, within=Reals, initialize=data.x,
   bounds=_bound_x)
model.xdot=Var(S_xRange,FE,CP, initialize=0.0)
model.C_plasma=Var(FE,CP,within=NonNegativeReals, initialize=0.0)
model.C_tumor=Var(FE,CP,within=NonNegativeReals, initialize=0.0)
model.u=Var(FE,within=NonNegativeReals,bounds=(0.0,None))


### ACTION RULE FIX VARIABLE##


def action_rule_1(model):
    for i in range(0,504*9):
        model.u[i] = 0.0
        model.u[i].fixed = True
    model.u[0].fixed = False
    model.u[168+72].fixed = False
    model.u[(168)*2+24].fixed = False
    model.u[0] = 0.30
    model.u[168+72] = 0.25
    model.u[(168)*2+24] = 0.15
    for i in range(1,8):
        model.u[0+504*i].fixed = False
        model.u[168+72+504*i].fixed = False
        model.u[(168)*2+24+504*i].fixed = False
        model.u[0+504*i] = 0.30
```

```
        model.u[168+72+504*i] = 0.25
        model.u[(168)*2+24+504*i] = 0.15
model.action_1 = BuildAction(rule = action_rule_1)

# Initialize Simulation
def action_initial(model):
    for i in FE:
        for j in CP:
            model.xdot[4,i,j]=ratio*k_growth_1*pow(10.0,(ratio
                -1.0)/ratio*data.x[4,i,j])-ratio*k_death*pow
                (10.0,(1.0-ratio)/(ratio*ratio)*data.x[4,i,j])-
                k_eff*data.C_tumor[i,j]
            model.xdot[5,i,j]= -0.0003227*data.x[5,i,j] -
                0.0001258*data.x[6,i,j] - 0.0003706*data.x[7,i,j] +
                 0.00244*data.x[8,i,j]- 1.147e-5*data.x[9,i,j]+
                0.1104*value(model.u[i])
            model.xdot[6,i,j]= 0.0003651*data.x[5,i,j] - 0.001133*
                data.x[6,i,j] - 0.0003706*data.x[7,i,j] + 0.00244*
                data.x[8,i,j] + 0.001631*data.x[9,i,j] - 0.06455*
                value(model.u[i])
            model.xdot[7,i,j]=-0.000815*data.x[5,i,j] + 0.004922*
                data.x[6,i,j] - 0.01027*data.x[7,i,j] - 0.007773*
                data.x[8,i,j] - 0.005653*data.x[9,i,j] + 0.135*
                value(model.u[i])
            model.xdot[8,i,j]=-0.0004651*data.x[5,i,j] + 0.00267*
                data.x[6,i,j] - 0.01128*data.x[7,i,j] - 0.03372*
                data.x[8,i,j] - 0.03837*data.x[9,i,j] + 0.07957*
                value(model.u[i])
            model.xdot[9,i,j]=-0.0002971*data.x[5,i,j] + 0.001775*
                data.x[6,i,j] - 0.007655*data.x[7,i,j] - 0.03837*
```

```
            data.x[8,i,j] - 0.1122*data.x[9,i,j] + 0.05083*
                value(model.u[i])
            model.xdot[10,i,j]=(BGmax*kN/(kN+data.x[16,i,j])
                -0.0014*data.x[10,i,j])
            model.xdot[11,i,j]=(0.00092174*data.x[10,i,j
                ]-0.00022174*data.x[11,i,j])
            model.xdot[12,i,j]=((Bmin*kG + Bmax*data.x[11,i,j])/(
                kG+data.x[11,i,j])-k_tr*data.x[12,i,j]-E_max*data.x
                [17,i,j]/(EC_50+data.x[17,i,j])*data.x[12,i,j])
            model.xdot[13,i,j]=k_tr*data.x[12,i,j]-k_tr*data.x[13,
                i,j]
            model.xdot[14,i,j]=k_tr*data.x[13,i,j]-k_tr*data.x[14,
                i,j]
            model.xdot[15,i,j]=k_tr*data.x[14,i,j]-k_tr*data.x[15,
                i,j]
            model.xdot[16,i,j]= k_tr*data.x[15,i,j]-k_d*data.x[16,
                i,j]
            model.xdot[17,i,j]= (k_vbm*data.C_plasma[i,j]-0.0802*
                data.x[17,i,j]*(1.0-data.x[17,i,j]/(0.0005+data.x
                [17,i,j])))
model.action_2=BuildAction(rule = action_initial)



# Setting up Model
def C_plasma_cal(m, i, j):
    return m.C_plasma[i,j]==(0.01279*m.x[5,i,j] - 0.06116*m.x[6,i,
        j] + 0.09328*m.x[7,i,j] + 0.07936*m.x[8,i,j] + 0.05068*m.x
        [9,i,j])*0.025
model.C_Plasma_con=Constraint(FE,CP, rule=C_plasma_cal)
```

```
def C_tumor_cal(m, i, j):
    return m.C_tumor[i,j]==(0.1096*m.x[5,i,j] - 0.02064*m.x[6,i,j]
        - 0.09764*m.x[7,i,j] - 0.005715*m.x[8,i,j] - 0.003903*m.x
        [9,i,j])*0.0007
model.C_Tumor_con=Constraint(FE,CP, rule=C_tumor_cal)

#### Tumor growth model
def xdot_4_cal(m,i,j):
    return m.xdot[4,i,j]==((ratio*k_growth_1*pow(10.0,(ratio-1.0)/
        ratio*m.x[4,i,j])-ratio*k_death*pow(10.0,(1.0-ratio)/(ratio
        *ratio)*m.x[4,i,j])-k_eff*m.C_tumor[i,j]))
model.N_tumor_con=Constraint(FE,CP, rule=xdot_4_cal)
### Pharamacokinetics_model
def xdot_5_cal(m, i, j):
   return m.xdot[5,i,j]==-0.0003227*m.x[5,i,j] - 0.0001258*m.x[6,i
      ,j] + 0.0005422*m.x[7,i,j] - 1.825e-5*m.x[8,i,j] - 1.147e-5*
      m.x[9,i,j]+ 0.1104*m.u[i]
model.xdot_5_con=Constraint(FE,CP, rule=xdot_5_cal)
def xdot_6_cal(m,i,j):
    return m.xdot[6,i,j]== 0.0003651*m.x[5,i,j] - 0.001133*m.x[6,i
        ,j] - 0.0003706*m.x[7,i,j] + 0.00244*m.x[8,i,j] + 0.001631*
        m.x[9,i,j] - 0.06455*m.u[i]
model.xdot_6_con=Constraint(FE,CP,rule=xdot_6_cal)
def xdot_7_cal(m,i,j):
    return m.xdot[7,i,j]==-0.000815*m.x[5,i,j] + 0.004922*m.x[6,i,
        j] - 0.01027*m.x[7,i,j] - 0.007773*m.x[8,i,j] - 0.005653*m.
        x[9,i,j] + 0.135*m.u[i]
model.xdot_7_co=Constraint(FE,CP,rule=xdot_7_cal)
def xdot_8_cal(m,i,j):
```

```
    return m.xdot[8,i,j]==-0.0004651*m.x[5,i,j] + 0.00267*m.x[6,i,
        j] - 0.01128*m.x[7,i,j] - 0.03372*m.x[8,i,j] - 0.03837*m.x
        [9,i,j] + 0.07957*m.u[i]
model.xdot_8_con=Constraint(FE,CP, rule=xdot_8_cal)
def xdot_9_cal(m,i,j):
    return m.xdot[9,i,j]==-0.0002971*m.x[5,i,j] + 0.001775*m.x[6,i
        ,j] - 0.007655*m.x[7,i,j] - 0.03837*m.x[8,i,j] - 0.1122*m.x
        [9,i,j] + 0.05083*m.u[i]
model.xdot_9_con=Constraint(FE,CP, rule=xdot_9_cal)
#### Toxicity model
# IL-17
def xdot_10_cal(m,i,j):
    return m.xdot[10,i,j]==(BGmax*kN/(kN+m.x[16,i,j]) -0.0014*m.x
        [10,i,j])
model.xdot_10_con=Constraint(FE,CP, rule=xdot_10_cal)
# G-CSF
def xdot_11_cal(m,i,j):
    return m.xdot[11,i,j]==(0.00092174*m.x[10,i,j]-0.00022174*m.x
        [11,i,j])#+k_sc_bl*m.x[18,i,j])
model.xdot_11_con=Constraint(FE,CP,rule=xdot_11_cal)
# Neutrophils Precursor (This is where the toxicity of drug acts)
def xdot_12_cal(m,i,j):
    return m.xdot[12,i,j]==((Bmin*kG + Bmax*m.x[11,i,j])/(kG+m.x
        [11,i,j])-k_tr*m.x[12,i,j]-E_max*m.x[17,i,j]/(EC_50+m.x[17,
        i,j])*m.x[12,i,j])
model.xdot_12_con=Constraint(FE,CP, rule=xdot_12_cal)
# Transition state 1
def xdot_13_cal(m,i,j):
    return m.xdot[13,i,j]==k_tr*m.x[12,i,j]-k_tr*m.x[13,i,j]
model.xdot_13_con=Constraint(FE,CP, rule=xdot_13_cal)
```

```
# Transition state 2
def xdot_14_cal(m,i,j):
    return m.xdot[14,i,j]==k_tr*m.x[13,i,j]-k_tr*m.x[14,i,j]
model.xdot_14_con=Constraint(FE,CP, rule=xdot_14_cal)
# Transistion state 3
def xdot_15_cal(m,i,j):
    return m.xdot[15,i,j]==k_tr*m.x[14,i,j]-k_tr*m.x[15,i,j]
model.xdot_15_con=Constraint(FE,CP, rule=xdot_15_cal)
# Circulating neutrophils ( This is where the measurement
    available)
def xdot_16_cal(m,i,j):
    return m.xdot[16,i,j]== k_tr*m.x[15,i,j]-k_d*m.x[16,i,j]
model.xdot_16_con=Constraint(FE,CP, rule=xdot_16_cal)
# drug toxicity
def xdot_17_cal(m,i,j):
    return m.xdot[17,i,j]== (k_vbm*m.C_plasma[i,j]-0.0802*m.x[17,i
        ,j]*(1.0-m.x[17,i,j]/(0.0005+m.x[17,i,j])))
model.xdot_17_con=Constraint(FE,CP, rule=xdot_17_cal)



# Maximum dose per week
def _3_weeks_max(m,k):
    return sum(m.u[i] for i in Weeks_range_dose[k])<=1.05
#model.weeks_3_con=Constraint(range(1),rule=_3_weeks_max)

#No Toxicity level 3 Constraint
def Neutrophils_c(m,i,j):
    return m.x[16,i,j]>= 4.49*2.0
#model.neutrophils_con=Constraint(FE,CP,rule=Neutrophils_c)
```

```
#Week to week Neutrophil Constraint
def _week_week(m, k):
    return sum(m.x[16,i,ncp-1] for i in Week[k]) >=4.49*3.0*7.0
#model.week_week_con=Constraint(Week_range, rule=_week_week)
def _7_days(m, k):
    return sum(m.x[16,i,ncp-1] for i in Day[k]) >=4.49*3.0*2.0
#model.seven_days_con=Constraint(Day_range_7, rule=_7_days)


def fecolx_rule(m,n,i,j):
    if i==0:
        return m.x[n,i,j]==x0[n] + h[i]*sum(m.a[k,j]*m.xdot[n,i,k]
            for k in CP)
    else:
        return m.x[n,i,j]==m.x[n,i-1,ncp-1]+h[i]*sum(m.a[k,j]*m.
            xdot[n,i,k] for k in CP)
model.fecolx =Constraint(S_xRange,FE,CP, rule=fecolx_rule)


#objective: minimizing dose per week and penalize the small dose (
    emphasis on the early tumor elimination)
def obj_rule(m):
    return \
        sum ((m.x[4,i,ncp-1]) for i in Weeks_6) +5.0*sum(m.u[i]**2
            for i in FE)

model.cost = Objective(rule=obj_rule, sense=minimize)
opt = SolverFactory('ipopt', solver_io='nl')
instance = model.create()
```

```
instance.weeks_3_con=Constraint(range(9),rule=_3_weeks_max)
instance.week_week_con=Constraint(Week_range, rule=_week_week)
instance.seven_days_con=Constraint(Day_range_7, rule=_7_days)

instance.preprocess()
results = opt.solve(instance,keepfiles=False,tee=True)
instance.load(results)
#instance.x.pprint()

# Printing result
f=open("result_no_grade_4th_max_dose_1_long_4.txt","w")
for i in FE:
  print>>f, model.C_tumor[i,ncp-1].value,''''''.rjust(10), model.
      C_plasma[i,ncp-1].value,''''''.rjust(10),model.u[i].value
```

BIBLIOGRAPHY

[1] L.E. Friberg, A. Henningsson, H. Maas, L. Nguyen, and M.O. Karlsson. Model of chemotherapy-induced myelosuppression with parameter consistency across drugs. *Journal of Clinical Oncology*, 20(24):4713–4721, 2002.

[2] G.H. Lyman. Neutropenia. *Encyclopedia of Cancer*, pages 2506–2509, 2012.

[3] F.E. de Jongh, J.M. Gallo, M. Shen, J. Verweij, and A. Sparreboom. Population pharmacokinetics of cisplatin in adult cancer patients. *Cancer chemotherapy and pharmacology*, 54(2):105–112, 2004.

[4] M.L. Pastor, C.M. Laffont, L. Gladieff, A. Schmitt, E. Chatelut, and D. Concordet. Model-based approach to describe g-csf effects in carboplatin-treated cancer patients. *Pharmaceutical research*, 30(11):2795–2807, 2013.

[5] J.A. Florian. *Modeling and dose schedule design for cyclic-specific chemotherapeutics*. Dissertation, University of Pittsburgh, 2008.

[6] B. Wang, T.M. Ludden, E.N. Cheung, G.G. Schwab, and L.K. Roskos. Population pharmacokineticpharmacodynamic modeling of filgrastim (r-methug-csf) in healthy volunteers. *Journal of Pharmacokinetics and Pharmacodynamics*, 28:321–342, 2001.

[7] A.F. Suffredini, D. Reda, S.M. Banks, M. Tropea, J. M. Agosti, and R. Miller. Effects of recombinant dimeric tnf receptor on human inflammatory responses following intravenous endotoxin administration. *The Journal of Immunology*, 155(10):5038–5045, 1995.

[8] T. Ho, G. Clermont, and R.S. Parker. A model of neutrophil dynamics in response to inflammatory and cancer chemotherapy challenges. *Computers & Chemical Engineering*, 2012.

[9] R.N. Bergman, L.S. Phillips, and C. Cobelli. Physiologic evaluation of factors controlling glucose tolerance in man: measurement of insulin sensitivity and beta-cell glucose sensitivity from the response to intravenous glucose. *Journal of Clinical Investigation*, 68(6):1456, 1981.

[10] D.M. Cutler and N.R. Sahni. If slow rate of health care spending growth persists, projections may be off by $770 billion. *Health Affairs*, 32(5):841–850, 2013.

[11] S.P. Keehan, A.M. Sisko, C.J. Truffer, J.A. Poisal, G.A. Cuckler, A.J. Madison, J.M. Lizonitz, and S.D. Smith. National health spending projections through 2020: economic recovery and reform drive faster spending growth. *Health Affairs*, 30(8):1594–1605, 2011.

[12] S.P. Keehan, G.A. Cuckler, A.M. Sisko, A.J. Madison, S.D. Smith, J.M. Lizonitz, J.A. Poisal, and C.J. Wolfe. National health expenditure projections: modest annual growth until coverage expands and economic growth accelerates. *Health Affairs*, 31(7):1600–1612, 2012.

[13] P.C. Wroe, J.A. Finkelstein, G.T. Ray, J.A. Linder, K.M. Johnson, S. Rifas-Shiman, M.R. Moore, and S.S. Huang. Aging population and future burden of pneumococcal pneumonia in the united states. *Journal of Infectious Diseases*, 205(10):1589–1592, 2012.

[14] D.G. Kirch, M.K. Henderson, and M.J. Dill. Physician workforce projections in an era of health care reform. *Annual review of medicine*, 63:435–445, 2012.

[15] Y. Orr, J.M. Taylor, P.G. Bannon, C. Geczy, and L. Kritharides. Circulating cd10+cd16low neutrophils provide a quantitative index of active bone marrow neutrophil release. *British Journal of Haematology*, 131(4):508–519, 2005.

[16] Y. Orr, D.P. Wilson, J.M. Taylor, P.G. Bannon, C. Geczy, M.P. Davenport, and L. Kritharides. A kinetic model of bone marrow neutrophil production that characterizes late phenotypic maturation. *American Journal of Physiology - Regulatory, Integrative and Comparative Physiology*, 292(4):R1707–R1716, 2007.

[17] W.A. Ritschel, G.L. Kearns, et al. *Handbook of basic pharmacokinetics–including clinical applications*. American Pharmacists Association Washington, DC, 2004.

[18] D A. Smith, C. Allerton, A.S. Kalgutkar, H. Waterbeemd, and D.K. Walker. *Pharmacokinetics and metabolism in drug design*. John Wiley & Sons, 2012.

[19] F.G. King, R.L. Dedrick, and F.F. Farris. Physiological pharmacokinetic modeling ofcis-dichlorodiammineplatinum (ii)(ddp) in several species. *Journal of Pharmacokinetics and Pharmacodynamics*, 14(2):131–155, 1986.

[20] Y. Chu, J. Hahn, et al. Model simplification procedure for signal transduction pathway models: An application to il-6 signaling. *Chemical engineering science*, 65(6):1964–1975, 2010.

[21] C.A. Floudas and C.E. Gounaris. A review of recent advances in global optimization. *Journal of Global Optimization*, 45(1):3–38, 2009.

[22] M.G. Safonov and R.Y. Chiang. A schur method for balanced-truncation model reduction. *Automatic Control, IEEE Transactions on*, 34(7):729–733, 1989.

[23] S. Daun, J. Rubin, Y. Vodovotz, A. Roy, R. Parker, and G. Clermont. An ensemble of models of the acute inflammatory response to bacterial lipopolysaccharide in rats: results from parameter space reduction. *Journal of theoretical biology*, 253(4):843–853, 2008.

[24] K. Murphy, P. Travers, and M. Walport. *Janeway's Immunobiology*. Taylor and Francis, 2011.

[25] C.N. Serhan, P.A. Ward, and D.W. Gilroy. *Fundamentals of inflammation*. Cambridge University Press, 2010.

[26] C. Summers, S.M. Rankin, A.M. Condliffe, N. Singh, A.M. Peters, and E.R. Chilvers. Neutrophil kinetics in health and disease. *Trends in Immunology*, 31(8):318 – 324, 2010.

[27] M. Rosinski, M.L. Yarmush, and F. Berthiaume. Quantitative dynamics of in vivo bone marrow neutrophil production and egress in response to injury and infection. *Annals of Biomedical Engineering*, 32:1109–1120, 2004.

[28] H. Lee and M. Ratajczak. Innate immunity: a key player in the mobilization of hematopoietic stem/progenitor cells. *Archivum Immunologiae et Therapiae Experimentalis*, 57:269–278, 2009.

[29] M.A. Stark, Y. Huo, T. L. Burcin, M. A. Morris, T. S. Olson, and K. Ley. Phagocytosis of apoptotic neutrophils tegulates granulopoiesis via il-23 and il-17. *Immunity*, 22(3):285 – 294, 2005.

[30] S.D. Kobayashi and F.R. DeLeo. Role of neutrophils in innate immunity: a systems biology-level approach. *Wiley Interdisciplinary Reviews: Systems Biology and Medicine*, 1(3):309–333, 2009.

[31] J.H. Pruitt, E.M. Copeland, and L.L. Moldawer. Interleukin-1 and interleukin-1 antagonism in sepsis, systemic inflammatory response syndrome, and septic shock. *Shock (Augusta, Ga.)*, 3(4), 04 1995.

[32] D.G. Remick, D.E. Newcomb, G.L. Bolgos, and D.R. Call. Comparison of the mortality and inflammatory response of two models of sepsis: lipopolysaccharide vs. cecal ligation and puncture. *Shock*, 13(2), 2000.

[33] J. Mestas and C.C. Hughes. Of mice and not men: differences between mouse and human immunology. *The Journal of Immunology*, 172(5):2731–2738, 2004.

[34] S. Copeland, H.S. Warren, S.F. Lowry, S.E. Calvano, D. Remick, et al. Acute inflammatory response to endotoxin in mice and humans. *Clinical and diagnostic laboratory immunology*, 12(1):60–67, 2005.

[35] J. Seok, H.S. Warren, A.G. Cuenca, M.N. Mindrinos, H.V. Baker, W. Xu, D.R. Richards, et al. Genomic responses in mouse models poorly mimic human inflammatory diseases. *Proceedings of the National Academy of Sciences*, 110(9):3507–3512, 2013.

[36] K. Buttenschoen and H. Radermacher, P.and Bracht. Endotoxin elimination in sepsis: physiology and therapeutic application. *Langenbeck's Archives of Surgery*, 395:597–605, 2010.

[37] L.E. Friberg and M.O. Karlsson. mechanistic models for myelosuppression. *Investigational New Drugs*, 21:183–194, 2003.

[38] M.O. Karlsson, T. Anehall, L.E. Friberg, A. Henningsson, C. Kloft, M. Sandstram, and R. Xie. Pharmacokinetic/pharmacodynamic modelling in oncological drug development. *Basic & Clinical Pharmacology & Toxicology*, 96(3):206–211, 2005.

[39] J.H. Lorch, O. Goloubeva, R.I. Haddad, K. Cullen, N. Sarlis, R. Tishler, M. Tan, J. Fasciano, D.E. Sammartino, and M.R. Posner. Induction chemotherapy with cisplatin and fluorouracil alone or in combination with docetaxel in locally advanced squamous-cell cancer of the head and neck: long-term results of the tax 324 randomised phase 3 trial. *The lancet oncology*, 12(2):153–159, 2011.

[40] M. Di Maio, C. Gridelli, C. Gallo, F. Shepherd, F.V. Piantedosi, S. Cigolari, L. Manzione, A. Illiano, S. Barbera, S.F. Robbiati, et al. Chemotherapy-induced neutropenia and treatment efficacy in advanced non-small-cell lung cancer: a pooled analysis of three randomised trials. *The lancet oncology*, 6(9):669–677, 2005.

[41] J. Cebon, J.E. Layton, D. Maher, and G. Morstyn. Endogenous haemopoietic growth factors in neutropenia and infection. *British Journal of Haematology*, 86(2):265–274, 1994.

[42] Y. Nakano and R. Okutani. Perioperative management for a patient with chronic pancytopenia: a case of aplastic anemia with persistent neutropenia following preoperative administration of g-csf. *Journal of Anesthesia*, 24:268–271, 2010.

[43] A. Bamias, G. Aravantinos, C. Deliveliotis, D. Bafaloukos, C. Kalofonos, N. Xiros, A. Zervas, D. Mitropoulos, E. Samantas, D. Pectasides, et al. Docetaxel and cisplatin with granulocyte colony-stimulating factor (g-csf) versus mvac with g-csf in advanced urothelial carcinoma: a multicenter, randomized, phase iii study from the hellenic cooperative oncology group. *Journal of Clinical Oncology*, 22(2):220–228, 2004.

[44] M.J. Dugan, R.T. Maziarz, W.I. Bensinger, A. Nademanee, J. Liesveld, K. Badel, C. Dehner, C. Gibney, G. Bridger, and G. Calandra. Safety and preliminary efficacy of plerixafor (mozobil) in combination with chemotherapy and g-csf: an open-label, multicenter, exploratory trial in patients with multiple myeloma and non-hodgkin's lymphoma undergoing stem cell mobilization. *Bone marrow transplantation*, 45(1):39–47, 2009.

[45] U. Steidl, R. Fenk, I. Bruns, F. Neumann, M. Kondakci, B. Hoyer, T. Gräf, U.P. Rohr, S. Bork, R. Kronenwett, et al. Successful transplantation of peripheral blood stem cells mobilized by chemotherapy and a single dose of pegylated g-csf in patients with multiple myeloma. *Bone marrow transplantation*, 35(1):33–36, 2004.

[46] W.P. Sheridan, C.G. Begley, L.B. To, A. Grigg, J. Szer, D. Maher, M.D. Green, P.A. Rowlings, K. M. McGrath, and J. Cebon. Phase ii study of autologous filgrastim (g-csf)-mobilized peripheral blood progenitor cells to restore hemopoiesis after high-dose chemotherapy for lymphoid malignancies. *Bone marrow transplantation*, 14(1):105–111, 1994.

[47] J. Bergh, T. Wiklund, B. Erikstein, E. Lidbrink, P. Lindman, H.and Malmström, P. Kellokumpu-Lehtinen, N. Bengtsson, G. Söderlund, G. Anker, et al. Tailored fluorouracil, epirubicin, and cyclophosphamide compared with marrow-supported high-dose chemotherapy as adjuvant treatment for high-risk breast cancer: a randomised trial. *The Lancet*, 356(9239):1384–1391, 2000.

[48] R. Malka, B. Wolach, R. Gavrieli, E. Shochat, V. Rom-Kedar, et al. Evidence for bistable bacteria-neutrophil interaction and its clinical implications. *The Journal of clinical investigation*, 122(8):3002–3011, 2012.

[49] E. Shochat, V. Rom-Kedar, and L. Segel. G-csf control of neutrophils dynamics in the blood. *Bulletin of Mathematical Biology*, 69:2299–2338, 2007.

[50] S.O. Song, J. Hogg, Z. Peng, R.S. Parker, J.A. Kellum, and G. Clermont. Ensemble models of neutrophil trafficking in severe sepsis. *PLoS computational biology*, 8(3):e1002422, 2012.

[51] Y. Vodovotz, G. Clermont, C. Chow, and G. An. Mathematical models of the acute inflammatory response. *Current Opinion in Critical Care*, 10(5):383–390, 2004.

[52] C.C. Chow, G. Clermont, R. Kumar, C. Lagoa, Z. Tawadrous, D. Gallo, B. Betten, J. Bartels, G. Constantine, M.P. Fink, T.R. Billiar, and Y. Vodovotz. The acute inflammatory response in diverse shock states. *Shock*, 24:74–84, 2005.

[53] M.N. Hamers, A.A. Bot, R.S. Weening, H.J. Sips, and D. Roos. Kinetics and mechanism of the bactericidal action of human neutrophils against escherichia coli. *Blood*, 64(3):635–641, 1984.

[54] A. Reynolds, J. Rubin, G. Clermont, J. Day, Y. Vodovotz, and B.G. Ermentrout. A reduced mathematical model of the acute inflammatory response: I. derivation of model and analysis of anti-inflammation. *Journal of Theoretical Biology*, 242(1):220 – 236, 2006.

[55] J. Day, J. Rubin, Y. Vodovotz, C.C. Chow, A. Reynolds, and G. Clermont. A reduced mathematical model of the acute inflammatory response ii. capturing scenarios

of repeated endotoxin administration. *Journal of theoretical biology*, 242(1):237–256, 2006.

[56] R.I. Walker and R. Willemze. Neutrophilkinetics and the regulation of granulopoiesis. *Reviews of Infectious Diseases*, 2(2):pp. 282–292, 1980.

[57] O.D. Rotstein. Modeling the two-hit hypothesis for evaluating strategies to prevent organ injury after shock/resuscitation. *Journal of Trauma-Injury, Infection, and Critical Care*, 54(5):S203–S206, 2003.

[58] A.B. Pigozzo, G.C. Macedo, R.W. dos Santos, and M. Lobosco. On the computational modeling of the innate immune system. *BMC bioinformatics*, 14(Suppl 6):S7, 2013.

[59] W.C. Zamboni, D.Z. DArgenio, C.F. Stewart, T. MacVittie, B.J. Delauter, A.M. Farese, D.M. Potter, N.M. Kubat, D. Tubergen, and M.J. Egorin. Pharmacodynamic model of topotecan-induced time course of neutropenia. *Clinical cancer research*, 7(8):2301–2308, 2001.

[60] J.C. Panetta, P. Schaiquevich, V.M. Santana, and C.F. Stewart. Using pharmacokinetic and pharmacodynamic modeling and simulation to evaluate importance of schedule in topotecan therapy for pediatric neuroblastoma. *Clinical Cancer Research*, 14(1):318–325, 2008.

[61] J.E. Wallin, L.E. Friberg, and M.O. Karlsson. A tool for neutrophil guided dose adaptation in chemotherapy. *Computer methods and programs in biomedicine*, 93(3):283–291, 03 2009.

[62] S.J. Kathman, D.H. Williams, J.P. Hodge, and M. Dar. A bayesian population pk–pd model for ispinesib/docetaxel combination-induced myelosuppression. *Cancer chemotherapy and pharmacology*, 63(3):469–476, 2009.

[63] C. Engel, M. Scholz, and M. Loeffler. A computational model of human granulopoiesis to simulate the hematotoxic effects of multicycle polychemotherapy. *Blood*, 104(8):2323–2331, 2004.

[64] O. Vainas, S. Ariad, O. Amir, W. Mermershtain, V. Vainstein, M. Kleiman, O. Inbar, R. Ben-Av, A. Mukherjee, S. Chan, et al. Personalising docetaxel and g-csf schedules in cancer patients by a clinically validated computational model. *British journal of cancer*, 107(5):814–822, 2012.

[65] E.K. Afenya. Recovery of normal hemopoiesis in disseminated cancer therapy–a model. *Mathematical biosciences*, 172(1):15–32, 2001.

[66] Z. Agur, R. Hassin, and S. Levy. Optimizing chemotherapy scheduling using local search heuristics. *Operations research*, 54(5):829–846, 2006.

[67] M. Alamir and S. Chareyron. State-constrained optimal control applied to cell-cycle-specific cancer chemotherapy. *Optimal Control Applications and Methods*, 28(3):175–190, 2007.

[68] M.S. Alam, M.A. Hossain, S. Algoul, M.A.A. Majumader, M.A. Al-Mamun, G. Sexton, and R. Phillips. Multi-objective multi-drug scheduling schemes for cell cycle specific cancer treatment. *Computers & Chemical Engineering*, 2013.

[69] Y. Batmani and H. Khaloozadeh. Multi objective optimization of drug regimens in cancer chemotherapy using a pk-pd model. In *Electrical Engineering (ICEE), 2011 19th Iranian Conference on*, pages 1–6. IEEE, 2011.

[70] C.A. Charles, V.K. Yee, S.W. Dusza, A.A. Marghoob, S.A. Oliveria, A. Kopf, D. Rigel, and A.C. Halpern. Variation in the diagnosis, treatment, and management of melanoma in situ: a survey of us dermatologists. *Archives of dermatology*, 141(6):723, 2005.

[71] M.I.S. Costa, J.L. Boldrini, and R.C. Bassanezi. Drug kinetics and drug resistance in optimal chemotherapy. *Mathematical biosciences*, 125(2):191–209, 1995.

[72] J.A. Florian Jr, J.L. Eiseman, and R.S. Parker. A nonlinear model predictive control algorithm for breast cancer treatment. In *Proc. DYCOPS*, volume 7, pages 1–12, 2004.

[73] M. Itik, M.U. Salamci, and S.P. Banks. Optimal control of drug therapy in cancer treatment. *Nonlinear Analysis: Theory, Methods & Applications*, 71(12):e1473–e1486, 2009.

[74] A. Iliadis and D. Barbolosi. Optimizing drug regimens in cancer chemotherapy by an efficacy–toxicity mathematical model. *Computers and Biomedical Research*, 33(3):211–226, 2000.

[75] R.B. Martin, M.E. Fisher, R.F. Minchin, and K.L. Teo. A mathematical model of cancer chemotherapy with an optimal selection of parameters. *Mathematical biosciences*, 99(2):205–230, 1990.

[76] J.M. Harrold and R.S. Parker. Clinically relevant cancer chemotherapy dose scheduling via mixed-integer optimization. *Computers & Chemical Engineering*, 33(12):2042–2054, 2009.

[77] R.B. Martin. Optimal control drug scheduling of cancer chemotherapy. *Automatica*, 28(6):1113–1123, 1992.

[78] R. Martin, K.L. Teo, and M. D'Incalci. *Optimal control of drug administration in cancer chemotherapy*. World Scientific, 1994.

[79] J.A. Florian, J.L. Eiseman, and R.S. Parker. Nonlinear model predictive control for dosing daily anticancer agents using a novel saturating-rate cell-cycle model. *Computers in Biology and Medicine*, 38(3):339–347, 2008.

[80] E. Pefani, N. Panoskaltsis, A. Mantalaris, M.C. Georgiadis, and E.N. Pistikopoulos. Design of optimal patient-specific chemotherapy protocols for the treatment of acute myeloid leukemia (aml). *Computers & Chemical Engineering*, 2013.

[81] G.W. Swan. Cancer chemotherapy: Optimal control using the verhulst-pearl equation. *Bulletin of Mathematical Biology*, 48(3):381–404, 1986.

[82] S. Zietz and C. Nicolini. Mathematical approaches to optimization of cancer chemotherapy. *Bulletin of Mathematical Biology*, 41(3):305–324, 1979.

[83] S. Nanda, H. Moore, and S. Lenhart. Optimal control of treatment in a mathematical model of chronic myelogenous leukemia. *Mathematical biosciences*, 210(1):143–156, 2007.

[84] F.L. Pereira, C.E. Pedreira, M.R. Pinho, M.H. Fernandes, and J.B. Sousa. An optimal control algorithm for multidrug cancer chemotherapy design. In *Engineering in Medicine and Biology Society, 1990., Proceedings of the Twelfth Annual International Conference of the IEEE*, pages 1021–1022. IEEE, 1990.

[85] J.C. Panetta and J. Adam. A mathematical model of cycle-specific chemotherapy. *Mathematical and computer modelling*, 22(2):67–82, 1995.

[86] U. Ledzewicz and H. Schattler. Analysis of a class of optimal control problems arising in cancer chemotherapy. In *American Control Conference, 2002. Proceedings of the 2002*, volume 5, pages 3460–3465. IEEE, 2002.

[87] U. Ledzewicz and H. Schättler. Optimal bang-bang controls for a two-compartment model in cancer chemotherapy. *Journal of Optimization Theory and Applications*, 114(3):609–637, 2002.

[88] S.M. Tse, Y. Liang, K. Leung, K. Lee, and T. Mok. A memetic algorithm for multiple-drug cancer chemotherapy schedule optimization. *Systems, Man, and Cybernetics, Part B: Cybernetics, IEEE Transactions on*, 37(1):84–91, 2007.

[89] A. Swierniak and J. Smieja. Cancer chemotherapy optimization under evolving drug resistance. *Nonlinear Analysis: Theory, Methods & Applications*, 47(1):375–386, 2001.

[90] D. Cella, A. Peterman, S. Hudgens, K. Webster, and M.A. Socinski. Measuring the side effects of taxane therapy in oncology. *Cancer*, 98(4):822–831, 2003.

[91] T. Thigpen. Maybe more is better. *Journal of clinical oncology*, 21(13):2454–2456, 2003.

[92] M. Kimmel and O. Gorlova. Stochastic models of progression of cancer and their use in controlling cancer-related mortality. In *American Control Conference, 2002. Proceedings of the 2002*, volume 5, pages 3443–3448. IEEE, 2002.

[93] W. Krabs and S. Pickl. An optimal control problem in cancer chemotherapy. *Applied Mathematics and Computation*, 217(3):1117–1124, 2010.

[94] J. McCall, A. Petrovski, and S. Shakya. Evolutionary algorithms for cancer chemotherapy optimization. *Computational Intelligence in Bioinformatics*, pages 265–296, 2008.

[95] G. Ochoa, M. Villasana, and E.K. Burke. An evolutionary approach to cancer chemotherapy scheduling. *Genetic Programming and Evolvable Machines*, 8(4):301–318, 2007.

[96] M.H.N. Skandari, H.R. Erfanian, A.V. Kamyad, and S. Mohammadi. Optimal control of bone marrow in cancer chemotherapy. *European Journal of Experimental Biology*, 2(3):562–569, 2012.

[97] E. Szlachcic, P. Porombka, and J. Kotowski. Multi-objective optimization of cancer chemotherapy treatment. In *Computer Aided Systems Theory–EUROCAST 2011*, pages 256–263. Springer, 2012.

[98] M. V. Kothare, V. Balakrishnan, and M. Morari. Robust constrained model predictive control using linear matrix inequalities. *Automatica*, 32(10):1361–1379, 1996.

[99] R. Bruno, N. Vivier, C. Veyrat-Follet, G. Montay, and G. R. Rhodes. Population pharmacokinetics and pharmacokinetic-pharmacodynamic relationships for docetaxel. *Investigational New Drugs*, 19:163–169, 2001.

[100] E.L. Bradshaw-Pierce, S.G. Eckhardt, and D. L. Gustafson. A physiologically based pharmacokinetic model of docetaxel disposition: from mouse to man. *Clinical Cancer Research*, 13(9):2768–2776, 2007.

[101] J. Crown. Docetaxel: overview of an active drug for breast cancer. *The Oncologist*, 6(suppl 3):1–4, 2001.

[102] M.J. Piccart-Gebhart, T. Burzykowski, M. Buyse, G. Sledge, J. Carmichael, et al. Taxanes alone or in combination with anthracyclines as first-line therapy of patients with metastatic breast cancer. *Journal of Clinical Oncology*, 26(12):1980–1986, April 20, 2008.

[103] S.D. Baker, M. Zhao, C.K.K. Lee, J. Verweij, Y. Zabelina, J.R. Brahmer, A.C. Wolff, A. Sparreboom, and M.A. Carducci. Comparative pharmacokinetics of weekly and every-three-weeks docetaxel. *Clinical Cancer Research*, 10(6):1976–1983, 2004.

[104] J. Tabernero, M.A. Climent, A. Lluch, J. Albanell, J.B. Vermorken, A. Barnadas, A. Antn, C. Laurent, J. I. Mayordomo, N. Estaun, I. Losa, V. Guillem, J. Garcia-Conde, J. L. Tisaire, and J. Baselga. A multicentre, randomised phase ii study of weekly or 3-weekly docetaxel in patients with metastatic breast cancer. *Annals of Oncology*, 15(9):1358–1365, 2004.

[105] F.A. Shepherd, J. Dancey, R. Ramlau, K. Mattson, R. Gralla, M. ORourke, N. Levitan, et al. Prospective randomized trial of docetaxel versus best supportive care in patients with non small-cell lung cancer previously treated with platinum-based chemotherapy. *Journal of Clinical Oncology*, 18(10):2095–2103, 2000.

[106] G. Morstyn, L. Campbell, G. Lieschke, J.E. Layton, D. Maher, M. O'Connor, M. Green, W. Sheridan, M. Vincent, and K. Alton. Treatment of chemotherapy-induced neutropenia by subcutaneously administered granulocyte colony-stimulating factor with optimization of dose and duration of therapy. *Journal of Clinical Oncology*, 7(10):1554–1562, 1989.

[107] M.D. Green, H. Koelbl, J. Baselga, A. Galid, V. Guillem, P. Gascon, S. Siena, R.I. Lalisang, H. Samonigg, M.R. Clemens, V. Zani, B.C. Liang, J. Renwick, and M.J. Piccart. A randomized double-blind multicenter phase iii study of fixed-dose single-administration pegfilgrastim versus daily filgrastim in patients receiving myelosuppressive chemotherapy. *Annals of Oncology*, 14(1):29–35, 2003.

[108] M. Dougan and G. Dranoff. Immune therapy for cancer. *Annual Review of Immunology*, 27(1):83–117, 2009.

[109] C.J. Henry, Y. Huang, A.M. Wynne, and J.P. Godbout. Peripheral lipopolysaccharide (lps) challenge promotes microglial hyperactivity in aged mice that is associated with exaggerated induction of both pro-inflammatory il-1β and anti-inflammatory il-10 cytokines. *Brain, behavior, and immunity*, 23(3):309–317, 2009.

[110] B.T. Suratt, S.K. Young, J. Lieber, J.A. Nick, P.M. Henson, and G.S. Worthen. Neutrophil maturation and activation determine anatomic site of clearance from circulation. *American Journal of Physiology - Lung Cellular and Molecular Physiology*, 281(4):L913–L921, 2001.

[111] N. Borregaard. Neutrophils, from marrow to microbes. *Immunity*, 33(5):657 – 670, 2010.

[112] National Cancer Institute (U.S.). Cancer Therapy Evaluation Program. *Guidelines for reporting of adverse drug reactions*. NCI, Division of Cancer Treatment, Cancer Therapy Evaluation Program, 1988.

[113] E. Briasoulis, V. Karavasilis, D. Anastasopoulos, E. Tzamakou, G. Fountzilas, D. Rammou, V. Kostadima, and N. Pavlidis. Weekly docetaxel in minimally pretreated cancer patients: A dose-escalation study focused on feasibility and cumulative toxicity of long-term administration. *Annals of Oncology*, 10(6):701–706, 1999.

[114] C. Akgul, D.A. Moulding, and S.W. Edwards. Molecular control of neutrophil apoptosis. *FEBS Letters*, 487(3):318 – 322, 2001.

[115] S. Zarei, A. Mirtar, F. Rohwer, D.J. Conrad, R.J. Theilmann, and P. Salamon. Mucus distribution model in a lung with cystic fibrosis. *Computational and mathematical methods in medicine*, 2012, 2012.

[116] T. Portz, Y. Kuang, and J.D. Nagy. A clinical data validated mathematical model of prostate cancer growth under intermittent androgen suppression therapy. *AIP Advances*, 2(1):011002–011002, 2012.

[117] G. Benzekry, S.and Chapuisat, J. Ciccolini, A. Erlinger, and F. Hubert. A new mathematical model for optimizing the combination between antiangiogenic and cytotoxic drugs in oncology. *Comptes Rendus Mathematique*, 350(1):23–28, 2012.

[118] J. Siepmann and N.A. Peppas. Modeling of drug release from delivery systems based on hydroxypropyl methylcellulose (hpmc). *Advanced drug delivery reviews*, 2012.

[119] A. Tsygvintsev, S. Marino, and D.E. Kirschner. A mathematical model of gene therapy for the treatment of cancer. In *Mathematical Methods and Models in Biomedicine*, pages 367–385. Springer, 2013.

[120] E.Y. Klein, D.L. Smith, R. Laxminarayan, and S. Levin. Superinfection and the evolution of resistance to antimalarial drugs. *Proceedings of the Royal Society B: Biological Sciences*, 279(1743):3834–3842, 2012.

[121] N. Olhoff, J. Rasmussen, and E. Lund. A method of exact mumerical differentiation for error elimination in finite-element-based semi-analytical shape sensitivity analyses*. *Journal of Structural Mechanics*, 21(1):1–66, 1993.

[122] J.A. Jacquez and P. Greif. Numerical parameter identifiability and estimability: Integrating identifiability, estimability, and optimal sampling design. *Mathematical Biosciences*, 77(1):201–227, 1985.

[123] H. Park, Z. Li, X.O. Yang, S.H. Chang, R. Nurieva, Y. Wang, Y. Wang, L. Hood, Z. Zhu, Q. Tian, et al. A distinct lineage of cd4 t cells regulates tissue inflammation by producing interleukin 17. *Nature immunology*, 6(11):1133–1141, 2005.

[124] S. Aggarwal, N. Ghilardi, M. Xie, F. J. de Sauvage, and A.L. Gurney. Interleukin-23 promotes a distinct cd4 t cell activation state characterized by the production of interleukin-17. *Journal of Biological Chemistry*, 278(3):1910–1914, 2003.

[125] T. Lapidot, A. Dar, and O. Kollet. How do stem cells find their way home? *Blood*, 106(6):1901–1910, 2005.

[126] A. Uccelli, L. Moretta, and V. Pistoia. Mesenchymal stem cells in health and disease. *Nature Reviews Immunology*, 8(9):726–736, 2008.

[127] J.B. Johnnidis, M.H. Harris, R.T. Wheeler, S. Stehling-Sun, M.H. Lam, O. Kirak, T.R. Brummelkamp, M.D. Fleming, and F.D. Camargo. Regulation of progenitor cell

proliferation and granulocyte function by microrna-223. *Nature*, 451(7182):1125–1129, 2008.

[128] P. Anderlini, D. Przepiorka, R. Champlin, and M. Korbling. Biologic and clinical effects of granulocyte colony-stimulating factor in normal individuals. *Blood*, 88(8):2819–2825, 1996.

[129] V. Witko-Sarsat, P. Rieu, B. Descamps-Latscha, P. Lesavre, and L. Halbwachs-Mecarelli. Neutrophils: molecules, functions and pathophysiological aspects. *Laboratory investigation*, 80(5):617–653, 2000.

[130] A.J. Wood, G.J. Lieschke, and A.W. Burgess. Granulocyte colony-stimulating factor and granulocyte-macrophage colony-stimulating factor. *New England Journal of Medicine*, 327(1):28–35, 1992.

[131] D. Yen, J. Cheung, H. Scheerens, F. Poulet, T. McClanahan, B. Mckenzie, M.A. Kleinschek, et al. Il-23 is essential for t cell–mediated colitis and promotes inflammation via il-17 and il-6. *Journal of Clinical Investigation*, 116(5):1310–1316, 2006.

[132] S. Nakae, S. Saijo, R. Horai, K. Sudo, S. Mori, and Y. Iwakura. Il-17 production from activated t cells is required for the spontaneous development of destructive arthritis in mice deficient in il-1 receptor antagonist. *Proceedings of the National Academy of Sciences*, 100(10):5986–5990, 2003.

[133] P. Ye, F.H. Rodriguez, S. Kanaly, J. Stocking, K.L .and Schurr, P. Schwarzenberger, P. Oliver, W. Huang, P. Zhang, J. Zhang, et al. Requirement of interleukin 17 receptor signaling for lung cxc chemokine and granulocyte colony-stimulating factor expression, neutrophil recruitment, and host defense. *The Journal of experimental medicine*, 194(4):519–528, 2001.

[134] F. Fossiez, O. Djossou, P. Chomarat, L. Flores-Romo, S. Ait-Yahia, C. Maat, J. Pin, P. Garrone, E. Garcia, S. Saeland, et al. T cell interleukin-17 induces stromal cells to produce proinflammatory and hematopoietic cytokines. *The Journal of experimental medicine*, 183(6):2593–2603, 1996.

[135] U. Brunnberg, M. Mohr, R. Noppeney, H.A. Dürk, M.C. Sauerland, C. Müller-Tidow, U. Krug, S. Koschmieder, T. Kessler, R.M. Mesters, et al. Induction therapy of aml with ara-c plus daunorubicin versus ara-c plus gemtuzumab ozogamicin: a randomized phase ii trial in elderly patients. *Annals of oncology*, page mdr346, 2011.

[136] Sanofi. Sanofi returns to growth in q4 2013. Press Release, February 2014. http://m-en.sanofi.com/Images/35598_20140206_Q4_2013_en.pdf.

[137] F. Fossella, J.R. Pereira, J. von Pawel, A. Pluzanska, V. Gorbounova, E. Kaukel, K.V. Mattson, R. Ramlau, A. Szczsna, P. Fidias, et al. Randomized, multinational, phase iii study of docetaxel plus platinum combinations versus vinorelbine plus cisplatin for

advanced non–small-cell lung cancer: The tax 326 study group. *Journal of Clinical Oncology*, 21(16):3016–3024, 2003.

[138] L.T. Biegler. Solution of dynamic optimization problems by successive quadratic programming and orthogonal collocation. *Computers & chemical engineering*, 8(3):243–247, 1984.

[139] L. Norton. A gompertzian model of human breast cancer growth. *Cancer research*, 48(24 Part 1):7067–7071, 1988.

[140] L. Norton and J. Massagué. Is cancer a disease of self-seeding? *Nature medicine*, 12(8):875–878, 2006.

[141] R. Simon and L. Norton. The norton–simon hypothesis: designing more effective and less toxic chemotherapeutic regimens. *Nature Clinical Practice Oncology*, 3(8):406–407, 2006.

[142] S. Fulda and K.M. Debatin. Extrinsic versus intrinsic apoptosis pathways in anticancer chemotherapy. *Oncogene*, 25(34):4798–4811, 2006.

[143] C.S. Adjiman, I.P. Androulakis, and C.A. Floudas. Global optimization of mixed-integer nonlinear problems. *AIChE Journal*, 46(9):1769–1797, 2004.

[144] M.L. Bergamini, I. Grossmann, N. Scenna, and P. Aguirre. An improved piecewise outer-approximation algorithm for the global optimization of minlp models involving concave and bilinear terms. *Computers & Chemical Engineering*, 32(3):477–493, 2008.

[145] W.E. Hart. Python optimization modeling objects (pyomo). In *Operations Research and Cyber-Infrastructure*, pages 3–19. Springer, 2009.

[146] P. Therasse, S.G. Arbuck, E.A. Eisenhauer, J. Wanders, R.S. Kaplan, L. Rubinstein, J. Verweij, M. Van Glabbeke, A.T. van Oosterom, M.C. Christian, et al. New guidelines to evaluate the response to treatment in solid tumors. *Journal of the National Cancer Institute*, 92(3):205–216, 2000.

[147] F. Ghiringhelli, C. Menard, P.E. Puig, S. Ladoire, F. Roux, S.and Martin, E. Solary, A. Le Cesne, L. Zitvogel, and B. Chauffert. Metronomic cyclophosphamide regimen selectively depletes cd4+ cd25+ regulatory t cells and restores t and nk effector functions in end stage cancer patients. *Cancer Immunology, Immunotherapy*, 56(5):641–648, 2007.

[148] D. Moreno, S. Zalba, H. Colom, I.F. Trocóniz, C. Tros de Ilarduya, and M.J. Garrido. Biopharmaceutic and pharmacodynamic modeling of the in vitro antiproliferative effect of new controlled delivery systems of cisplatin. *European Journal of Pharmaceutical Sciences*, 37(3):341–350, 2009.

[149] B. Desoize, G. Berthiot, L. Manot, P. Coninx, and P. Dumont. Evaluation of a prediction model of cisplatin dose based on total platinum plasma concentration. *European Journal of Cancer*, 32(10):1734–1738, 1996.

[150] B. Erdlenbruch, M. Nier, W. Kern, W. Hiddemann, A. Pekrun, and M. Lakomek. Pharmacokinetics of cisplatin and relation to nephrotoxicity in paediatric patients. *European journal of clinical pharmacology*, 57(5):393–402, 2001.

[151] M.H. Hanigan and P. Devarajan. Cisplatin nephrotoxicity: molecular mechanisms. *Cancer therapy*, 1:47, 2003.

[152] P.A. Reece, I. Stafford, J. Russell, M. Khan, and PG Gill. Creatinine clearance as a predictor of ultrafilterable platinum disposition in cancer patients treated with cisplatin: relationship between peak ultrafilterable platinum plasma levels and nephrotoxicity. *Journal of Clinical Oncology*, 5(2):304–309, 1987.

[153] J. Sastry and S.J. Kellie. Severe neurotoxicity, ototoxicity and nephrotoxicity following high-dose cisplatin and amifostine. *Pediatric Hematology-Oncology*, 22(5):441–445, 2005.

[154] N. Pabla and Z. Dong. Cisplatin nephrotoxicity: mechanisms and renoprotective strategies. *Kidney international*, 73(9):994–1007, 2008.

[155] J.T. Hartmann, L.M. Fels, S. Knop, H. Stolte, L. Kanz, and C. Bokemeyer. A randomized trial comparing the nephrotoxicity of cisplatin/ifosfamide-based combination chemotherapy with or without amifostine in patients with solid tumors. *Investigational new drugs*, 18(3):281–289, 2000.

[156] V. Sresht, J.R. Bellare, and S.K. Gupta. Modeling the cytotoxicity of cisplatin. *Industrial & Engineering Chemistry Research*, 50(23):12872–12880, 2011.

[157] W.J. van der Vijgh. Clinical pharmacokinetics of carboplatin. *Clinical pharmacokinetics*, 21(4):242–261, 1991.

[158] J. Gallaher, A. Babu, S. Plevritis, and A.R.A. Anderson. Bridging population and tissue scale tumor dynamics: A new paradigm for understanding differences in tumor growth and metastatic disease. *Cancer research*, 74(2):426–435, 2014.

[159] G. Van den Berghe, P. Wouters, C. Weekers, F.and Verwaest, F. Bruyninckx, D. Schetz, M.and Vlasselaers, P. Ferdinande, P. Lauwers, and R. Bouillon. Intensive insulin therapy in critically ill patients. *New England Journal of Medicine*, 345(19):1359–1367, 2001.

[160] R.C. Andrews, B.R. Walker, et al. Glucocorticoids and insulin resistance: old hormones, new targets. *Clinical Science*, 96:513–523, 1999.

[161] C.A. Chu, D.K. Sindelar, D.W. Neal, E.J. Allen, E.P. Donahue, and A.D. Cherrington. Comparison of the direct and indirect effects of epinephrine on hepatic glucose production. *Journal of Clinical Investigation*, 99(5):1044, 1997.

[162] N. Venkatesan, J. Lim, C. Bouch, D. Marciano, and M.B. Davidson. Dexamethasone-induced impairment in skeletal muscle glucose transport is not reversed by inhibition of free fatty acid oxidation. *Metabolism*, 45(1):92–100, 1996.

[163] S. Beitland, H. Opdahl, T. Aspelin, L. Saetre, and T. Lyberg. Blood leucocyte cytokine production after lps stimulation at different concentrations of glucose and/or insulin. *Acta Anaesthesiologica Scandinavica*, 53(2):183–189, 2009.

[164] Y.H. Chew, Y.L. Shia, C.T. Lee, F.A.A. Majid, L.S. Chua, M.R. Sarmidi, and R.A. Aziz. Modeling of glucose regulation and insulin-signaling pathways. *Molecular and cellular endocrinology*, 303(1):13–24, 2009.

[165] R. Bellomo and M. Egi. What is a nice-sugar for patients in the intensive care unit? In *Mayo Clinic Proceedings*, volume 84, page 400. Mayo Foundation, 2009.

[166] M. Egi, R. Bellomo, E. Stachowski, C.J. French, and G. Hart. Variability of blood glucose concentration and short-term mortality in critically ill patients. *Anesthesiology*, 105(2):244–252, 2006.

[167] F.M. Brunkhorst, C. Engel, F. Bloos, A. Meier-Hellmann, M. Ragaller, N. Weiler, O. Moerer, M. Gruendling, M. Oppert, S. Grond, et al. Intensive insulin therapy and pentastarch resuscitation in severe sepsis. *New England Journal of Medicine*, 358(2):125–139, 2008.

[168] R.P. Dellinger, M.M. Levy, J.M. Carlet, J. Bion, M.M. Parker, R. Jaeschke, K. Reinhart, D.C. Angus, C. Brun-Buisson, R. Beale, et al. Surviving sepsis campaign: international guidelines for management of severe sepsis and septic shock: 2008. *Intensive care medicine*, 34(1):17–60, 2008.

[169] J.C. Preiser, P. Devos, S. Ruiz-Santana, C. Mélot, D. Annane, J. Groeneveld, G. Iapichino, X. Leverve, G. Nitenberg, P. Singer, et al. A prospective randomised multi-centre controlled trial on tight glucose control by intensive insulin therapy in adult intensive care units: the glucontrol study. *Intensive care medicine*, 35(10):1738–1748, 2009.

[170] G. Van den Berghe, A. Wilmer, G. Hermans, W. Meersseman, P.J. Wouters, I. Milants, E. Van Wijngaerden, H. Bobbaers, R. Bouillon, et al. Intensive insulin therapy in the medical icu. *New England Journal of Medicine*, 354(5):449, 2006.

[171] D.E.G. Griesdale, R.J. De Souza, R.M. Van Dam, D.K. Heyland, D.J. Cook, A. Malhotra, R. Dhaliwal, W.R. Henderson, D.R. Chittock, S. Finfer, et al. Intensive insulin therapy and mortality among critically ill patients: a meta-analysis including nice-sugar study data. *Canadian Medical Association Journal*, 180(8):821–827, 2009.

[172] A. De Gaetano and O. Arino. Mathematical modelling of the intravenous glucose tolerance test. *Journal of Mathematical Biology*, 40(2):136–168, 2000.

[173] T.M. Wallace and D.R. Matthews. The assessment of insulin resistance in man. *Diabetic Medicine*, 19(7):527–534, 2002.

[174] R.N. Bergman, R. Prager, A. Volund, and J.M. Olefsky. Equivalence of the insulin sensitivity index in man derived by the minimal model method and the euglycemic glucose clamp. *Journal of Clinical Investigation*, 79(3):790, 1987.

[175] R.C. Boston, D. Stefanovski, P.J. Moate, A.E. Sumner, R.M. Watanabe, and R.N. Bergman. Minmod millennium: a computer program to calculate glucose effectiveness and insulin sensitivity from the frequently sampled intravenous glucose tolerance test. *Diabetes technology & therapeutics*, 5(6):1003–1015, 2003.

[176] R.N. Bergman. Orchestration of glucose homeostasis from a small acorn to the california oak. *Diabetes*, 56(6):1489–1501, 2007.

[177] I. TOLIĆ, E. Mosekilde, and J. Sturis. Modeling the insulin–glucose feedback system: the significance of pulsatile insulin secretion. *Journal of Theoretical Biology*, 207(3):361–375, 2000.

[178] A. Roy and R.S. Parker. Dynamic modeling of free fatty acid, glucose, and insulin: An extended" minimal model". *Diabetes technology & therapeutics*, 8(6):617–626, 2006.

[179] A. Roy and R.S. Parker. Mixed meal modeling and disturbance rejection in type i diabetic patients. In *Engineering in Medicine and Biology Society, 2006. EMBS'06. 28th Annual International Conference of the IEEE*, pages 323–326. IEEE, 2006.

[180] N. Hernjak and F.J. Doyle III. Glucose control design using nonlinearity assessment techniques. *AIChE Journal*, 51(2):544–554, 2005.

[181] R.S. Parker, F.J. Doyle III, and N.A. Peppas. A model-based algorithm for blood glucose control in type i diabetic patients. *Biomedical Engineering, IEEE Transactions on*, 46(2):148–157, 1999.

[182] M. Breton, A. Farret, D. Bruttomesso, S. Anderson, L. Magni, S. Patek, C. Dalla Man, J. Place, S. Demartini, S. Del Favero, et al. Fully integrated artificial pancreas in type 1 diabetes modular closed-loop glucose control maintains near normoglycemia. *Diabetes*, 61(9):2230–2237, 2012.

[183] B.P. Kovatchev, M. Breton, C. Dalla Man, and C. Cobelli. In silico preclinical trials: a proof of concept in closed-loop control of type 1 diabetes. *Journal of diabetes science and technology*, 3(1):44–55, 2009.

[184] K. van Heusden, E. Dassau, H.C. Zisser, D.E. Seborg, and F.J. Doyle. Control-relevant models for glucose control using a priori patient characteristics. *Biomedical Engineering, IEEE Transactions on*, 59(7):1839–1849, 2012.

[185] A. Patel, S. MacMahon, J. Chalmers, L. Neal, B.and Billot, M. Woodward, M. Marre, M. Cooper, P. Glasziou, D. Grobbee, et al. Intensive blood glucose control and vascular outcomes in patients with type 2 diabetes. 2008.

[186] B.W. Bequette. A critical assessment of algorithms and challenges in the development of a closed-loop artificial pancreas. *Diabetes technology & therapeutics*, 7(1):28–47, 2005.

[187] X.W. Wong, J.G. Chase, G.M. Shaw, C.E. Hann, T. Lotz, J. Lin, I. Singh-Levett, L.J. Hollingsworth, O.S.W. Wong, and S. Andreassen. Model predictive glycaemic regulation in critical illness using insulin and nutrition input: a pilot study. *Medical engineering & physics*, 28(7):665–681, 2006.

[188] J. Lin, N.N. Razak, C.G. Pretty, A. Le Compte, P. Docherty, J.D. Parente, G.M. Shaw, C.E. Hann, and J. Geoffrey Chase. A physiological intensive control insulin-nutrition-glucose (icing) model validated in critically ill patients. *Computer methods and programs in biomedicine*, 102(2):192–205, 2011.

[189] R. Hovorka, V. Canonico, L.J. Chassin, U. Haueter, M. Massi-Benedetti, M.O. Federici, T.R. Pieber, H.C. Schaller, L. Schaupp, T. Vering, et al. Nonlinear model predictive control of glucose concentration in subjects with type 1 diabetes. *Physiological measurement*, 25(4):905, 2004.

[190] R. Hovorka, L.J. Chassin, M. Ellmerer, J. Plank, and M.E. Wilinska. A simulation model of glucose regulation in the critically ill. *Physiological measurement*, 29(8):959, 2008.

[191] S. Visweswaran, J. Mezger, G. Clermont, M. Hauskrecht, and G.F. Cooper. Identifying deviations from usual medical care using a statistical approach. In *AMIA Annual Symposium Proceedings*, volume 2010, page 827. American Medical Informatics Association, 2010.

[192] P.E. Cryer. Hypoglycaemia: the limiting factor in the glycaemic management of the critically ill? *Diabetologia*, 49(8):1722–1725, 2006.

[193] S.J. Finney, C. Zekveld, A. Elia, and T.W. Evans. Glucose control and mortality in critically ill patients. *JAMA: the journal of the American Medical Association*, 290(15):2041–2047, 2003.

[194] J.S. Krinsley and A. Grover. Severe hypoglycemia in critically ill patients: Risk factors and outcomes*. *Critical care medicine*, 35(10):2262–2267, 2007.

[195] J.G. Chase, G. Shaw, A. Le Compte, T. Lonergan, M. Willacy, X.W. Wong, J. Lin, T. Lotz, D. Lee, and C. Hann. Implementation and evaluation of the sprint protocol for tight glycaemic control in critically ill patients: a clinical practice change. *Critical Care*, 12(2):R49, 2008.

[196] M. Schetz, I. Vanhorebeek, P.J. Wouters, A. Wilmer, and G. Van den Berghe. Tight blood glucose control is renoprotective in critically ill patients. *Journal of the American Society of Nephrology*, 19(3):571–578, 2008.

[197] G. Van den Berghe, P.J. Wouters, R. Bouillon, F. Weekers, C. Verwaest, M. Schetz, D. Vlasselaers, P. Ferdinande, and P. Lauwers. Outcome benefit of intensive insulin therapy in the critically ill: Insulin dose versus glycemic control*. *Critical care medicine*, 31(2):359–366, 2003.

[198] S. Finfer, D.R. Chittock, S.Y. Su, D. Blair, D. Foster, V. Dhingra, R. Bellomo, D. Cook, P. Dodek, W.R. Henderson, et al. Intensive versus conventional glucose control in critically ill patients. *N Engl J Med*, 360(13):1283–1297, 2009.

[199] E. Dassau, H. Zisser, R.A. Harvey, M.W. Percival, B. Grosman, W. Bevier, S. Atlas, E.band Miller, R. Nimri, L. Jovanovič, et al. Clinical evaluation of a personalized artificialpancreas. *Diabetes care*, 2012.

[200] R. Nimri, T. Danne, O. Kordonouri, E. Atlas, N. Bratina, T. Biester, M. Avbelj, S. Miller, I. Muller, M. Phillip, et al. Overnight automated type 1 diabetes control under md-logic closed-loop system: a randomized crossover trial. *Pediatric Diabetes*, 2013.

[201] J.J Lee, E. Dassau, H. Zisser, R.A. Harvey, L. Jovanovič, F.J. Doyle 3rd, et al. In silico evaluation of an artificial pancreas combining exogenous ultrafast-acting technosphere insulin with zone model predictive control. *Journal of diabetes science and technology*, 7(1):215–226, 2012.

[202] B.P. Kovatchev, E. Renard, C. Cobelli, H.C. Zisser, P. Keith-Hynes, S.M. Anderson, S.A. Brown, D.R. Chernavvsky, M.D. Breton, A. Farret, et al. Feasibility of outpatient fully integrated closed-loop control first studies of wearable artificial pancreas. *Diabetes care*, 36(7):1851–1858, 2013.

[203] E. Dassau, H. Zisser, R.A. Harvey, M.W. Percival, B. Grosman, W. Bevier, E. Atlas, S. Miller, R. Nimri, L. Jovanovič, et al. Clinical evaluation of a personalized artificial pancreas. *Diabetes care*, 36(4):801–809, 2013.

[204] G.M. Grodsky. A threshold distribution hypothesis for packet storage of insulin and its mathematical modeling. *Journal of Clinical Investigation*, 51(8):2047, 1972.

[205] M. Nomura, M. Shichiri, R. Kawamori, Y. Yamasaki, N. Iwama, and H. Abe. A mathematical insulin-secretion model and its validation in isolated rat pancreatic islets perifusion. *Computers and biomedical research*, 17(6):570–579, 1984.

[206] A.R. Sedaghat, A. Sherman, and M.J. Quon. A mathematical model of metabolic insulin signaling pathways. *American Journal of Physiology-Endocrinology and Metabolism*, 283(5):E1084–E1101, 2002.

[207] E. Barth, G. Fischer, E.M. Schneider, L.L. Moldawer, and M. Georgieff, M.and Weiss. Peaks of endogenous g-csf serum concentrations are followed by an increase in respiratory burst activity of granulocytes in patients with septic shock. *Cytokine*, 17(5):275–284, 2002.

[208] T.K. Bratanova-Tochkova, H. Cheng, S. Daniel, S. Gunawardana, Y. Liu, J. Mulvaney-Musa, T. Schermerhorn, S.G. Straub, H. Yajima, and G.W. Sharp. Triggering and augmentation mechanisms, granule pools, and biphasic insulin secretion. *Diabetes*, 51(suppl 1):S83–S90, 2002.

[209] M.G. Pedersen, A. Corradin, G.M. Toffolo, C. Cobelli, M.G. Pedersen, A. Corradin, G.M. Toffolo, and C. Cobelli. A subcellular model of glucose-stimulated pancreatic insulin secretion. *Philosophical Transactions of the Royal Society A: Mathematical, Physical and Engineering Sciences*, 366(1880):3525–3543, 2008.

[210] M.G. Pedersen, C.D. Man, and C. Cobelli. Multiscale modeling of insulin secretion. *Biomedical Engineering, IEEE Transactions on*, 58(10):3020–3023, 2011.

[211] M.G. Pedersen and C. Cobelli. Multiscale modelling of insulin secretion during an intravenous glucose tolerance test. *Interface Focus*, 3(2), 2013.

[212] W.L. Clarke. The original clarke error grid analysis (ega). *Diabetes technology & therapeutics*, 7(5):776–779, 2005.

[213] B.P. Kovatchev, L.A. Gonder-Frederick, D.J. Cox, and W.L. Clarke. Evaluating the accuracy of continuous glucose-monitoring sensors continuous glucose–error grid analysis illustrated by therasense freestyle navigator data. *Diabetes Care*, 27(8):1922–1928, 2004.

[214] G. Sabio, M. Das, A. Mora, Z. Zhang, J.Y. Jun, H.J. Ko, T. Barrett, J.K. Kim, and R.J. Davis. A stress signaling pathway in adipose tissue regulates hepatic insulin resistance. *Science Signalling*, 322(5907):1539, 2008.

[215] J.N. Clore and L. Thurby-Hay. Glucocorticoid-induced hyperglycemia. *Endocrine Practice*, 15(5):469–474, 2009.

[216] C. de Luca and J.M. Olefsky. Inflammation and insulin resistance. *FEBS letters*, 582(1):97–105, 2008.

[217] K.M. Dungan, S.S. Braithwaite, and J.C. Preiser. Stress hyperglycaemia. *The Lancet*, 373(9677):1798–1807, 2009.

[218] C.H. Hung, C.M. Lee, C.H. Chen, T.H. Hu, S.R. Jiang, J.H. Wang, S.N. Lu, and P.W. Wang. Association of inflammatory and anti-inflammatory cytokines with insulin resistance in chronic hepatitis c. *Liver International*, 29(7):1086–1093, 2009.

[219] A. Hvidberg, S. Jorgensen, and J. Hilsted. The effect of genetically engineered glucagon on glucose recovery after hypoglycaemia in man. *British journal of clinical pharmacology*, 34(6):547–550, 2012.

[220] G. Kewalramani, P.J. Bilan, and A. Klip. Muscle insulin resistance: assault by lipids, cytokines and local macrophages. *Current Opinion in Clinical Nutrition & Metabolic Care*, 13(4):382–390, 2010.

[221] G. Schmelzeisen-Redeker, A. Staib, M. Strasser, U. Müller, and M. Schoemaker. Overview of a novel sensor for continuous glucose monitoring. *Journal of diabetes science and technology*, 7(4):808–814, 2013.